# Spectroscopy in fragile 2D materials : from Graphene Oxide to single molecules at hexagonal Boron Nitride

Anna Tararan

NNT : 2016SACLS441

# Thèse de doctorat de l'Université Paris-Saclay préparée Université Paris-Sud

Ecole doctorale n°572
Ondes et matières
Spécialité de doctorat : Physique de la matière condensée

par

**Anna Tararan**

# Spectroscopy in Fragile 2D Materials: from Graphene Oxide to Single Molecules at Hexagonal Boron Nitride

Thèse présentée et soutenue à Orsay, le 2 décembre 2016.

Composition du Jury :

| | | | |
|---|---|---|---|
| M. | Gérald Dujardin | Directeur de recherche<br>Université Paris-Sud, ISMO | (Président du jury) |
| Mme. | Cecilia Mattevi | Directrice de recherche<br>Imperial College | (Rapporteur) |
| M. | Jeremy Sloan | Professeur associé<br>University of Warwick | (Rapporteur) |
| M. | Claudio Attaccalite | Chargé de recherche<br>CINaM, Marseille | (Examinateur) |
| M. | Mathieu Kociak | Directeur de recherche<br>Université Paris-Sud, LPS | (Directeur de thèse) |
| M. | Alberto Zobelli | Maître de conférences<br>Université Paris-Sud, LPS | (Co-encadrant de thèse) |

# ABSTRACT

Electron energy loss spectroscopy (EELS) and cathodoluminescence (CL) in a scanning transmission electron microscope (STEM) are extremely powerful techniques for the study of individual nanostructures. Nevertheless, fast electrons damage extremely sensitive thin specimens, imposing strong limitations on the spatial resolution and the intensity of spectroscopic signals. During this thesis we have overcome this restriction by developing material-specific acquisition protocols for the study of some archetypical fragile nanosystems. In the first part of this thesis we have characterized graphene oxide (GO) and reduced graphene oxide (RGO) thin flakes by EELS spectroscopy in the STEM. Thanks to the particular set-up of our microscope and by experimentally defining the optimal illumination conditions, we have derived oxygen quantification maps of (R)GO at an unprecedented spatial resolution. On the basis also of EELS fine structures analysis, we have revised the existing proposed atomic models for these materials. Another class of exceedingly sensitive nanometric systems is represented by individual molecules, which are strongly affected by both illumination and chemical/physical environment. We have performed the first CL-STEM investigation on the luminescence of isolated molecules, thanks to a watchful choice of the substrate. Hexagonal boron nitride (h-BN) is a flat, chemically inert 2D material, that actively takes part in the CL process by absorbing the incident energy. Excitation transfer from h-BN to molecules and the use of an innovative random scan acquisition routine in the STEM have allowed to considerably lower illumination effects and improve CL intensity. Afterwards, the attractive optical properties of h-BN have led to the study of its cubic phase (c-BN), which has been up to now hindered by the poor quality of the crystals. By EELS in the STEM we have analysed c-BN crystals of the highest available purity, identifying a wider optical band-gap with respect to previous experimental studies and in better agreement with recent calculations. In commercial crystals, several defect-related emissions have been identified and analysed in terms of characteristic energy, spatial distribution and lifetime using CL and Hanbury-Brown and Twiss intensity interferometry.

# RÉSUMÉ

La spectroscopie de perte d'énergie des électrons (EELS) et la cathodoluminescence (CL) dans un microscope électronique en transmission à balayage (STEM) sont des techniques puissantes pour l'étude des nanostructures isolées. Cependant, des électrons rapides peuvent endommager fortement des échantillons minces et fragiles, ce qui limite la résolution spatiale et l'intensité des signaux spectroscopiques. Pendant cette thèse, nous avons dépassé cette restriction par le développement de protocoles d'acquisition spécifiques pour l'étude de certains archétypes de nanosystèmes fragiles. Dans la première partie de cette thèse, nous avons caractérisé des flocons minces de graphène oxydé (GO) et GO réduit (RGO) par EELS dans le STEM. Grâce aux spécificités techniques de notre microscope et à la définition des conditions d'illumination optimales, nous avons dérivé des cartes du contenu d'oxygène dans le (R)GO à une résolution spatiale inédite. Aussi, par l'analyse des pics EELS de structure fine, nous avons révisé les modèles atomiques proposés dans la littérature. Des molécules isolées constituent une autre classe de nanomatériaux fortement sensibles à l'irradiation et aussi à l'environnement chimique et physique. Nous avons conduit des expériences de CL sur des molécules individuelles, grâce à un choix avisé du substrat. Le nitrure de bore hexagonal (h-BN) est un matériau bidimensionnel chimiquement inerte, qui participe activement au processus de CL en absorbant l'énergie incidente. Le transfert de l'excitation aux molécules et l'utilisation d'une routine innovante d'acquisition par balayage aléatoire ont permis de réduire les effets d'illumination. Ensuite, l'intérêt porté aux propriétés optiques du h-BN a inspiré l'étude de sa phase cubique (c-BN), qui a été peu caractérisé auparavant à cause d'impuretés dans les cristaux. Nous avons analysé des cristaux de c-BN de haute pureté par EELS, en identifiant une bande interdite d'énergie plus grande que précédemment rapportée et plus proche des calculs les plus récents. Dans des cristaux moins purs, nous avons identifié et analysé plusieurs émissions associées à des défauts, en termes d'énergie caractéristique, distribution spatiale et temps de vie, par CL et interférométrie en intensité de Hanbury-Brown et Twiss.

# ACKNOWLEDGEMENTS

In these lines I would like to acknowledge all those who have contributed to the work presented in this thesis.

First of all, I wish to thank Alberto Zobelli for being an attentive supervisor, for the time he has dedicated to discuss with me and for giving me valuable suggestions. I am grateful to Mathieu Kociak for directing my thesis. I have highly appreciated his judgement and advices about my work and repeated encouragement. I owe a special thank also to Odile Stéphan for her support and kindness, and for her time and tenacity in supervising some major results presented in this thesis.

While working at the microscope, the technical assistance of Marcel Tencé and Jean-Denis Blazit has been particularly precious. Their skills in upgrading, developing and repairing the microscope have been fundamental to obtain some of the more interesting results of my thesis. The work and experience of Romain Bourrellier, Sophie Meuret and Luiz Tizei have represented an essential basis for many of the experiments I have conducted. Furthermore, I wish to acknowledge Stefano Di Sabatino, Matteo Gatti and Lucia Reining, from the theoretical spectroscopy group in École Polytechnique, for our recent and ongoing collaboration. I finally acknowledge the European network for electron microscopy, Esteem2, for financial support.

The friendly atmosphere I felt within the STEM group has been very important for me. I wish to thank sincerely my colleagues for their help in everyday life at the lab, their sympathy, congeniality, and their jokes. At the STEM group I have met kind people and very dear friends.

I'm deeply grateful to my family, especially to my parents, for their continuous support in my studies during these last years, as well as before. I dearly thank Eugène for his constant moral assistance (and lately also for excusing me from cooking and dish washing). Last but not least, I heartly thank my friends here in Paris, Fabio, Virginia, Camille, Boris, and Francesca, and those more far away but only geographically, Sara, Valeria, Livia, Letizia, Marco, Elena, and Martina, for their kind support.

# Table of Contents

# List of Abbreviations

| | |
|---|---|
| AFM | Atomic force microscopy |
| BF | Bright field |
| c-BN | Cubic boron nitride |
| CL | Cathodoluminescence |
| DFT | Density functional theory |
| EELS | Electron energy loss spectroscopy |
| ELNES | Energy-loss near-edge structures |
| FRET | Förster resonance energy transfer |
| FTIR | Fourier transform infrared spectroscopy |
| GO | Graphene oxide |
| h-BN | Hexagonal boron nitride |
| HAADF | High-angle annular dark field |
| HBT | Hanbury-Brown and Twiss (intensity interferometer) |
| HOMO | Highest occupied molecular orbital |
| HRTEM | High resolution transmission electron microscopy |
| LDA | Local density approximation |
| LUMO | Lowest unoccupied molecular orbital |
| NMR | Nuclear magnetic resonance |
| PCA | Principal component analysis |
| RGO | Reduced graphene oxide |
| S/N | Signal to noise ratio |
| SAED | Selected area electron diffraction |

| | |
|---|---|
| SNOM | Scanning near-field optical microscopy |
| SPE | Single photon emitter |
| STEM | Scanning transmission electron microscopy |
| STM | Scanning tunneling microscopy |
| STML | Scanning tunneling microscopy luminescence |
| SEM | Scanning electron microscopy |
| TEM | Transmission electron microscopy |
| TGA | Thermal gravimetric analysis |
| TPD | Temperature programmed desorption |
| XANES | X-ray absorption near edge structure |
| XPS | X-ray photoelectron spectroscopy |
| XRD | X-ray diffraction |
| ZLP | Zero loss peak |
| ZPL | Zero phonon line |

CHAPTER 1

# INTRODUCTION

Modern scanning transmission electron microscopy (STEM) coupled with spectroscopy techniques allows to investigate the optoelectronic properties of materials at a subatomic spatial resolution. In the last years, this characterization technique has acquired more and more relevance, with the increasing interest in nanoparticles, quantum confined systems and crystal defects. Indeed, using fast electrons these nanostructures can be probed individually, even when they are separated by just few nanometres. Nevertheless, in the particular study of sensitive materials, STEM spatial resolution remains strongly affected by illumination damages. These materials require indeed specific operation protocols in order to lower their exposure to illumination below the damage threshold. As a result, spectroscopy of sensitive materials is generally characterized by degraded spatial resolution and poor signal-to-noise ratio (or even undetectable signal), especially when studying extremely localized and isolated systems. Illumination damages concern organic materials, luminescent defects in crystals and small molecules, which are investigated in future advanced optoelectronic devices such as light emitting diodes, photovoltaics, single photon emitters for quantum information, and many others. The investigation of fragile materials represents at present a chief objective in electron microscopy research.

The aim of this thesis is the spectroscopic investigation of sensitive materials in the STEM while forcing the spatial resolution close to the damage-free ultimate limit. Within the STEM microscope different kinds of characterization techniques can be performed: electron energy loss spectroscopy (EELS), cathodoluminescence spectroscopy (CL), and Hanbury Brown and Twiss intensity interferometry (HBT). During this thesis, all of these have been employed for the study of the chemistry and optical response of low dimensional systems such as 2D materials, individual molecules and point defects in wide band-gap semiconductors.

EELS provides information on the chemical, electronic and optical properties of the specimen. The STEM group in Orsay is endowed with

a long tradition of STEM-EELS [1–5], but the study of sensitive materials is still quite new [6] and precise acquisition protocols had not yet been defined. While EELS spectroscopy is nowadays performed by several electron microscopy groups in the world, CL in a STEM microscope is a specificity of the machine in Orsay. Indeed, STEM-CL has been achieved in 2010 by the design and development of a dedicated custom-made detection system for the acquisition of photon emission from the electron-excited specimen [5,7]. Finally, more recently the microscope has been coupled with an HBT interferometer for the measurement of time-correlation effects in the photon emission [8]. Further developments are envisaged in the forthcoming microscope to be installed at the LPS (CHROMATEM project), where sub-Ångström spatial resolution and higher EELS spectral resolution ($\sim$10 meV) will be combined with both cathodoluminescence and light absorption spectroscopy, at low temperatures.

The described techniques have been applied, in this thesis, to the study of different materials and systems, whose in-depth characterization has been up to now hindered by illumination damages and the lack of sufficiently localized probes. In the first part of this this work, we have investigated the chemistry of graphene oxide (GO), a carbon material whose atomic structure and chemistry are still greatly unknown after more than a century research (Chapter 2). Afterwards, we turned our attention to isolated luminescent molecules. Illumination damages on small molecules are extremely important and become absolutely limiting at the scale of the individual molecule (Chapter 3). Finally, promising results previously obtained in Orsay on the luminescence of hexagonal boron nitride (h-BN) [9,10] have encouraged an analogous study of the cubic polymorph of boron and nitrogen (cubic boron nitride, c-BN, Chapter 4). The variety of problematics tackled during this thesis has permitted to develop material-specific experimental protocols, which in future could be extended to the study of other experimental systems.

In the following we provide some additional details on the state of the art about these subjects and motivations for our study.

**The chemistry of GO**

GO is a very popular material with widespread applications, whose atomic structure remains significantly undetermined despite experimental research over more than a century. The reason is partly GO sensitivity to high energy illumination, which has prevented the use of strongly local probes in spectroscopy. In this thesis, the investigation of GO by STEM-EELS was intended to provide some fundamental insights into its local

chemical composition and atomic bonding configuration at an unprecedented spatial resolution.

The history of GO dates back to 1859 [11]. The material can be described as a graphene layer decorated with oxygen functional groups and it is obtained by liquid exfoliation of chemically oxidized graphite (graphite oxide) [11–13]. At a later stage, a graphene-like material known as reduced graphene oxide (RGO) can be derived from GO, by removing the oxygen functionalities [14, 15]. In the last years, it has attracted remarkable interest as a precursor for a large-scale and low-cost production of graphene-based materials and as a fundamental constituent in new functional composite materials for optoelectronics, photovoltaics and nano-biology devices [14, 16–18]. However, after more than 150 years since its discovery, many questions remain open about the exact chemistry and structure of GO at the atomic scale [14, 16–18].

Previously, several difficulties have prevented from exactly defining the oxygen content in GO and the kind of oxygen functional groups. First of all, GO appears as a very complex material, whose chemistry and structure strongly depend on the specific graphite precursor and oxidation parameters [14, 16]. As a consequence, GO samples do not look exactly alike and a non stoichiometric nature has been proposed for the GO structure [19]. Moreover GO turned out to be unstable in air and water, resulting in spontaneous reduction and flakes fragmentation [20–23]. The uncertainties on GO naturally reflect on RGO, whose chemistry and structure also depend on the particular reduction method and parameters [14, 16–18]. This lack of knowledge represents a strong limit for the understanding of (R)GO physical properties and hence for a controlled use of these promising functional materials.

New insights could be provided only through the use of improved characterization techniques. Up to now, several spectroscopic techniques have been used to determine the type and amount of oxygen functional groups. In previous studies, the oxygen content has been evaluated in a range between about 15 and 35 atomic percent (at.%), i.e. between $\sim$5:1 and $\sim$2:1 in terms of C/O atomic ratio. In RGO the oxygen content can be lowered to a limit of 0.4 at.% ($\sim$250:1 C/O atomic ratio), depending on the particular reduction process [14, 16–18]. However, these values can only be considered as spatial average quantifications, that cannot account for the irregular chemistry of GO. Indeed, strong structural inhomogeneities at the nanometre scale have been revealed in both GO and RGO by high resolution transmission electron microscopy (HRTEM) [24–27].

Decisive evidences on GO chemistry could only be derived by spectroscopy at the atomic scale. Standard STEM-EELS spectroscopy could in principle be suitable for such analysis, providing elemental quantification by core EELS mapping and chemical structure analysis through energy-loss near-edge structures (ELNES), down to the atomic scale [28]. However, the limited use of this technique for the study of GO and RGO [29,30] resides in the strong sensitivity of these materials to high energy electron irradiation. For instance, atoms mobility and fast amorphisation have been clearly demonstrated by time series of HRTEM images, at 80 kV acceleration voltage [25, 27]. Illumination sensitivity is indeed highly expected in the case of GO and RGO, since single or few layers thick specimens and light atoms are intrinsically more affected by radiation damages, such as knock-on of carbon atoms and radiolysis of oxygen functionalities resulting in mass loss. Irradiation effects in a STEM could in principle be strongly reduced by the use of low accelerating voltages, low electron-dose and sample cooling [31].

In this thesis work, thanks to a dedicated experimental set up combining a LN cooling system at the sample stage with a low noise LN cooled CCD camera, we have investigated few layer GO and RGO by core EELS spectrum imaging in a STEM microscope in low dose acquisition modes. We have shown that the oxygen content in individual (R)GO flakes is strongly heterogeneous at the nanometric scale and that specific near-edge carbon fine structures can be associated to different oxygen contents and bindings, indicating separated chemical phases. Finally, on the basis of these experimental evidences and complementary DFT-based numerical simulations, we have suggested a structural model for the highly oxidized regions in GO where all carbon atoms are functionalized by -OH groups.

**Luminescence from single molecules**

Single luminescent molecules are a prominent topic in current research. In the STEM-CL set-up in Orsay, we can take advantage from the high spatial resolution, but fast electron illumination easily destroys isolated molecules. In this thesis, we have investigated the CL emission from free molecules deposited on the surface of h-BN flakes. h-BN is a well-known material for its very intense CL in the far ultraviolet (UV) range [9, 10, 32]. The idea was hence to use h-BN as an effective absorber of energy from incident electrons and test the CL emission from the h-BN-molecules coupled system. Molecule excitation avoiding direct exposure to the beam could in principle solve the problem of illumination damages.

The interest in single molecules has kept growing in the fields of biol-

ogy and physics since the 1990's. Indeed, as their electronic properties are very sensitive to the local chemical environment, they represent nanometer size probes; fluorescent molecules are used to label biological objects for optical in vivo imaging, and particle tracking; as two-levels quantum systems, they can behave as single photon emitters, which are highly studied today for applications in quantum information and cryptography. The first optical detection of single molecule (isolated molecules in a crystalline matrix) was reported in 1989 by W. E. Moerner and L. Kador [33] and consisted in a particular signature in the absorption spectrum obtained by frequency double-modulation techniques. About one year later, fluorescence measurements were performed on single molecules [34, 35]. Since then, many microscopy and spectroscopy techniques have been applied to the study of single molecules and developed for this purpose, especially near-field fluorescence microscopy and other techniques leading to super-resolution microscopy, which was recognised with the Nobel prize in Chemistry 2014. Scanning probe techniques such as STM and AFM allow single molecule investigation at a submolecular spatial resolution.

Cathodoluminescence, performed in a scanning electron microscope (SEM), has been little used for the study of molecular dyes and related systems. First SEM-CL images of labelled biological samples were obtained in 1966 [36]. However, despite the higher spatial resolution, optical microscopies have been preferred in this field over electron-based techiniques, due to sample damaging by the electron beam and the technical difficulties in studying in vivo specimens (vacuum and cryogenic temperatures). SEM-CL emission from a wide list of dyes has been reported to be too weak for practical application in bio-CL and a decreased intensity upon exposure to the electron beam has been observed [37]. Finally, CL emission from a single molecule has not been reported yet.

A STEM-CL system would in principle allow molecular and submolecular spatial resolution. This technique presents several interesting features including a wide excitation spectral range, wide field of view, fast acquisition. Nevertheless, the way to excite a single molecule with an accelerated electron beam while avoiding illumination damages represents a strong limitation. In this study we have taken advantage from low temperatures at the sample stage and the use of the substrate as a mediator of the excitation. Indeed, an electron-hole excitation induced by the electron beam in a semiconductor may travel in the material and recombine at a defect site. A molecule deposited on the semiconductor's surface may act in the same way, introducing spatially localized electronic levels within the

material's band-gap, which could take part in the recombination process. If occupied and unoccupied molecular orbitals are comprised within the substrate's optical band-gap, there are chances to observe a pure molecular cathodoluminescence emission. For the choice of the substrate, h-BN thin flakes have appeared as an excellent candidate. Indeed, the pristine electronic structure of the deposited isolated molecules should not be altered by the flat and chemically inert surface of this material. h-BN displays a wide optical band-gap, which could be suitable to study a wide range of molecules. Finally, strong CL emissions have been observed [32], and recently characterized by STEM-CL in Orsay [9, 10]. Therefore, in a coupled system with isolated molecules on its surface, h-BN represents a good absorber and transmitter of electron excitations and a chemically inert environment for the molecules.

By STEM-CL from molecules deposited in high dilution regime on thin h-BN flakes, we have observed very sharp and spatially-localized emissions, which do not correspond to molecular crystal emissions and cannot be attributed to h-BN alone. However, the exact electron transitions giving rise to these luminescence peaks and the precise excitation-transfer mechanism remain unclear. Concerning illumination damages, it was observed that the traditional sequential line-by-line scan employed in hyperspectral image acquisition could be responsible for abrupt disappearance of the CL emission. A brand new algorithm for electron beam random scan has been tested. It is expected that in the random routine, the energy deposited in an illuminated area can be evacuated before an adjacent pixel is illuminated. We have demonstrated that the random scan offers new perspectives in CL investigation of sensitive materials and in terms of compressed sensing techniques. It's use might lead to considerable advantages also in EELS.

**Optical properties of c-BN**

Recent STEM-CL+HBT studies in Orsay have given promising insights into the optical properties of h-BN [9,10]. c-BN shares some interesting features with its hexagonal counterpart, such as a very intense luminescence, a wide energy band-gap, bright and stable luminescent crystal defects. In this thesis we have characterized the optical properties of c-BN crystals by STEM-EELS, CL and HBT techniques.

Cubic boron nitride was synthesized for the first time in 1957, by high-pressure high-temperature conversion from the hexagonal phase, in analogy with synthetic diamond [38, 39]. c-BN is the zinc-blende allotropic form of BN and it is the second hardest material after diamond, which

c-BN exceeds for its superior thermal and chemical stability [38, 40]. Sintered c-BN is used in industry as cutting and abrasive tool, especially in presence of ferrous metals, which are able to degrade diamond.

Similarly to h-BN, the study of c-BN optical properties has been for long hindered. Indeed, only recently high quality crystals have become available [41, 42] and CL experiments at high energies ($\sim$6 eV) have been performed [43]. The width of c-BN energy band-gap is expected to exceed that of h-BN, but its exact value is still unknown. Experimentally, a maximum value of 6.4 eV has been estimated from absorption and reflectance measurements since the 1970's [44, 45]. Theoretically, c-BN has been described as an indirect gap semiconductor and a proper treatment of many-body effects in the GW approximation provides a minimal onset for optical transitions at 11.75 eV. The addition of excitonic effects by solving the Bethe-Salpeter equation (BSE) has resulted into a final optical gap of 11.4 eV [46]. This value is in contrast with the experimental optical band-gap.

This discussion is quite similar to the case of h-BN. Indeed, the width and nature of h-BN band-gap have been for a long time evasive. Both experimental and theoretical studies have initially provided underestimated values [47, 48] and CL measurements in the UV on high purity crystals have been achieved only in 2004 [32]. Moreover, experiments affirmed a direct energy gap while numerical simulations predicted an indirect gap [32, 49, 50]. Also, the nature of the several observed excitonic emissions has been controversial [32,49–51]. The previous STEM-CL study here in Orsay has revealed the spatial distribution of these excitonic emissions along h-BN flakes, and their origin has been correlated with changes in the stacking order of the material, induced by folding of the atomic planes [9]. This very year, low temperature PL experiments have established that h-BN optical band-gap is 5.955 eV wide [52].

In addition to band-gap edge emissions, c-BN displays a wide series of luminescent phonon-assisted features within the energy gap. Since the earlier works in the 1980's, they have been attributed to electron transitions involving vacancy or impurity levels [53–58], as supported by several numerical simulations [59, 59–64]. However, the possibility of h-BN inclusions, the uncertainty about c-BN band-gap and the lack of spatially resolved optical measurements encourage further discussion. Moreover, by analogy with h-BN, interesting optical properties may be expected from luminescent defects in c-BN. Indeed, several emissions have been observed within h-BN band-gap and associated to crystal defects [48, 65–72].

In particular, the phonon-assisted emission at 4.09 eV [68,73,74] has been recently studied in Orsay using STEM-CL-HBT and attributed to a single point defect, most probably a substitutional carbon at a nitrogen site [10]. Other emissions with SPE character have been revealed at lower energies (1.63-2.15 eV) [69–72].

In this thesis we have investigated the optical properties of c-BN crystals by EELS and CL spectroscopy in the STEM microscope. New insights into the experimental determination of the optical band-gap have been pursued by studying high-purity c-BN crystals of the best quality currently available [42] and using EELS in the low-loss range. Indeed, the very low density of crystal defects present in these samples is a fundamental requirement in order to identify the real band edge, which could otherwise be confused with defect-related electronic levels below the gap. Moreover, EELS is the most suitable technique for this purpose, since the expected high energy value cannot be achieved by optical absorption. The absorption onset observed in our experiments appears higher than reported by previous experimental works [43]. Additional information on the optical properties has been derived by Kramers-Kronig analysis. We have studied also c-BN emissions within the band-gap. CL investigations were performed especially on commercial crystals, which bear more defects and impurities. Many phonon-assisted emissions have been revealed, some of them not yet reported in literature. For the higher energy features among these, HBT experiments have been conducted in order to establish the lifetime of the associated excited state and the possible SPE nature. Finally, the study of annealed c-BN crystals by both EELS and CL has suggested the formation of small h-BN phase inclusions.

CHAPTER 2

# EXPERIMENTAL TECHNIQUES

This chapter introduces some basic principles on the characterization techniques employed during this thesis: conventional and scanning transmission electron microscopy, electron energy loss spectroscopy, cathodoluminescence spectroscopy and Hanbury-Brown and Twiss intensity interferometry. Some notions concerning illumination damages in the microscope and data treatment by principal components analysis (PCA) will also be provided.

## 2.1 Transmission electron microscopy

Conventional TEM microscopy derives its origin from the work of E. Ruska and M. Knoll in 1932 (Nobel in Physics 1986) [75, 76]. The operating principle consists in a beam of fast electrons transmitted through a thin sample and focused by an optical system to form an enlarged image ($\sim 10^6\times$) on a fluorescent screen, as represented in figure 2.1. The electron beam is formed by condensing and accelerating electrons extracted from a sharp refractory metal tip (electron gun) by thermionic or field emission. Typical acceleration voltages are 60-300 kV. A series of electromagnetic lenses and apertures centred around the optical axis of the microscope allows to operate on the electron beam. Condenser lenses collimate the beam, which then reaches the specimen and is partially diffracted. The objective lens focuses the diffracted electrons and an image of the sample is formed on the image plane of the lens. The image is then enlarged by the intermediate lenses and finally projected by projector lenses on a phosphorescent screen or CCD camera (Fig. 2.1). Apertures may be inserted along the optical axis at the level of the objective focal plane (objective aperture) or image plane (selected area aperture). The first one allows to select particular spots of the diffraction pattern deriving from the illuminated specimen (Bragg diffraction) in order to restrict the contribution to image formation to only specific families of crystal planes. The selected

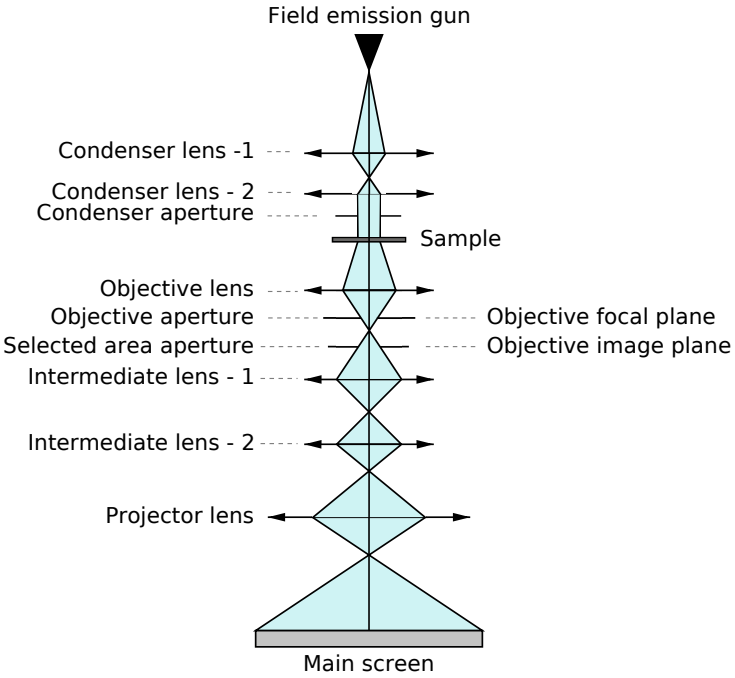


Figure 2.1: *Conventional TEM microscope. Collection and convergence angles are exaggerated for clarity. Real values are in the order of 10 mrad.*

area aperture is used to choose the area of the specimen whose diffraction pattern is projected on the fluorescent screen (diffraction imaging mode of the TEM microscope) [75].

The contrast in TEM image arises from the interference between elastically scattered electrons and primary electrons, while inelastically scattered electrons contribute only to a diffuse background. Primary beam electrons emerging from the condenser lenses may be described as coherent plane waves. As a result of the interaction with the total projected atomic potential of the specimen they undergo an amplitude decrease (negligible for thin specimens) and a dephasing. An additional dephasing is introduced by lens aberrations, while electrons scattered at high angles are suppressed by the insertion of an aperture (the microscope operates as a low pass filter in reciprocal space). This effect is fundamental for the image formation in the case of thin specimens, because if all diffracted electrons were driven to the fluorescent screen by a perfect objective lens, the incident beam would be perfectly reconstructed and no contrast would be visible. Since diffraction and interference events are at the origin of the image, its interpretation is not straightforward and is usually carried out

by comparison with simulations.

The image resolution is defined as the shortest distance between two features in the specimen that appear distinct in the image. It is quantified by the Rayleigh criterion as $r = 0.61\lambda/n\sin\mu$, where $\lambda$ is the probe wavelength and $n\sin\mu$ the numerical aperture the objective lens, with $\mu$ its semi-angle of collection. Typically, with an electron wavelength of 0.0037 nm (at 100 keV) and 10 mrad numerical aperture, the resolution is 0.22 nm.

**Akashi Topcon EM-002B**

The TEM microscope employed in this work is an Akashi Topcon EM-002B. The electron source is a $LaB_6$ tip, thermionic emission is obtained at a temperature of about 1700 K, and acceleration voltages may be tuned in the range of 60-200 kV. The vacuum level in the column is $\sim 3 \cdot 10^{-7}$ Torr. The side-entry specimen holder is provided with a double-tilt system allowing a $\pm 10^\circ$ rotation. The pole piece coefficients of spherical aberration ($C_s$) and chromatic aberration ($C_c$) are respectively 0.4 mm and 0.8 mm. The spatial resolution is 0.19 nm at 100 kV acceleration voltage.

## 2.2 Scanning transmission electron microscopy

In a STEM microscope the objective lens focuses the electron beam at the sample stage (Fig. 2.2), forming an illumination spot of size down to $0.5$ Å. A system of coils before the objective lens allows to deflect the beam in order to perform a scan over the sample. The image is thus acquired sequentially and the signal detected at each beam position over the specimen is responsible for one pixel of the image.

The detection of transmitted electrons is performed simultaneously using two detectors. The bright field (BF) detector (Fig. 2.2) is placed on the optical axis of the microscope and is thus exposed to primary unscattered electrons, elastically diffracted electrons and inelastically scattered electrons, up to a semiangle of less than $1^\circ$ (about 10 mrad). BF images are hence characterized by dark contrast over a bright background, as in TEM. The high-angle annular dark field (HAADF) detector, enclosing the BF detector, collects primary electrons elastically scattered by the electrostatic potential at atomic nuclei in the specimen (Rutherford scattering), in a semiangle range from about 2 to $9^\circ$ (50–150 mrad) [75]. In DF images, objects appear bright over a no-signal black background. The image intensity in this case is directly related to the scattering probability. As a function of the semiangle acceptance range $\beta$ of the DF detector, the image

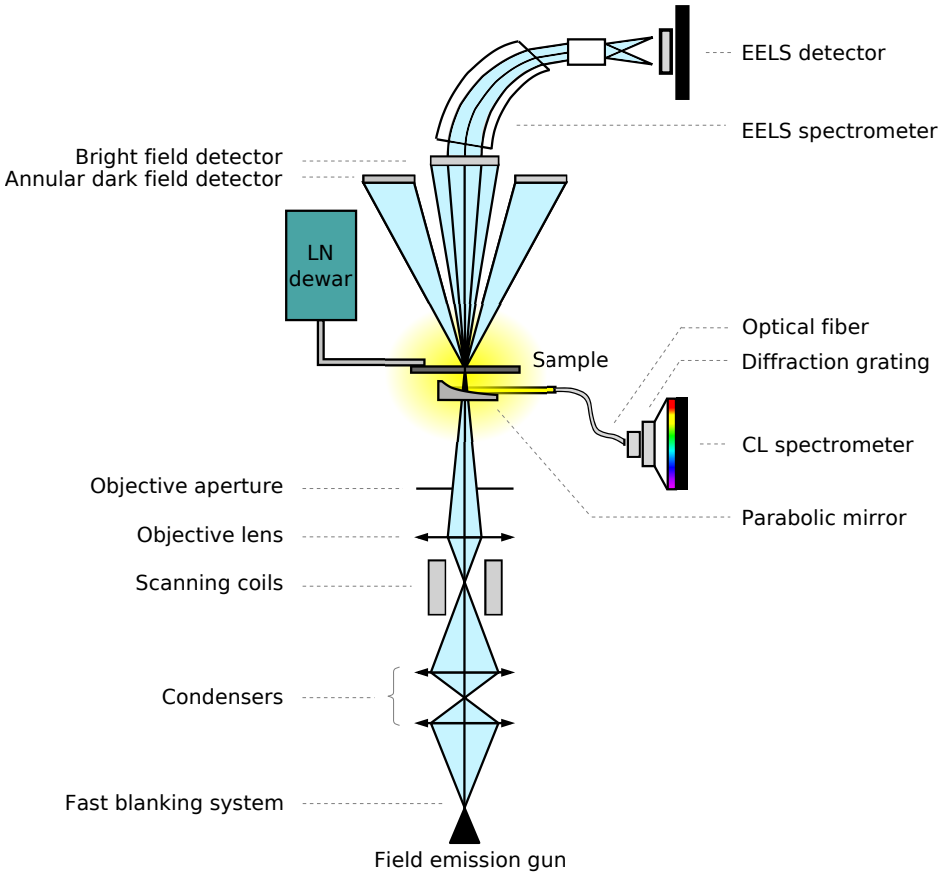


Figure 2.2: *STEM microscope equipped with a liquid nitrogen system at the sample stage (LN dewar) and detection systems for EELS and CL spectroscopy. Collection and convergence angles are exaggerated for clarity. Real values are in the order of 10 mrad.*

intensity is described by

$$I(\beta) = I_0(\beta)\rho t\sigma(\beta), \tag{2.1}$$

where $I_0(\beta)$ is the incoming beam intensity, $\rho$ and $t$ are the specimen atomic density and thickness, and $\sigma(\beta)$ is the elastic cross section. This last one conceals a dependence on the atomic number $Z$ as $Z^{4/3}$ [75]. If more elements constitute the illuminated volume, an effective $Z$ should be considered, obtained as the sum of the atomic numbers of the single

elements, weighted by their atomic ratio $f$ [28]:

$$Z_{eff} \approx \frac{\sum_i f_i Z_i^{1.3}}{\sum_i f_i Z_i^{0.3}}. \tag{2.2}$$

For this reason, heavier (in terms of $Z$), thicker and/or denser objects appear brighter in the images.

The simultaneous acquisition and comparison of BF and DF images is particularly helpful for image interpretation. In addition, multiple spectroscopic signals can be collected at the same time: the microscope used during this thesis is fitted with an EELS spectrometer and a light collection system connected with a spectrometer for CL spectroscopy (as represented in Fig. 2.2); the CL spectrometer can be easily replaced with an HBT interferometer. These techniques will be described in the following sections. The interest in performing such spectroscopic investigations in a STEM is of course the very small excitation volume defined in the material by the focused electron beam. Moreover, one spectrum can be acquired at every pixel of a STEM image: one spectrum at every position of the electron beam during the scan of the sample (Fig. 2.3). This acquisition mode produces a 3D data set known as hyperspectral image (or spectrum image) [1]. The data processing of hyperspectral images allows to correlate spectroscopic signals and sample morphology. Spatially resolved maps of particular spectroscopic features may be extracted, such as EELS chemical maps or CL filtered emission maps.

## 2.3 Electron energy loss spectroscopy

EELS spectroscopy provides information on the chemical composition, chemical bonding, optical and electronic properties of the specimen, by measuring the energy loss experienced by the incident electrons during their interaction with the matter. Fig. 2.4 shows a typical EELS spectrum. The great majority of primary fast electrons passes through the sample without undergoing any scattering event. They reach the spectrometer conserving their initial energy and form the zero-loss peak (ZLP, or elastic peak), at zero energy loss. This is the most intense feature in the spectrum. Inelastic scattering with single valence electrons or plasmons in the specimen are responsible for small energy losses: this is the low-loss region of the spectrum, below 100 eV energy loss. Interaction with core level electrons induces energy losses of the order of keV. The core-loss region of the

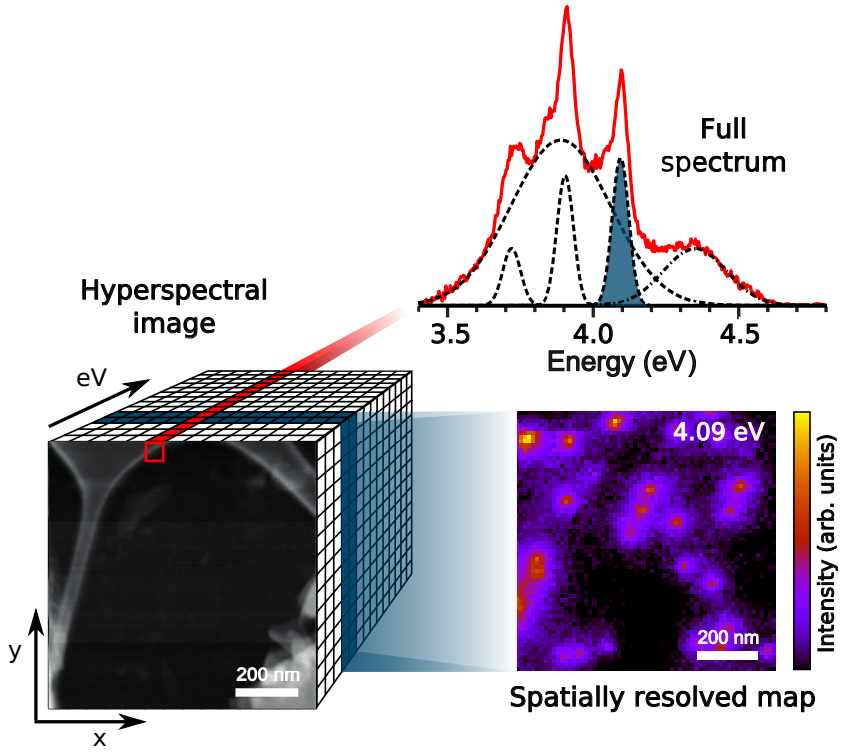


Figure 2.3: *Graphic representation of a hyperspectral image. Height and length are the spatial coordinates (the STEM image), while the depth is the energy. Each row of pixels along the energy axis corresponds to the full spectrum acquired in that pixel of the image. Processing of all the spectra allows to derive spatially resolved maps associated with individual spectral components.*

EELS spectra is characterized by much weaker intensity and contains the chemical information about the sample [28,75].

## 2.4 Low-loss EELS

Energy losses in the low-loss region correspond to single or collective excitations of valence electrons in the material. Collective excitations (plasmons) are the most intense feature in the EELS spectrum after the ZLP (Fig. 2.4). In the free-electron gas approximation, the energy of the volume plasmon is $E_p = \hbar\omega_p$, where the $\omega_p$ is the plasmon frequency derived in the Drude model $\omega_p = \sqrt{ne^2/\epsilon_0 m}$, with $n$ the electron density, $e$ and $m$ respectively the electron charge and mass, and $\epsilon_0$ the permittivity of free space [28]. Other possible energy-loss induced excitations in the specimen are surface plasmons and inter-/intra-band individual elec-

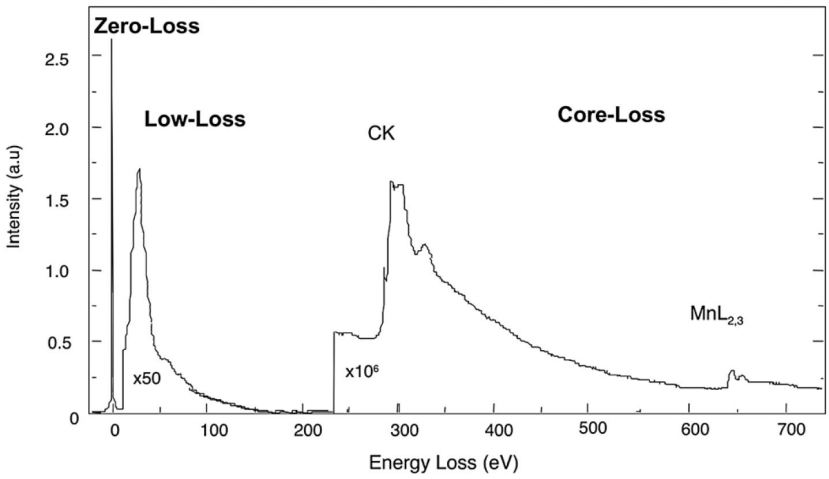


Figure 2.4: *EELS spectrum of a carbon nanotube filled with manganese showing the intensity ratio between zero loss peak, low-loss region and core-loss region. Figure extracted from ref. [77].*

tronic transitions with possible excitonic effects, which add fine structures to the plasmon peak. In the case of single-electron excitations, the energy-loss function is related to the local band structure of the material and reflects the joint density of states between the initial and final states of the excited electron (valence and conduction bands in the case of semiconductors), weighted by the transition matrix element (Fermi's golden rule). Moreover, the presence of a region with a low intensity between the ZLP and the rise of the low-loss signature is indicative of an energy gap in the material band structure [75]. The analysis of low-loss spectra allows to derive several local quantitative information about the specimen: the free-electron density, optical properties such as the local dielectric constant, absorption coefficient and reflectivity, the local thickness, the width of the energy band-gap, and the energy associated with local (possibily defect-related) single-electron excitations.

**Kramers-Kronig analysis**

In the single-scattering approximation, the energy-loss function depends on the complex relative permittivity (or dielectric function) $\epsilon(E) = \epsilon_1(E) + i\epsilon_2(E)$ as

$$I(E) \propto \Im\left[\frac{-1}{\epsilon(E)}\right], \tag{2.3}$$

where $E$ indicates the energy loss. The Kramers-Kronig (K-K) relations allow to calculate the $\Re\left[1/\epsilon(E)\right]$ as a function of $\Im\left[-1/\epsilon(E)\right]$

$$\Re\left[1/\epsilon(E)\right] = 1 - \frac{2}{\pi} P \int_0^\infty \Im\left[-1/\epsilon(E')\right] \frac{E' dE'}{E'^2 - E^2}, \tag{2.4}$$

where $P$ indicates the Cauchy's principal part around the pole $E = E'$. The dielectric function $\epsilon(E)$, can then be obtained from

$$\epsilon(E) = \epsilon_1(E) + i\epsilon_2(E) = \frac{\Re\left[1/\epsilon(E)\right] + i\Im\left[-1/\epsilon(E)\right]}{\left\{\Re\left[1/\epsilon(E)\right]\right\}^2 + \left\{\Im\left[-1/\epsilon(E)\right]\right\}^2}. \tag{2.5}$$

and $\epsilon_1(E)$ and $\epsilon_2(E)$ can be derived by equating real and imaginary parts of this relation. The local absorption coefficient and reflectivity of the specimen can then be calculated, as well as the specimen local thickness [28].

**Deconvolution**

However, in order to apply the K-K analysis, the single-scattering low-loss spectrum must be retrieved from the experimental spectrum, which in general contains a plural scattering component and is affected by the instrument response. This can be obtained through deconvolution techniques. The Fourier-log deconvolution method is based on the observation that in the assumption of independent scattering events the spectral intensity associated to $n$ inelastic scattering events and integrated over energy loss is governed by a Poisson distribution

$$I_n = I_0 P(n; t/\lambda) = I_0 \frac{(t/\lambda)^n}{n!} e^{-t/\lambda} \tag{2.6}$$

where $\lambda$ is the mean free path for inelastic scattering. The experimental spectrum in the case of $n = 0$ inelastic scattering events (that is simply the ZLP) is the convolution of the response function of the instrument with the real spectrum. Inelastic scattering of order $n$ corresponds to $n$ times selfconvolutions of the real spectrum. By working with Fourier transforms the convolutions become products and the real low-loss spectrum can be calculated [28].

## 2.5 Core-loss EELS

In the case of core-losses, the energy loss of the primary electron allows the transition of a core electron in the material (e.g. $1s$ state) to an unoccu-

pied level (e.g. $p$ state in the conduction band). Hence, core EELS signals consists of a sharp absorption edge at the energy loss corresponding to the inner-electron binding energy (ionization threshold), followed by a decaying intensity arising from higher energy transfers [75]. Since core electrons binding energy is typical of the chemical element, absorption edges are associated with specific elements and core shells (i.e. $K$, $L_1$, $L_{2,3}$, etc. for $1s$, $2s$, $2p$, etc. electrons). For example, carbon K-edge and manganese $L_{2,3}$-edge are shown in Fig. 2.4.

**Elemental quantification**

Quantification of the atomic amount of chemical species in the sample can be performed by integration of the core-loss absorption signals. In the approximation of single ionization events, the total EELS spectral intensity $I$ is proportional to the primary beam intensity $I_0$, the elemental (and shell) specific cross section for the inelastic scattering $\sigma$ and the number of scattering centres in the specimen $N$ (i.e. the surface projected density of atoms):

$$I(\beta, \Delta E) \approx N I_0(\beta, \Delta E)\sigma(\beta, \Delta E) \tag{2.7}$$

for a specific acceptance semiangle $\beta$ at the entrance of the spectrometer and an energy window of width $\Delta E$ for spectrum integration. From this relation, the relative amount (atomic ratio) of two different elements A and B in the specimen, can be evaluated by:

$$\frac{N_A}{N_B} = \frac{I_A(\beta, \Delta E)\sigma_B(\beta, \Delta E)}{I_B(\beta, \Delta E)\sigma_A(\beta, \Delta E)}. \tag{2.8}$$

**ELNES structures**

For atoms inside a material (crystals or amorphous structures) the core EELS spectrum profile bears additional oscillations in the ~50 eV above the ionization edge, known as energy-loss near-edge fine structures (ELNES) (Fig. 2.5). These additional features reflect the local density of unoccupied states (LDOS) localized on the ionized atom, in agreement with the EELS selection rules for the electronic transition.

In the single scattering and one-electron approximations, the energy loss function is related to the transition probability $\Gamma$ of electron transitions of energy $\hbar\omega = E$ in the specimen derived from the Fermi's golden rule [78,79]

$$\Gamma(E) \propto \frac{2\pi}{\hbar} \sum_{i,f} \left| \langle \phi_f | e^{i\vec{q}\cdot\vec{r}} | \phi_i \rangle \right|^2 \delta(E_f - E_i - E) \tag{2.9}$$

where $\phi_i$ and $\phi_f$ are the initial and final states of an electron in the spec-

imen, $e^{i\vec{q}\cdot\vec{r}}$ is the transition operator representing the primary electron (plane wave), $\vec{q}$ is the momentum transfer and $E$ the incident electron energy loss, which must be equal to energy of the transition $E_f - E_i$. The inelastically scattered electrons have a negligible angular distribution around the optical axis (they are essentially forward-scattered) [75] and the differential cross section $\partial\sigma/\partial\Omega$ decays as $q^{-4}$ [28]. Hence, for typical spectrometer acceptance angles (typically 20-30 mrad) the dipole approximation is legitimate:

$$q \to 0,\ e^{i\vec{q}\cdot\vec{r}} \approx 1 + i\vec{q}\cdot\vec{r}. \tag{2.10}$$

This corresponds to vertical electron transitions ($q \to 0$) in the energy band structure of the material. Moreover, the dipole approximation imposes a selection rule on the transition: $\phi_i$ and $\phi_f$ being orthogonal wavefunctions, the matrix element reduces to the term containing $\vec{q}\cdot\vec{r}$, which is and odd operator. For the term to be nonzero, the angular parts of the wavefunctions (spherical harmonics) must have different parities. As a consequence, the dipole selection rule on the angular momentum quantum number $\Delta l = \pm 1$ must be respected (e.g. $p$ symmetry final state for a $1s$ electron). This means that, more precisely, the ELNES reflects the symmetry-projected LDOS. Also, considering all transitions between initial and final states separated by the energy loss $E$, the ELNES is related to the symmetry-projected joint LDOS.

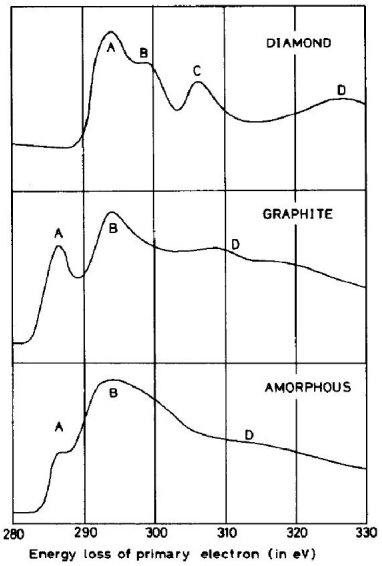


Figure 2.5: *Core-loss ionization threshold at the carbon K-edge for different carbon allotropes. ELNES peaks allow to distinguish amorphous carbon, graphite and diamond. Figure from ref. [80]*

Therefore, the ELNES region of core loss signals contains information about the chemical configuration around the ionized atom, in terms of bonding configuration (crystal structure) and chemical environment. As an example, Fig. 2.5 shows the different carbon K-edges for diamond, graphite and amorphous carbon. In the specific case of graphite, the two peaks arise from $1s$ electron excitations towards the $2p-\pi^*$ and $2p-\sigma^*$ unoccupied bands ($\pi$- and $\sigma$-symmetry antibonds).

## 2.6 Cathodoluminescence

As already discussed, the inelastic interaction with primary electrons induces single or collective excitations of outer-shell electrons in the materials. Their relaxation to the ground state may follow radiative or nonradiative decay channels: CL spectroscopy analyses the light emitted by the specimen (Fig. 2.2). In semiconductor materials, valence electrons excitation to the conduction band generates hole-electron pairs (h-e) and light emission arises from their recombination across the energy band-gap. In the case of metals, visible radiation arises from the excitation of surface plasmons, whose energy is propagated to the far-field. These inelastic events can then be simultaneously observed in the STEM microscope in terms of absorption by EELS and in terms of emission by CL. A comparison of CL with photoluminescence (PL) is also worthy: by different excitation probes (electrons or photons) these techniques detect the same radiative decay [81]. However, differences reside in the fact the CL attains the nanometre spatial resolution and has access to all possible excitations, given the high energy of the probe electrons. On the other hand, for the same reason probe electrons interact little with the specimen, so the quantum yield of the luminescence can be lower, especially in the case of very thin specimens. A large difference in the statistical properties of CL and PL emission has also been demonstrated [82].

**Excitation and recombination mechanism**

In the interaction with a semiconductor or insulating sample, an incident fast electron can excite a plasmon, which decays generating several h-e pairs. The excited charge carriers have an excess energy, which is rapidly dissipated by collision with phonons and defects. Once they attain thermal equilibrium, electrons and holes are respectively at the bottom and top of the conduction and valence bands and can interact forming excitons. Radiative e-h recombination can be classified as intrinsic or extrinsic. The first type concerns simple band-to-band recombinations and excitonic effects, while the second is related to impurities responsible for spatially localized shallow acceptor or donor electronic levels within the band-gap

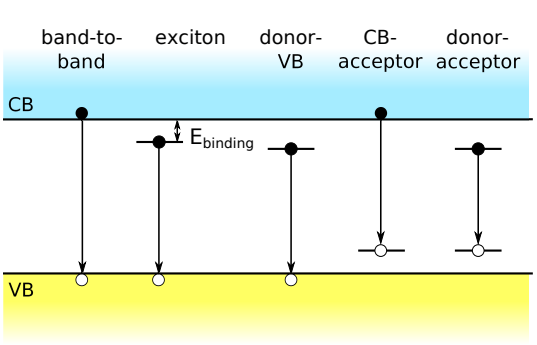


Figure 2.6: *Schemes of radiative recombination in a semiconductor.*

(Fig. 2.6) [83].

**Phonon coupling and Huang-Rhys factor**

CL emissions consisting in several lines separated by equal energy intervals have often been observed during the experiments of this thesis. They are interpreted as phonon-assisted emissions. Spatially localized luminescence centres (i.e. donor and acceptor levels on the associated defect or impurity) may strongly couple with phonons in the host lattice. A very simplified description is provided by the Franck-Condon model. The ground state and excited state electronic levels are associated to different lattice configurations $Q$ ad $Q'$ (nuclear positions, i.e. in the simplest case the internuclear distance in a diatomic molecule), as shown in Fig. 2.7. The phonon-coupling introduces additional quantized vibronic states transforming each electronic level in a band. The Franck-Condon principle states that since electronic transitions are much more rapid than nuclear motions, they are vertical transitions in the configuration diagram (Fig. 2.7). Hence the excitation transition from the ground state in $Q$ ends in an excited vibrational level of the excited electronic state; the system relaxes to a different nuclear configuration $Q'$, corresponding to the fundamental vibrational state, by the emission of phonons; successively it decays into the vibrational level of the ground state at the same $Q'$ and finally relaxes to the ground state minima at the initial configuration $Q$ [79, 84].

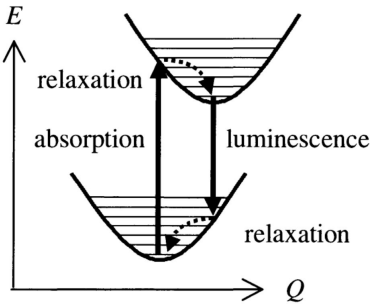


Figure 2.7: *Scheme of phonon-assisted radiative transitions at luminescence centres, extracted from ref. [84]. The electronic states E(Q) are represented as a function of the configuration coordinate Q and display vibronic levels. The ground and excited states have their minima at different Q.*

This phenomenon results in a series of lines in the optical (absorption) emission spectrum, at equal energy intervals corresponding to the phonon energy (Fig. 2.8). The (lowest-) highest-energy emission line corresponds to the transition between the lowest vibrational levels of excited and ground state and is called zero-phonon line (ZPL). The maximum of intensity of the spectrum corresponds to the (absorption) emission transition at fixed nuclear configuration ($Q$) $Q'$ described above. The Franck-Condon vibronic model provides a semiquantitative description of this lineshape. The definition of the Huang-Rhys parameter S allows to express the energy of the absorption transition as $\hbar\omega_{abs} = \hbar\omega_{ZPL} + S\hbar\omega_{phon}$ where $\omega_{phon}$ is the frequency of

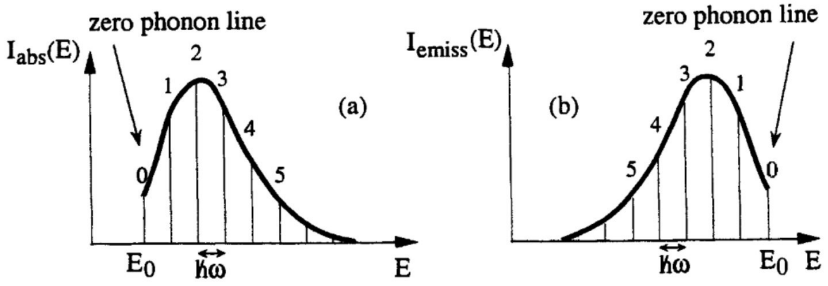


Figure 2.8: *Lineshapes of the absorption and emission spectra explained by the electron-phonon coupling and a Huang-Rhys factor of 2.5, from [79]. $E$ indicates the energy $\hbar\omega$ of the absorption or emission transition, $E_0$ is the ZPL transition energy $\hbar\omega_{ZPL}$.*

the nuclear motion and $\hbar\omega_{phon}$ is the energy of one phonon (the energy difference between two consecutive vibronic levels) [79]. Similarly, for the emission transition $\hbar\omega_{emiss} = \hbar\omega_{ZPL} - S\hbar\omega_{phon}$. Hence, the absorption and emission energies differ by $2S\hbar\omega_{phon}$, accounting for the redshift generally encountered in optical spectroscopy between absorption and emission bands and known as Stokes shift [79, 83].

The quantum treatment of this problem in terms of a displaced and undisplaced harmonic oscillators allows to derive the emission spectral intensity as [79]

$$I(\hbar\omega_{emiss}) = \frac{S^n}{n!} e^{-S} \delta(\hbar\omega_{ZPL} - n\hbar\omega_{phon} - \hbar\omega_{emiss}) \tag{2.11}$$

where $n$ indexes the oscillator states and hence the number of phonons. This intensity corresponds to a Poisson distribution (Fig. 2.8), where the maximum of intensity occurs at $n \approx S$ and the intensity $I_n$ of the $n^{th}$ phonon line is related to the intensity of the ZPL ($n = 0$) by

$$I_n = \frac{S^n}{n!} I_{ZPL} \tag{2.12}$$

as shown in Fig. 2.8, for $S = 2$. Therefore, the strength of the electron-phonon coupling can be easily derived from the CL emission spectrum by estimating the Huang-Rhys factor.

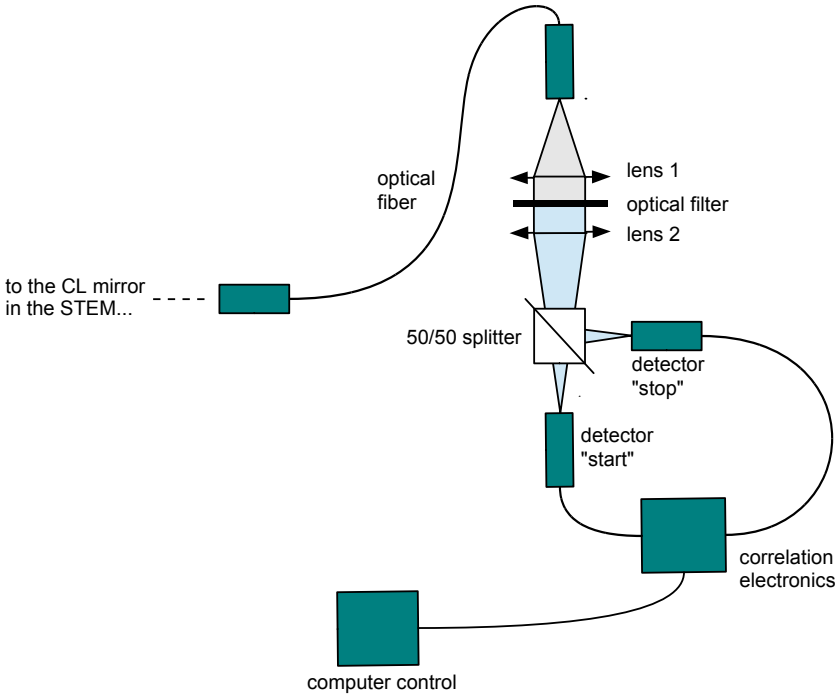


Figure 2.9: *HBT experimental set-up.*

## 2.7 Hanbury-Brown and Twiss intensity interferometry

The HBT interferometer was elaborated by R. Hanbury-Brown and R. Q. Twiss in the 50's and was originally used to estimate the angular diameter of the star Sirius, by measuring the spatial correlation between the star light intensities recorded independently by two detectors. Immediately after, the interferometer was applied to the study of time correlation and anti-correlation effects to investigate the nature of a light beam. [85]. A scheme of the instrument is shown in Fig. 2.9. Photons in a beam are directed through a 50/50 beamsplitter toward two detectors named start and stop. A clock measures the time interval between the detection of a first photon on detector start and a second photon on detector stop. A correlation electronic then provides a histogram of the measured time delays $\tau$, corresponding to the probability of detecting two photons with a $\tau$ time interval separation.

**Bunching and anti-bunching**

Considering a source with constant time average intensity $\langle I(t)\rangle$ the normalized second-order intensity correlation function of the light is defined as

$$g^{(2)}(\tau) = \frac{\langle I(t)I(t+\tau)\rangle}{\langle I(t)\rangle^2} \tag{2.13}$$

At a time-scale much bigger than the coherence time of the light source ($\tau \gg \tau_c$), the intensity fluctuations at $\tau$ delay are completely uncorrelated and $g^{(2)}(\tau) = 1$. On the other hand, at $\tau \ll \tau_c$ the intensity fluctuations of the light are correlated and reflect the nature of the light: in the case of coherent light (i.e. laser) $g^{(2)}(\tau) = 1$, while chaotic light (i.e. atomic discharge lamp) has $g^{(2)}(0) \geq 1$ and tends towards 1 for $\tau \gg \tau_c$ [86]. In the quantum treatment, $g^{(2)}(\tau)$ represents the probability that a first photon is detected at time $t$ (detector start) and a second photon at time $t+\tau$ (detector stop), that is two photons are detected with a time delay $\tau$. Photons in a beam might be distributed with different statistics, corresponding to antibunched, coherent and bunched light (Fig. 2.10.a). They are characterized respectively by $g^{(2)}(0) < 1$ (two photons can never be detected at the same time), $g^{(2)}(0) = 1$ and $g^{(2)}(0) > 1$ (Fig. 2.10.b). While coherent and bunched light are similar respectively to coherent and chaotic classical light, antibunching is a purely quantum phenomenon [86]. Experimentally, it is observed in the luminescence from single photon emitters (SPE) such as point defects in semiconductors [8, 10] or individual molecules [88–91]. Bunching at zero time-delay can be observed by CL of luminescence centres in semiconductors, as a consequence of the synchronous excitation of several centres [82].

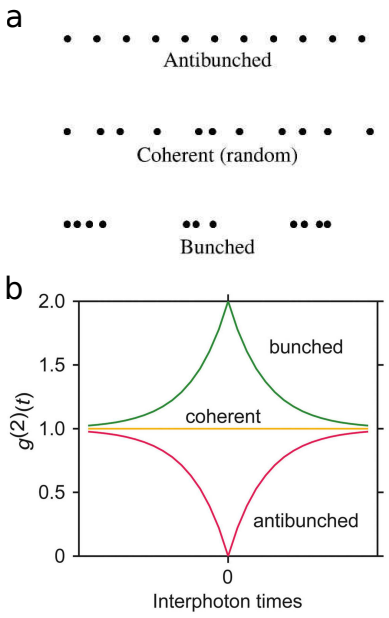


Figure 2.10: *(a) Possible statistical distributions of photon emission, from ref. [86]. Second-order correlation functions typical of these kinds of light [87].*

The width of the antibunching and bunching peaks provides a quantitative estimation of the lifetime of the excitation, that is the typical time interval between the detection of two single photons or two bunches of photons. Indeed, the probability of detecting a second photon from a SPE (or a second bunch of photons) is governed by the pop-

ulation of the excited state. In the assumption of an exponential behaviour, the probability function in the case of antibunching can be fitted as [8, 92]

$$g^{(2)}(\tau) = \begin{cases} 1 - ge^{-\tau/\tau_e} & if\ \tau \geq 0 \\ 1 - ge^{\tau/\tau_e} & if\ \tau < 0 \end{cases}$$

and similarly for the bunching [82]

$$g^{(2)}(\tau) = \begin{cases} 1 + ge^{-\tau/\tau_e} & if\ \tau \geq 0 \\ 1 + ge^{\tau/\tau_e} & if\ \tau < 0 \end{cases}$$

where $\tau_e$ is the lifetime of the excited state (Fig. 2.10.b, with g=1).

## 2.8 STEM-spectroscopy in Orsay

The STEM microscope employed during this thesis is a VG-HB501 instrument, shown in Fig. 2.11.a. The electron gun consists in a tungsten tip, operating by field emission at room temperature and pressure $10^{-11}$ Torr, with acceleration voltages 60-80-100 kV. A pressure level of about $5 \cdot 10^{-8}$ Torr at the sample stage is ensured by an oil-free pumping system. The top-entry sample holder design grants a high mechanical stability. A home made LN cooling system connected with the sample holder (figure 2.2 and 2.11.a) keeps the specimen temperature at about 150 K. The importance and advantages of the use of low temperatures will be discussed in the next section (2.9). The electron beam characterized by a 0.3 eV energy width, the convergence semiangle of the objective lens is 7.5 mrad and its pole piece has a spherical aberration coefficient $C_s$ of 3.1 mm. The electron probe size at the sample stage corresponds to 1 nm. Semiangles of collections are 1.25 mrad for the BF and 25-200 mrad for the DF detectors.

**EELS**

EELS spectra are acquired by collecting transmitted electrons within the 22 mrad spectrometer semiangle of collection. Inside the spectrometer (Gatan), a magnetic field induces an energy (velocity) dependent curvature (Lorentz force) in the trajectory of transmitted electrons. In this way the beam is spread along one direction and finally strikes a CCD detector. The CCD camera is cooled with liquid nitrogen, resulting in a low read-out noise of three counts r.m.s. and a negligible dark count noise.

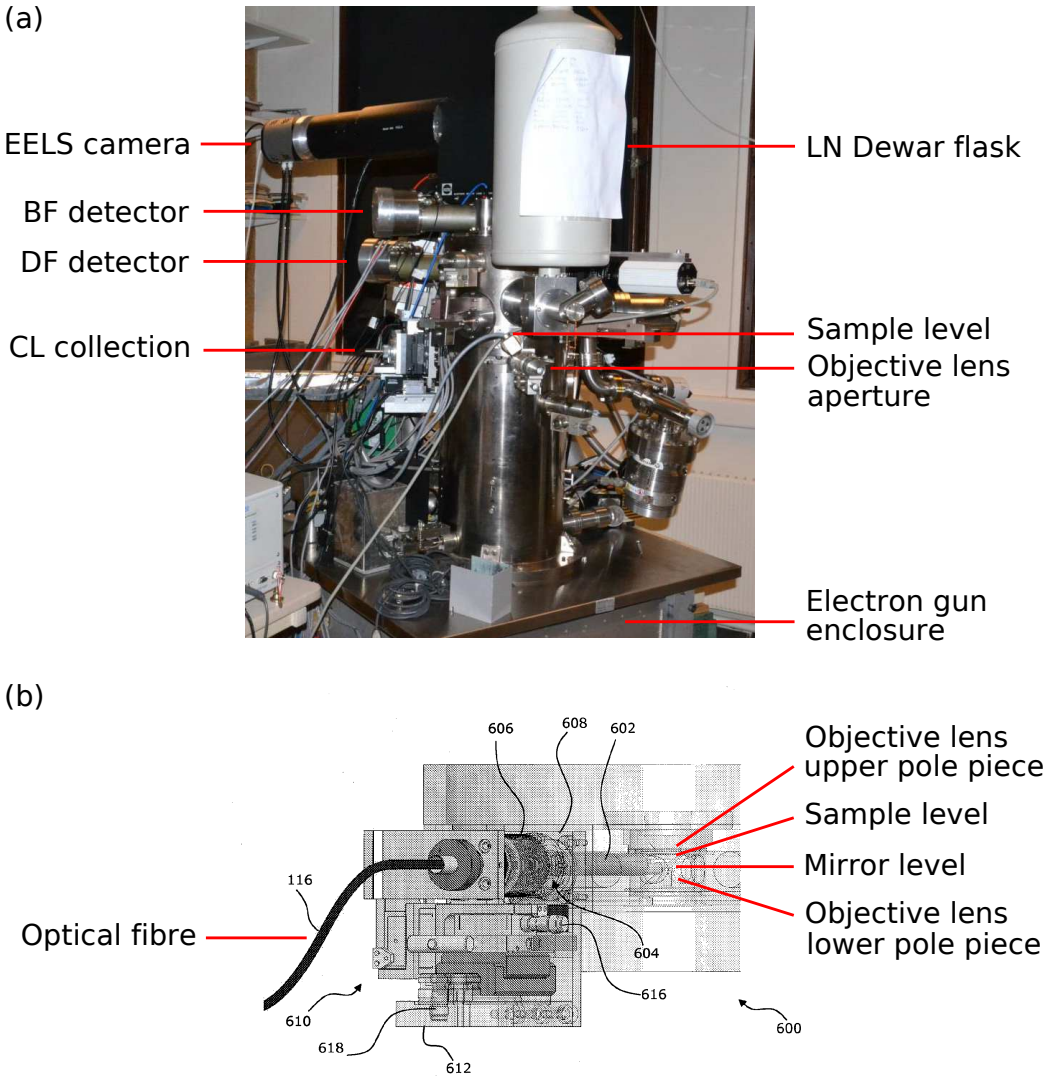


Figure 2.11: *(a) The VG-HB501 in Orsay. (b) The CL collection system from patent No. PCT/FR2011/050986.*

**CL** CL in the VG-HB501 STEM is realised thanks to a home-make dedicated collection system (patent No. PCT/FR2011/050986). An aluminium parabolic mirror (about 1 mm in thickness) with a high numerical aperture NA of 0.6 and a focal point of about 300 μm. is inserted in the small cavity formed by the bottom polar piece of the objective lens and the sample holder (Fig. 2.2, 2.11.b), and aligned with the electron beam illumination spot at the sample surface. The collected light is conveyed as a parallel beam to a $MgF_2$ window and focused by a lens at the entrance of a bundle optical fibre, placed outside the microscope. At the other extremity of the bundle, the optical fibres are aligned in a line to match the spectrometer slit entrance. In the spectrometer (Princeton Instrument), three different diffraction gratings can be easily switched, according to the spectral range of the CL radiation: for NIR blazed at 1.2 eV (covering the range 1.1-1.45 eV), for the visible blazed at 2.5 eV (1.5-4.2 eV range) and for the UV blazed at 4.1 eV (range 3-6 eV). The diffracted beam is finally detected by a Princeton EMCCD (electron multiplying charge coupled device).

CL in the Orsay VG-HB501 has allowed to access the optical properties of individual nanostructures such as quantum disks in semiconducting nanowires [7, 93], quantum dots [81], stacking faults and point defects in 3D and 2D wide band-gap semiconductors [8–10, 82], and metallic nanoparticles [77, 94]. The investigation by hyperspectral imaging allows to derive intensity maps of specific CL peaks by filtering the 3D data set in the related energy interval (Fig. 2.3). Emissions from luminescence centres, for example, appear as spots in the map. For their interpretation it must be considered that the intensity in the map does not necessary indicate the position of the emitter: the emission is correlated to the excitation spot, i.e. the position of the electron beam. The emission can originate anywhere in the material within the range of the carriers diffusion length from the illumination spot. At high hyperspectral spatial resolution this might correspond to several pixels. Of course, the probability of excitation of a luminescence centre increases when the beam gets closer to the emitter, so the most intense pixel in the emission spot can usually be identified as the position of the emitter.

**HBT** The HBT intensity interferometer can be connected to the VG-HB501 CL system, representing the unique STEM+HBT set-up existent at present. The light is conveyed from the mirror to the interferometer by a single optical fibre of 100 μm diameter core. The detectors employed in the UV range are Hamamatsu photomultiplier tubes (PMT) H10682-210 with a

quantum efficiency larger than to 50 % between 320 and 470 nm. The correlation measurement is provided by a Time-Correlated Single Photon Counting (TCSPC) system with a time sampling tunable from 4 ps to 512 ps (Time Harp correlation electronics from Picoquant). To measure the full second-order autocorrelation function, which is symmetrical at positive and negative time delays, the role of the two detectors (start and stop) should be interchanged. Instead, an artificial time delay is introduced between the detector stop and the TCSPC system (a 23 metres cable resulting in 120 ns delay). In this way the real zero-delay channel of the histogram is shifted from the first channel at the left to a known (measurable) offset and the full autocorrelation function can be obtained. The room background during the experiments are typically $10^2$ counts/s. STEM+HBT in Orsay has been successfully applied to the study of single photon emitters in diamond and h-BN [8, 10] and more recently for the determination of the lifetime of individual quantum emitters [82, 93].

## 2.9 Electron dose and gentle illumination techniques

The use of fast electrons (or ionizing radiation such x-rays) inevitably requires an evaluation of possible illumination damages. Permanent modifications up to even destruction of the sample atomic structure are induced by energy and momentum transfers from the incident (primary) electrons to electrons or atoms in the specimen, or through the generation of secondary electrons. Indeed, when a valence electron in the material is excited to the conduction band by an inelastic scattering, it acquires an energy several times bigger the optical energy gap, and before decaying to the bottom of the conduction band (thermalization) it might generate several e-h pairs [31]. Illumination damages are more important in the case of thin specimens and light elements, and are particularly limiting in the study of organic and biological samples [95].

**Knock-on displacement**

Illumination damages are classified in knock-on displacements and radiolysis. The first arises from elastic scattering between primary electrons and atomic nuclei in the specimen, resulting in a momentum transfer. The amplitude of the displacement can be high enough to determine the ejection of surface atoms (electron-induced sputtering). For knock-on displacement in the bulk or surface sputtering to occur, the energy of the

incoming electron must overcome a certain threshold. For many low-Z atoms this is threshold is below 100 keV [95] (i.e. about 80 eV for cabon in graphene [96,97]). During the collision, an amount of energy up to tens of eV can be transferred to the atom, with a dependence on the scattering angle: the transferred energy is maximal for 180°scattering angle (backscattered electron, head-on collision). This kind of illumination damage is the dominant mechanism in conductors, while in semiconductors and especially organic compounds the main source of damage is radiolysis [31,95].

**Radiolysis**

Radiolysis (or ionization damage) consists in the definitive breakage of a covalent chemical bond by inelastic interaction with primary or secondary electrons: (i) excitation of outer-shell electrons, with possible generation of secondary electrons, and (ii) excitation of inner-shell electrons (with lower probability but higher energy loss), also contributing to secondary events, including Auger electrons [31,95,98,99]. For radiolysis to occur, the threshold on the incident electron energy is only few eV. This mechanism is not important in conducting materials because, given their large reservoir of electrons, the valence-band holes are immediately filled or screened (in less than 1 fs) [31]. On the contrary, in semiconductors the excitation lifetime is longer (µs) than the timescale of lattice vibrations (less than 1 ps) and the system can rearrange before h-e pair recombination and relax with bond breaking and formation of radicals (leading to mass loss) [31].

**Damage threshold and electron dose**

The occurrence of illumination damages can be asserted on the basis of variations in some experimental quantities: decrease of the intensity of some spectral features, appearance of new spectral features, fading or disappearance of diffraction spots, changes in the stoichiometry (mass loss) [28,95,100]. These ones can be successfully used as criteria to determine damage thresholds and optimize acquisition conditions. The total electron dose constitutes an useful parameter. It is defined as

$$Electron\ Dose = \frac{It}{eA} \tag{2.14}$$

where $I$ is an estimate of the electron current, $t$ is the integration time, $e$ the electron charge and $A$ the illuminated area. Also, the energy deposited per unit volume by one electron travelling through the specimen (electronic stopping power) is quantified by $\rho E_m \sigma_i$, where $\rho$ is the atomic density, $E_m$ the average energy loss per inelastic collision and $\sigma_i$ the inelastic cross

section [95]. It is intuitive and it has been experimentally observed that the probability of damage is proportional to the electron dose [101]. This one should than be lowered, hopefully while conserving an acceptable Signal/Noise (S/N) ratio.

**Reducing the damaging**

The electron dose might be reduced by lowering the beam current or the acquisition time, or increasing the illuminated area by defocusing the beam. However, this entails worse S/N ratio in the first case, and degradation of the spatial resolution in the second [31, 101]. Reduction of the current may also be helpful against damages arising from beam heating and electrostatic charging [95]. The electron energy represents another important factor. As already discussed, lowering the acceleration voltage below the knock-on threshold allows to avoid surface atom sputtering, while little improvement is achieved against radiolysis. Indeed, lowering the electron energy strengthens radiolysis effects, because the inelastic cross section scales inversely with respect to the incident electron energy (the energy threshold for radiolysis is only few eV) [31, 95]. In order to reduce radiolysis, the most efficient method is lowering the temperature of the specimen.

**Low temperature**

Cooling below -100°C has been demonstrated to considerably increase the total electron dose tolerable by the sample before occurrence of damage evidences [31, 95, 98, 101]. The major benefit is represented by the reduction of mass loss. Indeed, in radiolysis two stages can be identified: inelastic scattering with bond breakage and then migration of chemical species [101]. Low temperatures seem to be particularly effective in limiting this effect (at 77 K the diffusion coefficients are $10^{20}$ lower) [101].

## 2.10 Principal component analysis

The principal component analysis (PCA) was first developed by Karl Pearson in 1901 [102] and later H. Hotelling (1933) [103]. It is aimed at reducing the dimensionality of a data set of interrelated variables, while conserving the maximum of information contained in the data. This method allows to outline the most important features of the data and remove redundant or valueless information such as noise. A set of data of $n$ objects of $p$ random variables $x_i$, is represented as a set of points in the $p$-dimensional space of the variables. They may show a more pronounced

distribution along certain axis, called principal components (PC, Fig. 2.12). The PC are linear combinations of the original variables $z_k = \sum_{i=1,p} \alpha_{ki} x_i$ , they are in number $p$, are orthogonal (uncorrelated), and are ordered with respect to their variance: the first PC $z_1$ has the highest variance, the second $z_2$ has the second highest variance and is orthogonal to $z_1$, and so on. They are obtained by calculating and diagonalizing the covariance matrix $\Sigma_{ij} = E[(x_i - E(x_i))(x_j - E(x_j))]$ (where $E$ is the expectation value) of the vector $\vec{x}$ of random variables. Indeed, the variance of $z_k$ is maximal when the normalized coefficients vector $\vec{\alpha_k}$ is an eigenvector of $\Sigma$, with eigenvalue the variance itself. In the practical application of the PCA, the $n \times p$ matrix $X$ of the original $n$ objects of $p$ variables is transformed into the matrix $Z$ of the PC scores ($n \times p$, with $p$ the index of PC): $Z = XA$, where $A$ is the $p \times p$ matrix of the coefficients. The original data can be obtained again by the inverse transformation $X = ZA^T$, where $A^T$ is the transpose of $A$. However, only the first $m$ (typically $m$) PC are expected to measure some substantial variation in the variables (i.e. contain information), while the following essentially measure only noise. Hence, dimensionality reduction and denoising is performed by reconstructing the original variables using only the first $m$ PC: $X = ZA^T$, where $Z$ has $n \times m$ dimensions and $A^T$ has $m \times p$. The number $m$ is usually estimated by plotting the PC variances as a function of the PC index (scree plot) [103].

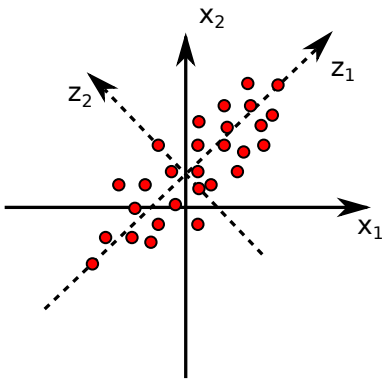


Figure 2.12: *Example of a distribution of data in two-dimensional space of the variables. The dotted lines represent the directions along which the data are mostly distributed.*

In the application of PCA to the treatment of STEM hyperspectral images, each spectrum of the image represents a point in a $p$-dimensional space, where $p$ is the number of spectrometer channels (variables).

CHAPTER 3

# REVISITING GRAPHENE OXIDE CHEMISTRY VIA SPATIALLY-RESOLVED ELECTRON ENERGY LOSS SPECTROSCOPY

The origins of graphene oxide (GO) date back to 1859, thanks to B. C. Brodie's experiments on the chemical modification of natural graphite [11]. By the action of strong oxidative agents in an acidic environment, Brodie obtained a form of graphite enriched in oxygen and hydrogen. This new material was baptized graphon, but it is better known under the name of graphite oxide. Several modifications to Brodie's procedure have been investigated afterwards. Currently, the most widely used method is the Hummers and Offeman's, followed by Brodie's.

The oxidation process has been demonstrated to be partially reversible, yielding the so-called reduced graphene oxide (RGO). The decomposition of graphite oxide by heating was already observed by Brodie [11] while the efficacy of chemical reduction treatments was reported in the 1960's by Boehm et al., who obtained films of few- and mono-layer RGO [104, 105]. The discovery of graphene and its unique properties in 2004 [106] has brought a renewed interest in GO as a precursor for a low-cost and large-scale production of graphene [107] (Fig. 3.1).

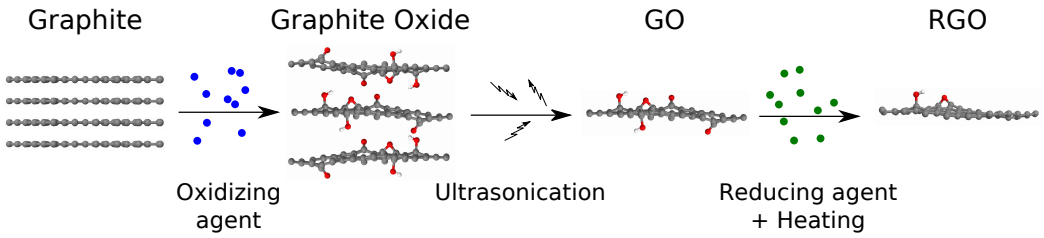


Figure 3.1: *From natural graphite to RGO.*

Nevertheless, our knowledge of GO and RGO is far from being complete. Their chemical and physical properties are found to vary from sample to sample and depending on the oxidation (or reduction) parameters. Several atomic models have been suggested to explain this behaviour but decisive experimental evidences are still missing. Indeed, despite microscopy images show a strong nonhomogeneity in GO's atomic structure, spectroscopic characterizations could not provide a picture of the material at the same scale. One of the purposes of this thesis has been to fill this gap by taking advantage from the high spatial localization of STEM-EELS and developing the specific operation conditions complying with the specimen sensitivity to illumination. After an overview of GO and RGO state of the art, the results on the EELS spatially-resolved oxygen quantification and carbon fine structures analysis are presented at section 3.9 and following.

## 3.1 GO and RGO: very promising functional materials

The chemical and physical features of GO are remarkably different from those of the parent graphite. Nevertheless, graphite's properties are quite surprisingly recovered up to a good extent by simple reduction process. Both these materials are attractive for a wide range of applications.

**Some insights into GO's structure**

The oxidation of graphite is a harsh process, that induces important distortions in the carbon lattice. However, the overall layered structure is retained and the material appears in the form of flakes (Fig. 3.2.a). With respect to the parent graphite, the interlayer distance is expanded: in dried samples, the carbon planes are 6-7 Å apart (3.35 Å in graphite [108]), as measured by X-ray diffraction (XRD) [16, 109–111] (Fig. 3.2.b), and this value is quite in agreement with DFT simulations predicting 5-6 Å [18, 112]. In hydrated conditions, a further interlayer separation is observed, up to about 12 Å in samples immersed in liquid water [16,113]. Moreover, the absorption of oxygen groups decouples the van der Waals interactions between adjacent carbon layers, so that graphite AB stacking is gradually lost and the structure becomes turbostratic [16].

Within the individual planes, the oxygen functionalization locally affects the arrangement of carbon atoms. In graphite carbon atoms are $sp^2$ hybridized and form three covalent $\sigma$ bonds in a planar configuration, giving rise to an hexagonal lattice. The remaining (non hybridized) $p_z$ orbital

forms a covalent $\pi$ bond, resonant with adjacent $p_z$ orbitals, so the $p_z$ electrons are delocalized over all the plane. Oxygen absorption occurs via a covalent $\sigma$ bond with carbon $p_z$ orbital. As a consequence, the carbon atom becomes partially $sp^3$ hybridized and is slightly puckered out of the plane. Therefore, an important functionalization of the carbon basal plane, is expected to highly distort the lattice. However, electron diffraction shows that in GO the hexagonal symmetry is overall retained (Fig. 3.2.c).

**Processability**

GO can be dispersed in water and polar solvents [16] and thin flakes with lateral dimensions from 10 nm to 100 μm can be obtained by ultrasonication [114] (Fig. 3.2.a). Solution-based exfoliation of GO is very effective, thanks to its expanded interlayer distance. In particular, exfoliation of GO in water dispersions is very efficient and GO sheets up to 3 mm wide have been obtained [16, 115]. Indeed, GO is highly hydrophilic, since the ionization of oxygen functional groups generates a negative surface charge on GO platelets, which repulse each other and readily interact with water molecules forming hydrogen bonds [16, 116, 117]. Aqueous dispersions of GO are hence stabilized by electrostatic interaction between water and the ionized oxygen functional groups [118, 119]. In addition to chemical exfoliation, thermal exfoliation by rapid heating is also possible but inevitably removes oxygen functionalities, yielding RGO [120, 121]. Solution-based exfoliation is more convenient also in sight of further treatments, that can be applied on a large scale and effectively (high surface area of about 736 $m^2g^{-1}$ in aqueous environment [122]) and for deposition on various substrates.

**GO's physical properties**

GO shows interesting mechanical properties, with a Young's modulus for the mono-layer of about 207 GPa [123], while paper-like GO displays higher stiffness and strength than many other paper-like materials [124]. With a Young's modulus of about 32 GPa [124], GO paper is thought to respond to uniaxial tension by conversion of the stress into shear deformation [124].

The optoelectrical properties of GO have been investigated over a variety of samples ranging from single sheets to films and compressed powders. Electrical measurements have demonstrated that the material is insulating, with conductivity comprised between order of $10^{-4}$ S/m and $10^{-1}$ S/m [118, 125–128] and sheet resistance in the range of $10^9$-$10^{12}$ $\Omega$/sq [16, 129–131]. This has been ascribed to the disruption of graphene delocalized $\pi$-electron network by the formation of the oxidized $sp^3$ regions, that

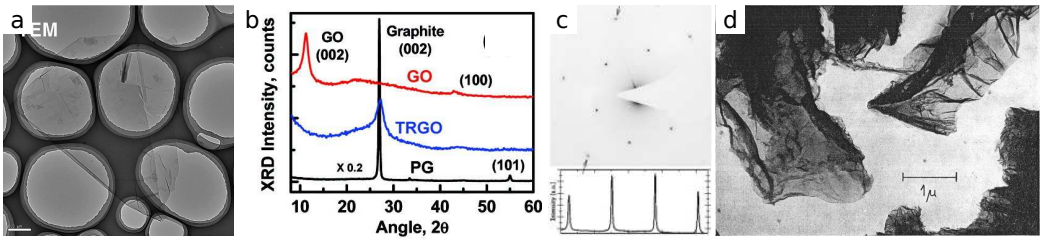


Figure 3.2: *(a) TEM image of a GO flake on a carbon membrane [111]. The scale bar is 0.5 $\mu$m. (b) Graphite (PG), graphite oxide (GO) and reduced graphite oxide (TRGO) interlayer distance by XRD [147]. (c) TEM-SAED of single layer GO, with peak intensity profile [27]. (d)TEM image of RGO [104].*

act as transport barriers [128, 132]. Diffuse reflectance measurements have suggested a value for the band gap in the range of 1.7-2.4 eV [16]. Fluorescence has also been reported in the near-infrared (NIR) or ultraviolet-visible regions [17, 133, 134], and associated to electron-hole recombinations in isolated $sp^2$ clusters, where $\pi$ electrons get confined: the clusters size is thought to locally determine the width of the energy gap [17, 134]. Indeed, the evaluation of the band gap width is not trivial, since it is seen to depend on the extent of the local oxidation [16, 17, 135], which is related to the specific oxidation parameters (parent graphite, choice and amount of the oxidizing agents, temperature and duration of the systhesis' steps...) [114, 136–142]. Moreover, macroscopic conductivity is affected by the lateral size of the GO sheets and their mutual interactions (i.e. inter-sheet contact resistance) within the GO film [141]. Finally, slight reversible variations in the atomic structure and hence physical properties of GO can be induced by environmental factors such as relative humidity conditions [113, 143–146]. As a matter of fact, the tunability and control of the optoelectrical properties represents one of the most interesting features in GO, in sight of practical applications (i.e. sensors).

**Sensitivity to external agents**

GO is highly sensitive to the environmental conditions. As anticipated above, simple chemical treatments, UV irradiation or heating, even at mild temperatures (about 130-200°C) cause a consistent reduction of the oxygen content in the material [111, 128, 147–150]. However, gradual structural changes have been demonstrated already at (almost) room temperatures and in no reducing chemical environments. Indeed, the formation of $CO_2$ among GO layers seems to start already at 50 °C [22] and ageing, in terms of diminished oxygen content, lowered resistivity or spec-

troscopic changes, has been reported at room or mild temperature (80°C) storage conditions, on the scale of one month [20, 131, 151]. Even in water dispersion, GO degradation occurs as a progressive fragmentation of the flakes because of C-C bond cleavage by the interaction with water molecules [23, 152].

**Changes upon reduction**

The efficacy of the reduction treatments (RGO sheets are shown in Fig. 3.2.d) is undoubtedly testified by several physical changes in the GO films or dispersions. First of all the material (film or dispersion) darkens in colour and assumes a metallic lustre, thanks to reflectivity improvement [15] (Fig. 3.3.a,b and 3.7.a). The hydrophilic character is reduced and stable dispersions in water cannot be obtained [118, 153]. Upon reduction, the interlayer spacing shrinks back to values typical of graphite [147, 154], confirming a substantial removal of the oxygen groups (Fig. 3.3.b). RGO paper displays a tensile modulus of 35 GPa, which is close to that of GO paper [117]. On the contrary RGO monolayers show an extraordinary stiffness, with a Young's modulus of 250 GPa [155] (graphene's being 1 TPa, for comparison [156]).

The progressive deoxygenation of GO determines a transition from insulator to semi-metal [157–159], with conductivity between $10^2$ and $10^5$ S/m [118, 125–128, 159, 160], which is 5-6 order of magnitudes higher than GO's, but still about 1 order lower than graphene's and ITO's [118, 125]. This is ascribed to the presence of residual oxygen and the formation of defects [18, 26]. As for GO, the tunability of the optoelectronic properties is an interesting feature of RGO. In addition to the extent of the reduction (affecting transparency and conductivity), RGO properties can be adjusted by varying the films thickness (i.e. more than 80% light transmittance by few layer RGO [125]) and doping by chemisorption or physisorption of molecules, ions, functional groups, metals particles, or ionic liquid [16].

## 3.2 GO and RGO applications

Like many layered materials, GO is effective as solid lubricant for micro/nanoelectromechanical devices [164]. GO thin films are obtained by drop casting, dip coating, spray coating, spin coating, vacuum filtration, Langmuir-Blodgett deposition and electrophoresis [16]. Vacuum filtration of colloidal dispersions of GO allows the fabrication of free-

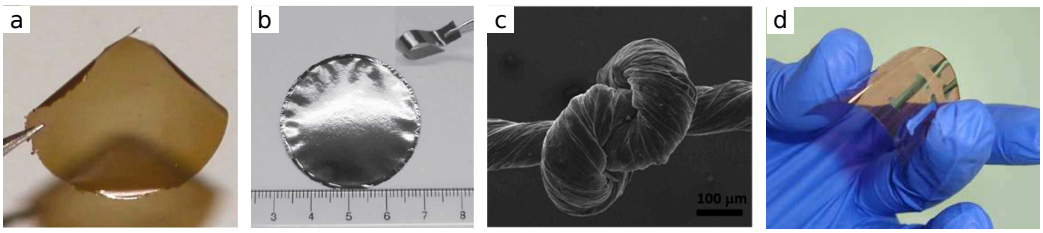


Figure 3.3: *Processing and applications of GO and RGO: (a) GO paper [161], (b) RGO paper [117], (c) GO fibers [162] and RGO film on a plastic substrate for flexible electronics [163].*

standing GO paper, where GO mono-layers are well-aligned [16,124] (Fig. 3.3.a). Thanks to its hydrophilic character and impermeability to other molecules, GO paper is employed as chemical filter, in particular for water desalination and decontamination [161, 165, 166]. RGO paper (Fig. 3.3.b) can be obtained by GO paper treatment with a reducing vapour [167].

GO can also by tailored in the form of strong fibres (Fig. 3.3.c), which are produced by thin films rolling or wet spinning of highly concentrated GO water dispersions, whose liquid crystal character assures GO sheets alignment [162,168–170]. GO fibres can be made conductive by thermal or chemical treatments ($\sim 2.5 \cdot 10^4$ S/m [169]) and employed in the fabrication of functional textiles [162,169].

As a dielectric or semiconductor (depending on the oxidation level), GO can be directly employed in electronic devices such as epitaxial-graphene/GO junctions, capacitors and field effect transistors, nonvolatile memories and charge storage and optical devices [133, 171–174]. Moreover, GO optoelectrical properties can be tuned by further functionalization, since oxygen groups in GO work as potential active sites [14, 17, 114, 175, 176]. As a consequence, functionalized GO can be efficiently employed in gas sensors (i.e. $NO_2$) [177,178], humidity sensors [143–146] and hydrogen storage [179–181]. Other practical applications include functionalized GO with improved dispersability properties [153], charge carrier extraction layers in solar cells [182–184], optoelectronic devices [185], magnetic materials [186], energy storage devices [187, 188]. In particular, thanks to its solubility in water at physiological pH, functionalized GO for biomedical applications represents a very extended field of research [17,176]. Applications number bacteria and DNA sensors [189,190], biomolecules labelling and live cells fluorescence imaging [191], targeted drug delivery (of water-insoluble drugs) inside cells and even nuclei

[191–193], cancer photo(NIR)-thermal therapy [194]. Moreover, even non-functionalized GO is studied as antibacterics [195] and substrate for stem cells growth and differentiation [196]. Toxicity studies required for clinical applications have shown a higher biocompatibility with respect to graphene (thanks to GO hydrophilicity), which is enhanced by functionalization. The toxicity level appears low but more studies are needed [193].

The use of GO and functionalized GO in composite materials allows to tailor the mechanical, thermal and electrical properties of host matrices such as polymers or ceramics [16, 176]. As a filler material in silica films [197] or polystyrene [198], novel composites can be obtained and made conductive by subsequent simple reduction treatments. The addition of functionalized GO in Nylon nanofibers results in an increased Young's modulus [199].

GO is highly chemically reactive and can be used as a catalyst or, thanks to its remarkable surface area and the large number of functionalities acting as anchoring sites, as a platform for supported heterogeneous catalysis [176]. Electrocatalytic activity of pure and doped GO quantum dots has been reported for the oxygen reduction reaction, with further possible application in water remediation [200, 201]. Finally, GO can be employed as photocatalyst for $H_2$ generation from aqueous methanol solution or pure water under UV and visible light irradiation [202]. The interest in GO as a substrate has been shown also in TEM microscopy. Indeed, GO (or partially reduced GO) constitutes a cheap and easy-to-fabricate electron transparent membrane, particularly fit for biological nanostructures and molecules, under low electron dose illumination conditions [24, 203–205].

Among these numerous applications of GO, certainly the most relevant is the employment of GO as a precursor for a large-scale low-cost production of chemically modified graphene (CMG) [107, 118, 153, 198, 206, 207]. Indeed, graphite is inexpensive and naturally abundant, mass production is easily achieved thanks to the solution-based approach and GO's expanded interlayer distance and hydrophilic character make liquid exfoliation much more effective than in the case of pristine graphite [16,17,125]; completely exfoliated GO can be easily processed, deposited on any substrate or integrated in composites, and made conductive by simple treatments [16, 118, 153, 198]. Thermal expansion of GO, driven by the decomposition of oxygen groups, is also industrially important [208]. The overall synthesis procedure to obtain RGO (or CMG) is much less costly than other methods such as mechanical exfoliation, chemical vapour deposition and thermal decomposition of $SiC$. Although RGO cannot bear compari-

son with mechanically exfoliated graphene in terms of quality, because of residual oxygen and a higher concentration of defects [118, 209], it stands out as a valuable substitute of graphene in applications such as transparent window electrode in solar cells, organic light-emitting diodes and displays and touch screens (i.e. RGO film on a plastic substrate [141, 163], Fig. 3.3) [17, 125, 160]. It is also attractive for replacing the nonflexible transparent conductor indium-tin-oxide (ITO), whose already high cost is increasing due to indium scarcity [16, 17, 125].

RGO paper (Fig. 3.3.b) can be directly obtained by deposition of chemically reduced GO dispersions [117, 141]. Doped or undoped RGO is also promising for the catalysis of oxygen reduction reactions in fuel cells [18]. As GO, RGO is studied for biomedical applications such as drug delivery [210, 211], antibacterics [212], bacterial and chemical/molecular sensor [16, 189, 213, 214]. Functionalized RGO and RGO-composites are also attractive novel materials [14,114], i.e. RGO-magnetite for arsenic removal from water [215] and polymer nanocomposites with improved thermal and mechanical properties [216]. Other applications enumerate RGO employement in energy storage (supercapacitors, electrochemical capacitors and rechargeable batteries [217–222]), field-effect (thin-film) transistors [128, 130, 209, 223], photodetectors [224], nanomechanical devices [225], non-volatile memory devices [16, 226]. Finally, the use of local thermal reducing techniques based on lasers or an AFM tip enables to obtain microcircuits on GO films [227, 228].

## 3.3 The synthesis of GO

**Brodie's method**

The first synthesis of GO, performed by Brodie in 1859 (Fig. 3.4), was based on the use of sulfuric acid ($H_2SO_4$), fuming nitric acid ($HNO_3$) and potassium chlorate ($KClO_3$) [11]. The procedure consisted in mixing graphite with $KClO_3$ in the ratio of 1:3. Fuming $HNO_3$ was then added and the suspension was kept in a water bath at 60°C for 3-4 days. The product of the reaction was washed with abundant water and the whole process repeated four times, after which no further oxidation was observed. The material was finally dried in vacuum at 100°C.

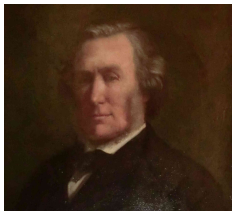

Figure 3.4: *B. C. Brodie, from ref. [229].*

In 1898 Staudenmaier modified this procedure by adding $KClO_3$ in aliquots during the reaction and sulfuric acid ($H_2SO_4$) to increase the acid-

ity of the mixture [12]. On the whole, the synthesis required many days of preparation and presented some hazardous issues. Indeed, the addition of $KClO_3$ produces chlorine dioxide ($ClO_2$) gas, which is explosive at high concentrations [13, 230]. Another drawback is represented by the significant amount of $KClO_3$, compared to that of graphite [13].

**Hummers and Offeman's method**

In 1958 Hummers and Offeman proposed a quicker, safer and more efficient process employing potassium permanganate ($KMnO_4$) as the oxidative agent [13]. Graphite powder and sodium nitrate ($NaNO_3$) are mixed in the ratio of 2:1 in concentrated $H_2SO_4$, in an ice-bath. $KMnO_4$ is added while keeping the temperature of the suspension below 20°C. The ice-bath removed, the reaction is carried out for 30 minutes at 35°C. The mixture thickens in a brownish pasty while the effervescence lowers. The addition of water causes a violent effervescence and a raise in temperature to 98°C. After 15 minutes a large amount of water is added and the suspension is treated with oxygen peroxide ($H_2O_2$) to remove residual $Mn$-containing species. Finally, the resulting bright yellow suspension is filtered, washed several times with water and dried. The whole procedure requires less than 2 hours.

Slight modifications to the Hummers and Offeman's method have been proposed afterwards and generally consist in different chemical agents or time and temperature parameters. For example, the use of longer oxidation and purification times [136], concentrated $H_2SO_4/H_3PO_4$ (phosphoric acid) 9:1 mixture while no $NaNO_3$ [138], temperatures below 10°C during all the procedure [139] and a preoxidation phase based on potassium persulfate ($K_2S_2O$) [140] have been reported. These variations affect the extent of the oxidation and the distribution of oxygen groups but the overall process remains hardly controllable.

**The oxidation mechanism**

While much effort has been devoted to the optimization of the synthesis process, the specific oxidation mechanism has been little investigated for a long time. The issue concerns the nature of the active oxidant species, and the dynamics and phases of the process. Dreyer et al. have suggested that oxidant element $Mn(VII)$ exists as $Mn_2O_7$ [14] while Dimiev and Tour believe the permanyl cation ($MnO_3^+$) more likely [231].

The first description of Hummers' GO oxidative reaction was proposed by Nakajima in 1988, on the basis of XRD results [232]. He identified two intermediate steps consisting in the formation of a stage-2 graphite intercalation compound (GIC) of $H_2SO_4$ (i.e. one intercalated layer every two

graphite layers), followed by a transition to stage-1 GIC (one intercalated layer every graphite layer) upon addition of $KMnO_4$, after which the oxidation starts. Only very recently, an experimental characterization of GO at different phases of the synthesis and using several techniques has been reported.

Dimiev and Tour [231] have demonstrated that $H_2SO_4$ forms a stage 1 GIC by a very rapid reaction (3-5 minutes). Then, the addition of $KMnO_4$ starts the oxidation, that can last from some hours to even days. By incorporating $KMnO_4$ as a series of equivalents, they have monitored the evolution of the oxidation. The reaction appears to progress in a front-like way, from the edge to the centre of GIC flakes, as the oxidant diffuses along the interlayer galleries, as allowed by the particular flake's morphology (Fig. 3.5). During the oxidation $CO_2$ emission is detected, indicating carbon vacancy formation [152]. When GO is washed with water, the residual $Mn$-containing species are removed. However, GO interacts with water and undergoes structural changes entailing flakes fragmentation (C-C bonds cleavage) and formation of new acidic sites (generation and accumulation of negative charges on the flakes). Concerning this last reaction, other authors have concluded that, after the addition of water, permanganate ($MnO_4^-$) takes part in the oxidation and the C-C bonds breaking [233].

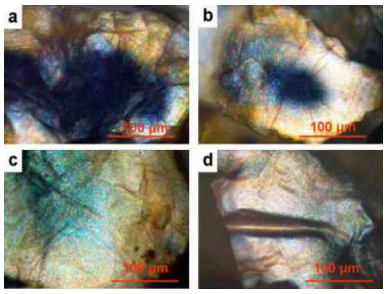


Figure 3.5: *Optical microphotographs of GO flakes from the same reaction mixture. Blue areas are less oxidized.*

However the exact mechanism of the formation of oxygen functionalities is still elusive. Spectroscopic results are interpreted in terms of the basic oxygen groups which can be found in organic molecules: epoxide (1,2-ethers, i.e. -O- in bridge position over a C-C bond), hydroxyl (-OH), carbonyl (-CO) and carboxyl (-COOH) (Fig. 3.6). The first two are characterized by the formation of a single bond between carbon and oxygen, while the other form a double bond. It is evident that carbon atoms within a perfect graphene sheet can in principle be functionalized with epoxides and hydroxyls through the $p_z$ orbitals, while one or two C-C bonds must be broken for carbonyl or carboxyl absorption.

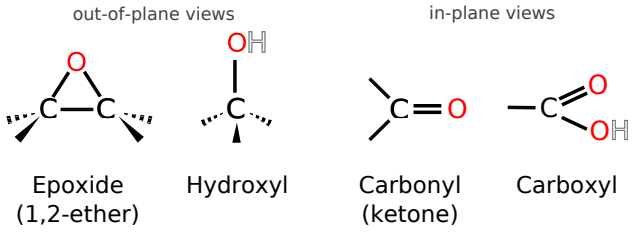


Figure 3.6: *Basic oxygen-containing functional groups.*

## 3.4 From GO to RGO

The oxygen groups decorating GO carbon atomic layer can be partially removed by simple thermal and/or chemical treatments [15, 18]. The choice of their specific parameters of temperature, duration, chemical environment (atmosphere or reducing agent) affect the extent of the deoxygenation and consequent lattice relaxation. A mild reduction induces a drastic change in GO physical properties, i.e. darker color (Fig. 3.7.a), while extensive reduction yields an almost graphene-like material. Indeed, despite the much higher concentration of defects, RGO can be considered quite similar to mechanically exfoliated graphene.

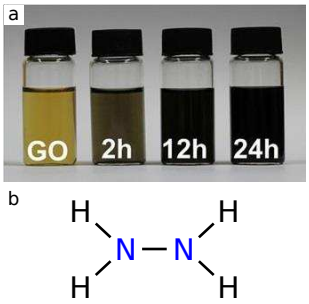


Figure 3.7: *(a) GO reduction with caffeic acid [222]. (b) Hydrazine reducing agent.*

Thermal reduction can be performed in a variety of atmospheres, pressure and temperature conditions. Ultra-High-Vacuum (UHV) has been reported as the most effective environment [148], but reduction can be achieved satisfactorily also in inert gases such as $Ar$ and $N_2$, usually in flowing regime, reducing gases as $NH_3$ or $H_2$, and even in air [25, 111, 125, 128, 148, 234–236]. Possible heating sources are microwave, flash light, laser, electron beam generated plasma, electric current, heated AFM tip and electron beam lithography [15, 16, 18, 237]. Mild reduction is obtained by annealing at low temperature (150-200 $^{\circ}C$) [120, 125, 128]. At higher temperature the deoxygenation rate is lower and complete oxygen removal is difficult. Indeed, even at 1100 $^{\circ}C$ few atomic oxygen percent are still measured [128, 147, 148, 238]. For higher temperatures, the quality of the vacuum (absence of oxygen) becomes a limiting factor [125]. Thermally reduced RGO is largely affected by the formation of carbon vacancies [15]. In fact, if from one side heating favours lattice relaxation, the

removal of oxygen functionalities easily occurs with carbon loss: $CO$ and $CO_2$ are detected already at 130-150 $^{\circ}C$ [22, 239, 240]. Moreover, thermal reduction is costly and not compatible with plastic or glass substrates. In such cases, low temperature chemical reduction is preferable.

Solution-based reduction can be achieved by a variety of chemical agents. Hydrazine ($N_2H_4$, Fig. 3.7.b) and its derivatives, also in the vapour phase, are the most common reduction agents. Its successful use on graphite oxide was first reported in the 1960's [105,241] while only in 2006 it was employed on colloidal GO dispersions [118,242]. Other widespread reduction agents are sodium borohydride $NaBH_4$, hydriodic acid ($HI$), alkaline compounds such as sodium hydroxide ($NaOH$, i.e. lye or caustic soda) and potassium hydroxide ($KOH$, caustic potash), ammonia ($NH_3$), metal powders (Fe/Al, Zn), N-methyl-2-pyrrolidinone (NMP, solvothermal reduction) and acetic acid [15, 18]. However, green reduction routes (in terms of solvents, reducing or anti-oxidant species and kind of treatments [243, 244]) have been demonstrated as an alternative to these traditional chemical agents, in particular toxic ones, such as hydrazine [15, 18]. Environmentally friendly techniques include high-temperature alcohol vapour reduction, UV irradiation, UV photocatalytic reduction using $TiO_2$ nanoparticles, evaporation of atomic $Ti$, electrochemical reduction, hydrogen plasma, heating in deionized water and the resort to reducing agents as urea, ascorbic acid (vitamin C), green tea, melatonin saccharides, and caffeic acid [15,18,150,222,245–250]. Some of them (in particular vitamin C and electrochemical reduction) are very efficient, with results at least comparable to those obtained by hydrazine [15]. Solution-based reduction, in addition to substrate compatibility, is attractive also for its scalability and easy deposition. On the other hand, a drawback is represented by the possibility of impurity incorporation. For example, in the case of hydrazine, residual nitrogen has been identified [109,118,125,209,234,251,252]. Thermal and chemical techniques have also been combined in multi-step reduction processes, in order to achieve better reduction and remove chemical residues [25, 130, 209, 235, 253].

**Reduction mechanism**

The reaction pathway of oxygen removal from GO is unclear and complicated by the nonstoichiometry and uncertainty character of GO atomic structure. Thermogravimetric analysis combined with a mass spectrometer (TGA-MS) and temperature programmed desorption analysis (TPD) have clearly established that oxygen desorption occurs already at mild temperatures, with generation of $H_2O$, $CO$ and $CO_2$ ($O_2$ below detection

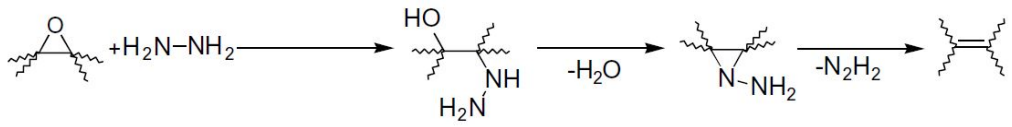


Figure 3.8: *Proposed epoxide reduction mechanism by hydrazine [118].*

threshold) attesting GO carbon network decomposition starting from 130 °C [22, 239, 240]. In general TGA shows a drastic mass loss at 150-200 °C followed by a progressive decomposition with a lower rate, in agreement with XPS elemental quantification as a function of temperature [128, 147], but in some cases a second harsh loss is observed around 600 °C [18]. The reduction below 200 °C is associated to epoxide and hydroxyl removal on a large extent [18], but these groups are still identified in a small amount at high temperature (1000 °C, XPS [128, 147]).

Several deoxygenation routes have been tested by means of DFT and molecular dynamics (MD) numerical simulations [15, 254, 255]. The study of the temperature effect on the reduction process has highlighted a critical temperatures of 100-150°C for the removal of carboxyls, 650 °C for hydroxyls and 1730 °C for carbonyls [255]. Another important factor to be considered is the oxidation level of GO. Indeed, the interaction among adjacent groups and the consecutive lattice distortion favours their removal [256].

Concerning chemical reduction, Stankovich et al. have proposed a step mechanism for epoxide removal by hydrazine (Fig. 3.8): the epoxide ring is opened by hydrazine bonding with carbon as -$N_2H_3$ and conversion of the epoxide oxygen in a hydroxyl group, which is then removed by nitrogen bonding to the second carbon as -$N_2H_2$. The final step of the reduction is the removal of the hydrazine residue, whose incompleteness would explain nitrogen residues in RGO. Based on DFT simulations, other possible routes for epoxide reduction by hydrazine or its derivatives have been proposed [251, 255], and the reduction appears to become more and more difficult as epoxide concentration lowers [255]. On the other hand the possibility of hydroxyl reduction by hydrazine is still under discussion, and no reduction route has been reported for carbonyl and carboxyl groups [251, 255].

## 3.5 GO and RGO atomic structure: still an open question

After more than 150 years since GO was synthesized for the first time, its exact atomic structure still remains elusive. Indeed, the study of this material appears extremely complex for several reasons.

First, the oxidation is a non controllable process, which highly depends on the choice of the parameters and their combination. The mechanism of the chemical reaction is not clear and it affects the starting graphite in a non uniform way. This means that the extent of the oxidation level and configuration (in terms of number, kind and distribution of oxygen groups) changes from synthesis to synthesis and even among samples derived from the same reaction vessel [14, 16, 114, 137, 142, 231]. Moreover, washing, drying and storing may alter GO's structure. In fact, drying at mild temperatures can readily induce oxygen groups decomposition [23,120,125,128] and the interaction of GO with water has been shown to result in oxygen groups conversion and removal, with C-C bond breakage and carbon sheet fragmentation [23]. Therefore, GO's structure should be better conceived in terms of limit configurations and as a dynamical model [23] instead of as an exact structure.

From the point of view of experimental investigations, the comparison of different results might be misleading. In fact, studies have been performed on quite a great variety of samples (GO powders, compressed powders, films, papers, flakes, mono-layers) and with local or nonlocal techniques: elemental analysis, thermal gravimetric analysis (TGA), temperature programmed desorption (TPD), x-ray diffraction (XRD), Raman, Fourier transform infrared spectroscopy (FTIR), nuclear magnetic resonance (NMR), x-ray photoelectron spectroscopy (XPS), x-ray absorption near edge structure (XANES), SEM, TEM, EELS...). Given the non homogeneous character of graphite's oxidation, lateral (depending of the probe size) and bulk averaging during the investigation must be taken into account. Sheets alignment could also slightly affect the results of angle dependent techniques (i.e. XANES). Moreover, the demonstrated sensitivity of GO to environmental conditions [20, 22, 23, 131, 151, 152] imposes attention to sample preparation and possible illumination damages (under x-ray radiation and accelerated electrons [25, 27]), which have in many cases been neglected. Another obstacle is represented by the absence of direct references for the interpretation of spectroscopic peaks , the overlap

of oxygen spectral features and possible interactions between neighbouring functional groups [147,257–259]. Indeed, the lack of suitable analytical technique and hence the need for new approaches for the study of GO has been reported [14,16,114].

Therefore, the kind, amount and distribution of oxygen functional groups in GO remains a fundamental open question, which preclude our knowledge, prediction and control of the physical and chemical properties of this material and its reduced derivative. Insights into the atomic structures of GO and RGO are necessary to explain the mechanical features, the origin of insulating character and conductivity recovery, the recombination mechanism underlying fluorescence and optimize further processing like functionalization.

**Atomic models for GO**

The first analysis of GO's chemical composition was performed by Brodie, who derived a stoichiometric ratio of $C_{11}H_4O_5$ [11]. The first atomic models, based on XRD, infrared spectroscopy, NMR and FTIR investigations, appeared almost one century later.

- In 1939 Hofmann and Holst proposed an atomic model based on only epoxides (as 1,2-ethers), for a molecular formula of $C_2O$ [14, 260] (Fig. 3.9.a). They derived a C/O ratio of about 2.2 [260], which corresponds to an almost complete functionalization of the carbon network.

- In 1946, Ruess considered epoxides in the form of 1,3-ethers and introduced hydroxyls, both randomly distributed (Fig. 3.9.b) [14,261]. In this model, carbon atoms are no more purely $sp^2$ hybridized and the carbon sheet, composed of trans-linked cyclohexane chairs, is wrinkled.

- In the model promoted by Clauss, Boehm and Hofmann (1957), part of the hydroxyls were adjacent to C=C double bonds (forming enol groups) (Fig. 3.9.c), which are in equilibrium with the carboxyls (keto) groups (keto-enol tautomerism) [262,264].

- In 1969 Scholz and Boehm completely disregarded epoxide, and imagined a carbon sheet with planar nonfunctionalized stripes separated by corrugated lines of cleaved C-C bonds functionalized with hydroxyls and carbonyls (Fig. 3.9.d) [14,263,264].

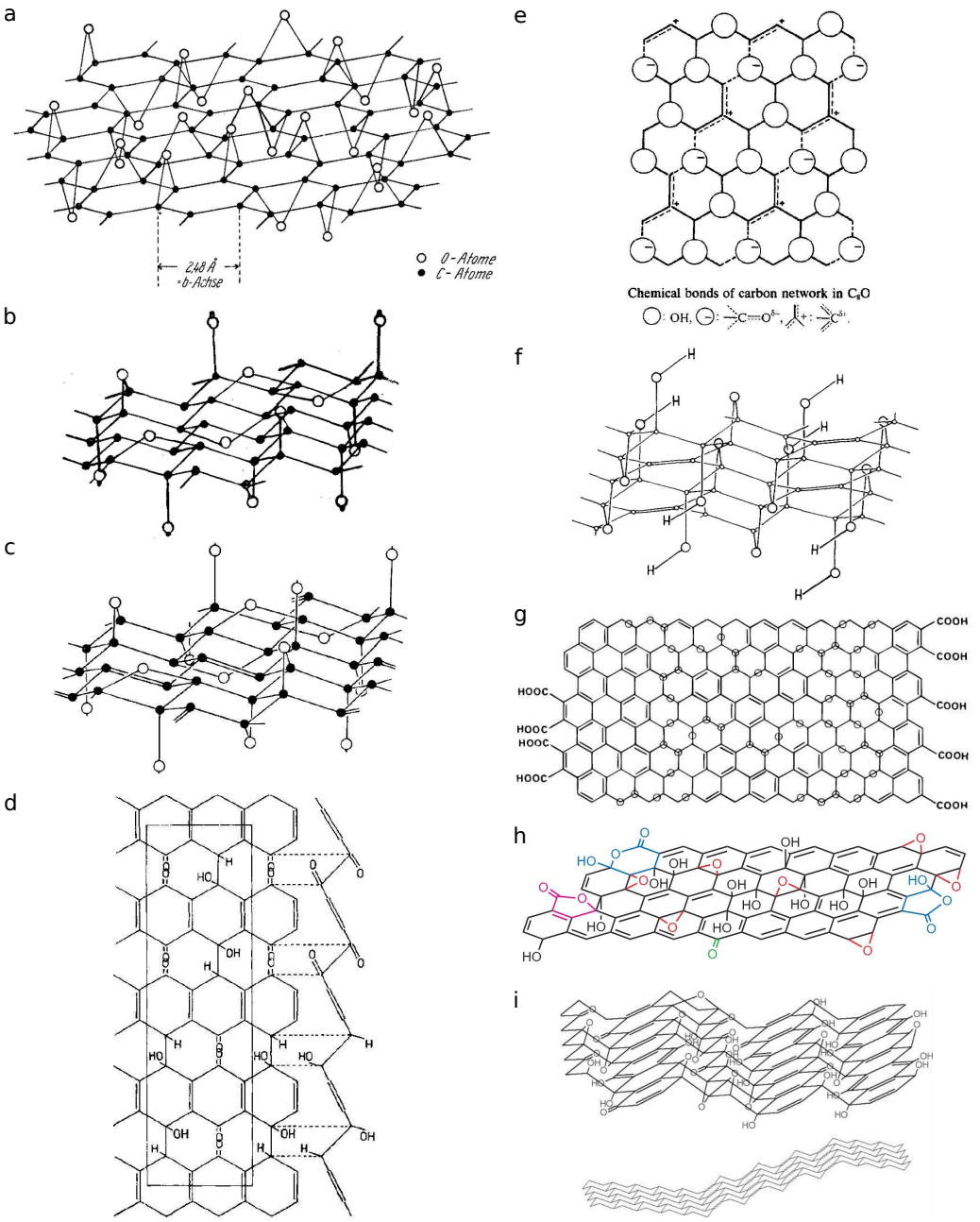


Figure 3.9: *GO models proposed by (a) Hofmann and Holst [260], (b) Ruess [261], (c) Clauss, Bohem and Hofmann [262] (d) Scholz and Boehm [263], (e) Nakajima [232], (f) Mermoux [264] (g) Lerf and Klinowski [19], (h) Gao [127], and (i) Szabó Dékány [137].*

- Later, Nakajima et al. proposed a structure similar to poly(dicarbon monofluoride) $(C_2F)_n$, where each two carbon layers are linked by vertical bonds between $sp^3$ hybridized carbons (1988, Fig. 3.9.e) [232]. The oxygen functionalities are carbonyls and hydroxyls and the stoichiometry is expressed by $C_8O_{2-x}(OH)_{2x}$ [232].

- Mermoux et al. (1991) agree with the Ruess's model but in a regular arrangement corresponding to a stoichiometry of $C_8O_2(OH)_2$ [264] (Fig. 3.9.f).

- The Lerf and Klinowski's model [19] (1998) (Fig. 3.9.g) is the most widely acknowledged today and has represented a considerable innovation in the understanding of GO, which starts to be considered a nonstoichiometric compound. In the Lerf and Klinowski's model, epoxides and hydroxyls are randomly distributed on both sides of carbon basal plane, and are expected to be in close proximity. The formation of 1,3-ethers is considered unlikely to occur. The presence of carboxyl groups is predicted at the sheet's edges. The structure is only partially functionalized and non-oxidized aromatic $sp^2$ regions are thought to survive among the oxidized $sp^3$ areas. The carbon network is on the whole almost flat, with slightly distortions due to hydroxyls. The Lerf and Klinowski's model has been supported by following studies [265, 266], which have also proposed the presence of five and six-membered-ring lactols and ester carbonyls at the edges of the basal plane (represented respectively in blue and purple in Fig. 3.9.h) [127] .

- In 2006 Szabó Dékány revived Ruess and Scholz's models [137] (Fig. 3.9.i), proposing a corrugated carbon network, with flat ribbon-like regions formed by C=C double bonds. The corrugated regions consists of lines of periodically cleaved cyclohexane chairs and have variable width. Hence, Szabó Dékány agree with Lerf and Klinowski on the existence of small aromatic areas. The expected functionalities are 1,3-ethers, hydroxyls, carbonyls (ketones) and quinones (two carbonyls in the same aromatic ring).

In the last five years additional perspectives have been opened in the debate on GO atomic structures. They will be discussed in section 3.7, after a brief overview on the state of the art of GO experimental investigation.

## 3.6 Spectroscopy and microscopy of GO

The oxygen content has been usually evaluated by means of elemental analysis and XPS and only very rarely by EELS. The calculated values cover quite a wide range: from about 15 to 35 at. oxygen% (considering only oxygen and carbon), which correspond to C/O ratios of about 5:1 and 2:1 [14–16, 18, 206]. This spreading of the results can be explained by the non homogeneity of GO samples (from powders to films, obtained with different oxidation conditions) and can be consistent with the Lerf and Klinowski model, that is a partially functionalized carbon network. However, these measurements cannot give precise insights on the atomic structure of the material, since the techniques used are not spatially resolved, while the material's chemical composition (Lerf and Klinowski model) varies at the atomic scale.

**Functional groups investigation**

XPS is the most common technique used to efficiently verify the extent of the overall oxidation as well as the efficiency of reduction treatments, also at intermediate steps of these processes, and ageing effects [20, 110, 111, 128, 137, 147, 148, 267–269]. In GO, the carbon 1s peak shows clear additional components at higher energies raising from carbon atoms in different chemical environments [137] and in well oxidized samples the $sp^2$ carbon peak even completely disappears [137]. The interpretation of the non purely $sp^2$ peaks is non trivial. They are expected to include contributions from C-O single bonds in epoxides and hydroxyls, double C=O bonds in carbonyls or both in carboxyls. Possible bonds with oxidation residues (i.e. nitrogen) should also appear in this spectral region. However, the choice of the number of fitting components is not unique (in literature, 2 to 4 components may be found). Moreover, the chemical shift of these individual contributions in different samples is not clear and the information is spatially averaged. For these reasons it is difficult to extract precise structural details on the kind of functional groups.

The nature of oxygen groups has been investigated also by infrared [137, 264, 270] and NMR spectroscopy [110, 111, 137, 271]. Indeed, the Lerf and Klinowski model and its following revisions are based on NMR studies [19, 127, 265, 266]. However spectral features are often superimposed and precise assignment becomes difficult. For instance, in infrared spectroscopy the identification of carbonyls and carboxyl groups is difficult, and they are mostly referred to as carbonyls [137, 257]. Also, no clear distinction seems possible between peaks related to O-H bonds inside hy-

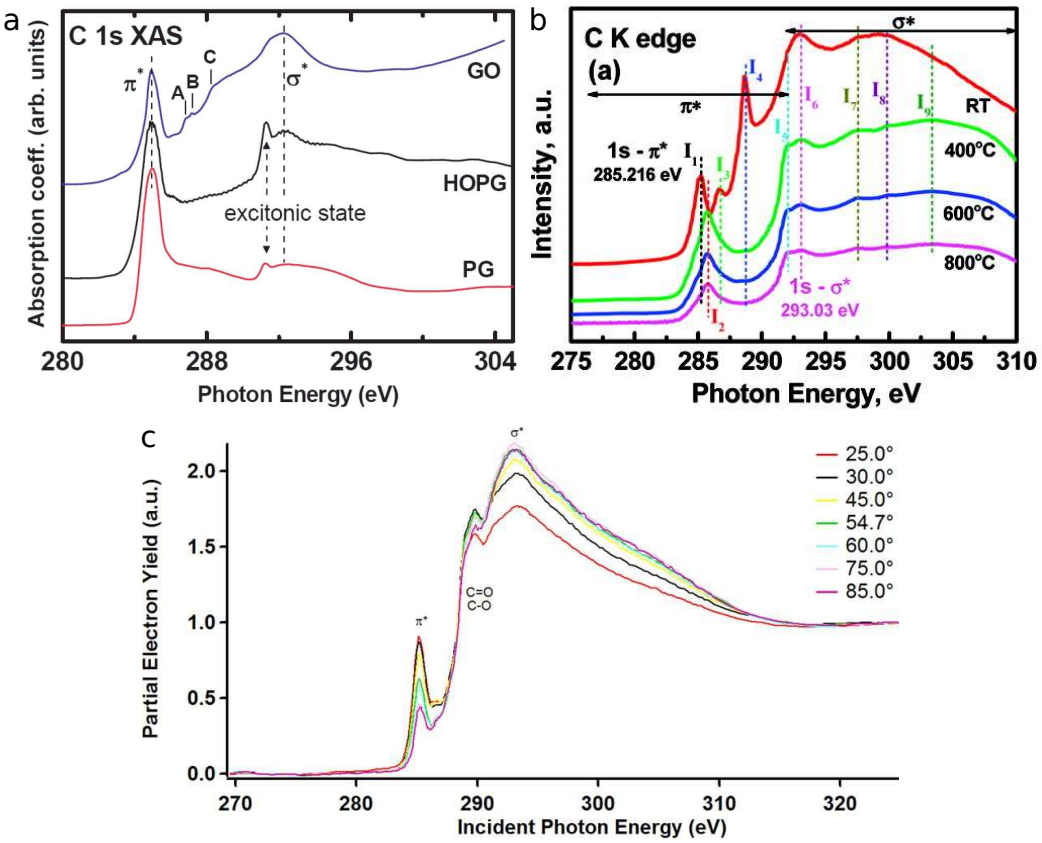


Figure 3.10: *Carbon K-edge XANES spectra of GO. (a) GO and reference graphite [270], (b) GO before and after thermal treatment [147] and (c) GO under different incidence angles [258].*

droxyl groups (-OH) and $H_2O$ [137].

XANES has also been widely used (Fig. 3.10) [27,147,258,259,270,272–274]. In GO, the carbon absorption edge shows a loss of the purely $sp^2$ hybridization of carbon atoms. Indeed, the $\pi^*$ and $\sigma^*$ absorption peaks, respectively at 285 eV and 292.7 and associated to electron transitions from the 1s state to unoccupied states in the $\pi^*$ or $\sigma^*$ bands above the Fermi level, are much weaker than in the case of graphite [275–277]. Additional features appear in the energy range between the $\pi^*$ and $\sigma^*$ peaks and are associated to C-O bonds. Generally features at 286-288 eV are associated to hydroxyl and epoxide functionalities (single C-O bonds) while those at 288-289 eV to carboxyls and in some cases carbonyls (double C=O bonds) [147, 258, 259, 270, 272–274]. The spectra in literature are not easily comparable. In addition to the acknowledged non homogeneity of GO

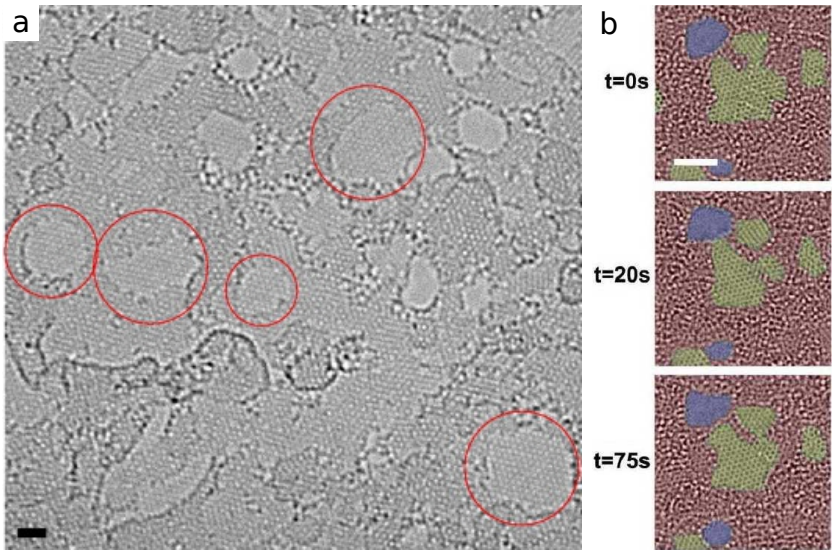


Figure 3.11: *HRTEM images of single-layer GO. (a) Red circles indicate hexagonally arranged area, the scale bar is 1 nm [27]. (b) Evolution of a GO mono-layer under continuous electron beam illumination at 80 kV voltage and* $2.8 \cdot 10^4$ $e^- s^{-1} A^{-2}$ *electron dose rate. The scale bar is 2 nm. Hexagonally arranged regions are shaded in yellow, disordered regions in red and holes in blue. [25].*

samples, effects due to the probe angle of incidence and polarization might contribute (i.e. $\pi^*$ and $\sigma^*$ relative intensity in graphite [276,278,279]).

Moreover, all these spectroscopic techniques suffer from the lack of direct references for the exact interpretation of the oxygen related features. Indeed, the assignments to individual functional groups are still largely debated and are based on comparison with reference spectroscopic signatures of aromatic molecules or small compounds (NMR [19,265], XANES [280,281], infrared spectroscopy [282]) or spectra simulations on hypothetical GO atomic structures [266,283]. However, molecular references are not completely reliable, considered the different carbon hybridization, bonding geometry and random proximity of the oxygen functional groups, which are expected to induce chemical shifts in the spectrum.

**Microscopy**

Some important insights into GO structure have been obtained by HRTEM imaging, although very few works have been reported [24,25,27]. In mono-layer GO, 1-6 nm$^2$ wide hexagonally arranged areas surrounded by disordered regions have been observed (Fig. 3.11) [25,27], in agreement with the Lerf and Klinowski's model. However, as expressed by Pacilé et

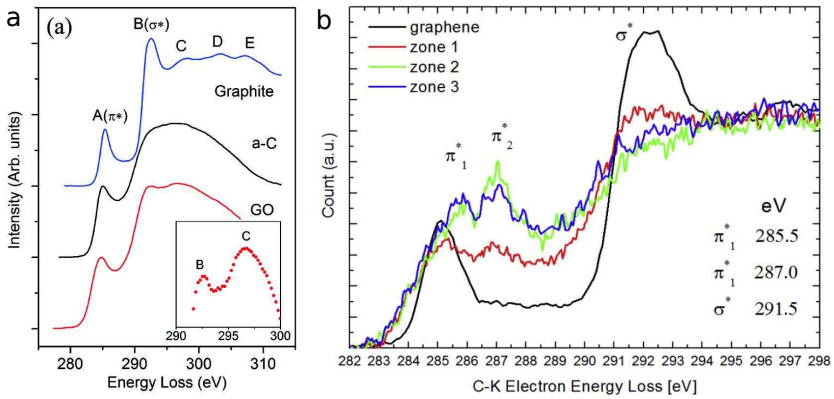


Figure 3.12: *Carbon K-edge core EELS spectra of GO (a) at 100 kV [29] and (b) at 60 kV [30].*

al. [27], further conclusions about GO structure seem difficult, because of the similar contrast of carbon and oxygen atoms. Moreover, hydrocarbons physisorbed on GO's surface could appear undistinguishable from functional groups. Indeed, since GO is very sensitive, the common heating procedure to remove carbonaceous adsorbates is not practicable [24, 27]. Finally, illumination damages have been demonstrated to occur under fast electrons illumination, even at relatively low acceleration voltages as 80 kV: radial wrinkles have been observed outside a region imaged with a total dose about $10^6$ $e^- A^{-2}$ [27] and mobility of the oxygen functionalities has been shown under continuous illumination with an electron dose rate of $2.8 \cdot 10^4$ $e^- s^{-1} A^{-2}$ [25] (Fig. 3.11.b). Only one study of atomically resolved STM microscopy of GO has been reported, revealing the presence of disordered areas and periodically arranged areas in a rectangular lattice, which has been interpreted in terms of epoxides absorbed on one side of GO's surface [284].

High-resolution microscopy images have therefore demonstrated the non homogeneity of GO structure at the atomic scale. This casts a new light on the previous spectroscopic characterizations and makes it clear that further advances in our knowledge of GO require very local spectroscopic techniques. Chemical investigation at a subatomic spatial resolution can in principle be attained by core EELS spectroscopy in a STEM microscope. However, GO sensitivity imposes serious limitations. Up to now, very few STEM-EELS studies have been conducted [29, 30]. The first one, by Mkhoyan et al. [29], reports an EELS spectrum from a mono-layer

GO, obtained by averaging many spectra acquired in different areas (Fig. 3.12.a). The authors exclude illumination damages in their specific experimental conditions and record the EELS spectra in area mode, to lower the electron dose. However, the carbon K-edge does not show any additional fine structure features and appears much likely to the amorphous carbon reference. This might be due to excessive spatial integration (leading to averaging and broadening of possible fine structures) or illumination damages (100 keV accelerated electrons induce defects already in graphene [285]). More recently, D'Angelo and coworkers have performed core EELS hyperspectral analysis, using 60 kV acceleration voltage. They have aquired a hyperspectral image over an area about 130 nm wide, with a spatial resolution of about 6.5 nm. Carbon K-edge spectra for different beam positions show the non-homogeneity of an additional C-O fine structure at 287.0 eV, which is associated to a predominance of epoxides by comparison with simulated spectra (Fig. 3.12.b). Nevertheless, only an average oxygen content has been calculated (O/C=0.22, i.e. 18 atomic oxygen %). Spatially resolved oxygen maps have not yet been reported.

**DFT**

Besides experimental investigations, complementary information have been obtained through numerical simulations conducted within and *ab initio* approach [21, 120, 251, 254–256, 266, 286–295]. Of course, the nonstoichiometry of GO's structure represents a fundamental issue, which affects the choice of functional groups configuration and the size of graphene supercell (defining the interaction between oxygen groups in neighbouring supercells). Structural optimizations have confirmed the deformation of the carbon lattice by absorption of isolated individual epoxides and hydroxyls: carbons atoms directly bound to oxygen are puckered out of graphene plane, with consequent relaxation of the surrounding carbon lattice; in addition, the C-C bond in the epoxide ring (-C-O-C-, Fig. 3.6) results strained and elongated [120, 256, 291]. With increasing degree of functionalization, the clusterization of functional groups absorbed on both sides of the carbon plane is energetically favoured because of strain minimization and formation of hydrogen bonds between hydroxyls and nearby oxygen atoms [21, 256, 286, 289, 293], and bond lengths between functionalized carbons progressively grow from graphene's 1.42 Å up to about 1.6 Å (1.54 Å in diamond) [256].

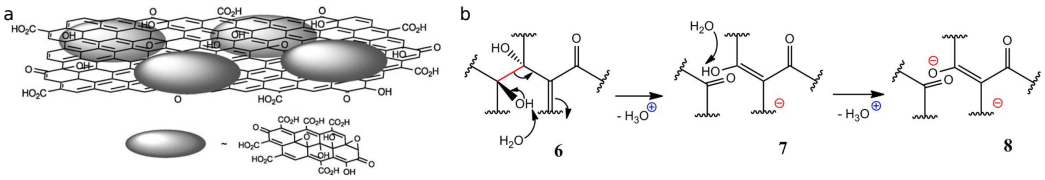


Figure 3.13: *Most recent hypothesis of GO atomic structure: (a) slightly oxidized GO with oxidative debris [296] and (b) possible route for GO degradation in water, leading to the dynamic structural model [23].*

## 3.7 Most recent hypothesis and models

Very recently, new elements have been introduced in our understanding of GO atomic structure. In 2011 Rourke et al. proposed that GO is composed of little oxidized graphene, identified as the real GO, to which highly oxidized debris produced by the oxidation process are strongly adhered [296] (Fig. 3.13.a). Insipired by analogous works of single walled carbon nanotubes, the model is based on the observation that the addition of $NaOH$ to a water dispersion of GO induces an irreversible phase separation resulting in a black aggregation and a colorless supernatant [296]. The reprotonated and washed aggregate is believed to consist of the purified GO, while the supernatant contains the oxidative debris. The debris are described as subnanometre size highly oxidized graphene layers, bearing the same kind of oxygen functional groups usually contemplated in GO. They are expected to be tightly bound to GO surface, such as to resist ultrasonication in water, and represent about 30% in mass of the starting nonwashed GO [296,297]. The original model has been supported by other publications by the same group [297,298] and received quite wide attention, although strong criticism has recently been raised.

Previously, strong alkaline environments such as $NaOH$ and $KOH$ were known for their deoxygenating properties [271] and commonly used to obtain RGO [299], as reported by many reviews [15,16,18,114]. Indeed, Fan et al. observed that the addition of $NaOH$ to GO dispersion causes a fast color change from yellow-brow to black and spectroscopic analysis confirmed the deoxygenation [271]. Differently from Rourke et al., they found the reacted suspension stable over several days. Moreover, Wang et al. have verified the interlayer distance shrinking down to almost graphene's value and a conductivity increase in the $NaOH$ treated GO [299].

As a matter of fact, the interaction of GO with $NaOH$ is not clear and the discussion has been lately revived by the work of Dimiev, Alemany and

Tour [23, 152]. Believing that the little number of carboxyl groups in GO cannot account alone for GO's acidity in aqueous solutions, they demonstrate that new acidic sites are formed on GO's surface by interaction with water (Fig. 3.13.b). This also entails C-C bonds cleavage, promoting GO sheets fragmentation. Moreover, the authors find that the role of $\mathrm{NaOH}$ is to accelerate the reaction between GO and water, $\mathrm{Na}^+$ counterbalancing the negative charge on GO's surface and $\mathrm{OH}^-$ being more effective than $\mathrm{H_2O}$ in the nucleophilic attack of GO's active sites. Hence, Dimiev et al. suggest a dynamic structural model (DSM) for GO, where the atomic structure of GO continuously changes, with a progressive decomposition of the basal plane [23]. More recently, Dimiev and Polson have reported elements against the existence of the oxidative debris [300].

Another evidence in disagreement with the debris model has been reported few months ago by Naumov et al. [301], based on the comparison of the optical properties of as-produced GO and a two component GO obtained by separately synthesizing lowly oxidized GO by a method previously elaborated by the same group [139] and oxidative debris, as specified in the literature [296]. The two systems displaying different optical responses, the authors exclude an appreciable contribution from the oxidative debris to explain GO's absorption and fluorescence properties [301].

## 3.8 About RGO's atomic structure

The definition of RGO's atomic structure suffers from the same incertitudes as in the case of GO, about the interpretation of the spectroscopic signatures. Moreover, a strong dependence may be expected on the particular reduction process employed, concerning the specific temperature used in thermal reduction or the particular choice of chemical reducing agent (as already discussed in section 3.4, these ones may have different efficiency against the various functional groups).

RGO obtained by mild thermal reduction at 200 $^\circ\mathrm{C}$ displays a drastic reduction of the oxygen content, as observed by XPS, with a visible increase of the $sp^2$ character of carbon [128, 147]. The extensive recovery in conductivity has been associated to the percolation between $sp^2$ areas [128]. In highly reduced RGO, the residual oxygen content can be lowered down to 0.4 at.% ($\sim$250:1 C/O atomic ratio) [14, 16–18]. The $sp^2$ hybridization is restored on a quite good extent, as indicated by XANES sharper $\pi^*$ and $\sigma^*$ peaks [119,147,258] and XPS [118,125,128,147,148,252].

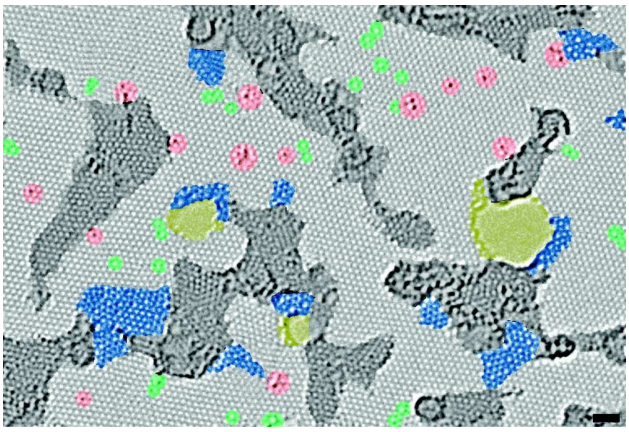

Figure 3.14: *RGO obtained by hydrogen plasma treatment. Contaminated regions are shaded in dark gray, desordered regions in blue, individual ad-atoms or substitutions in red, isolated defects in green and holes in yellow. The scale bar is 1 nm [26].*

In HRTEM images, 3-6 nm wide graphitic clean areas are observed [25,26] (Fig. 3.14), although many topological defects are also present (blue and green shaded areas in the figure). About the nature of the residual oxygen groups, there is not universal agreement on the dominance of hydroxyls or epoxides [147, 148, 288]. In the case of reduction with hydrazine, the removal of epoxides is reckoned more effective with respect to the other oxygen groups [255].

## 3.9 GO and RGO EELS investigation in the STEM microscope

Despite the long and rich discussion that has characterized of the last 20 years of research, GO atomic nature remains fundamentally elusive. Reasons can be found in the variability of the material depending of the synthesis, its non stoichiometry and sensitivity to external agents. Several models have tried to describe the arrangement of oxygen functional groups, but definitive experimental evidences are missing because local spectroscopic techniques could not yet match the gentle illumination conditions required by the fragile structure of GO.

In this thesis we aimed at quantifying the oxygen content at a nanometric scale using EELS spectroscopy in a STEM microscope. Fine structure peaks at the carbon K-edge were investigated in the search of additional

information on the kind of oxygen functional groups. The illumination conditions avoiding evident changes in GO's structure were defined at the beginning of the study.

This section introduces the sample preparation protocol and the experimental conditions for the STEM-EELS investigations. The precise acquisition parameters for the EELS spectra (i.e. illumination conditions optimized on GO) will be specified in the next section, followed by the presentation and discussion of the experimental results.

**Sample preparation**

Graphene oxide has been synthesized by the modified Hummers' method [13, 235] (section 3.3), and successive reduction has been achieved by hydrazine and thermal treatments. Both materials have been provided by Ana M. Benito and Wolfgang K. Maser, from the Department of Chemical Processes and Nanotechnology at Instituto de Carboquímica ICB-CSIC in Zaragoza. Few layers flakes with an average lateral size of few micrometers have been obtained by dispersion of the dried material in ethanol and ultrasonication. TEM grids were dried in air, firstly placed in the STEM microscope air lock ($< 2 \cdot 10^{-5}$ mbar) and then moved in the microscope column ($3 \cdot 10^{-8}$ mbar) and cooled down to about 150 K. High angle annular dark field (HAADF) images show a non homogeneous thickness of the flakes, with thinner regions some hundreds nm wide located at the flakes borders. Elemental investigations through core EELS indicate a clear dominance of carbon and oxygen with only negligible residues of nitrogen (in RGO, deriving from the hydrazine reduction agent [118, 235]) at few limited regions of the flakes (about 20 nm wide).

**Electron energy loss spectroscopy**

EELS spectra were acquired in a VG 501 Scanning Transmission Electron Microscope, provided with a liquid nitrogen cooling system at the sample stage (150 K). Low temperatures have been proven to reduce the mass loss damage by decreasing the atomic mobility [101] (section 2.9). Transmitted electrons were collected on a liquid nitrogen cooled CCD camera with a low read-out noise of three counts r.m.s. and a negligible dark count noise. The energy dispersion of the spectra was 0.27 eV, to allow simultaneous acquisition of carbon and oxygen K-edges. The effective energy resolution, resulting from microscope instabilities and spectrometer aberrations, is estimated to 0.5 eV on the carbon K-edge. The accelerating voltage has been limited to 60 kV and a low electron dose working mode was set by optimization of the acquiring parameters (beam current, illumination area and time) on (R)GO few layer flakes. During spectrum

imaging the beam focus (i.e. illumination area at the sample stage) has been adjusted to match the pixel size in order to avoid oversampling. The exposure of the material to the electron beam before spectra acquisition has been prevented by a fast blanking system before the sample, following the same procedure as in a previous study in the Orsay's microscope [6]. Equally, EELS spectra were acquired prior to the corresponding STEM images.

## 3.10 Gentle spectroscopy

In order to define optimal conditions for gentle illumination with a 60 keV electron beam, we have monitored the evolution of oxygen content and carbon near-edge fine structures in GO as a function of the irradiating electron dose. In Fig. 3.15.a we present the analysis of a time series of core EELS spectra acquired under homogeneous illumination over an extended area of a GO flake ($44 \times 44$ nm$^2$) with a 4 pA electron beam current and an integration time of 2.4 s, corresponding to an electron dose rate as low as $1.3 \cdot 10^2$ e$^-$Å$^{-2}$s$^{-1}$. The illuminated region has an initial oxygen content of about 45% (as derived from the spectrum in Fig. 3.15.a) that progressively reduces as a result of the increasing electron dose, as shown in Fig. 3.15.b (more details on the elemental quantification routine may be found later in section 3.11). Furthermore, the lowering of the oxygen content is associated with significant changes in C K-edge ELNES fine structures (Fig. 3.15.c). Variations in the near-edge fine structures are a typical indicator of radiation damages affecting chemical bonding and atomic orbital hybridization. [31] On these basis, it has been possible to define an upper limit for the electron dose of about $3 \cdot 10^3$ e$^-$Å$^{-2}$, below which no substantial changes occur neither in the flakes stoichiometry nor in EELS fine structures.

The need of low electron dose imposes constraints on STEM spatial resolution. [31] Indeed, the total acquired spectral intensity is proportional to the electron dose (fixed by irradiation conditions), the elemental specific cross section, the surface projected density of atoms i.e. the number of scattering centres (depending on the sample thickness) and the size of the illuminated area. Gentle illumination lowers the intrinsically weak intensity of core EELS signals and high spatial resolution implies that a very low number of scattering centres contribute to the EELS signal. In the specific set-up of our microscope, the highly efficient CCD camera and the

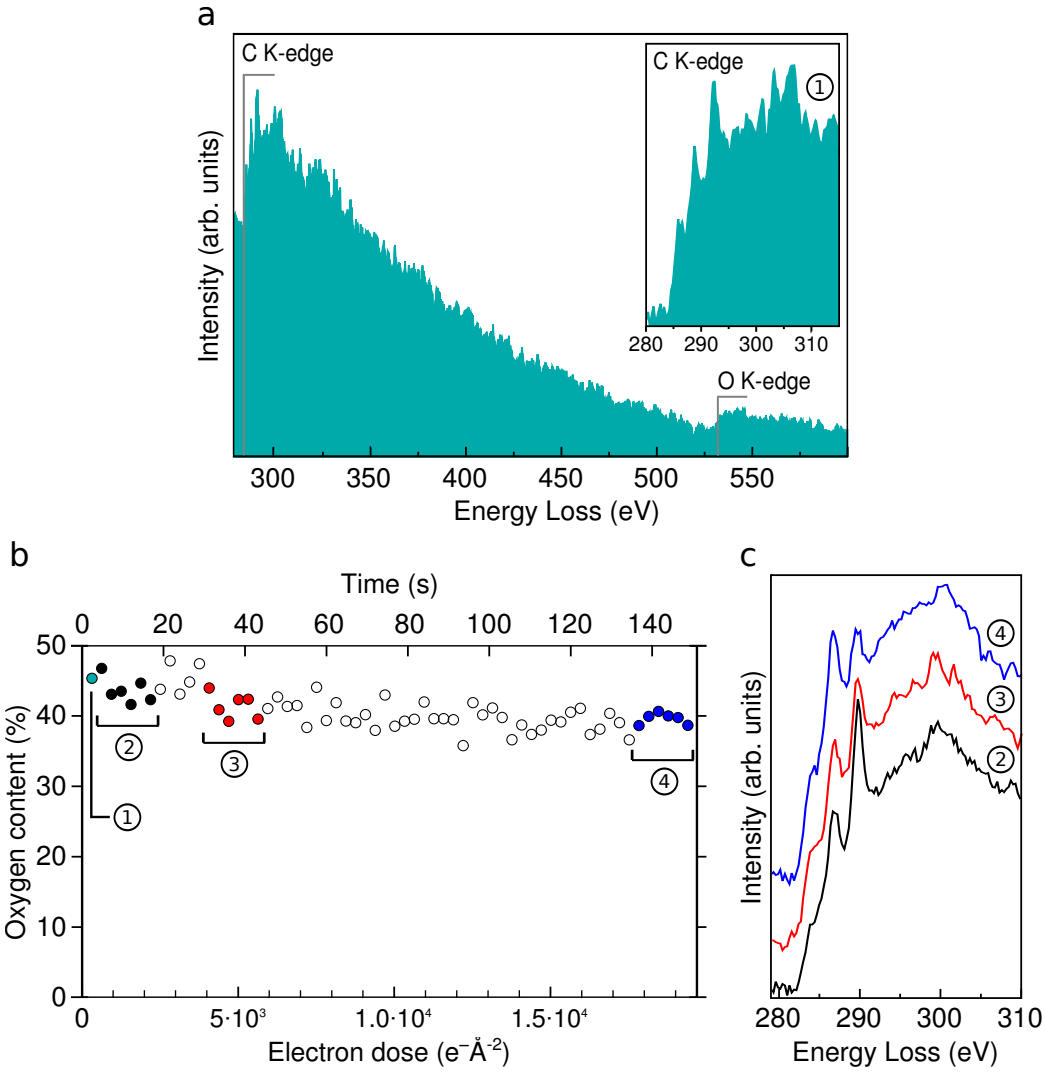


Figure 3.15: *Results from a time series of core EELS spectra acquired from a* $44 \times 44$ *nm*$^2$ *wide thin area of a GO flakes. (a) The first EELS spectrum, as acquired. (b) Evolution of the oxygen content during continuous exposure. The spectrum in (a) corresponds to dot (1). (c) Carbon K-edge spectra corresponding to exposure times indicated by the integration windows in panel (b).*

higher electron dose granted by sample cooling [31] allows to improve the EELS signal intensity. The Signal/Noise (S/N) ratio that is compatible with elemental quantification ultimately defines a ∼3 nm wide minimal illumination area for the study of GO.

## 3.11 Elemental quantification

The spatial distribution of oxygen in GO and RGO has been investigated by STEM-EELS spectrum imaging. This acquisition mode consists in collecting simultaneously the HAADF intensity and a complete EELS spectrum at each position of the electron beam during the scan, with a ∼3 nm minimal beam size and scanning step (no oversampling), to be compatible with the illumination conditions defined above. The limit on the spatial resolution derives from S/N requirements for elemental quantification: at equal electron dose, smaller illumination area correspond to a lower number of scattering centres, hence a less intense EELS signal.

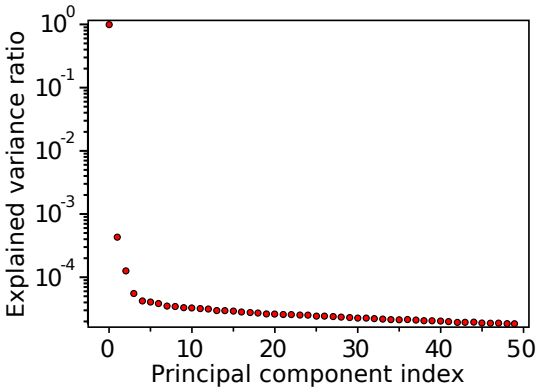


Figure 3.16: *Example of (also called scree-plot) typical of GO STEM-EELS hyperspectral images acquired in this work. The number of components to be retained for denoising is generally identified as the index at which the variance decrease becomes linear (in this example, it is 5).*

**Quantification procedure**

Elemental quantification was performed considering carbon and oxygen edges, within a 25 eV energy window. Specific cross sections were derived from the Hartree-Slater model. An error of a few percent may be assumed on the quantification results [302]. EELS spectra collected in a low electron dose mode are characterized by little intensity of the signals. Oxygen quantification has been performed on denoised spectra. Principal component analysis (PCA, section 2.12) represents a common technique for noise reduction in core EELS elemental mapping [303]. PCA analysis has been performed on hyperspectral images using the HyperSpy software [304]. Signal reconstruction is usually obtained from the first few principal components, which contain almost all of the information of the

original data (the other ones, with a low statistical weight, should only contain noise). The number of components to retain is estimated from the scree plot (Fig. 3.16), which shows the variance (i.e. amount of information) associated to each component. However, signal reconstruction using only the first few principal components (i.e. 5 in the case of Fig. 3.16) has been observed to contain considerable artefacts in the region of carbon K-edge fine structures. Indeed, when these peaks are weak and spatially localized, their statistical weight is low. Hence, the number of principal components has been raised to 15, and the quantification maps obtained have been verified to be compatible with results from untreated data. In any case, fine structure analysis has been performed on the as-acquired hyperspectral images, not treated with PCA, and the S/N ratio has been improved by integrating spectra from few consecutive pixels.

**Oxygen quantification in GO**

In Fig. 3.17 we report an example of EELS oxygen quantification on an individual few layer GO flake. The HAADF and bright field (BF) images of the whole flake are presented in Fig. 3.17.a-b respectively. A spectrum image has been acquired over the $1.3 \times 0.6\ \mu m^2$ wide area marked in Fig. 3.17.a and the resulting HAADF image is shown in Fig. 3.17.c. Acquisition parameters were 10 nm spatial resolution (probe size and scanning step), a 15 pA current and 0.15 s integration time, that corresponds to a $\sim 1.3 \cdot 10^3$ $e^- Å^{-2}$ total electron dose per spectrum. The HAADF intensity depends on both the amount of matter (thickness and areal density) and the chemical species (atomic number). These information appear separated in the integrated K-shell ionization edges maps derived from the spectrum image (Fig. 3.17.d-e), that show the spatial variation of the surface projected amount of carbon (hence the number of carbon layers) and oxygen respectively. In the quantification map of oxygen relative to carbon (Fig. 3.17.f) two well separated domains with oxidation levels centred at $\sim$32 at.% and $\sim$40 at.% are visible, as confirmed by the associated image histogram in Fig. 3.17.g. A third less extended domain (bottom left corner in the map) corresponds to $\sim$45 at.% with maximum local content of almost 50 at.%. When interpreting these results it must be considered that for each pixel the EELS signal is integrated over the specimen thickness. Hence, a non homogeneity in the relative quantification map can result from a spatial variation of the local oxidation level in regions with a constant number of layers or from the local superposition of additional layers with different oxidation level. In Fig. 3.17.f an increase of the oxygen relative content is visible from the left to the right side of the map forming two well sepa-

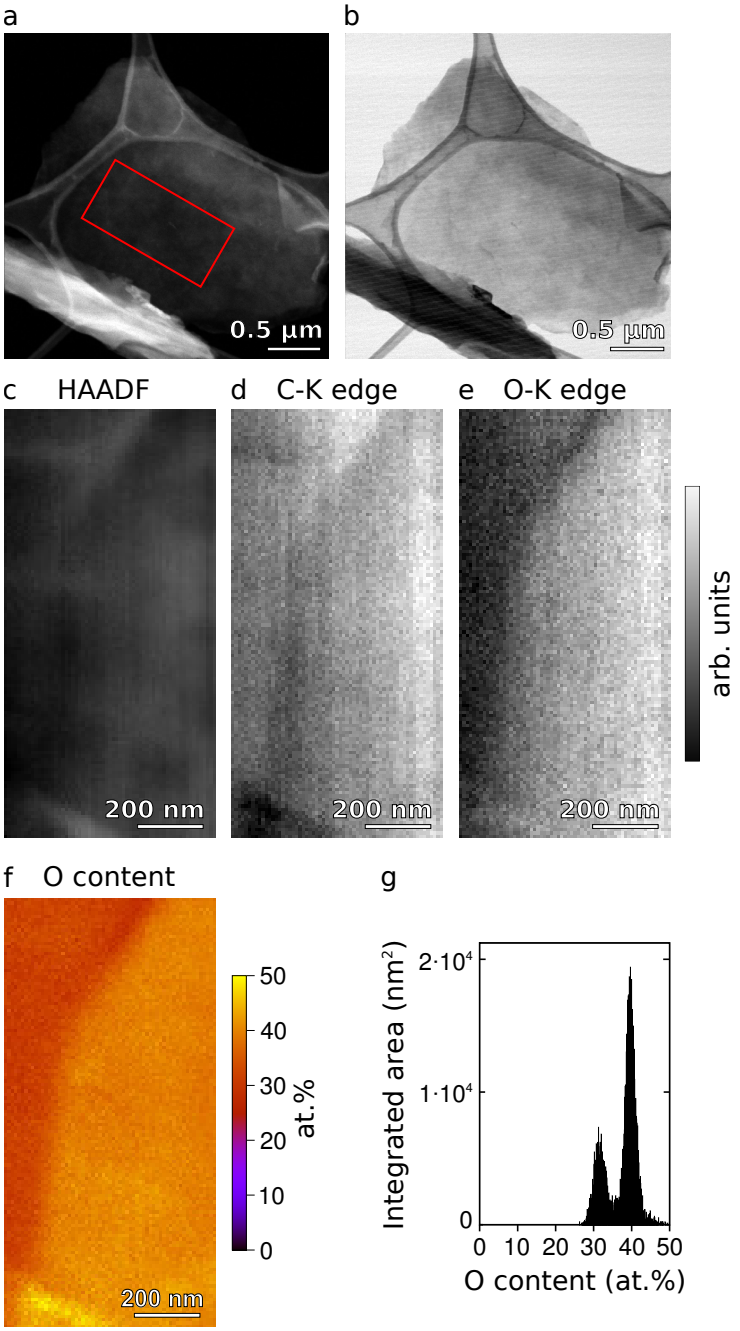


Figure 3.17: *Results from a spectrum image on GO. (a) HAADF image and (b) BF image of the whole flake. The spectrum image has been acquired over the region marked by the red rectangle. (c) HAADF image , maps of (d) carbon and (e) oxygen EELS K-edge integrated signals derived from the spectrum image. (f) Map of the relative oxygen content and (g) associated image histogram.*

rated regions. The oxygen integrated K-edge map (Fig. 3.17.e) shows the same trend: the right side area does contain a higher amount of oxygen. On the contrary, the intensity of the carbon integrated K-edge (Fig. 3.17.d) is almost uniform, indicating that the flake has a constant carbon thickness along the region displaying the oxygen gradient. Therefore these results show a variation of the oxidation level within an individual flake, forming spatially well separated oxidation phases which are not correlated with the flake thickness.

Overall the oxygen content in GO has been observed to vary between $\sim$10 at.% and $\sim$50 at.% (C/O ratio of 9:1 and 1:1 respectively). The higher oxidation level (30-50 at.%) seems to characterize about one quarter of the analysed material, while in extremely rare cases the oxygen content fells below the detection limit (unoxidized flakes), confirming the heterogeneity of GO. Therefore despite the fact that the local oxygen concentration can be extremely high, the average oxygen content in individual flakes is $\sim$25 at.%, which is in good agreement with spatially averaged values reported in literature [14, 16–18]. Regions up to few hundreds nanometres wide are characterised by an almost uniform oxidation level (at a 3-10 nm scale), while the transition between two oxidation phases occurs in the space of few tens of nanometres. This observation is compatible with a recently proposed oxidation mechanism where the reaction progresses within graphite flakes in a front-like diffusive-controlled pathway [231].

**Oxygen quantification in RGO**

STEM images and spectroscopic analysis from RGO are shown in Fig. 3.18. HAADF and BF images of the whole flake are shown in Fig. 3.18.a-b. A spectrum image has been collected over the region marked in Fig. 3.18.a, over an area of about $330 \times 190$ nm$^2$. Acquisition parameters were: 3 nm spatial resolution, 11 pA current and 0.04 s integration time, for a total electron dose per spectrum of $\sim 3.0 \cdot 10^3$ e$^-$Å$^{-2}$. Fig. 3.18.c-g shows the associated HAADF image, the integrated K-shell ionization edges maps of carbon and oxygen, the quantification map of oxygen relative to carbon and its associated image histogram. As in GO, the carbon and oxygen K-edge integrated intensity maps appear mainly non correlated. Weak correlations appear occasionally, not systematically, in some limited areas. Namely, in the central region of the spectrum image the carbon K-edge intensity is almost constant, while the oxygen K-edge signal varies and may be responsible for the contrast variation in the HAADF image. The distribution of oxygen forms patches few tens of nm wide (Fig. 3.18.e-f) that correspond to an unimodal distribution centred at about 5 at.% (Fig.

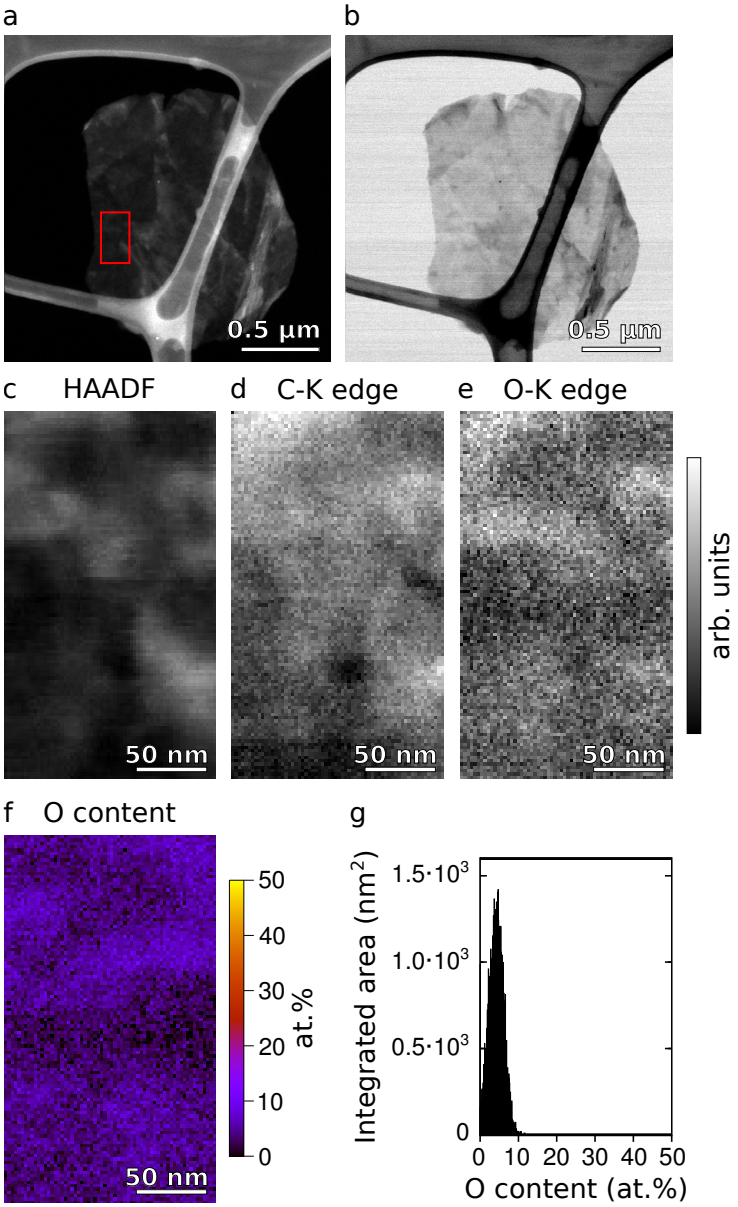


Figure 3.18: *Spectrum imaging on a RGO flake. (a) HAADF image and (b) BF image of the whole flake. The region investigated in the spectrum image is marked by a red rectangle. (c) HAADF image, maps of (d) carbon and (e) oxygen EELS K-edge integrated signals derived from the spectrum image. (f) Map of the relative oxygen content with (g) associated image histogram.*

3.18.g), with a local upper limit of 12 at.% (local residual oxygen up to 20 at.% has been observed in other flakes, over limited regions). These values are situated in the range of spatially averaged oxygen quantifications reported in literature [14, 16–18].

## 3.12 Core EELS fine structures at the carbon K-edge

Besides oxygen quantification, coordination states and chemical bonds for different oxidation phases can be extracted from spectrum images through energy-loss near-edge structures analysis. The spatial resolution of the spectrum images has been optimised for elemental analysis; the higher S/N ratio required for fine structure investigation can be obtained by integrating the spectrum images over regions few tens of nanometres wide, having a uniform oxygen content. In Fig. 3.19 we present fine structures at the carbon K-edge that are representative of particular ranges of oxygen content. Fig. 3.19.a shows the fine structure signatures observed in GO areas characterised by 10 to 50 oxygen at.%. In both spectra corresponding to low oxygen concentration ($\sim$20 at.%), the $\pi^*$ and $\sigma^*$ signatures associated to $sp^2$ carbon are visible respectively at 285.0 eV and 292.7 eV [277]. Two additional peaks at 287.2 eV (A) and 288.2 eV (B) could be isolated over two distinct areas of GO (in this particular cases showing 20 and 25 oxygen at.% respectively). These features generally show a feeble intensity and can appear simultaneously in the same spectrum, resulting in mixed features that can hardly be identified. In GO regions containing $\sim$30 oxygen at.%, the intensity of the $\pi^*$ peak lowers while the 287.2 eV peak (A) remains intense (32 oxygen at.% for the here reported spectrum). An additional feature rises at 290.1 eV (C) followed by a broad triangular-shaped signal at about 300 eV (D). For higher oxidized GO regions (40-50 at.%, the reported spectrum corresponding to 40%), the $\pi^*$ peak further lowers while the peaks at 287.2 eV (A) and 290.1 eV (C) get stronger and very well-defined. The 290.1 eV peak appears particularly sensitive to irradiation damages, as shown by Fig. 3.15.c.

After reduction (Fig. 3.19.b) the sharpness of the $\pi^*$ and $\sigma^*$ peaks, with a trace of $\sigma^*$ excitonic feature at 291.6 eV [275, 276], reveals a very good recovery of the graphitic network. An additional well-defined peak at 287.2 eV (A) is observed (the two spectra shown correspond to 7 oxygen at.% and 12 at.%). Rarely and in some limited regions, other weak fine struc-

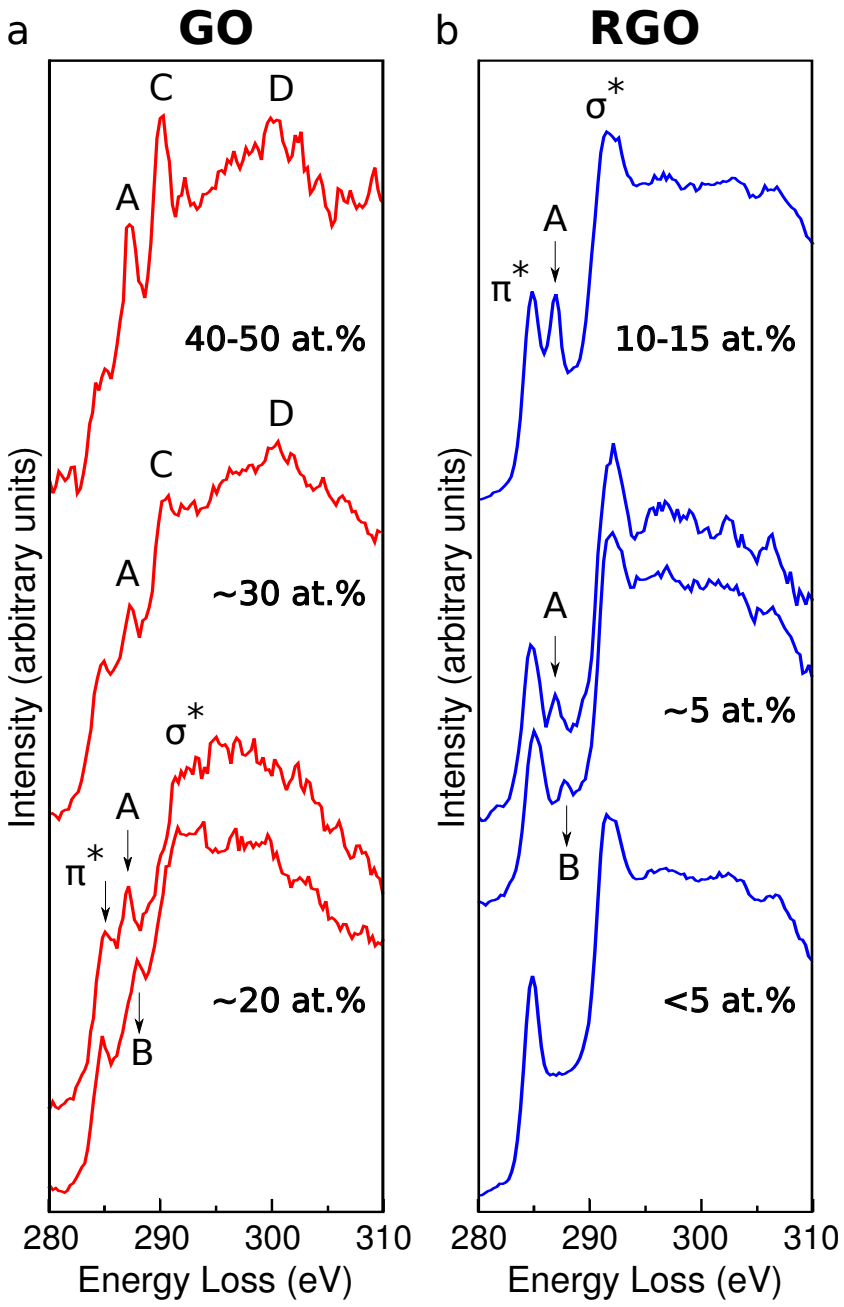


Figure 3.19: *Carbon K-edge EELS spectra of GO (a) and RGO (b) from homogeneous regions of the flakes, corresponding to an oxygen content comprised in the indicated range.*

ture peaks have been distinguished, i.e. peak B (5 oxygen at.%). These A and B spectral features are below the detection limit for lower oxygen concentrations.

These results show that specific near-edge fine structures and thus coordination states of the carbon atoms correspond to different oxidation rates. The energies of EELS peaks in Fig. 3.19 are compatible with previous XANES results which however could not separate the specific near-edge fine structures shown here due to spatial averaging over wide regions with different oxygen levels. Absorption peaks indicated as A-C had been attributed in the literature to C-O $\pi$ symmetry antibonds: lower energy peaks to single bonds and higher energy peaks to double bonds. More precisely, hydroxyl groups had been generally associated to peak A, epoxide groups to peak A or B, carbonyl and carboxyl groups to peak B or C [147, 258, 259, 270, 272–274, 305]. In the $\sigma^*$ region, carbonyl groups have been related to peak D [27, 147]. In a recent STEM-EELS investigation a shallow peak A has been observed at the carbon K-edge and assigned to epoxide, while no peak C has been detected [30] (as discussed in section 3.5, Fig. 3.12.b). These assignments, still largely debated, have been obtained by comparison with reference spectroscopic signatures of aromatic molecules [280, 281] or spectra simulations on hypothetical GO atomic structures [30, 283]. However, as shown a number of times by numerical simulations [256, 286, 290, 293, 306], the spatial configuration of functional groups within (R)GO deeply affects their orbital associated energies and these might strongly differ from those of the same groups within molecules. Moreover, the sensitivity of the material suggests the need of caution while comparing spectroscopic results. In particular, the illumination conditions can induce changes in the relative intensity of fine structure peaks by transformation of the functional groups (possibly hydroxyls into epoxides) or selective sputtering of the oxygen groups.

## 3.13 Structural model

The structure of GO can be revisited on the basis of the here reported spatially resolved spectroscopic results. Several complex atomic models for GO have been proposed in the last twenty years [14, 16–18]. Oxygen absorption is usually described in terms of the basic functional groups of epoxide, hydroxyl, carbonyl (-CO) and carboxyl (-COOH). The last two groups involve multiple bonding with a single carbon atom, which can

occur at edges or at defects within the graphene lattice. On the contrary, a complete and in principle reversible functionalization of a perfect graphene network can be achieved with epoxides and hydroxyls, resulting in a C/O ratio of 2:1 (33 oxygen at.%) for solely epoxides functionalization, 1:1 (50 oxygen at.%) for solely hydroxyls functionalization and intermediate values for mixed structures. With respect to our experimental observation, the Lerf-Klinowski model is consistent with GO regions with a 20 oxygen at.% content but cannot account for the much higher oxygen concentration locally observed by EELS ($\sim$45 at.%).

The presence of water molecules in the atomic structure of GO is still under debate. Water molecules are expected to form hydrogen bonds with oxygen functional groups on GO [19]. We expect reasonably that any possible intercalated water would have been removed from the here observed flakes, during the preparation process. Indeed, differently from the common protocol where GO is directly deposited on a substrate as a water dispersion, in this work we employed dried GO which was successively redispersed in ethanol and ultrasonicated. Moreover observation conditions involve high vacuum levels ($3 \cdot 10^{-8}$ mbar), resulting most probably in evaporation of residual water molecules. On the basis of these considerations we expect a negligible amount of water. This hypothesis is corroborated by our observed EELS fine structures. Indeed, the strong intensity and sharpness of the fine structure peaks at the carbon K-edge correlated with a high oxygen content (Fig. 3.19.a) suggest that a significant amount of carbon atoms are involved in a specific kind of carbon-oxygen bond. Thus, the $\sim$45 oxygen at.% in GO cannot arise from intercalated water and should be ascribed to oxygen directly bound to carbon.

Recently it has also been proposed that GO surface could be decorated by strongly bound highly oxidized debris coming from the oxidation process [296]. In the present work, an important contribution of such debris to the calculated oxygen content is not compatible with our spectroscopic investigations: their presence would result in an increase of intensity in the K-edge maps of both oxygen and carbon (as an additional GO layer), and hence in a correlation between the two maps, which is not observed in Fig. 3.17.d-e. Moreover, the highly oxidized residues could contain at most $\sim$50 oxygen at.%, considering a fully functionalized structure (hydroxyls on the basal plane and carbonyls-carboxyls at the edges, as discussed above). In Fig. 3.17.g the local oxygen content reaches almost 50 at.% and represents an integrated measurement over the flake thickness: even assuming the presence of debris, the underlying GO layer(s) has to

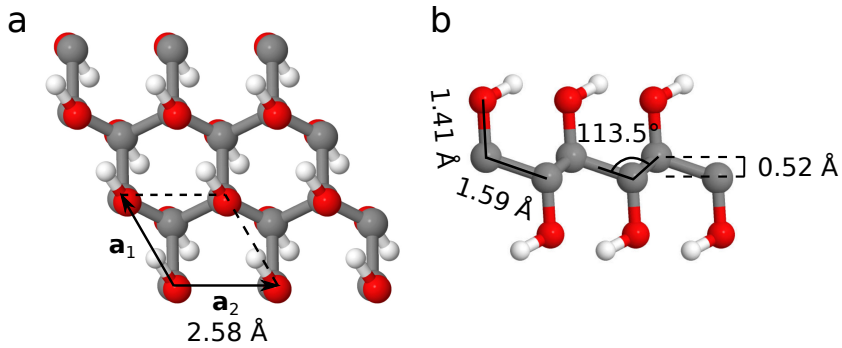


Figure 3.20: *Limit structure allowing a C/O ratio of 1:1. Top (a) and side (b) view. The indicated structural parameters have been obtained after full DFT-LDA relaxation.*

be necessarily almost 50 at.% oxidized. These experimental evidences reinforce the criticism recently risen against the debris GO model [300].

Previous first principle simulations have shown that in GO there is a strong driving force towards a phase separation in fully functionalized regions (epoxides and/or hydroxyls) and pristine graphene regions [21, 287, 290, 293]. The limit of 50 at.% local oxygen concentration observed in this work is not consistent with a full functionalization dominated by epoxides, since the oxygen content would tend to 33 at.%. A large presence of carboxyl and carbonyl groups should also be excluded, because such a highly defective structure could hardly be reduced to a highly graphitic arrangement compatible with the carbon K-edge fine structures observed in RGO flakes. GO containing almost 50 at.% of oxygen and converting into a highly graphitic structure when reduced can be explained only by an almost hydroxyl saturated graphene lattice (Fig. 3.20). This limit structure is analogous to graphane [307] (i.e. hydrogen saturated graphene) and hydroxyl groups should alternate at the two sides of the carbon plane in order to minimize strain [256, 289].

## 3.14 ELNES peaks interpretation

EELS fine structures for highly oxidized GO (30-50 oxygen at.%, Fig. 3.19.a) can thus be interpreted in the limit of this hydroxyl saturated graphene model. The extremely low intensity of the $\pi^*$ peak can be ascribed to the loss of $sp^2$ hybridization at carbon atoms. The 287.2 eV peak (A), which is observed also for lower oxygen rates, can be assigned to C-

OH antibonds, in agreement with previous XANES works [258, 259, 274]. The peak at 290.1 eV (C) cannot be associated to C-O antibonds of other oxygen functional groups, because they are expected to be present only in a small amount and this is not compatible with the strong intensity of the peak. Nevertheless, the interpretation of this feature remains not clear.

Fine structures for lower oxidation rates (10-30 oxygen at.%, Fig. 3.19.a) are much less defined. This can be due to a higher variety of functional groups and the high number of possible configurations that they can assume at the graphene network. The presence of the $\pi^*$ peak and of a weak $sp^2$ $\sigma^*$ peak lets infer a limited presence of non functionalized carbons. Aside the peak A ascribed to hydroxyl groups, peak B can be attributed to epoxide groups. After reduction the very intense and sharp peak A observed at higher residual oxygen regions (Fig. 3.19.c, $\sim$15 oxygen at.%) would then correspond to the presence of solely hydroxyl groups. This interpretation is compatible with the identification of several simple reaction routes for epoxide reduction by hydrazine, while hydroxyl removal mechanisms are still debated [118,255]. Considering the same assignments as in GO, the weak peak B in RGO indicates a small residual amount of epoxides. Again, the difference in the intensity of features A and B can derive from their relative amount (hydroxyl probably remain the dominant species also after reduction) and the different number of configurations that these functional groups can form at the carbon network.

## 3.15 Numerical simulations

Previous numerical simulations have shown that the agglomeration of epoxides and hydroxyls in the form of islands or chains is stabilized by lattice strain release and hydrogen bonding (involving hydroxyls), while the formation of conjugated nonoxidized regions is energetically favoured with respect to isolated nonfunctionalized carbons [21, 148, 254, 287, 290, 291, 293]. Moreover, the formation of larger graphitic areas reduces the interfaces with oxidized regions and the relative interfacial energy [131]. Nevertheless, the overall results from simulations do not yet provide a clear vision of GO and RGO. For example, there is not total agreement on the relative stability of epoxides and hydroxyls: for some authors epoxides are the most stable [251, 286, 288] while for others the epoxide rings are strained and more reactive than hydroxyls [20, 256, 289]. Surely, the concentration and proximity of the functional groups is a fundamental factor

(hence the importance of graphene supercell dimension). Several different configurations of epoxides and hydroxyls have been studied from an energetic point on view, to determine the most favourable ones. Following our experimental results, we're particularly interested in hydroxyls absorption and clusterization. For this reason we have conducted numerical simulations to compare the formation energy of isolated hydroxyls and epoxides and the binding energy of two hydroxyls in different absorption configurations.

We have performed structural optimizations within the framework of density functional theory (DFT) under the local density approximation (LDA) as implemented in the AIMPRO code [308, 309]. Carbon, oxygen and hydrogen pseudopotentials have been generated using the Hartwingsen-Goedecker-Hutter scheme [310]. Valence orbitals have been represented by a set of cartesian gaussians of s-, p-, and d-type basis functions centred at the atomic sites. We have used a basis set of 22 independent functions for carbon (pdpp gaussian exponents), 40 functions for oxygen (dddd) and 12 functions for hydrogen (ppp). The optimization of the cell parameter has been performed simultaneously with the relaxation of all atomic positions, using a conjugate gradients algorithm.

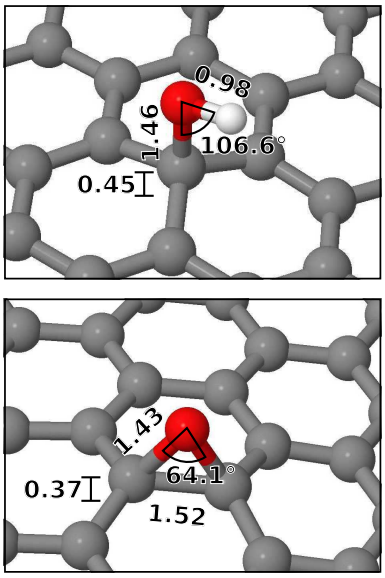


Figure 3.21: *DFT-LDA relaxed structures of hydroxyl and epoxide in high dilution regime (6×6 graphene supercell).*

The hydroxyl fully functionalized limit configuration is presented in Fig. 3.20 after optimization by DFT-LDA. The graphene network is shown to be strongly distorted, with carbon atoms puckered out of plane by about 0.26 Å, leading to a change of their hybridization state from pure $sp^2$ to partial $sp^3$. In contrast with graphane, where the $sp^3$ carbon hybridization reduces the in plane cell parameter (∼2.42 Å) [307], we obtain an increased cell parameter of 2.58 Å, (about 5% higher than DFT-LDA optimized graphene) and a C-C bond length higher than diamond (1.59 Å). Oxygen steric hindrance and hydrogen bonding between neighboring groups forming hydroxyl chains are responsible for this in plane expansion as for graphene edges functionalized by hydroxyl groups where the accumulated strain is released via the formation of static out-of-plane ripples [311].

Formation energies of hydroxyls and epoxide in the case of high dilution (C:O=72:1, 6×6 graphene supercell) have been calculated after structural relaxation (Fig. 3.21) as

$$E_{OH}^{form} = E_{GO} - N\mu_C - \mu_O - \mu_H$$

where $E_{GO}$ is the total energy of the oxidized system, N is the number of graphene unit cells and $\mu_C$, $\mu_O$ and $\mu_H$ are the chemical potentials of respectively carbon, oxygen and hydrogen. Formation energy of epoxide was analogously estimated. Previous works in literature have reported formation energies considering an oxidizing environment [21,256,287,312], but the comparison between oxidizing and reducing atmospheres could give important insights into the atomic structure of GO, given the complexity of the synthesis process. We have estimated oxygen and hydrogen chemical potentials for the extreme cases of highly oxidizing and reducing environments from the relations

$$oxid. \quad \begin{cases} \mu_O = \frac{1}{2}E_{O_2} \\ \mu_H = \frac{1}{2}E_{H_2O} - \frac{1}{4}E_{O_2} \end{cases}$$

$$red. \quad \begin{cases} \mu_O = E_{H_2O} - E_{H_2} \\ \mu_H = \frac{1}{2}E_{H_2} \end{cases}$$

while carbon chemical potential has been estimated as the total energy of graphene unit cell. Formation energies are shown in Fig. 3.22.a as a function of oxygen chemical potential. The formation energies in reducing and oxidizing atmosphere have been calculated using the above relations for the chemical potentials, and intermediate states are linear in $\mu_O$. Since hydrogen and oxygen chemical potentials are interrelated by $\mu_H = 1/2E_{H_2O} - 1/2\mu_O$, only oxygen chemical potential is shown in the figure. Epoxide is confirmed as the more stable functional group in strongly oxidizing environment. However, in a wide range of oxygen chemical potential corresponding to an oxidizing atmosphere, hydroxyl formation is favoured with respect to epoxide. Therefore, for specific chemical environments during the synthesis, graphene oxide functionalization can be dominated by hydroxyls groups.

DFT simulations have demonstrated that oxygen groups absorbed on graphene surface tend to clusterize [21,148,254,287,290,291,293]. The energy gains determined by the clusterization of two hydroxyls in different

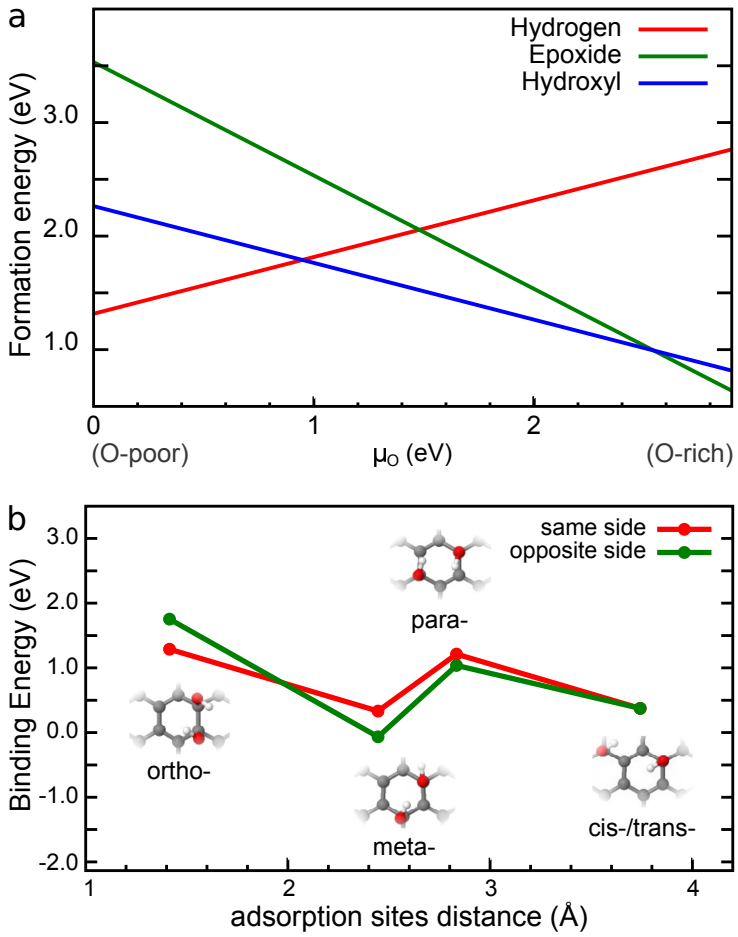


Figure 3.22: *(a) Formation energy in reducing and oxidative environment for high diluted structures (one functional group per 72 carbon atoms). (b) Binding energy for two hydroxyl groups in a high diluted structure, for the cases of both hdroxyls on the same side of the carbon sheet and one on each side.*

absorption configurations have been calculated, identifying the absorption at two neighbouring carbons (ortho-configuration) on opposite sides of the carbon sheet as the most favourable [21, 289, 290, 306]. Nevertheless, the comparison of all possible configurations would provide a more complete picture of two-hydroxyls interaction. We have calculated binding energies for the absorption of two hydroxyls on the same and opposite sides of the carbon plane up to third neighbours. The graph in Fig. 3.22.b summarizes binding energies as a function of the distance between the absorption site carbons. For simplicity we have reported the distances between the absorption sites (carbon atoms) as calculated in flat graphene.

Binding energies have been derived from relaxed structures. The ortho-configuration is the most energetically favourable, followed by para-. The interaction between the hydroxyls groups remarkably affects the energy of the system. For the ortho- arrangement hydroxyls absorption on opposite sides minimizes the lattice strain, while the meta- configuration is more stable when hydroxyls are situated on the same side and the formation of hydrogen bonds lowers the energy. These results confirm a strong driving force towards formation of fully -OH functionalized domains, especially in the graphane-like arrangement (Fig. 3.20).

## 3.16 Perspectives

In this chapter we have demonstrated that the oxygen content in GO and RGO is not spatially uniform and two oxidation phases corresponding to high and low oxidation levels are well separated in GO. The presence of domains fully covered with hydroxyl groups has critical implications for the engineering of the electronic structure of individual flakes. Indeed, it strongly affects the hydrophilicity of the flakes and the interaction with molecules from the gas and vapour phase [113]. Furthermore, the presence of a dense hydroxyl layer on (R)GO sheets has important consequences for the anchoring of metal and ceramic nano particles or biomolecules and the assembly of individual flakes into corresponding macroscopic forms [313]. The obtained results may thus be helpful for a more controlled use of GO in applications.

Several points about GO and RGO atomic structure still need to be cleared. By STEM-EELS spectroscopy, more insights could be searched for using lower acceleration voltages (i.e. 30 keV). However, illumination damages arise from different dynamics and not all of them would necessarily benefit from lower voltages. Indeed, electron-beam induced atom knock-on displacement (and sputtering) derive from elastic scattering between incident electrons and nuclei in the specimen. This kind of interaction is reduced by lowering the electron energy below the element-specific threshold, which is 80 keV for carbon in graphene [96] but only 2 keV for hydrogen [95]). Hence, acceleration voltages lower than 60 keV might not provide considerable advantages in terms of knock-on displacement. The other source of illumination damages is inelastic scattering, which causes chemical bonds breakage (radiolysis). This is the principal damage dynamics in organic specimens and can be expected to be very important in

GO, where it could be responsible for oxygen functional groups rearrangement or removal. The inelastic cross section increases inversely with the voltage, so radiolysis would become more significant. At the same time, the EELS signal would also be more intense, so the two effects might compensate [31, 95, 285]. The most effective method to reduce the mass loss damage deriving from radiolysis is lowering the temperature below -100 °C [31, 95].

As far as the kind of oxygen functional groups, complementary results may be expected by the technical development of other spectroscopic techniques. For example, the spatial resolution diffraction limit in some spectroscopy techniques based on laser probes has recently been overcome thanks to tip-enhancement or other strategies. In particular, nano-infrared spectroscopy has been achieved on a sample back-illuminated with an infrared beam, using as a sensor an AFM tip in contact mode with the sample surface [314]. This kind of technique could provide access to the local chemical composition in GO in terms of functional groups, possibly revealing the spatial variation of hydroxyls and epoxides concentrations.

DFT optimized structures of the hydroxyl full functionalization shows an increase in the in-plane lattice parameter. However this has not yet been observed by electron diffraction. The accurate measure of the C-C distance and in-plane lattice parameter is a non trivial technique. In 2D materials the reciprocal space of monolayers consists of rods: a slight tilt of the specimen with respect to the correct perpendicular orientation with respect to the electron beam results in wrong reciprocal space distances in the diffraction pattern [315]. The right orientation can be identified by maximizing the diffraction spots intensity (although it varies slowly in the case of one monolayer) and minimizing the spots broadening that comes from the nonflatness of the atomic layer inside the illuminated area [315]. Most importantly, to observe the lattice parameter increase, the specimen within the illuminated area (several hundreds of nanometres, SAED aperture) must be uniform, while hydroxyl saturated regions are expected to be very little extended (it is only a limit structure). Although the average in-plane C-C distance has been found equal to that of graphene [24], the presence in GO of lattice distortions and strain at the nanometre scale has been deduced from the nonlinear broadening of the diffraction spots as a function of the tilt angle [316].

Finally, in the lack of experimental references, further understanding of GO and RGO spectroscopic signatures might be provided by theoretical simulations. Indeed, moderate attention has been brought up to the

present to spectra simulations [30, 283, 292]. Many body effects are expected to be important and 2D materials typically display strong excitonic signatures. These last ones are critical in core spectroscopy such as EELS and XANES, where the core hole and the excited electron may form a core exciton. These effects cannot be properly taken into account by standard DFT treatments, but the solution of the Bethe-Salpeter equation in future simulations might provide a more realistic description.

CHAPTER 4

# LUMINESCENCE FROM SINGLE MOLECULES ON HEXAGONAL BORON NITRIDE

The optical detection and spectroscopy of isolated individual molecules dates back to 1989, with the work of W. E. Moerner and L. Kador based on frequency modulation (FM) spectroscopy [33]. Since then, the field has kept developing, opening new frontiers in microscopy, biology, electronics and fundamental physics. Extraordinary breakthroughs in reducing optical probes size have allowed the passage from the characterization of ensemble of identical molecules to the investigation of single molecules one by one. This has unveiled the heterogeneity of single molecules optical properties, depending on their local environment. The nanometre size of the STEM electron probe makes STEM-CL a promising technique for the study of single molecules. Several advantages may be identified with respect to other techniques, in terms of acquisition conditions and time, sample preparation and versatility. However, illumination damages represent a strong limitation. This obstacle can be bypassed relying on an indirect excitation mechanism, completely avoiding molecules irradiation.

The first part of this chapter will give some insights into the properties and applications of single molecules and the specific imaging and spectroscopic techniques. The results obtained by STEM-CL in this thesis will be presented starting from section 4.8.

## 4.1 From ensembles to single molecules

When addressing ensembles of identical molecules, broad spectroscopic lines are obtained, which represent an average of all single molecule contributions. A great deal of information is buried in this signal, and it can only be extracted by reducing the excitation volume to probe single

molecules one by one.

In order to be isolated and as far as possible immobilized for investigation, single molecules at a very low concentration are usually dispersed in a medium such as a crystal [33, 34], a polymer matrix [317, 318], a solvent [35] or deposited on a surface [319, 320]. Numerous factors can characterize the local environment of a single molecule, including type of crystal site, presence and distance of crystal defects, molecule orientation in the polymer matrix, adsorption or chemisorption configuration on a surface and many others.

As a first demonstration of the environment effect, the spectroscopic lines of several individual molecules sitting in different sites of a crystalline host at cryogenic temperatures can be distinguished even by ensemble spectroscopy [321]. Indeed, the absorption resonant frequency is shifted depending on the type of crystal site, and the intensity and frequency of the fluorescence transitions as well as the molecule photostability are observed to vary [322].

The width of these spectroscopic lines is much wider than their expected intrinsic width (homogeneous width), which, at low temperatures, should be limited only by the lifetime of the excited state [321]. The observed broadening is known as inhomogeneous broadening, and originates from the contribution of many individual molecules, each one experiencing additional perturbations from a slightly different local environment. Indeed, the presence and distance of neighbouring defects in the crystal (also represented by other molecules) or local electric fields induce slight modifications in the electronic structure of the molecule, and hence a shift of the molecule resonant frequency. The inhomogeneous width arise from the contribution of many single-molecule lines slightly apart from to the central frequency [321, 323, 324], as in Fig. 4.1.

Moreover, frequency shifts and jumps of single-molecule lines occur in time, induced by dynamical factors such as configurational changes in the host crystal, thermal fluctuations of the molecules or photoinduced processes. This effect was named spectral diffusion [317, 318, 320, 321, 325–327]. Furthermore, variations in single molecule line width or excited state lifetime have also been attributed to changes in the local environment [317, 318, 328].

Hence, scaling up to the single molecule level has unveiled an extremely heterogeneous reality. The removal of the ensemble average has allowed to observed unexpected effects in single-molecules and has opened exciting perspective in fundamental physics, biology and technol-

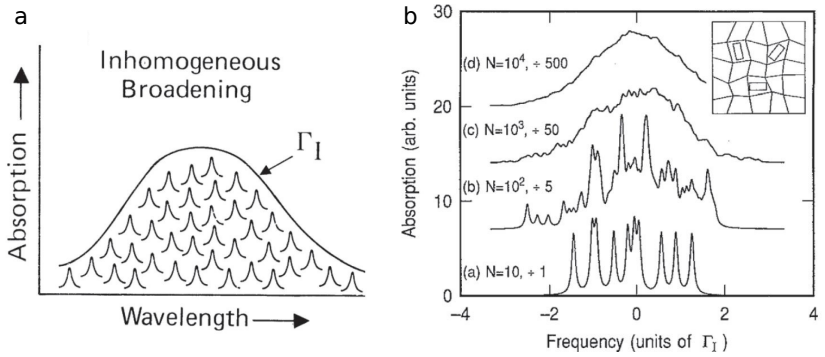


Figure 4.1: *(a) Schematic representation of inhomogeneous broadening and (b) its effect simulated for an increasing number N of molecules. The inset shows a schematic of molecules in different local environments. Both the images were extracted from ref. [321].*

ogy.

## 4.2 Single molecules for advanced research and technology

**Molecular physics**

The possibility of addressing a single molecule and probing its optical properties by spectroscopic techniques has opened new experimental prospects in molecular physics. Indeed, the removal of the inhomogeneous broadening and the monitoring of spectral diffusion at cryogenic temperature allow to obtain very narrow optical lines and measure precise molecular states, dynamical events and derive statistical information. Moreover, spectroscopy of single molecules have enabled to observe new phenomena as intermittent fluorescence, known as blinking [324,333] reversible switching between bistable molecular states [333–339] and photochemically-induced irreversible stop of the fluoresence (photobleaching) [319, 325]. As well, the influence of the local environment on the molecule physical properties can be studied.

**Nanoreporters**

Thanks to the susceptibility of molecular optical properties to the chemical and physical nature of the local surroundings and dynamics, single molecules act as good nanoreporters, with the high sensitivity deriving from the narrow optical line widths [321, 325]. Single fluorescent molecules are indeed efficient sensors of biochemical processes and cat-

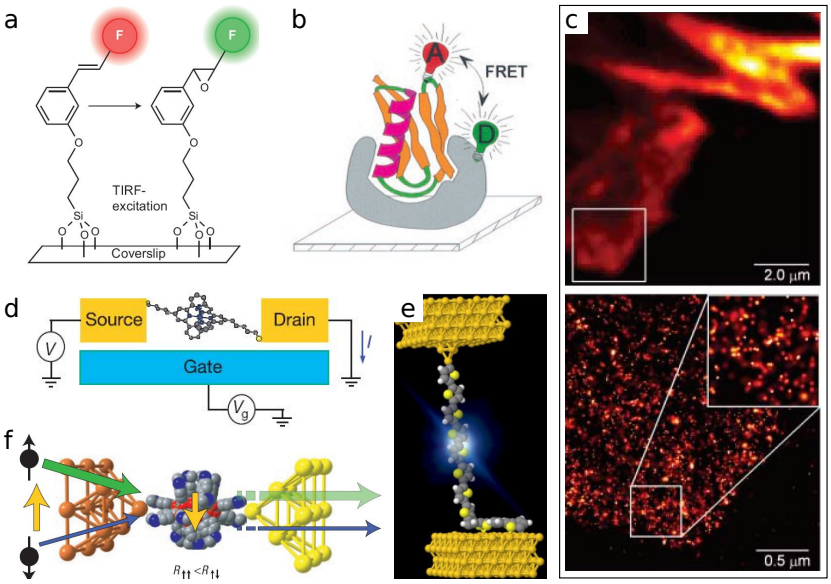


Figure 4.2: *Some applications of single molecules. (a) Example of nanoreporter activity of a single molecule during a chemical reaction [329] and (b) of a pair of molecules (donor D and acceptor A, for investigation by FRET) during a biological process. (c) Comparison between (upper panel) an image obtained by total internal reflection fluorescence and (lower panel) PALM image corresponding to the area in the white square. (d-f) Schematics of single-molecule optoelectronic and spintronic devices: (d) a transistor [330], (e) a light emitting junction [331] and (f) a spin-valve favoring the flow of minority spin-down electrons [332].*

alytic reactions. Transformations occurring during chemical reactions are revealed by variation of molecular photophysical properties, typically as on-off switching of the fluorescence, or shifts in the spectrum (Fig. 4.2.a). For example, donor-acceptor systems can be formed by specific pairs of molecules: one molecule absorbs the incident radiation and transfers non-radiatively the excitation to the other molecule, which then emits (Förster resonance energy transfer, FRET). The interest of this phenomenon is that the intensity of the acceptor emission depends on the distance between the two molecules. In biological samples, functionalization with donor-acceptor molecules allows to monitor changes in the conformation or binding state of enzymes, by the variation of the FRET efficiency, as shown in Fig. 4.2.b [328, 329, 340, 341]. In inorganic heterogeneous catalysis, the use of single-molecule fluorophores has allowed to learn information about the shape of porous materials, reveal dynamics by single-molecule tracking and locate active sites on surfaces [328, 329, 341].

**Nanosources of light**

Single-molecules also represent a nanosize source of light. Dye molecules have been used since the 70's as a tag of biological cells and macromolecules for fluorescence imaging [328], but single-molecule detection and in particular the studies on the green fluorescent protein [333] have considerably increased image resolution and the sensitivity of the technique, allowing to label different sites on the same macromolecules [328]. However, the dimension of the observed fluorescence spots is much wider than the real size of the emitter, because of the response function of the microscope optical system (diffraction limit) [328]. This limitation has been circumvented by E. Betzig and coworkers by combining super-localization techniques, selective excitation of some fluorophores, and image reconstruction [342, 343]. This method is known as photoactivated localization microscopy (PALM) and is one of the super-resolution techniques for which W. E. Moerner, E. Betzig and S. W. Hell have been awarded with the Nobel prize in Chemistry 2014 [321, 344, 345]. Super-localization consists in identifying the molecule position as the centre of the emission spot. This is obtained by fitting the emission spot in a Gaussian approximation (of the Airy intensity profile). The selective excitation of the molecules is based on their different resonant frequencies or lifetimes. Images are then acquired for each kind of fluorophore, and the super-localized calculated positions are finally superimposed. Hence, in the reconstructed image, emission spots closer than their Airy disk width appear as distinct. Fig. 4.2.c shows a comparison between a non super-resolved fluorescence image and a PALM reconstructed image of the area indicated in white. Several techniques similar to PALM have been developed, among them STORM (stochastic optical reconstruction microscopy) [346], F-PALM (fluorescence photoactivation localization microscopy) [347].

**Single Photons and Quantum Information**

The quantum nature of molecular fluorescence has been demonstrated by photon correlation experiments in the early 90's [88, 90, 91, 348]. Indeed, molecules can be approximated as a two-level system, where the transition from the excited state to the ground state occurs with emission of only one photon. Single photons from a single molecule can be obtained on demand at room temperature using a pulsed laser excitation [91]. As single photon emitters (SPEs), single molecules are quite attractive with respect to other single photon sources: they are characterized by higher emission rate than atoms [349–351] and longer coherence time than quantum dots [350]. Molecular SPEs show good photostability when trapped in

a crystal matrix at cryogenic temperature [350,352] and their photobleaching at room temperature can be reduced if the molecules are protected from atmospheric oxygen, in a rigid crystalline matrix [90, 91]. Moreover, the emission of indistinguishable photons has been demonstrated at room temperature [350, 353]. These characteristics are very interesting in the frame of photonic quantum information processing, which include quantum information storage, communication and cryptography [354]. Indeed, quantum memories based on photon storage have been fabricated using the two lowest vibrational levels in the ground state of hydrogen molecules as quantum bits and Raman scattering to populate them [355]. Otherwise, atomic transitions in an alkali vapours have been employed and excited by single photons from a single molecule [351]. In addition, the use of molecules as SPEs has been reported in single-photon spectroscopy of a single molecule, which has demonstrated the possibility of coupling two quantum emitters via single photons [356].

**Optoelectronics**

Single molecules are also attractive candidates as elemental components in novel nano-optoelectronic devices, in the pursuing of circuits miniaturization. Single-molecule electronics [357–359] is based on a molecular wire contacted to two electrodes, forming a metal-molecule-metal junction. This kind of device can be efficiently obtained using different configurations [359, 360] including break junctions [361], AFM junctions with contacted tip [362], and STM cavities (double-barrier junctions) [363], especially in contact mode [331]. Single-molecule junctions have also been integrated in transistors (Fig. 4.2.d) [330, 364–367]. The electric conduction occurs by electron tunneling between the Fermi levels of the electrodes through molecular electronic levels, when a potential difference is applied. Depending on the molecule spatial symmetry, the junction can display a current rectifying activity [368,369]; induced single-molecule switching between bistable states is also attractive for memory and logic gates [337–339, 358, 370–372]. Finally, recently an optoelectrical device has been fabricated by electron tunneling-induced fluorescence from a single molecule in metal junction [331] (Fig. 4.2.e).

**Spintronics**

Spin-electron transport at the molecular scale is the object of the emerging field of single-molecule spintronics [332, 373, 374]. A single molecule on a metal surface undergoes orbitals hybridization resulting in an energy broadening and shift of the molecular levels. In the case of a ferromagnetic substrate, these variations are spin-dependent and result in

a splitting of the molecular energy states and a spin polarization of the molecular orbitals. As a result, molecule deposition can determine an enhancement or sign inversion of the original spin polarization of the ferromagnet [374]. This effect can be used to tune the spin-dependent transport (spin-injection) in optoelectronic devices [374]. In addition, magnetic single molecules, also known as single-molecule magnets, can be integrated in junctions and transistors. Possible devices include spin-valves (Fig. 4.2.f), to control the spin-dependent current through a junction [332, 373], and spin reading, manipulating and writing for sensors, logic devices and quantum computation, where the information is stored as the spin state [373]. Spin-crossover compounds are an interesting class of molecules containing a single transition metal ion and whose spin state can be affected by light, temperature, pressure or the local electrostatic environment [373, 375]. Another interesting class is represented by lanthanide ion complexes, which present both intrinsic spin and intense luminescence properties [332, 376, 377].

## 4.3 Detection, imaging and spectroscopy of single molecules

The quest for the detection of individual molecules began almost a century ago with the works of Jean Perrin on the fluorescence from molecules in diluted solutions in an optical microscope [378]. The identification of single molecules has been for a long time hindered by the impossibility of reducing the optical probes size down to the molecular scale, the challenging detection of a weak single-molecule signal unmasked by the background arising from the surrounding environment and the destruction of the fluorescent system under illumination, this last one already observed by Perrin [378].

**First spectra**

First optical detection of an individual molecule was obtained in 1989 by W. E. Moerner and L. Kador [33]. They addressed pentacene molecules dispersed at very low concentration in a thin crystal at cryogenic temperature and achieving the selective excitation of one single molecule by tuning the laser frequency in the range of one tail of an inhomogeneously broadened absorption peak (Fig. 4.1), where the average number of resonant molecules tends to zero. Using frequency-modulation spectroscopy with a double modulation to reduced the background contribution, they ob-

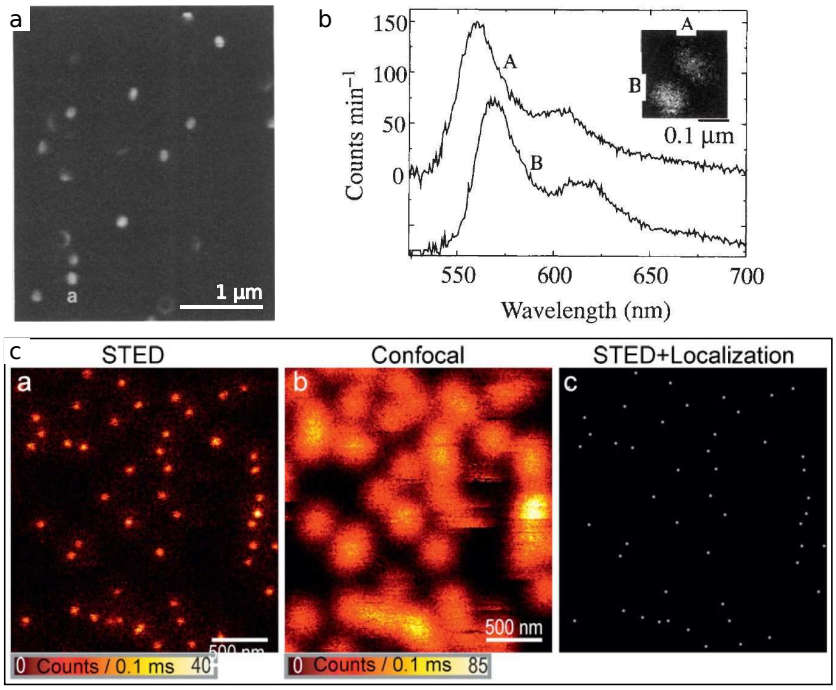


Figure 4.3: *(a) Near-field fluorescence images of single molecules [379]. (b) Independent spectra of two molecules separated by 150 nm, acquired by SNOM [318]. (c) Comparison between STED, non super-resolved imaging, and STED with super-localization [380].*

tained the absorption signature expected for a single molecule. About one year later, the first single-molecule fluorescence excitation spectrum was acquired by M. Orrit and J. Bernard on the same kind of sample [34], while E. Brooks-Shera et al. detected the fluorescence from individual molecule in solution [35].

**Single photon emission**

The quantum nature of molecular fluorescence was soon afterwards verified. After the observation of photon bunching in autocorrelation measurements, which was attributed to the phenomenon of blinking [34], at shorter times the antibunching signature was detected in 1992 [88]. Later, antibunching was discerned also at room temperature [89,90] and specific excitation techniques have been tested to control and trigger the molecule excitation [91,348]. By using short laser pulses, single photons can be obtained on demand from a single molecule at room temperature [91].

**Optical techniques**

Considerable advances in fluorescence imaging were made possible with the advent of near-field scanning optical microscopy (SNOM) in the 80's [381–384]. In this technique, a subwavelength size (few tens of nanometres) probe is obtained by driving the incoming laser through a small aperture at the end of an aluminium-coated optical fibre at close distance from the sample surface. The probe is then scanned over the sample to get a super-resolved image [383, 384]. The great advantage of this technique for single-molecule imaging and fluorescence is the strongly reduced dimensions of the excitation volume in the specimen, allowing to both better localize the molecule and lower the background spectral signal arising from the host matrix. The first near-field images of single molecules on PMMA (polymethylmethacrylate) at ambient conditions were obtained in 1993 by E. Betzig and R. J. Chichester, and different molecular dipole orientations were distinguished [379] (Fig. 4.3.a). Near-field fluorescence microscopy was then successfully employed in the immediately following years in the study of single-molecule photobleaching [319], resonant frequencies (Fig. 4.3.b), spectral diffusion and spectral width [318] (Fig. 4.3.a), lifetimes [320, 385], single molecule Förster resonance energy transfer (FRET) [340], and has later opened the way to PALM [343, 344]. Important achievements in the study of single molecules at room temperature have been obtained during the 90's also using fluorescence correlation, magnetic resonance and surface enhanced Raman spectroscopy [386–390], and far-field fluorescence microscopy techniques based on epi-illumination, confocal and total internal reflection [317, 391–394]. In particular, the development of stimulated emission depletion (STED) fluorescence scanning microscopy by S. W. Hell and J. Wichmann has allowed to overtake the diffraction resolution limit also in far-field microscopy [345, 395]. STED is based on the use of a laser beam to promote a molecule to its first excited state, and a second coaxial laser, with a doughnut shape, to stimulate the molecule transition back into the ground state. This way, only the molecules at the centre of the doughnut contribute to the detected fluorescence. This technique and its evolutions (ground state depletion, GSD, and saturated pattern excitation microscopy, SPEM) are grouped under the name of reversible saturable/switchable optically linear fluorescence transitions (RESOLFT) [396]. The final spatial resolution depends on the fluorophore used and is typically 20-40 nm [345]. However, although capable of molecular resolution [380, 397] (Fig. 4.3.c), STED has been little used for the study of single molecules and mainly employed on molecular ensembles to obtain

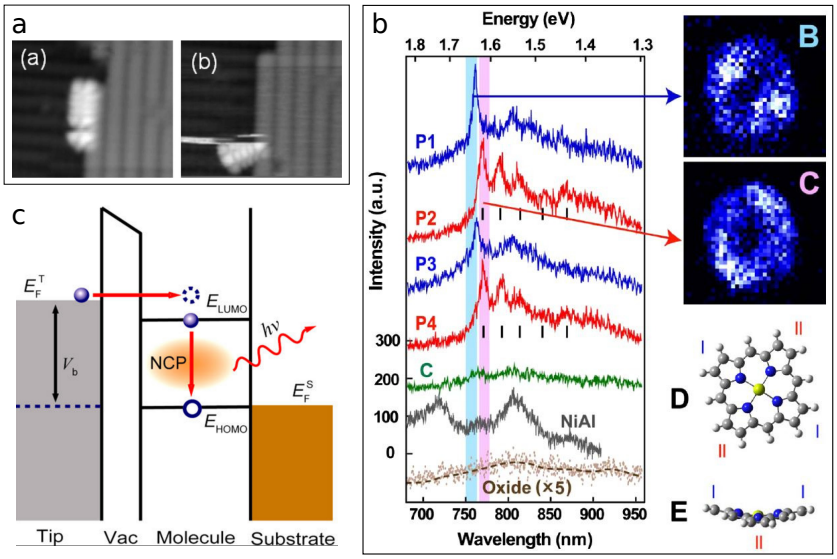


Figure 4.4: *(a) Low-temperature STM images of a pentacene molecule (occupied states) along a step edge on a hydrogenated Si(100) surface, showing a slight translation (left) and rotation (right) of the molecule during the scan. (b) STML by electron-hole recombination at a single molecules: electron tunneling from the tip to the LUMO, followed by nanocavity plasmon (NCP) enhanced radiative transition to the HOMO, which had been emptied by electron tunneling into the substrate [398]. (c) STML at subnanometre scale: emission observed at some particular tip position over a Mg porphyrin molecule, associated photon maps and molecular conformations [399].*

super-resolved images [396].

**STM and STML**

Concomitant with the development of near-field and far-field optical microscopy, scanning tunneling microscopy (STM) has also contributed greatly to the study of single molecules. Indeed, this technique has allowed to perform submolecular resolution imaging (Fig. 4.4.a) and vibrational spectroscopy, as well as to induce single-molecule luminescence and dynamics. STM studies of single molecules started in the late 80's, with the first experiments showing single-molecule manipulations such as pinning and removal from a surface [400], sliding [401] and tip-induced dissociation [402]. Vibrational spectroscopy and photon emission were first demonstrated on molecules in clusters [403–405] and few years later on isolated molecules [406]. Other tip-induced dynamics on adsorbed single-molecules have afterwards been reported: reversible rotation of a molecule on a surface by vibrational excitation [407], synthesis of a single molecule [408, 409], room-temperature irreversible modifications

[410, 411] and low-temperature reversible switching between two bistable configurations [337–339] driven by electronic excitations or electrostatic force. Moreover, STM-induced luminescence (STML, or electroluminescence, EL) from single-molecules has been achieved at submolecular resolution. Generally, the mechanism underlying STML is radiative inelastic electron tunneling (IET), where part of the tunnel electron's energy is converted in photon emission directly or through surface plasmon excitation or molecular electronic transitions, often by a combination of them [412]. In the case of a molecular junction, luminescence can arise from IET between tip and molecular electronic levels [413, 414] or intramolecular electronic transitions. In this last case, molecular excited states can be induced through [409] elastic electron tunneling into an unoccupied molecular level (electron attachement), resulting in a charged molecular state, which can de-excite in a charged lower molecular state [413, 415, 416]. Alternatively, electron and hole pair attachment respectively to the lowest unoccupied molecular level (LUMO) and the highest occupied molecular level (HOMO) results in a neutral excited state like in natural fluorescence [398, 399, 417–419] (Fig. 4.4.b). Finally, direct excitation of the molecule through local surface plasmons (IET) is possible [419–421]. Considering the multiple tunneling paths, the identification of the exact luminescence mechanism might be difficult [412, 418]. More recently, photon emission maps at subnanometric resolution have been reported, showing the spatial distribution of vibronic excitations within single molecules [399, 416] (Fig. 4.4.c).

Single molecule imaging at submolecular resolution has been achieved also by AFM, providing complementary information with respect to STM. Indeed, while STM imaging allows to probe the molecule's local electron density of states near the Fermi level (molecular orbitals), AFM is able to to address the chemical structure of molecules [422–426].

**Antenna enhancement**

In the last twenty years, scanning near-field optical microscopy of single molecules has known another step forward, in terms of minimization of the excitation volume, with the development of tip-enhanced optical microscopy [427]. This is obtained by replacing the aluminium coated optical fibre (with uncoated tip forming the subwavelength aperture) with an apertureless pointed metal probe, strongly interacting with the incoming radiation field. Indeed, laser-irradiation of a metal tip using a polarization parallel to the tip axes induces surface charge oscillations (plasmons) resulting in an enhanced electric field confined at the apex of the

tip [427, 428]. Alternatively, a metal nanoparticle (silver or gold) can be attached at the end of a glass tapered optical fibre and centred in the laser focus [429]. The effect of these systems is to convert the propagating incoming radiation in a localized field, and for this reason they are known as optical antennas [427]. Gold and silver nanoparticle-terminated probes have been used for the study of single molecules [430–433], showing an enhancement of the excitation and fluorescence between 10 and 20 times, depending on the probe-sample distance and probe metal [431–433], associated to a reduced lifetime of the excited state [431]. Using an efficient antenna-molecule coupling, the image spatial resolution is considerably improved [433]. Alternatively, fluorescence antenna-enhancement has also been obtained in a confocal microscope, on a sample consisting of a gold bowtie antenna coated with single molecules. For the molecules in the bowtie gap, the fluorescence enhancement was found ten times higher than the previous reports [434].

Moreover, optical antennas have largely benefited also Raman spectroscopy, increasing both signal intensity and spatial resolution. On single molecules, tip-enhanced Raman spectroscopy (TERS) in AFM or STM microscopes has allowed signal enhancement of at least a factor $10^6$, with a resolution of about 10 nm [435–437] and, more recently, even subnanometric resolution [438].

## 4.4 TEM microscopy and CL spectroscopy

We have examined, up to this point, single-molecule spectroscopy and imaging by means of optical excitation and tunneling electrons. Here we analyse the state of the art of single molecules characterization using accelerated electrons in transmission electron microscopes (TEM), scanning electron microscopes (SEM), and cathodoluminescence spectroscopy (CL).

**TEM**

The high resolution provided by TEM microscopy has allowed to image single molecules on suitable substrates at room temperature (Fig. 4.5). Several issues had to be solved in order to achieve this result: small molecules give rise to a very shallow image contrast, which can be easily masked by the substrate, they tend to move laterally and out of focus, and, most importantly, are extremely sensitive to a fast electron beam. TEM observation of fullerenes molecules ($C_{60}$) inside a single-wall carbon nanotube (SWNT) was reported in 1998 [439]. In the following years

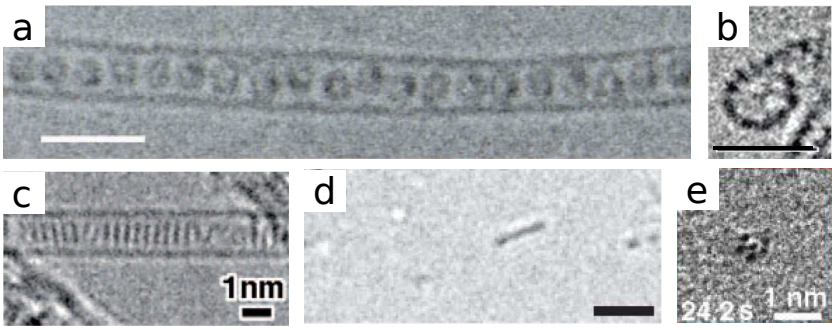


Figure 4.5: *Series of TEM images of molecule on different substrates. (a) Fullerenes molecules encapsulating a Gd atom, in a carbon nanotube (peapod structure) [442]. The scale bar is 3 nm. (b) A functionalized fullerene attached to the surface ot a carbon nanotube [458]. The scale bar is 1 nm. (c) Coronene molecules stacked inside a carbon nanotube [451]. (d) A carbon chain on graphene surface [454]. The scale bar is 2 nm. (e) Last image of a time series of images of a polyoxometalate ion on GO [203].*

analogous peapod structures of fullerenes, fullerenes encapsulating a single atom and fullerenes functionalized with carbon chains have been imaged by TEM [440–446]. In particular, a STEM-EELS study of Gd-containg fullerenes in 2000 has demonstrated the feasibility of single-atom EELS spectroscopy (Fig. 4.5.a) [442]. In almost all these studies, illumination damages by 80–120 keV electrons have been identified in fullerenes deformation and coalescence [439, 441, 443, 447, 448]. Spectroscopy requires a higher total electron dose, for an acceptable S/N ratio with a beam focused on a subnanometric area. A core EELS study of the fine structures at the carbon K-edge of single fullerenes could be performed in 2014 at only 30 kV acceleration voltage [446]. Also other small carbon-based molecules, for example planar coronenes, have been inserted in SWNTs and imaged (Fig. 4.5.c) [449–453]. Moreover, some molecules have been observed directly, anchored at the surface of nanotubes or nanohorns (Fig. 4.5.b) [444, 445, 447] and deposed on graphene [454–457] or GO, where molecules interaction with functional groups on its surface represents an additional advantage [203] (Fig. 4.5.d-e). Finally, molecules have been observed to move: image series have been shown molecules rotating and translating inside nanotubes or migrating on graphene, and carbon chains bound to fullerenes protruding outside small holes in the nanotubes and going back inside again [203, 444, 445, 454, 456, 457].

CL Cathodoluminescence of molecular structures, in particular low atomic number and aromatic compounds, is employed in the field of electron scintillators [459, 460]. However, the efficiency of these devices is reduced by illumination damages after prolonged irradiation [461]. In the 60's, CL from molecules has started to be used also for labelling biological specimens in SEM microscopes [36]. The field has little developed, because of some major problems [37, 462]. Difficulties concern sample preparation, the need for vacuum and low temperature preventing in vivo observations (see environmental SEM and TEM [463]), background signal, and poor CL yield [462]. Indeed, organic substances are characterized by a CL photon yield of several orders of magnitude lower than inorganic materials [36], and in general the CL efficiency is not correlated with the photoluminescence yield [37, 464]. A weaker CL intensity in some materials is probably cause by the formation of electron-induce defects, that quench the emission. Most importantly, illumination damages have represented a strong limitation since the first experiments [36]: molecular crystals or powders show decreasing CL as a function of illumination (Fig. 4.6) [37, 464, 465], even at low temperature and low magnification [465]. All these factors degrade the spatial resolution in the case of organic chromophores and scales below molecular powders could not be addressed. STEM-CL from individual molecules has not been reported.

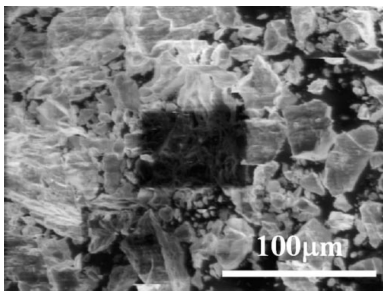


Figure 4.6: *SEM-CL image of Europium complexes Eu(dbm)3(phen) powders showing reduced CL at the centre (dark region) because of electron beam irradiation [37].*

## 4.5 STEM-CL: attractive features

In the light of this overview of the most advanced techniques employed in the study of single molecules, STEM-CL presents some potential incomparable features.

- **High spatial resolution with fast acquisition.** The focused electron beam defines an illumination spot of about 1 nm in size. An electron current of typically one hundred of pA flows through this small area. The intensity and S/N ratio of the CL signal depends both on the

current density and the specimen, in terms of material's response to electron illumination and local thickness (more electron interactions in a thicker sample). This considered, a CL spectrum typically requires acquisition times of the order of $10^{-1}$-$10^{-2}$ s, which is much shorter than required for example by IET-STML, where spectra are integrated over several minutes [406, 414].

- **Wide field of view.** STEM allows to easily switch from nanometre or subnanometre spatial resolution to wide field of views, by simply changing the beam-scan amplitude. This is a remarkable advantage with respect to near-field techniques and STM (typical scan is $20\times20$ nm), especially in the case of heterogeneous samples. Specifically in the case of deposited molecules, whose distribution might be non uniform over the sample, wide field surveys are certainly helpful to localized regions of interest.

- **Wide spectral range.** In STEM (and SEM), the specimen excitation is achieved by inelastic interaction with the incoming fast electrons, which transfer a small part of their energy to electrons or ions in the material. Electrons in the specimen can hence be excited towards unoccupied levels at high energies with respect to the Fermi level. This differs from optical techniques, where the extent of the excitation is limited by the laser frequency, or STM, where the bias between tip and substrate is typically less than 2-3 V. Hence, by STEM-CL photon emission can be detected from near infrared to middle UV (1.1-6 eV, 1100-200 nm).

- **Far-field.** The STEM-CL technique does not suffer of sample-tip interaction, as it occurs in near-field techniques, where the probe is placed at about 10 nm from the sample surface [318, 320, 379]. For example, alterations of the molecular fluorescence lifetime in SNOM have been associated to the position of the aluminium coated tip with respect to the molecule and attributed to nonradiative energy transfer to electrons in the metal [320, 385]. Emission quenching occurs also in antenna-enhanced fluorescence, at small antenna-emitter distances [433]. Also the STM tip can induce alterations in the molecules [409]. Moreover, heating of the metallic coating of the SNOM tip has been reported [319, 466]. In the STEM, the metal surface of the CL mirror is too far from the sample to induce any perturbation. Nevertheless, sample modification can derive by interaction

with the electron beam, as it will be discussed later, and the specimen is placed within the objective lens magnetic field.

- **Multiple signal acquisition.** In the STEM, CL spectra and image (both BF and HAADF) are acquired simultaneously, in the hyperspectral mode. If the integration times and sample requirements are comparable, CL and EELS spectra might be collected at the same time as the HAADF image. Hence, the spectral features can be correlated with the topography of the sample. Moreover, the image and spectra arise from different phenomena (basically elastic interaction the first, inelastic interaction the second) so that their comparison can be particularly fruitful.

- **Versatility.** The absence of sample-tip interaction in the STEM removes the necessity typical of near-field techniques of according the tip material with the requirements of the particular experiment. Indeed, the choice of the tip termination is important in AFM studies [422]. STML and antenna-enhanced near-field fluorescence are strongly dependent on the tip/antenna metal, because surface plasmon natural frequencies are material-dependent. In STML tip surface plasmons can be excited by inelastic electron tunneling and decay by photon emission [412, 415]. In the case of molecular fluorescence in the STM, plasmon excitation mediates the detection of the radiation in the far-field [415]. Hence the plasmon properties are responsible for differences in the luminescence spectra [415]. In antenna-enhancement the conversion of the propagating radiation in a local field is mediated by the excitation of surface plasmons: stronger enhancement is obtained for molecule fluorescence at lower frequencies than the plasmon resonance [433]. While these techniques require the test and choice of suitable tips depending on the sample and the spectral range of interest, the STEM-CL set-up is fixed.

- **Substrate requirements.** In order to isolate and immobilize individual molecules, host matrices are usually employed in optical microscopy. They include crystals, such as p-terphenyl (a molecular crystals) [33, 34, 431]), and polymer films, mainly PMMA [317, 318, 348, 371, 379, 432, 433]. However, host matrices constitute a rigid environment which can affect the conformation [321] and orientation [379] of the molecules, and their excited state [371]. Rarely,

methanol dispersions of molecules have been directly deposited by spin coating on silica surfaces, for fluorescence imaging and lifetime or photobleaching measurements, but not for spectra acquisition [319, 320]. In STM, molecules are generally sublimated in UHV over a clean surface. The substrate must be conductive in order to support electron tunneling, but metallic surfaces shift and broaden the energy levels of isolated molecules [374, 415] and their luminescence is quenched by energy transfer to the metal. To decouple the molecules from the conductive substrate, thin insulating layers (like $Al_2O_3$ [399, 413, 415, 416] or $NaCl$ [417, 467]) and molecular multilayers [418, 420, 468] have been introduced. Surface passivation of a semiconducting substrated with hydrogen has also been demonstrated effective [469] and self-decoupling molecules, functionalized with a radical acting as spacer, have been synthesized [398]. The use of (doped) $SiC$, which has a wide band-gap of about 3 eV, has recently been tested [414] in order to remove the possibility of nonradiative energy transfer from the molecules to the substrate. In STEM-CL experiments, an insulating substrate can be employed directly.

- **Experimental conditions.** Although optical microscopy operates at atmospheric pressure, the vacuum level in the STEM microscope is not extremely demanding (in the order of $10^{-8}$ Torr). Since STEM-CL is not a surface technique, UHV conditions are not essential. A non perfectly clean surface might affect the substrate-molecules coupling, but the use of a chemically inert substrate and the removal of solvent residues by annealing have allowed to observe intense CL emissions.

## 4.6 The indirect excitation mechanism

**Illumination damages**

Despite the above summarized advantages, STEM-CL suffers from a major difficulty: molecules are very small and fragile physical systems which are highly sensitive to illumination, as it is well acknowledged in fluorescence measurements. Indeed, continuous illumination with visible light leads at some point to an irreversible chemical modification of the molecule, accompanied by the disappearance of fluorescence [378]. This phenomenon, known as photobleaching, has been studied at the level of single molecules by SNOM [319], allowing to quantify the maximum

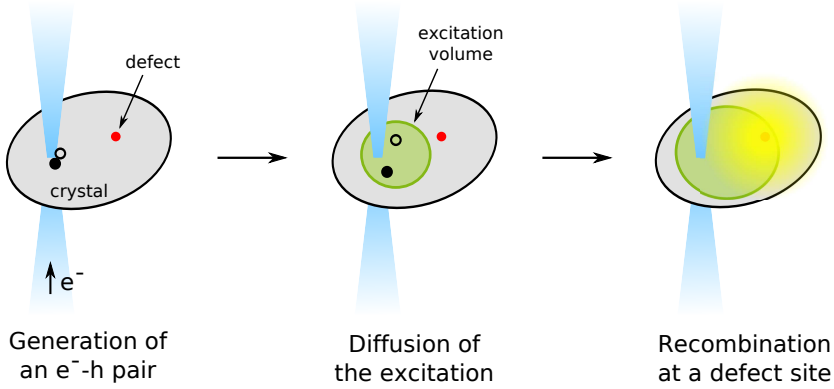


Figure 4.7: *Schematic of the proposed mechanism for h-BN excitation by fast electrons and electron-hole recombination at some distance from the illumination spot, based on ref. [8].*

number of optical excitation-emission cycles supported by a molecule at about $10^7$ [319]. In the case of fast electrons, illumination damages on molecules should mainly consist in radiolysis, although knock-on of atoms could also destabilise the system. Low temperatures are expected to limit molecules (atoms) mobility on the substrate and reduce lattice vibrations in this last one, but cannot avoid radiolysis. The use of lower electron current and low electron dose conditions would not be effective neither.

In this thesis, a solution to the constraint of illumination damages has been attempted by avoiding (as far as possible) the direct exposure of the molecules to the electron beam, and using an absorbent substrate to mediate the excitation. Indeed, STEM-CL excitation of defects in wide band-gap semiconductors can be achieved even by irradiating the material at some tens of nanometres far from the defects.

**Excitation and recombination mechanism**

STEM-CL has been successfully employed in the study of nanodiamonds and h-BN [8–10, 470]. These wide band-gap semiconductors display a very intense CL, resulting from an efficient interaction with incident electrons, which is proportional to the local particle thickness (typically less than 200 nm), and radiative recombination involving excitonic states and impurity centres. In STEM-CL the beam size at the sample stage defines the illumination area, inside which primary electrons generate e-h pairs. Excited charged carriers and plasmons can create additional e-h pairs and the free carriers can diffuse outside the illumination area within the radius defined by the carriers diffusion length. This defines the excitation volume. If a luminescence centre is included in

the excitation volume, e-h recombination can take place (Fig. 4.7). The probability of recombination at a specific centre increases with the number of charge carriers, so the emission is more intense when the electron beam is closer. According to this, CL intensity maps derived from hyperspectral images show more or less isotropic spots (depending on the morphology of the particle) and the maximum of intensity within the spot can be associated to the location of the luminescence centre.

As an example, Fig. 4.8 shows an HAADF image of a single diamond particle and the associated intensity map of the emission typical of $NV^0$ (neutral nitrogen vacancy) centres. The luminescence in this case is thought to arise from one single $NV^0$ complex and the CL signal is detected even when the electron beam is almost 100 nm far from it. This mechanism is certainly very interesting for the case of individual molecules: point defects in a semiconductor introduce spatially localized electronic levels within the band-gap of the material; the band-to-band excitation is transferred to the defect levels, where the e-h recombination occurs. Molecular levels are expected as well to be located within the band-gap of a semiconducting substrate, and could take part in the de-excitation process. The possibility of free carriers recombination at molecular levels has inspired the use of an absorbent substrate as a strategy to perform gentle spectroscopy.

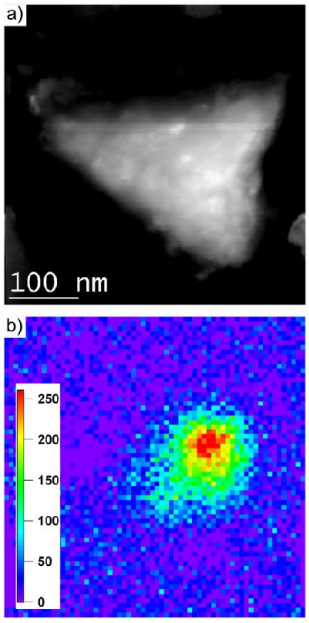


Figure 4.8: *HAADF of a nanodiamond and related CL intensity map of the emission from an $NV^0$ centre, from ref. [470]. The emission can be observed up to 100 nm far from the centre.*

## 4.7 h-BN as the ideal substrate

The choice of the substrate is fundamental. It is required to be a good absorbent, with a suitable charge carriers diffusion length, and to assure a good coupling with the molecules. Possibly, it shall also negligibly perturb the molecular electronic structure, in order to investigate molecules intrinsic luminescence. For the molecular levels to be isolated, the substrate must lack surface states. This constraint excludes the majority of common semiconductors. An excellent candidate satisfying all these requirements

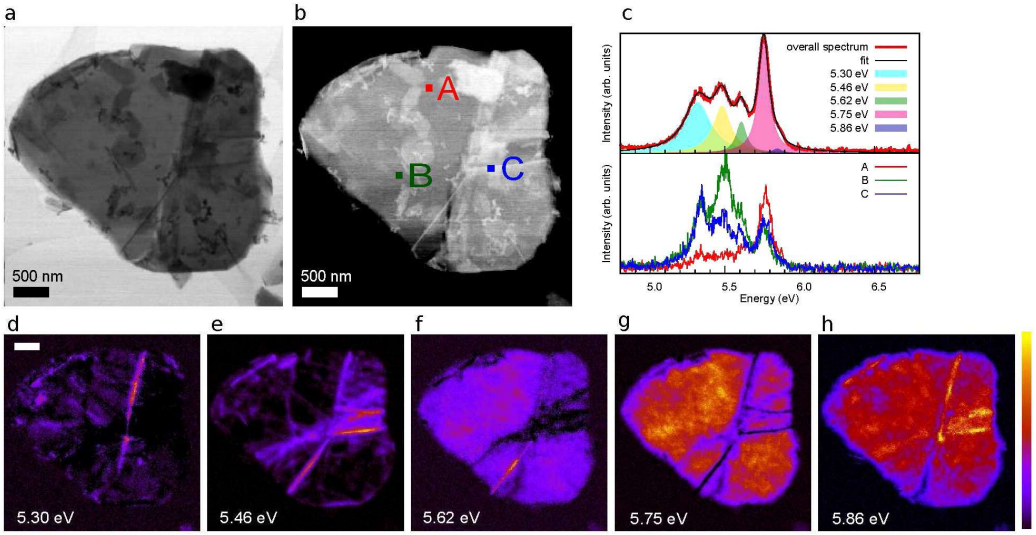


Figure 4.9: *Spatially resolved CL emission near the band edge in h-BN, from ref. [9]. BF (a) and HAADF (b) images of a whole flake, CL spectrum (c) showing different spectral components. In (d-h) CL intensity maps of the individual components.*

has been identified in h-BN.

h-BN is a layered material with an atomic structure similar to that of graphite. Synthesized for the first time in 1842, it consists of weakly interacting atomic planes, where boron and nitrogen atoms alternate in an hexagonal lattice. The interaction of h-BN with incoming electrons is highly effective and results in remarkably intense emissions [9] (Fig. 4.9). The mechanism of e-h generation, diffusion and recombination at more favourable sites, where the e-h energy separation is lower, is demonstrated by the spatial extent of STEM-CL emission spots both in the case of excitonic emissions at folds of the flakes (Fig. 4.9) and luminescence from point defects (Fig. 4.10). Even in the case of a single point defect, the CL emission spot corresponds to about 80 nm in diameter [10]. h-BN flat and chemically inert surface (with no surface states [471]) is expected to only slightly perturb the molecules electronic structure, and molecules should be only physisorbed. Thanks to its wide band-gap, h-BN could be include more than one molecular level of a large variety of molecules.

Monolayer h-BN on copper (inducing a surface potential modulation) and h-BN flakes have already been used as a substrate for respectively STM and XPS of porphyrins [472, 473], while another wide band-gap semicondutor (SiC, $\sim$3 eV energy gap) has been employed for STML of

perylene-derived molecules [414]. Nevertheless, the intrinsic luminescence of h-BN represents a slight drawback, since emissions from the molecules might superimpose on h-BN peaks.

## 4.8 STEM-CL of individual molecules on h-BN

In this thesis, the luminescence of molecules deposited on h-BN flakes was studied by spatially resolved CL. Molecules were spread on the substrate by drop casting of a solution with a very low concentration. This very simple sample preparation (alternative to molecules embedded in a matrix or sublimated and chemisorbed on a substrate) has the advantage of little constrain the molecules, especially during their transition to an excited state. On the other hand, molecules are free to move. The very high dilution regime reduces the possibility of molecules aggregation by migration on the substrate surface.

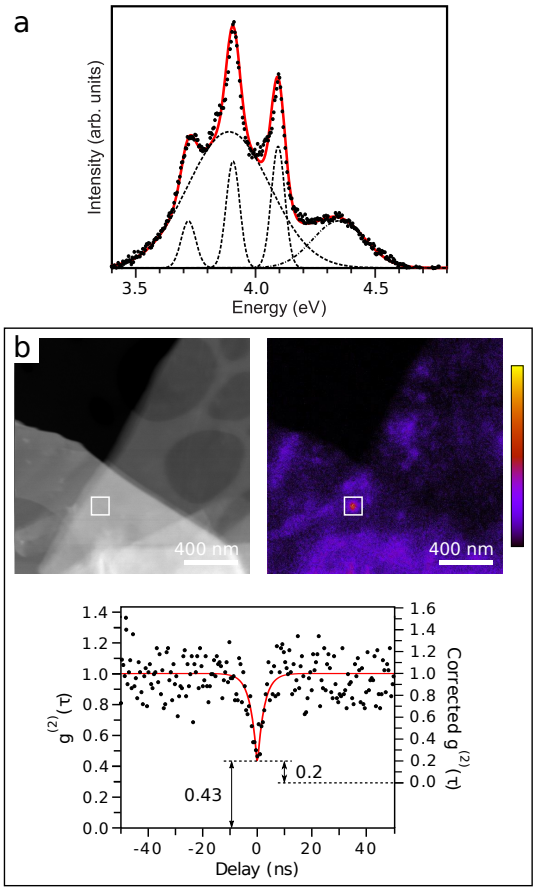


Figure 4.10: *SPE point defect in h-BN, from ref. [10]. (a) Spectrum of the emission, with components obtained from a fit. (b) HAADF image and CL-filtered image (in the 3.65–4.13 eV energy window) of the luminescence centre. In the lower panel of (b), measurement of the intensity autocorrelation function, demonstrating the SPE character of the defect.*

Few kinds of molecules have been tested: coronenes, europium complexes, pyrromethenes, rhodamines, and perylense. They have been chosen on the basis of their high emission quantum yield (nominally between 0.2 and 0.8) and/or the planar geometry of their structure, for a higher stability after deposition on flat h-BN and possibly better coupling with this last one. They have been deposited on h-BN in high dilution regime to lower the possibility of clus-

terization. This protocol, which would be problematic for near-field microscopy, could be employed here thanks to the wide field of view accessible in the STEM, which allows to easily move on the sample and take CL overviews in search of regions of interest. Coronenes and europium complexes (Eu-complexes) have provided the most interesting results, which will be discussed in the following. Pyrromethene has also been associated to some remarkably intense emissions, and it shall be further characterized in the near future. Very weak emissions have been observed from rhodamines, none from perylene, but these experiments should be considered only preliminary.

**Sample preparation**

High-purity h-BN flakes were synthesized under high pressure and at high temperature in $\mathrm{BaBN}$ solvent and provided by T. Taniguchi and K. Watanabe from National Institute for Materials Science in Tsukuba, Japan [42]. Wide and relatively thin flakes have been obtained following an experienced method [10,474,475], by 30–60 minutes ultrasonication of crystals dispersions in isopropanol (IPA). TEM samples have been prepared by pouring a drop of the solution on suspended TEM grids. Solvent residues have been removed by annealing in a tube furnace at 550 $^{\circ}\mathrm{C}$ for 2 h at 600 mbar pressure in a reducing atmosphere ($\mathrm{N_2}$–5% $\mathrm{H_2}$). This treatment have been observed to reduce also the CL emissions in the 3–4 eV range. Alternatively to annealing, 10 s plasma cleaning ($\mathrm{Ar}$–25% $\mathrm{O_2}$) has also been employed. In sight of using h-BN as a substrate for the molecules, the intrinsic luminescence from h-BN must be carefully characterized: it is fundamental to distinguish the luminescence arising from the molecules from that of the substrate. Despite the high purity of h-BN crystals, few defect-related emissions have been observed. They have been characterized by studying lower quality commercial h-BN powders (Sigma Aldrich), containing a higher concentration of these luminescence centres. TEM grids have been produced using the same procedure described above, though dispersions have been ultrasonicated for 8–10 h.

Powders of coronenes and Eu-complexes (tris(benzoylacetonato) mono(phenanthroline) europium(III), $\mathrm{C_{42}H_{35}EuN_2O_6}$) have been purchased from Sigma Aldrich. Molecular crystals have been dispersed in ethanol (EtOH) and a drop of solution was pured on TEM grids placed on a filter paper. Molecular crystals have been dissolved by diluting EtOH dispersions in little toluene ($10^{-4}$–$10^{-2}$ M). Deposition on clean h-BN grids have been performed on filter paper in order to rapidly remove the solvent and reduce molecules aggregation on h-BN surface. For the same purpose,

grids have been previously heated for some minutes under a lamp. Only a small fraction of the molecules in the dispersion is expected to deposit on h-BN, the majority of them flowing directly to the filter paper.

For the CL experiments, the microscope was operated at 60 kV. This is the acceleration voltage employed in the previous studies of h-BN in this microscope [9,10], below the threshold for atmic displacement irradiation damage [96,285,476]. The sample temperature was about 150K. CL spectra have been acquired with integration times of typically 300-500 ms. Hyperspectral images have been acquired at resolution varying from 40 to 5 nm, with a focused electron beam. At the spectrometer stage, the diffraction grating blazed at 2.5 eV has determined a spectral dispersion of $\sim$0.34 nm. CL

After a short characterization of the substrate in the spectral emission range of interest for the molecules (section 4.9), and a preliminary study of molecules in their crystalline aggregation state (section 4.10), results on the CL of molecules deposited in high dilution on h-BN will be presented in section 4.11.

## 4.9 h-BN luminescence in the visible range

The characterization of the luminescence properties of the h-BN substrate has been the first step of the study of isolated molecules. h-BN displays strong CL emissions, which must be extensively characterized in order to discern the appearance of additional emissions from the molecules.

h-BN is a wide band-gap semiconductor with an experimental optical gap of almost 6 eV [32], and displays remarkably strong CL emissions in the far UV [32,51,477,478]. A recent STEM-CL study in Orsay has revealed the spatial distribution of CL emissions near the band-gap edge [9] (Fig. 4.9). Among the five excitonic emissions between 5.30 and 5.86 eV, the three of them at higher energy are present all over h-BN flakes, while others are spatially localized along lines. These last ones are correlated with lines appearing in the STEM images and crossing the h-BN flakes. Such morphological features have been related to folds of h-BN sheets. The localized emissions have then been correlated with a local different stacking order at folds [9].

h-BN displays other few emissions, at lower energy within the band-gap. The most widely studied is certainly the one at 4.09 eV, accompanied by two phonon replicas at 3.91 and 3.73 eV. These luminescence features

are often superimposed on a broad band centred at about 3.9 eV [10, 42, 48, 68, 73, 74, 479–483]. The 4.09 eV emission was attributed to defect levels arising from substitutional carbon atoms at nitrogen sites [68, 479, 484] and this interpretation is quite largely shared [10, 42, 74, 482, 483, 485], although the role of oxygen impurities and vacancies has also been suggested [42, 482, 483, 486]. Lately, by HBT experiments in the same microscope used during this thesis we have demonstrated that the luminescence centre responsible for this emission behaves as a SPE [10] (antibunching nature of the emitted photons in Fig. 4.10). The additional broad band emission at 3.9 eV has also appeared spatially localized in STEM-CL maps (Fig. 4.10) and seems related to illumination damages [10]. The origin of this feature has been associated with e-h recombinations at donor-acceptor pairs, involving intrinsic defects [10, 74].

In the last months confocal photoluminescence and HBT experiments have revealed other SPEs, responsible for phonon-assisted emissions at much lower energy: 1.63–2.15 eV [69–72]. Some of these luminescence centres appeared photostable [70, 71], while others showed a blinking behaviour and bleaching [69, 72]. Interestingly, few of the SPE emissions share similar phonon side-bands, and appear as identical features only shifted in energy. Two series of such luminescences with ZPL peaks in the ranges 1.63 – 1.82 and 1.9 – 2.15 eV have been ascribed to defects with a similar crystallographic structure [71], while the pair of emissions with ZPL at 1.97 and 2.08 eV has been associated with different charge states of a same defect [72].

These low-energy SPE signatures have not been observed in our samples, while another series of spatially localized emissions has been identified with ZPL in the range 2.32–2.46 eV (Fig. 4.11.a). The existence of the lowest-energy peak at 2.32 eV had already been announced in R. Bourrellier's PhD thesis in Orsay in 2014 [475]. The emission appeared highly unstable, switching on and off during successive electron-beam fast scans, which precluded to perform HBT measurements. During this thesis, additional emissions with ZPL at 2.35, 2.42 and 2.46 eV have been observed, all bearing the same phonon-bands profile as the 2.32 eV emission. As shown in Fig. 4.11.a the phonon-assisted emissions appear at 65 and 160 meV lower than the ZLP peak, with similar relative intensities in all the four signatures. By comparison with the phonon DOS calculated by Kern et al. [487] (and indexed after refs. [488] and [489]) we attribute these side-bands respectively to ZO and TO/LO phonons.

Fig. 4.11.c shows the spatially localized character of these emissions.

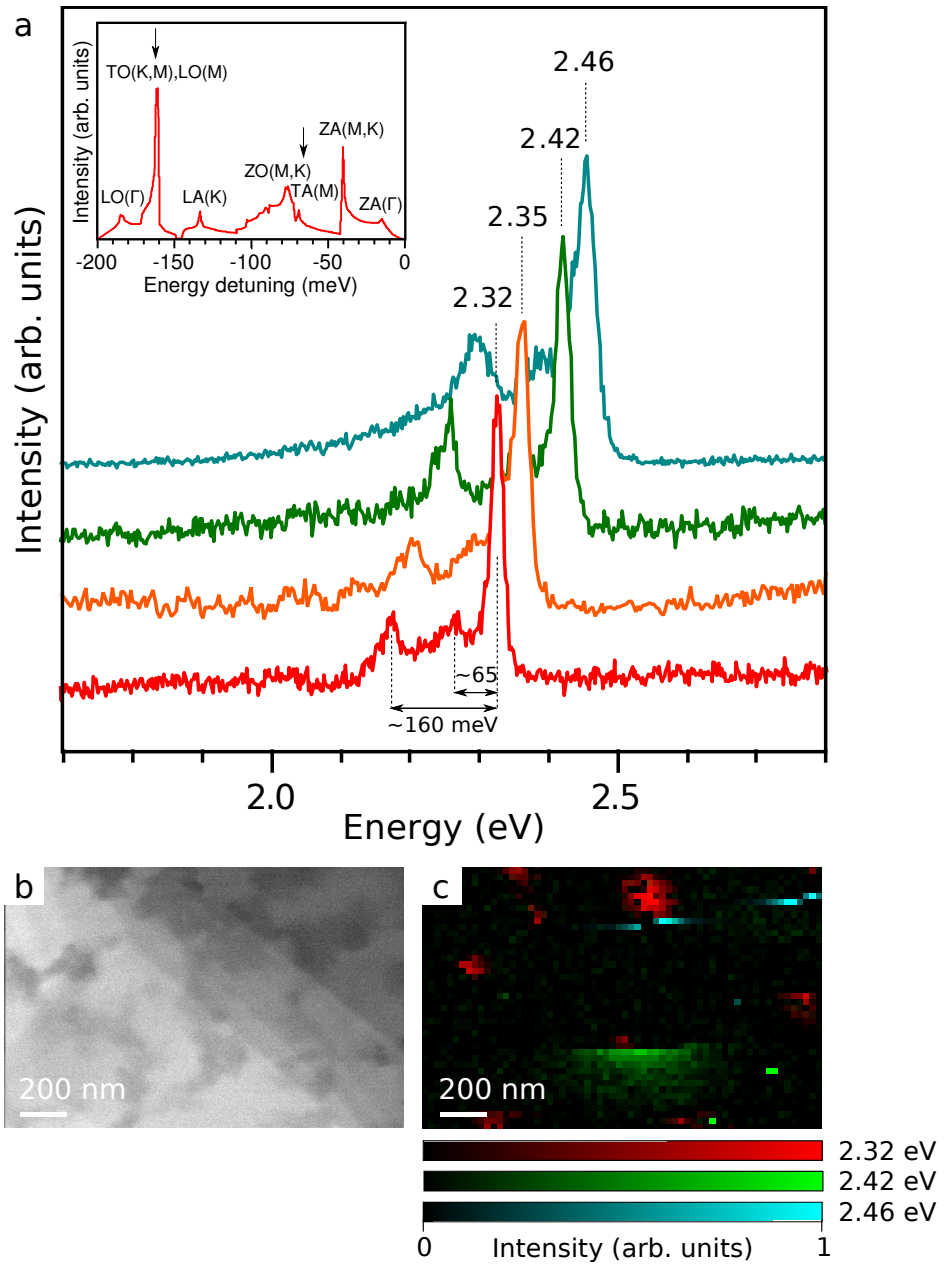


Figure 4.11: *(a) CL emissions in the visible, from exfoliated commercial h-BN flakes: comparison of four emissions with similar phonon coupling. In the inset calculated phonon DOS from ref. [487]. (b) BF acquired after hyperspectral imaging on a selected regions of an h-BN flake. (c) Superposition of CL intensity maps derived for three of the four emissions in panel (a). The colour scale represents the intensity of the ZLP, represented by its integral in an energy window of about 10 meV centred on the maximum, after background subtraction.*

The region in Fig. 4.11.b (BF image) has been investigated by hyperspectral imaging, revealing the presence of three of the emission kinds described above. CL intensity maps have been derived for each emission by integrating the ZPL peak within an energy window of about 10 meV centred at the intensity maximum, after background subtraction with almost flat linear interpolation between two energy windows at the sides of the whole signals. The so obtained maps are presented superposed in Fig. 4.11.c, for an easier comparison. Each colour is associated with one ZPL, with the same colour code used in the spectrum above (Fig. 4.11.a). The brightness scales indicate the peaks intensity and the contrast has been readjusted separately in each map. Considering that the scan proceeds line by line from the top to the bottom of the image and moves from left to right in each line, the shape of localized CL spots agrees with the above-mentioned emission instability. Indeed, the emission can be suddenly activated at some beam-position (pixel of the map) or inversely suddenly destroyed, as in the case of the blue and green spots. The on/off switching may occur many times as in the red spot. Fig. 4.12 shows the same effect on a longer time scale: a series of spectra has been acquired from a selected region of a flake during fast beam scanning (order of 1 ms per scan, 500 ms integration time per spectrum) and the integrated intensity of the ZPL in each spectrum is represented as a function of time. Given the relatively long integration time per spectrum, the measurement is not limited by the excited state lifetime. The on/off behaviour of the emissions is clear and reminds the experiments reported in ref. [72]. The intensity instability is likely to be driven by the electron beam and to involve a variation in the charge state of the luminescence defect centres. Charging of the sample in the STEM typically occurs by the emission of secondary electrons from the material. Moreover, the charge hypothesis has already been suggested in ref. [72], where the charge variation is optically-induced (PL measurements).

While the concentration of these defects is quite high in commercial h-BN, while they are rare in high-purity crystals. These last ones have therefore been employed in our study of isolated molecules.

## 4.10 CL from molecular crystals

The CL emission from molecular crystals is a necessary reference for the study of individual molecules. Here we introduce properties and uses

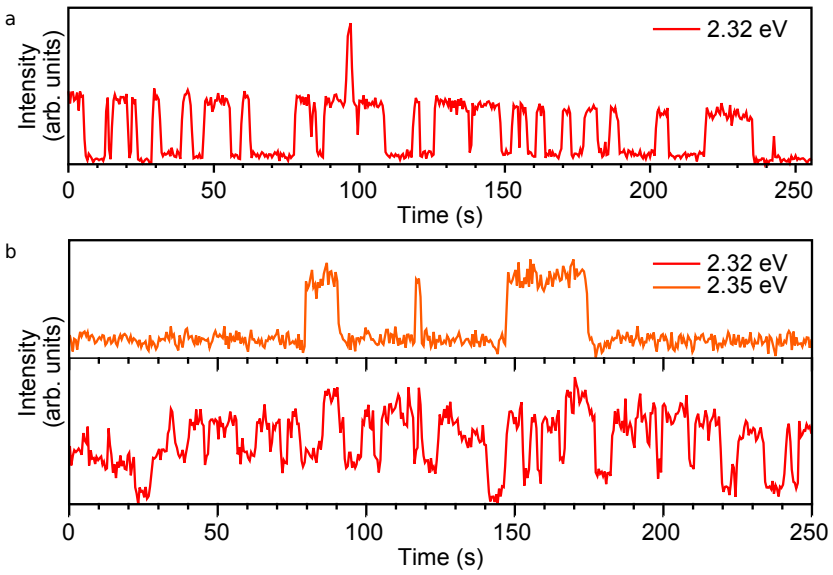


Figure 4.12: *Emission from defects at 2.32 (red) and 2.35 (orange): intensity oscillation as a function of continuous illumination. Series of spectra acquired from areas about 30 nm (a) and 160 nm (b) wide.*

of Eu-complexes and coronenes and compare the luminescence of their molecular crystals with the literature.

**Eu-complexes**

Lanthanide complexes are a class of molecules constituted by a central trivalent rare earth ion surrounded by organic chemical groups called ligands. This kind of composites have a high fluorescence quantum yield (for Eu up to 0.8, depending on the ligands [490,491]) and typically show very narrow absorption and emission lines [492]. They correspond to $4f - 4f$ electronic transitions localized at the metal ion. These transitions are in general forbidden by the Laporte selection rule ($\Delta l$ must be $\pm 1$), but the presence of the ligands perturbs the centrosymmetry of the ion, making these transitions partially allowed. Moreover, the ligands act as antennas for the incident radiation: the $4f - 4f$ transitions of the lanthanide would naturally be very weak, but the ligands absorb the incoming radiation and transfer nonradiatively the excitation to the lanthanide (by electron exchange, Dexter energy transfer). This mechanism is named sensitization [492, 493]. The emission from the lanthanide complex arises solely from the rare earth ion because the $4f$ electrons are screened by the 5th close shell ($5s^2 5p^6$). Nevertheless, the splitting of the energy levels of the ion is affected by the crystal field formed by the ligands. $Eu^{3+}$ has 6 elec-

trons in the $4f$ shell: following Hund's rules the ground state is $^7F_0$, where the total spin $S$ is 3 ($2S + 1 = 7$), the total angular momentum is $L = 3$ (term F) and the spin-orbit coupling $J$ is the lowest ($|L - S| = 0$). The emission spectrum of Eu-complexes generally contains the electron transitions from the $^5D_0$ to the $^7F_J$ multiplets ($J = 1, ...6$), and the $^5D_0 \rightarrow {}^7F_2$ at about 2.02 eV is the most intense line [493]. $\mathrm{Eu}^{3+}$ is used as red phosphor ($\mathrm{Y_2O_3}$:$\mathrm{Eu}^{3+}$) in fluorescent lamps, cathode-ray tubes [493] and as dopant in new optoelectronic devices, for example in c-BN [494]. Eu-complexes are employed in organic LEDs [495], fluorescence imaging of biological objects and in biological sensors [496]. Divalent Eu may also be found, especially as a dopant in several crystalline hosts for phosphor materials engineering [497–502]. $\mathrm{Eu}^{2+}$ complexes can also be synthesized [503]. With 7 electrons in the $4f$ shell, $\mathrm{Eu}^{2+}$ luminescence displays both sharp lines from intra-configurational $4f - 4f$ transitions [498, 500–502] and a broad band from the inter-configurational $5d^1 \rightarrow 4f^7$ transition in the visible range [499,502,504,505]. The energy range of $\mathrm{Eu}^{3+}$ and $\mathrm{Eu}^{2+}$ emission transitions are superimposed, as shown later in the text, in Fig. 4.16.

The specific Eu-complex used in this thesis is the tris(benzoylacetonato) mono(phenanthroline) europium(III), $\mathrm{C_{42}H_{35}EuN_2O_6}$, usually indicated as Eu(ba)3(phen). Its chemical structure is shown in Fig. 4.13.b. As shown in Fig. 4.13.c, molecular crystals appear as rods (other Eu-complexes are found in an orthorombic lattice [506,507]). The typical CL spectrum in Fig. 4.13.a (red line), displays the expected emission lines around 2.0 eV, and it is in good agreement with the luminescence spectrum of $\mathrm{Eu}^{3+}$ in a different complex (Eu(tta)3(phen)) (black line). The electron-beam damaging of the molecular crystals, already demonstrated by SEM-CL [37] (Fig. 4.6), has been confirmed by the the lowering of the CL intensity under continous illumination, as shown by the plot in Fig. 4.13.d: after the acquisition of the first spectrum of time series, the intensity drops by 20%.

**Coronenes**

Coronenes are a planar, carbon and hydrogen compound ($\mathrm{C_{24}H_{12}}$) formed by six aromatic rings around a central one (Fig. 4.14.a). They belong to the class of the polycyclic aromatic hydrocarbons (PAH), which groups all carbon-hydrogen chemicals based on aromatic rings, with delocalized $\pi$ electrons. This kind of molecules are naturally abundant, produced by combustion of organic substances, and suspected of carcinogenic activity [508]. They are also present in the interstellar medium [508]. In the crystalline phase, coronenes appear as needle-shaped monoclinic crys-

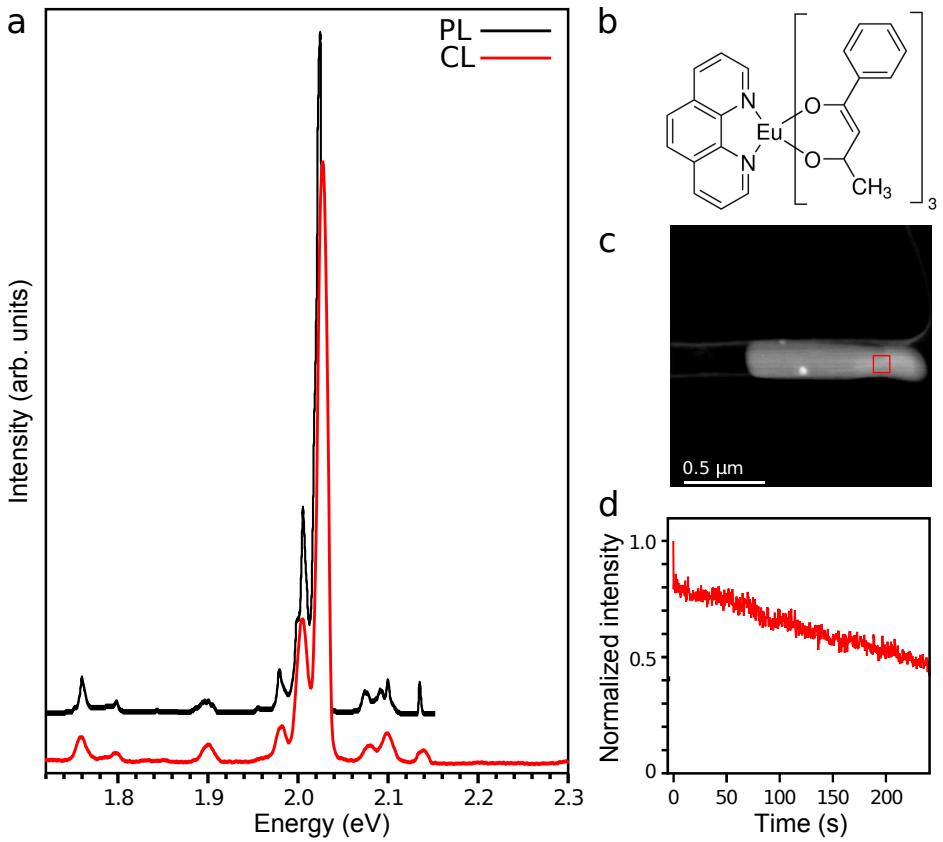


Figure 4.13: *(a) CL spectrum (red) of a molecular crystal of Europium complexes, acquired at 150 K form the marked area in the HAADF image (c) and luminescence spectrum at 77 K of Eu(tta)3(phen) complex, extracted from ref [493]. (b) Eu-complex molecular structure from Sigma Aldrich website. (d) Intensity plot of the principal emission peak (612 nm, 2.03 eV) as a function of time.*

tals, where coronenes are stacked by $\pi$ stacking, with an interplanar distance of 3.4 Å and are inclined at about 45° with respect to the needle axis [509, 510] (Fig. 4.14.b). As purchased coronenes crystal rods appear as a yellow powder (Fig. 4.14.c). Coronenes fluorescence quantum yield has been estimated about 0.2-0.3 [508, 511, 512], and the quantum yield of higher excited states has been demonstrated to increase with increasing excitation energy [513]. Coronenes can be employed in blue light-emitting diodes [514] and single-crystal optical nanofibers [510]. Another important application is the synthesis of nanoribbons (within carbon nanotubes) and graphene by individual molecules coalescence by heating above the melting temperature (438 °C) [515, 516]. Coronenes are also often chosen as basic system for theoretical simulations of nanographenes [452].

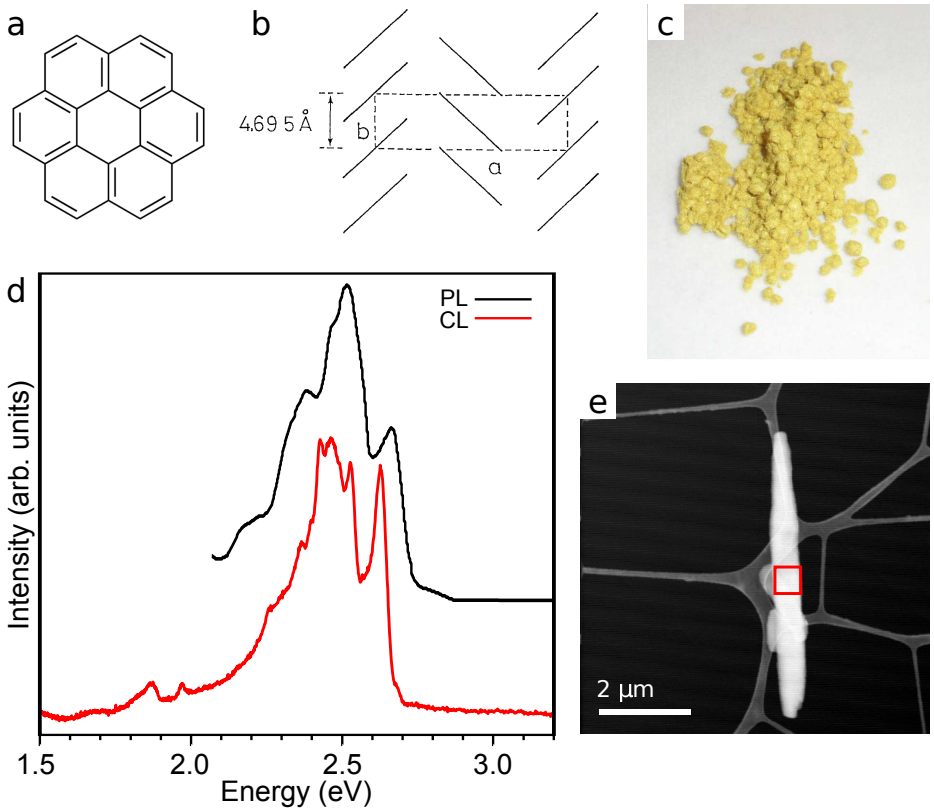


Figure 4.14: *(a) Molecular structure from Sigma Aldrich website and (b) molecular crystal structure, from ref. [517]. (c) Coronene crystals powder, from Graphene Supermarket website. (d) CL spectrum (red line) of a molecular crystal, acquired at 150 K form the area marked in the HAADF image (e), compared with a luminescence spectrum (black line) acquired with* $\lambda = 405$ *nm excitation, extracted from ref. [510].*

Coronenes have been considered in this thesis for both their fluorescence properties and their planar hexagonal symmetry, which might favour the deposition on the flat h-BN substrate. Fig. 4.14.d presents a typical CL spectrum (red line) acquired during this thesis from coronenes molecular crystals (Fig. 4.14.e). The emission spectrum is in agreement with previous CL (SEM) measurements from molecular crystals [465] and with fluorescence measurements (black line in Fig. 4.14.d) [510, 514, 517]. The slight shift of the CL signal with respect to the luminescence spectrum in Fig. 4.14.d may be due to different temperature or sample purity. As already reported during the first CL experiments in the 70's [465], coronene needles are sensitive to electron-beam irradiation. Also in the STEM-CL experiments here reported the luminescence intensity has been observed

to lower after a couple of seconds of continuous illumination and accompanied by morphological damages visible in the image (slight diameter reduction, bending of thin rods).

## 4.11 Cathodoluminescence from the h-BN-molecules system

The STEM-CL analysis of highly diluted Eu-complexes distributed on h-BN flakes has revealed emissions in the range 1.5–3.5 eV, not present in the pristine BN substrate. Fig. 4.15 shows the results obtained from two hyperspectral images on different flakes, acquired with 500 ms integration time per spectrum and 44 nm spatial resolution. Fig. 4.15.a presents the observed emissions, integrated over few pixels of the hyperspectra, together with the molecular crystal spectrum, for comparison. Fig. 4.15.b,d show the regions where the hyperspectra have been acquired (indicated by the squares) and the associated CL intensity maps are presented in Fig. 4.15.c,e. The maps have been derived by integrating the most intense peak of each emission, within an energy window of about 40 meV. The intensity is represented on a colour scale going from black to the same colour used in the spectrum above. The CL maps from the first hyperspectrum have been superimposed.

The additional emissions observed in these samples (Fig. 4.15.a) cannot be attributed to h-BN and are different from the molecular crystal luminescence. They remain however compatible with the energy range expected for electron transitions from higher electronic levels of Eu, as represented in Fig. 4.16 from the energy values reported in ref. [493] and experimental references [493, 498–502, 502, 504, 505, 518, 519]. The additional emissions are more intense than h-BN excitonic peaks (shadowed in grey) and sometimes appear in pairs, separated by no more than 200 meV (140 meV in the blue spectrum, and 200 meV in the green one). When visible in these spectra, the excitons replicas that can appear between 2.65 eV and 2.93 eV and are produced by higher diffraction orders by the spectrometer diffraction grating, have been removed by subtracting them using a multi-Gaussian fit. Since the replicas might be superimposed on real spectral features (not replicas), in future experiments the excitonic emissions might be completely blocked with a low-pass filter before the spectrometer entrance. All the emissions appear spatially localized (Fig. 4.15.d,e), down to the pixel size of 44 nm. The emission spots extending over more

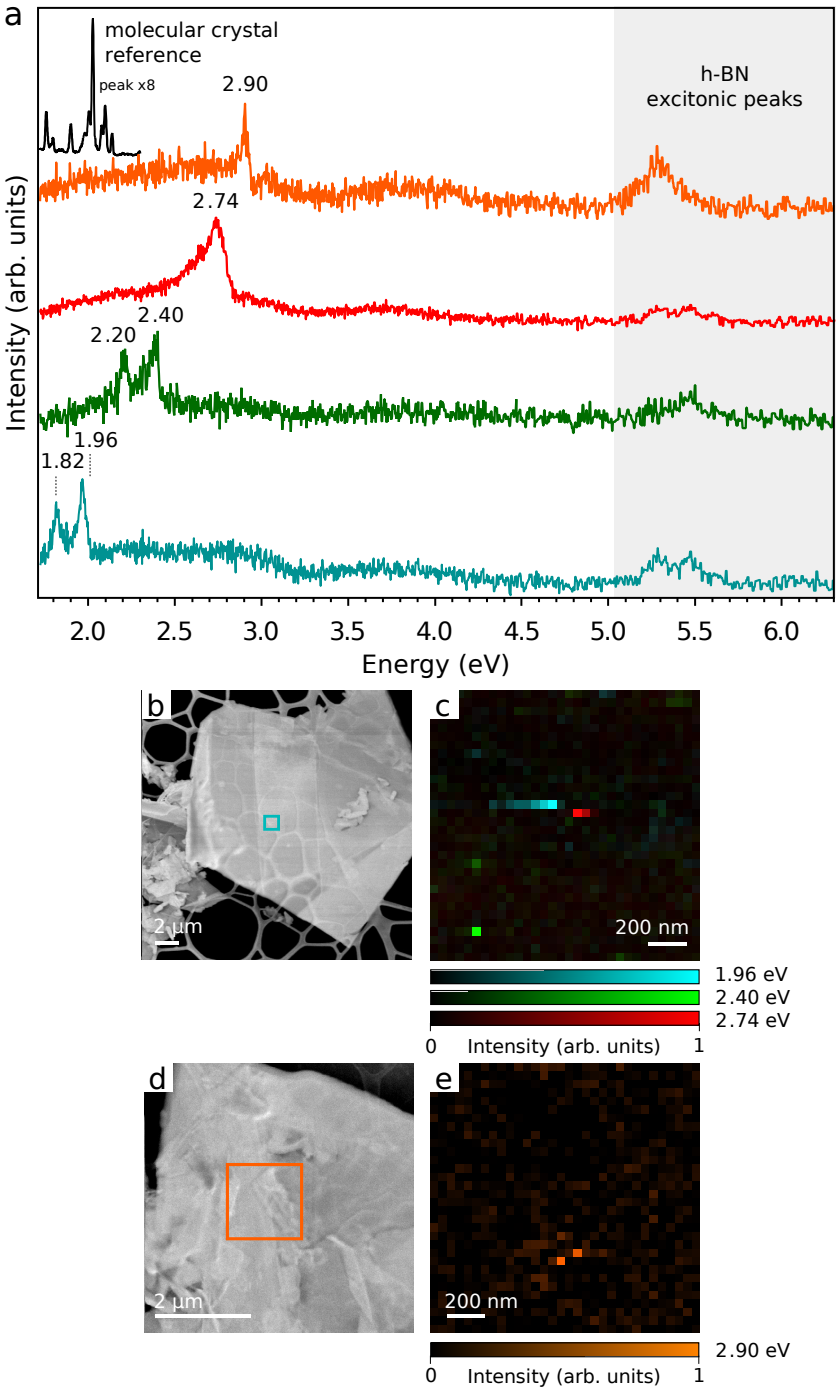


Figure 4.15: *Results form two hyperspectral images of molecules deposited on annealed h-BN flakes: (a) CL spectra, (b,d) HAADF images and (c,e) intensity maps. The squares in (b,d) indicate the regions where the hyperspectra have been acquired.*

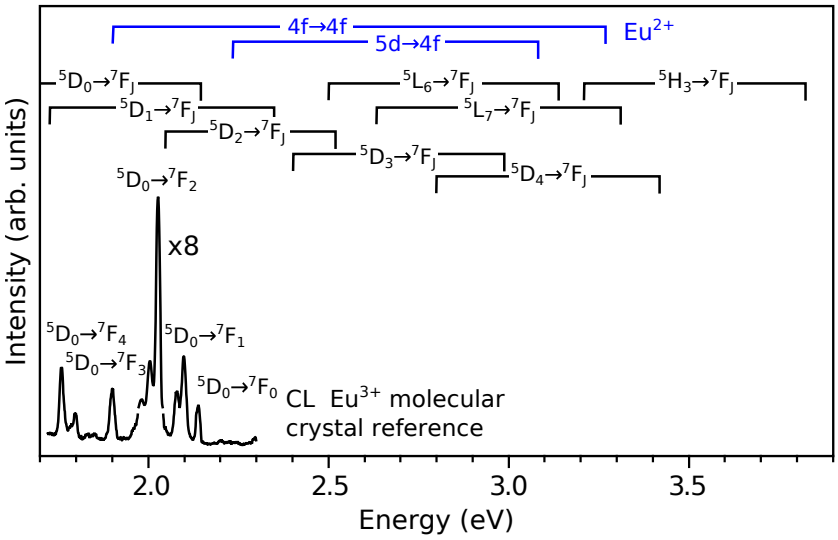


Figure 4.16: *CL spectrum of Eu-complexes molecular crystal acquired in the STEM, with energy ranges of higher energy electron transitions in* $\mathrm{Eu}^{3+}$*, from the calculated values reported in ref. [493], and most of them experimentally observed in complexes and doped crystals [493, 518, 519]. In blue, experimental ranges of* $\mathrm{Eu}^{2+}$ *sharp and broad transitions, from refs. [498–502,504,505] are also reported.*

than one pixel are not symmetrical. In particular, the blue spot is extended along a line of the scan: the emission intensity gets stronger and stronger while the electron beam proceeds towards the right and suddenly drops.

Fig. 4.17 shows another example of Eu-complex on h-BN, where the flakes have been treated with 10 s plasma cleaning before molecules deposition, in an attempt of limiting molecules mobility by a less regular substrate surface. The hyperspectrum has been acquired with 300 ms integration time and 10 nm spatial resolution. The data are presented in the same form as Fig. 4.15. In the case of multiple emissions, the CL intensity maps derived from each peak are similar (they appear simultaneously over all the emission spot) and only one map is presented in the figure. The double emissions are separated by about 210 meV at most (210 meV in the green spectrum, 190 meV in the blue, 160 meV in the orange). Triple emissions have been observed as well, and in both cases the peaks are 180 meV apart from their neighbours. The emission spots are again in general not symmetrical, especially the blue, green and purple ones. The emission spots in Fig. 4.17 display a variable spatial extension from few tens of nanometres (the green spot) to about 100 nm (the orange one).

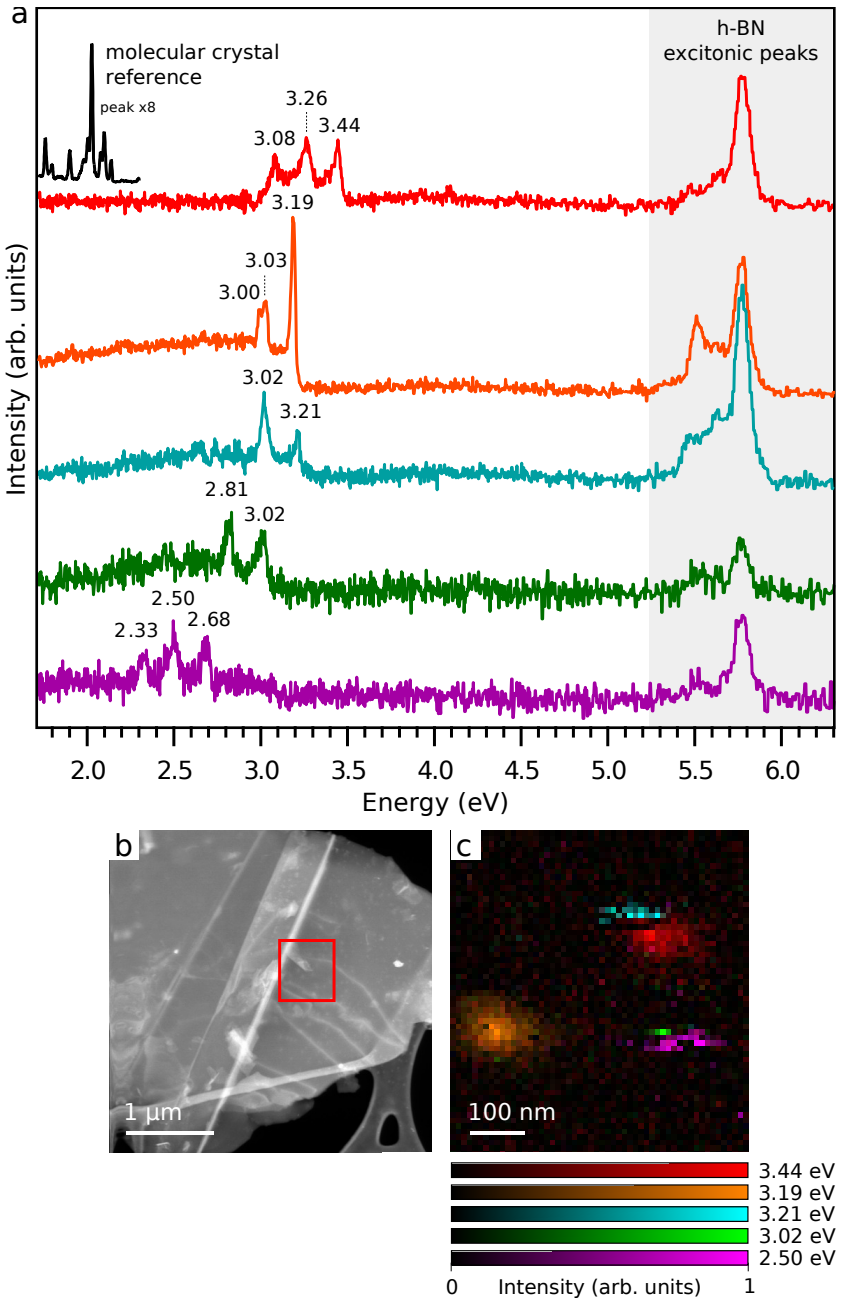


Figure 4.17: *Results from an hyperspectrum acquired on Eu-complexes deposited on h-BN flakes treated with 10 s plasma cleaning. (a) CL spectra extracted from few contiguous pixels, (b) HAADF image and (c) superimposed intensity maps of the different emissions in (a).*

## 4.12 Illumination damages

The asymmetrical shape of the emission spots in Fig. 4.15.c and 4.17.c reminds the behaviour of h-BN defects around 2.32–2.46 eV and is symptomatic of sudden modifications of the emitting system, induced by the electron beam. On the contrary, the CL of a photostable point emitter should appear as symmetric isotropic intensity maximum in the CL maps, as it has been observed for the h-BN SPE defect al 4.09 eV. Independently of the real origin of the emissions, which will be discussed later (section 4.15), the contribution of h-BN to the excitation seems confirmed by the spatial extension of the emission spots. Of course, in general their dimension may depend on the number and distribution of the emitters. However, the intensity profile of the spots, where the intensity progressively fades away with increasing distance from the intensity maximum, is compatible with the indirect excitation mechanism and previous experiments on h-BN luminescent defects (sections 4.9). The indirect excitation through h-BN allows to detect the CL from the molecules when the electron beam is at a certain distance, but during the scan the beam inevitably approaches to the emitting centre. The mismatch between the pixel size in the hyperspectra and the beam size (tens of nanometres against about 1 nanometre) reduces the possibility to directly irradiate the molecules. However, molecules modification and destruction by direct interaction with the beam is still possible.

**Bleaching, blinking and diffusion**

The sudden and definitive interruption of the luminescence (as in the blue spot in Fig. 4.15.c or the line-shaped spots in Fig. 4.17.c) is associated to molecule bleaching. This phenomenon is explained as the occurrence of a chemical modification of the molecule, which permanently prevents fluorescence. Accelerated electrons can easily destroy small molecules (sections 2.9 and 4.4).

Dark pixels in the emission spots might derive also from blinking, that is the transition of the molecule toward a dark, nonemitting state. For example, after nonradiative transition (called intersystem crossing) from the first singlet excited state to a triplet state, the radiative relaxation to the singlet ground state, called phosphorescence, is a forbidden transition. Hence the triplet state has a much longer lifetime with respect to the singlet, typically order of μs against ns, and the radiative transition is weak [520]. Blinking on the scale of seconds has been observed by fluorescence intensity measurements and fluorescence excitation spec-

troscopy [88, 326, 333, 521]. In fluorescence measurements with a fixed laser frequency, blinking can be due to spontaneous or optically-driven (switch) shift of the resonant frequency of the molecule (spectral diffusion) [88, 326, 333, 521]. This effect should be visible by CL, where the beam electrons can transfer a variable amount of energy to the molecule, and would still be able to excite the molecule after resonance shift. As a matter of fact, the blue-red and green-purple emission spots in Fig. 4.17.c might represent such an example, since in each case the emissions are spatially close and not superimposed. Beam-induced variations in the energy of Eu-complexes emission could occur through damaging of the ligands with possible alteration of the crystal field around the Eu ion or charging of the complex, or potentially (it cannot be excluded) a change of Eu oxidation state ($+3 \rightarrow +2$).

Another crucial effect for the evaluation of illumination damages is the mobility of the molecules on h-BN's surface. Indeed, the line-shaped blue spot in Fig. 4.15.c can be interpreted in these terms. The assumption that the molecule was located at the most intense pixel can explain the increasing signal intensity along the scan direction (from left to right), while the beam approaches to the molecule. However, for the same reason, emission should be detected also in the previously scanned lines just above. The observed behaviour is instead compatible with the molecule being initially located in a line below the emission spot and being attracted and dragged by the beam. The observed consequent bleaching appears then as the result of a long-lasting and progressively increasing excitation of the molecule. In order to avoid this kind of illumination effect, an innovative random scan acquisition mode has been elaborated and is presented in the next section.

## 4.13 Hyperspectral imaging by random scan

An innovative acquisition mode based on a random scan of the electron beam over the specimen has been implemented within the STEM microscope by Marcel Tencé, from our research group in Orsay, and it has been tested for the first time on the molecules-h-BN samples. The motivation for a new acquisition routine is the molecules sensitivity to illumination with fast electrons, and in particular the observation of unusual emission spots such as the blue spot in Fig. 4.15.c. Here, the spot appears elongated in the scan direction and the emission intensity increases up to final

bleaching. The absence of emission in the previous (upper) scan lines is compatible with the molecule(s) being initially placed in a pixel row below the spot and moving to the right with the beam. This results in a long-lasting indirect excitation of the molecule. Indeed, during the scan the electron beam pauses over each pixel for about the time interval required for spectrum acquisition (typically 300-500 ms). During its interaction with a specimen, a certain amount of energy is transferred to or deposited on the specimen. In a traditional raster scan, the beam visits consecutive pixels, that is the illuminated pixel is just to the right of an area which might be still in an excited state. In the case of a mobile molecule, this leads to an accumulation of the energy deposited by the beam, which finally is able to destroy the molecule. The random scan is based on the idea of moving the electron beam far away after each pixel illumination. This should afford sufficient time for evacuating the deposited energy and thus reduce the illumination damages.

**Operating principle**

The random scan allows to acquire a complete hyperspectrum. The beam follows a random path and each pixel is tested only once. The random path is generated by considering all the pixels of the hyperspectrum as a list. Afterwards, the list is shuffled and represents the history of the incoming random acquisition. The so generated random path is then loaded into a dedicated scan generator. For each pixel, the beam is present on the specimen strictly for the time required for signals acquisition (image and spectrum) and is diverted far from the specimen for the rest of the time, thanks to a fast blanking system. Fig. 4.18 provides a sketch of the random scan operation: the pixels of the image are coloured as a function of the order of acquisition. The applications of this innovative acquisition routine are multiple. Besides reducing the illumination damages, it is a powerful tool for the investigation of highly diluted systems. Indeed, it allows fast surveys with a wide field of view for effective tracing of regions of interest.

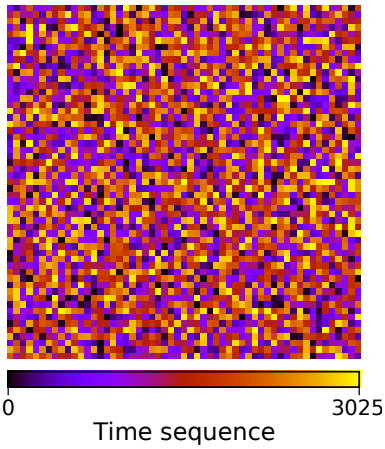


Figure 4.18: *Example of random scan acquisition. The colour scale represents the acquisition history of the 3025 pixels composing the hyperspectral image.*

Fig. 4.19 presents a comparison between random and raster scan.

Three hyperspectra have been acquired by random scan, and for two of them an hyperspectrum has been acquired immediately afterwards by raster scan. In the example reported in Fig. 4.19.b-d (300 ms per spectrum, 10 nm spatial resolution), the emitter does not show illumination damages. Nevertheless, while the emission spot provided by the raster scan is very symmetrical, that of the random scan appears noisy. This can be justified by the fact that the CL intensity is proportional to the beam current and that we are using a field emission gun. The electron current emitted by this kind of source typically lowers as a function of time. In raster scan measurements the beam current lowering between the beginning and the end of the acquisition appears as a gradual effect and locally in the image it is little evident. On the contrary, at the end of a random scan acquisition, pixels corresponding to relatively different beam currents are contiguous and the effect becomes remarkable. Fig. 4.19.e-g (300 ms, 10 nm resolution), on the contrary, shows the superiority of the random scan: although noisy, the random scan provides a symmetrical emission spot; at the beginning of the raster scan the emission is still detected, but it is rapidly and suddendly stopped. Finally, Fig. 4.19.h.i presents another example of random scan acquisition (300 ms, 10 nm resolution). In general, with this scanning mode the unusual emission spots extending along a single row of pixels (a scan segment) have not been observed and a higher number of spectra of a same emission can be acquired.

## 4.14 Coronene single molecules

The investigation of highly diluted coronene molecules by random walk acquisition has led to interesting developments also in the case of coronenes. Fig. 4.20, shows the results from two hyperspectra, acquired with 10 nm spatial resolution and 100 ms spectrum integration. The CL intensity maps in Fig. 4.20.c (green) shows that the pixels containing the emission are quite apart from each other. This might derive from two causes: the molecule(s) has moved outside of the imaged region or the emission has stopped, temporarily or permantly, during the the hyperspectrum acquisition (because of blinking or bleaching). In principle, the analysis of the scan history may provide important elements to answer this question.

The scan history could be acquired in the hyperspectral acquisition in Fig. 4.20.d-f. In this case the CL intensity maps show two intersecting

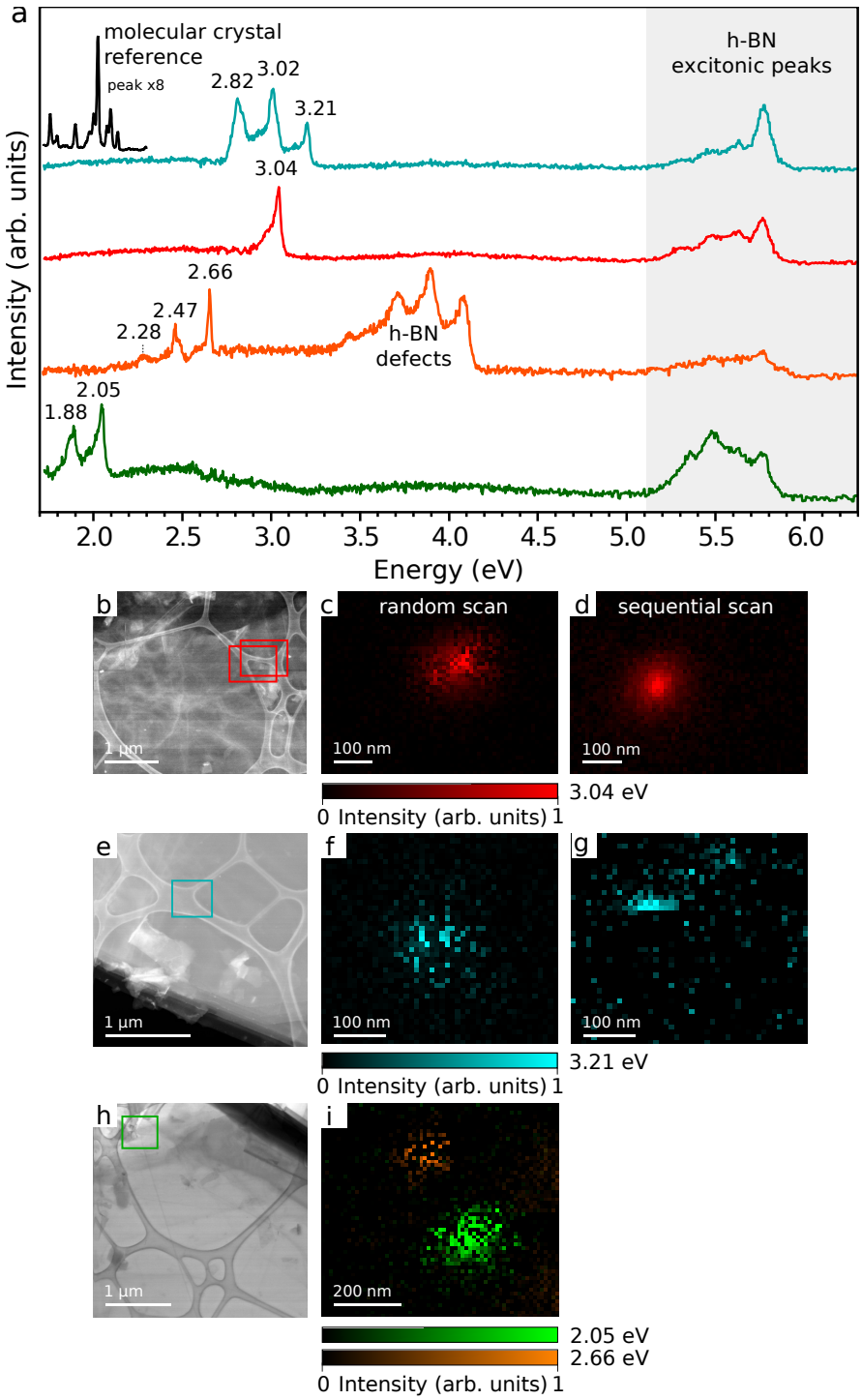


Figure 4.19: *Results from hyperspectral imaging of Eu-complexes on plasma cleaned h-BN: comparison between random scan and traditional raster scan. (a) Spectra, (b,e,h) HAADF images, (c,f,i) maps derived from random scan and (d,g) maps derived from a subsequent raster scan.*

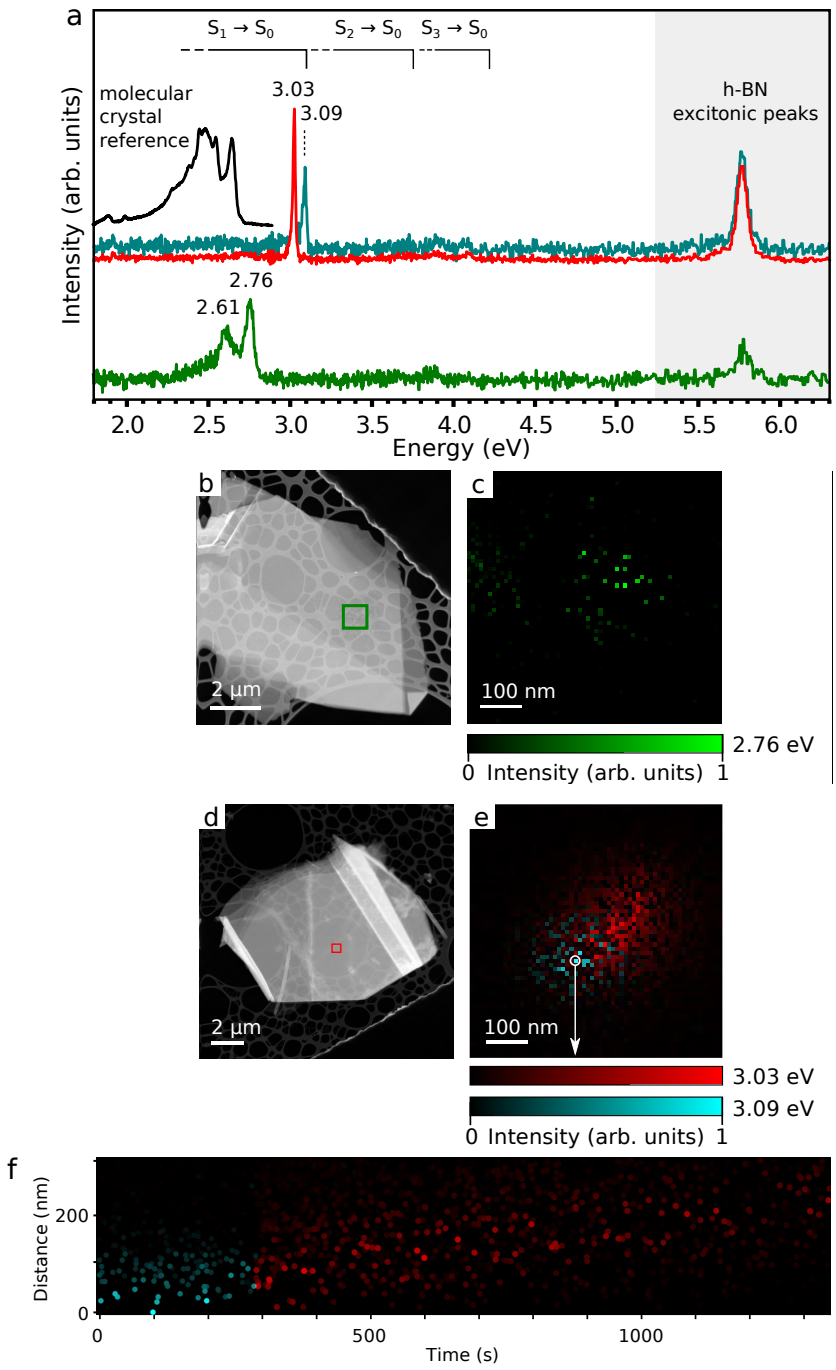


Figure 4.20: *Coronenes on plasma cleaned h-BN. (a) Spectra of some emissions. Approximate transition energy ranges marked above have been extracted from ref. [513]. (b,d) HAADF images and (c,e) associated CL intensity maps acquired in the regions marked by the squares and representing the intensity of the emissions in (a). (f) Plot of Fig. (e) as a function of acquisition history (x-axis) and distance from the white circle (y-axis).*

emission spots, corresponding to the very sharp emissions at 3.03 and 3.09 eV in Fig. 4.20.a. The graph in Fig. 4.20.f has been obtained by plotting the pixels of the intensity maps as a function of the order of acquisition, with in the ordinate axis the calculated distance of the pixel from a pixel arbitrarily identified as the centre of the blue spot (indicated by the white circle), and the same colour scale as in the CL maps (intensity). This representation of the data reveals that the emission at 3.09 eV (blue) was present from the beginning of the acquisition up to about 300 s, while that at 3.03 eV (red) is present from that moment on. The fact that the two emissions do not superimpose in time is an important observation describing the emission dynamics. Moreover, the graph indicates the displacement of the emitter with respect to the location assumed as centre. This behaviour is compatible with a single molecule whose optical properties undergo a change, after a variation in the local environment (orientation or conformation of the molecule, h-BN surface defect) or electron-beam induced modification (i.e. charging or damaging). This is similar to light-induced fluorescence switches observed in several isolated molecules [334,335], and other kinds of switches such as in molecules orientation/conformation or conductance have been attributed to induced structural changes [371] or charging effects in an STM [337–339].

In the results presented up to now a considerable variety of previously unobserved emissions has been reported, which represents only a selection of all the molecules-related emissions observed during this work. Several factors associate these luminescence features with molecules.

- These emissions do not correspond to the molecular crystals peaks and they have not been observed in pristine h-BN, nor in our STEM-CL investigations (during this thesis and that of R. Bourrellier [475]) neither in the previous studies reported in the extensive literature.

- They are spatially localized, forming emission spots about 100 nm wide.

- They are beam-sensitive, showing bleaching, blinking and variations of the emission frequency.

- Most importantly they are remarkably sharp. The 3.03 eV emission in Fig. 4.20.a displays a full width at half maximum of $9\pm1$ meV, which is most probably limited by the optical chain in the experimental set-up used (but easy to improve). This is a strong evidence

indicating the molecular character of the emission. The luminescence from h-BN defects is characterized by broader peaks (15-45 meV, at 150 K) and a strong phonon coupling.

The observation of individual sharp peaks such as the 3.03 and 3.09 eV lines suggests a radiative recombination involving individual molecules.

## 4.15 Possible excitation mechanisms

The dimension of the CL emission spots reported in the previous sections confirms that excitation is mediated by h-BN. However, the mechanisms of excitation in h-BN, transfer of the excitation and emission transitions remain unclear and may follow many different paths. Moreover, a large variety of emissions has been observed, which seem little reproducible from experiment to experiment.

**Excitation in h-BN**

After thermalization, the excited charge carriers are in their lower excited state. This may correspond, in order of decreasing e-h energy separation, to top and bottom of valence and conduction bands, excitonic levels or impurity levels (those last ones are highly spatially localized). The energy transfer to the molecules is in competition with e-h recombination within h-BN, and although the luminescence from the molecules can be more intense than the h-BN excitonic peaks, those last ones are never completely suppressed. Considering that the exciton recombination may take place wherever within the excitation volume, the recombination involving molecular levels seems to be very efficient. The CL from h-BN defects, if present, can also be conserved at the same time as molecular peaks appear.

**Excitation transfer**

Molecule excitation could be induced directly by the electric field of the beam travelling electrons, as the generation of a dipole optical transition in the molecule. However, this requires a high proximity between the beam and the molecule, while the CL emission spots are about 100 nm in size. Moreover, the direct interaction with the electron beam is typical of larger objects such as nanoparticles, where plasmon excitation occurs with a cross section proportional to the object volume [77]. Therefore, this mechanism is not likely in the case of individual molecules.

The indirect excitation depicted in section 4.6 can be described in terms of a donor-acceptor energy transfer. This may follow several paths: radiative energy transfer, Förster or Dexter energy non-radiative energy trans-

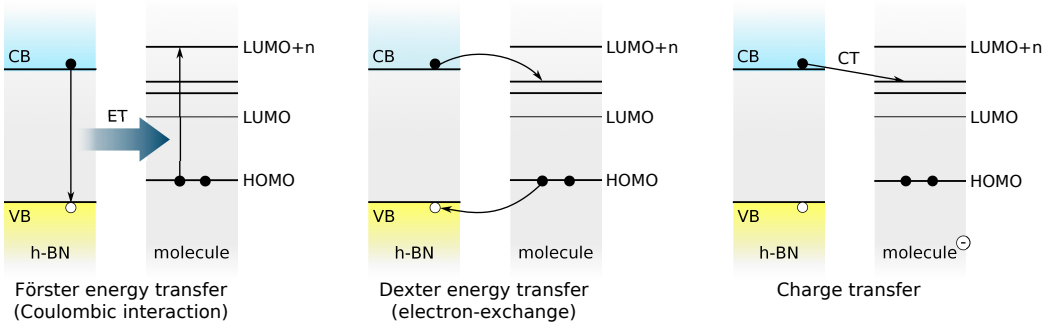


Figure 4.21: *Possible mechanisms for the excitation transfer. For simplicity, excitonic and defect levels h-BN, vibrational levels associated to molecular electronic levels are not represented.*

fer or charge transfer. The radiative transfer consists in a photon emitted by the donor (h-BN) being absorbed by the acceptor (the molecule). The absorption spectrum of the donor and the emission spectrum of the acceptor must then overlap. This mechanism is dominant at relatively large donor-acceptor distances $R$ ($kR \gg 1$, radiative limit) and the transfer rate is very small [522]. For this reason, it seems to be little likely to occur.

Non-radiative Förster resonant energy transfer (FRET) is based on the dipole-dipole Coulombic interaction between donor and acceptor: an e-h pair dipole in h-BN can induce a transition dipole moment in the nearby molecular system, as allowed by the dipole selection rules (Fig. 4.21). Since it is a resonant energy transfer, the absorption spectrum of the donor and the emission spectrum of the acceptor must overlap, as for the radiative transfer. The transfer rate decays as $(R_0/R)^6\gamma_0$, where $R_0$ is the Förster radius and $\gamma_0$ is the decay rate of the donor alone, with no acceptor. The Förster radius indicates the distance R at which the energy transfer dominates and depends on the refractive index of the medium, the spectral overlap and the relative orientation of the dipoles. It usually corresponds to less than 10 nm [522]. This dependence on the distance is at the basis of near-field FRET imaging, to measure distances [340,522]. The FRET mechanism is used for biological sensing (as mentioned in section 4.2), chemical sensor or to tune the optical properties of organic nanoparticles and nanowires [523]. Very recently, Förster energy transfer has been reported in transition metal dichalcogenides, between in-plane strongly bound excitons in adjacent layers [524].

Dexter energy transfer consists in an electron exchange: one donor's electron in the LUMO moves to the acceptor's LUMO and an acceptor's

electron in the HOMO moves the donor's HOMO (Fig. 4.21). This mechanism accounts for the occurrence of forbidden transitions [525], which involve spin flip (transitions between singlet and triplet states). This happens if donor and acceptor exchange two electrons with different spin projection. For electron exchange, donor and acceptor's wavefunctions must overlap. Indeed, the interaction is very short-range: the transfer rate decays exponentially with the distance $R$ and typical distances are less than 1 nm. This is still compatible with our molecules-h-BN system. For example, the gap between coronenes and the clean h-BN surface may be expected to correspond to graphite or h-BN interlayer distance of 0.3 nm.

**Charge transfer**

An alternative excitation mechanism is represented by the transfer of an electron from h-BN to the molecule, resulting in a charged molecule (Fig. 4.21). Luminescence might arise from intramolecular transitions of the additional electron, from higher energy levels (LUMO+n) to the LUMO, as it often occurs in STML, where an electron is provided by tunneling from the tip [413, 415, 416]. Otherwise, the detected emission could derive from the radiative recombination of the additional electron on the molecule and a hole in h-BN [526]. Indeed, charge transfer excitons are known in molecular crystals [527, 528]. In particular, a charge exciton is predicted by GW-BSE simulations in coronenes crystals, delocalized up the first neighbouring molecules [528]. Charge transfer is also known to occur at the interface between molecules [529,530], polymer and molecules [526, 531–533]. This effect is sought for achieving charge separation in organic photovoltaic devices. Charge transfer has been observed between transition metal dichalcogenides and deposited molecules, as a modification of the substrate's PL features. The interpretation of the transfer mechanism requires generally electron transfer from the molecules to the substrate, and hole transfer from fullerenes to $WSe_2$ [534].

## 4.16 Origin of additional emissions

Despite the uncertainties deriving from the variability of the excitation transfer mechanism and of the excitation energy amplitude (depending on the nature of the excitation in h-BN), some hypothesis can be suggested about the the origin of the emissions. As already outlined in the previous section, luminescence can in principle arise both from intramolecular electron transitions towards the HOMO level, and radiative recombina-

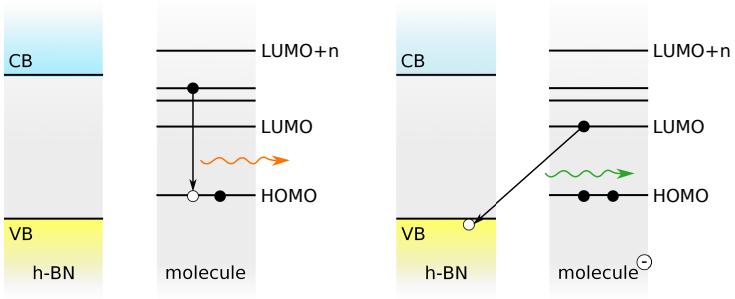


Figure 4.22: *Possible mechanisms for radiative recombination. For simplicity, excitonic and defect levels h-BN, vibrational levels associated to molecular electronic levels are not represented.*

tion of electron and holes localized respectively on the molecule and h-BN (similarly to PL reported from a molecule/polymer interface [526]), as sketched in Fig. 4.22. Intramolecular emission transitions in neutral molecules should occur from the lowest vibrational level of the excited state, reached by a fast radiationless decay called internal conversion (Kasha's rule [535]). Another radiationless internal transition may occur from the first singlet excited state $S_1$ to the first triplet state $T_1$ (intersystem crossing [535]). The emission transition from $S_1$ or $T_1$ to the ground state $S_0$ gives rise respectively to fluorescence and phosphorescence. Fluorescence from higher excited states is usually not observed, since they rapidly convert by radiationless decay to the first excited state [352,536], but this interpretation for the CL peaks observed in this thesis shall not completely be ruled out. Photon emission from the recombination of charge states (Fig. 4.21) raises the question about molecular and h-BN levels relative energy alignment. The HOMO level is expected to lie within h-BN gap and, given the wide amplitude of the gap; also the LUMO should be included, possibly together with higher molecular levels. However, the exact alignment is not known.

The interpretation of the multiple emissions is also not clear. They could arise from several situations. First of all, it could be the luminescence of groups of two or three molecules, close enough that their individual emission spots cannot be distinguished. Otherwise, in the assumption that a single molecule is responsible for the CL features, the molecule could be excited to different excited states in the time interval of spectrum integration (300-500 ms). Else, the lower energy peaks could represent vibrational levels of the ground state. In particular, the observed triplets

of peaks, equally separated in energy, are compatible with such an hypothesis, although the energy difference of 180 meV might be too high for vibrational levels. The coupling with phonons in the h-BN crystal is also possible. Finally, multiple emissions could derive by composite radiative electron transitions of multiple intramolecular de-excitations or including both intramolecular and molecule-h-BN transitions.

## 4.17 Perspectives

Molecules excitation through h-BN and the use of a random walk scanning acquisition have been demonstrated to considerably lower the illumination damages. We have shown that molecules deposition on h-BN flakes by a very simple synthesis procedure is responsible for the appearance of new emission features, which are not intrinsic of the substrate and do not exactly correspond to the molecular crystal emission. Several elements suggest that the observed emissions arise from very few molecules, and in some cases probably individual molecules. This kind of experiments has never been attempted before and the results obtained open new perspectives in the study of molecules by STEM-CL. Nevertheless, many aspects of the observed luminescence remain unknown. The excitation mechanisms might depend on the type of molecule and specific local environment around the molecules. Forster and Dexter energy transfers could in principle be distinguishable by the temperature dependence of their transfer rates [524], but such an experiment on the molecule-h-BN system looks arduous.

In general, the interpretation of the luminescence properties of molecules (or molecules-substrate system) is not trivial, and the problem is not limited to the particular kind of spectroscopy used in this work. Especially in the case of multiple peaks, the confirmation that molecules are indeed isolated could be helpful. HBT experiments would in principle allow to distinguish between the excitation of one or more than one single photon emitters, but our attempts have not been successful for the moment. The experiment requires a high emission yield and a relatively stable source, and molecules probably cannot fulfil these demands. Another road could be high resolution microscopy: in our STEM-VG microscope the spatial resolution is too low, and an aberration corrected microscope should be used. Europium complexes, in particular, would be more easily identified in HAADF, thanks to Eu's high atomic number. However, the

molecules position must be correlated with their CL emission. Such an experiment could be soon performed in Orsay's CHROMATEM microscope, with the additional advantage of a lower temperature.

From a technical point of view, the innovative random walk scanning acquisition opens new exciting perspectives in microscopy and spectroscopy. With reliable image reconstruction algorithms, it would enable hyperspectral imaging by acquiring only a little percentage of the pixels, allowing to considerably lower the exposition of sensitive materials to the electron beam. Compressive sensing techniques are being developed at present for the same aim. However, they are based on a single sequential scan of the region of interest, during which the beam is blanked (diverted far from the optical axis and the specimen) for most of the acquisition time. With this respect, the random scan is more attractive. For example, the illumination spots are on average more spaced, so the evacuation of the deposited energy and charge could be more efficient. Mobile nanostructures, which move under or near the electron beam, (as it is the case of molecules on h-BN) should suffer littler displacement with the random scan than with compressive sensing. Moreover, the random scan can be run up to completion of the acquisition and the image or CL/EELS hyperspectral images can be filtered a posteriori as a function of the acquisition history. Studies of the critical total electron dose could be performed in this way. Finally, at low spatial resolution, the random scan is helpful to locate spectroscopic signatures. In the particular case of this thesis, where molecules could not be distinguished in the image, random overviews of the CL emission have allowed to identify regions of interest for hyperspectral acquisition. However, a drawback is represented by the longer total acquisition time, deriving from the dead time associated to beam displacement. The difference might be seizable in the application to EELS investigations (to be tested yet), but it is not for CL measurements, where the integration time per spectrum is longer.

The use of the random scan should be tested on molecules such as pyrromethenes and rhodamines, which have shown more ore less intense STEM-CL emissions by the traditional raster scan. Fig. 4.23 provides a schematic summary of the CL features observed during this thesis. Of course, the investigation of other kinds of fluorescent molecules (Alexa488, Nile Blue, Cyanine...) would be interesting.

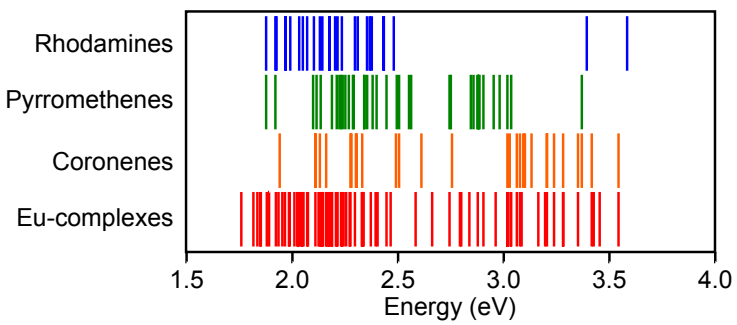


Figure 4.23: *Graphical representation of all the CL emissions observed during the experiments described in this chapter. In each molecular series, some of the lines have been observed simultaneously (double or triple emissions) but no distinction is made in this graph.*

CHAPTER 5

# OPTICAL PROPERTIES OF CUBIC BORON NITRIDE

The optical properties of c-BN have attracted a considerable interest in the 60's. The investigation of the energy band-gap width has been for a long time hindered by the lack of pure and defect-free crystals and suitable investigation techniques. In 2001 highly pure crystals [42, 43] have become available, but first experimental investigation of the optical band-gap amplitude has confirmed previous results, providing a value of about 6.3 eV [43, 44]. Nevertheless, several aspects suggest that the band-gap must be much wider. Indeed, the band-gap of h-BN is estimated about 6 eV, and, by comparison with the isoelectronic forms of carbon represented by graphite and diamond, c-BN band-gap value is expected to be much higher than h-BN's. Moreover, modern theoretical simulations in 2004 have predicted an optical onset of 11.4 eV [46]. Hence, the band-gap is most likely too wide to be accessed by optical excitation techniques (PL, absorption). Even using CL, where higher excitations can be addressed, the limitation comes from the detection of far UV radiation. In this thesis, we study high purity c-BN crystals [42] by EELS spectroscopy in the low-loss region, in order to investigate c-BN optical properties above 6 eV.

Besides the concern about the band-gap, PL and CL studies have revealed since the 60's a wide series of emissions at energies below the experimental band-gap [45]. They have been associated with defects or defect complexes involving B and N vacancies and C and O impurities, but interpretation remains difficult. The research in this field has slowed down after the 80's and no related study has been reported in the last ten years, leaving the characterization of c-BN luminescence properties incomplete. In this thesis we have studied c-BN pure crystals and commercial powders by spatially resolved CL in the STEM microscope, in order to investigate c-BN optical properties below 6 eV. Several localized emissions have been identified and their coupling with crystal phonons and their quantum nature have been analysed.

In this chapter, after the description of the structure and synthesis of c-BN, the optoelectronic properties will be addressed. Previous investigations about the band-gap and the low-loss EELS results obtained during this thesis will by presented at section 5.2, followed by an introduction to the defect-related emissions known in the literature and the present STEM-CL+HBT characterization, from section 5.5).

## 5.1 Properties and synthesis of c-BN

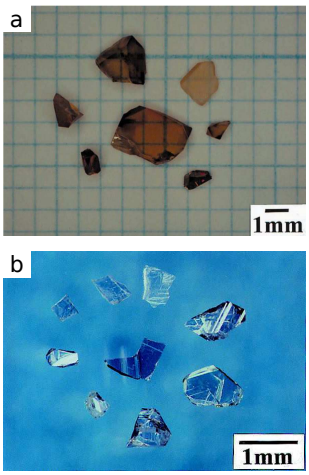


Figure 5.1: *(a) Amber coloured and (b) colourless c-BN crystals grown by the temperature gradient method using respectively* $Li_3BN_2$ *and barium boron nitride as the solvent [41].*

c-BN is the hardest material after diamond and it is characterized by extremely high thermal and chemical stability (both superior to diamond) [45]. Sintered c-BN finds then a natural application in industry as cutting tool and abrasive, especially in presence of ferrous metals, which are able to degrade diamond [40]. Being a wide band-gap semiconductor, c-BN single crystals are intrinsically colourless. However, intrinsic and extrinsic defects are generally introduced during the synthesis process, resulting in coloured crystals: carbon and oxygen impurities are suspected to be responsible for amber colour, while yellow and black crystals have been associated respectively with N- and B-rich structures [40, 57] (Fig. 5.1.a).

Coloured crystals have been obtained also by artificial doping. Blue p-type crystals have been reported for the introduction of Be impurities, yellow n-type crystals for S and Si impurities, from yellow to reddish-brown for $CN^-$ [39]. Doping with rare earth atoms (Eu and Tb) has also been investigated, in sight of optoelectronic applications [494, 537].

**Structural properties and allotropes**

c-BN is the zinc-blende or sphalerite phase of BN (Fig. 5.2). Boron and nitrogen are tetrahedrally coordinated, forming a double face centred cubic (FCC) lattice. This structure is analogous to that of diamond, with a lattice parameter mismatch of less than 2% (3.62 Å in c-BN, 3.57 Å in diamond). BN can exist also in another $sp^3$ based form: wurtzite (w-BN). It corresponds to an hexagonal lattice with AB stacking, isoelectronic with

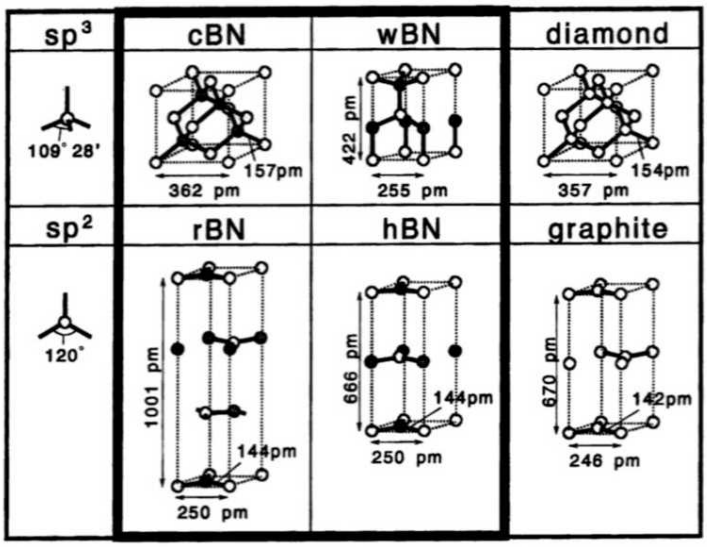


Figure 5.2: *Crystal lattices of BN, from ref. [45].*

the carbon allotrope lonsdaleite. On the other hand, $sp^2$ coordination gives rise to the two layered structures of h-BN and rhombohedral BN (r-BN), where weakly interacting planes of hexagonally arranged B and N atoms are stacked respectively in a AA' and ABC order. h-BN is the BN equivalent of graphite. At ambient conditions, h-BN is the most stable phase of BN, while the c-BN form is metastable. w-BN might also be a metastable phase [45].

**Synthesis**

c-BN is a synthetic material, obtained by structural conversion of h-BN. Inspired by the achievement of diamond synthesis by a high-pressure high-temperature (HP/HT) treatment of graphite [538,539], R. H. Wentorf succeeded by a similar procedure in the first synthesis of c-BN (General Electrics, 1957). Single crystals are produced by the temperature gradient method, where a BN material is dissolved in presence of a catalyst and c-BN nucleation and growth occurs by precipitation in the solvent, at moderately high temperature and pressure of about 1500 °C and 5 GPa [41, 45] (Fig. 5.3). Among the remark-

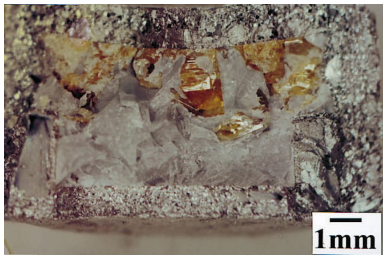


Figure 5.3: *Molybdenum chamber used for the HP/HT growth of c-BN crystals in* $Li_3BN_2$ *solvent. Crystals nucleate at the interface with the Mo wall of the chamber (upper side, in the image). [41]*

able variety of catalysts/solvents that have been reported, boron nitrides of alkali or alkaline earth are considered superior [45]. However, yellow-amber coloured crystals are usually obtained, indicating a the presence of defects and/or impurities. This represents a strong limitation of the synthesis method. In 2001 colourless crystals up to about 1 mm in size have been obtained by HP/HT treatment of h-BN rods, using barium boron nitride ($Ba_3B_2N_4$) as the solvent [41] (Fig. 5.1.b). Secondary ion mass spectrometry (SIMS) has shown that the carbon and oxygen content in these crystals is much lower than in $Li_3BN_2$ grown crystals and the precursor h-BN material [42]. However, it has been observed that the use of degraded $Ba_3B_2N_4$ solvent, which is very reactive with air and humidity, leads to lower quality crystals, in terms of impurity concentration [42].

**h-BN to c-BN conversion**

Nevertheless, the phase conversion from the hexagonal to the cubic form is not straightforward. Fig. 5.4 shows the phase diagram of h-BN and c-BN, indicating the pressure and temperature coordinates at which the h-BN and c-BN phases are stable. However, the stacking similarities between the different BN structures suggest that the conversion of h-BN into w-BN and r-BN into c-BN can be driven by simple compression, through the formation of new covalent bonds [540, 541]. On the contrary, h-BN to c-BN transition requires bond-breaking and atom diffusion to transform the AB stacked h-BN atomic planes into the ABC ordered puckered lattice planes in the $\langle 111 \rangle$ direction of c-BN FCC lattice (Fig. 5.2). HRTEM studies have reported evidences against a direct h-BN to c-BN transformation, in favour of the formation of transient phases mediating the conversion [541, 542]. Single and multiwalled nanoarches formed by joining dangling bonds at h-BN sheets edges have been observed in the starting h-BN material [541] (Fig. 5.5). At the beginning of the HP/HT conversion, compression and local folding of h-BN planes occurs, inducing a transition to a monoclinic crystal structure [541, 542].

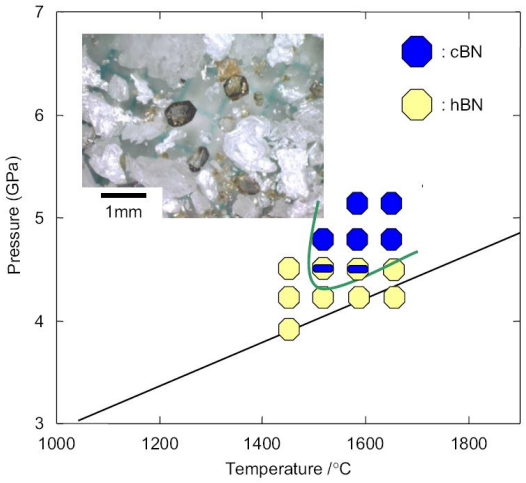


Figure 5.4: *Phase diagram of c-BN formation in* $Ba^{-}BN$ *solvent and, in the inset, HP/HT grown BN crystals after acid treatment, from ref. [42].*

Moreover, additional nanoarches forms and are believed to act as nucleation sites for c-BN crystallites (the nanoarches planes becoming the (111) planes of cubic lattice) [541]. The coalescence of pairs of h-BN planes promoting the stacking order change is associated with an r-BN arrangement. In small c-BN grains, w-BN areas have been observed [542]. These findings suggest the possible presence of extended defects in c-BN consisting in inclusions of hexagonal-related phases.

**Other synthesis methods**

Alternatively to the HP/HT method, chemical vapour deposition (CVD) can be used for the synthesis of c-BN films. The necessary high pressure conditions are obtained by ion bombardment of the growing film, on Si or diamond as the substrate [543,544]. Otherwise, BN films containing single crystals c-BN grains of about less than 1 μm in size, with small h-BN islands at the film surface, have been obtained by plasma jet CVD [545]. CVD BN films obtained with these techniques contain between 50% and 90% c-BN phase, relative to h-BN [543,545]. The use of a pulsed laser treatment for h-BN to c-BN conversion at ambient temperature and pressure has also been reported [546].

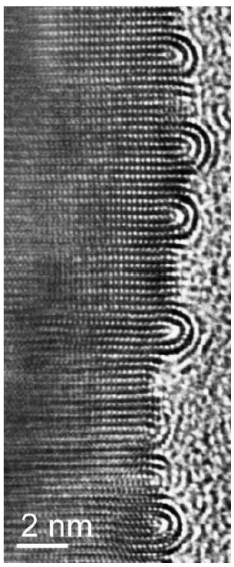


Figure 5.5: *HRTEM image of nanoarches at the edges of h-BN nanocrystallites, from ref. [541].*

## 5.2 Electronic structure and band-gap

In the comparison of BN with its carbon counterparts, the ionic character of B-N bond plays an important contribution in the determination of BN band structure. While graphite is a semimetal, h-BN has a wide energy band-gap of about 6 eV. By analogy, c-BN band-gap may be expected to be much wider than that of diamond (5 eV). Theoretical simulations have shown that h-BN, c-BN and w-BN are all indirect band-gap semiconductors, with valence and conduction bands extremities at respectively $H_v - M_c$, $\Gamma_v - X_c$ and $\Gamma_v - K_c$ [49,547] (Fig. 5.6). However the exact value of the band-gap is still a subject of discussion, both from the experimental and theoretical point of view.

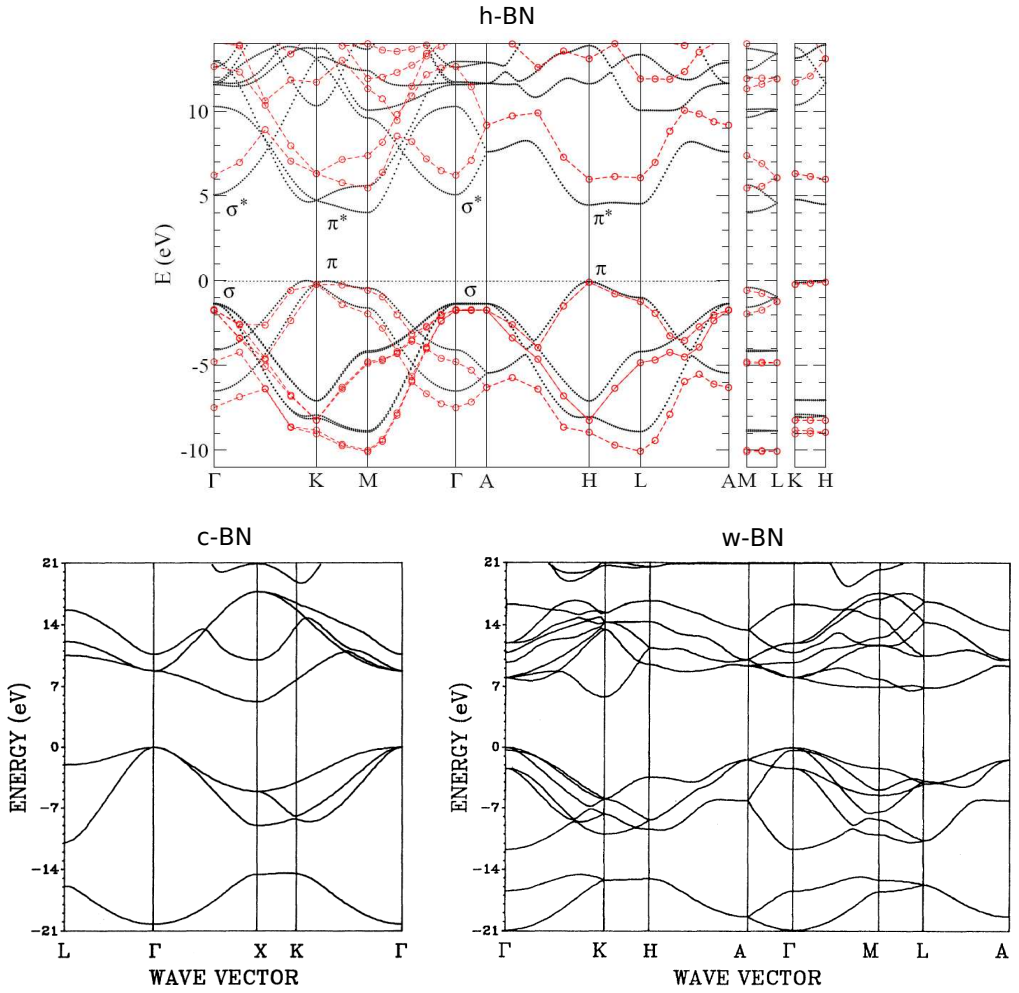


Figure 5.6: *Calculated band structures of h-BN from ref. [49], w-BN and c-BN from ref. [547].*

**Experimental band-gap**

The experimental investigation of c-BN band-gap width dates back to the 60's. The highest reported value of 6.4 $\pm$ 0.5 eV has been obtained by ultraviolet optical absorption [44]. Considering the possible presence of defects, the authors identify in this estimate a minimum value for the band-gap, and on the basis of the calculated band structure they associate it with the indirect band-gap. Later, reflectance measurements and soft x-ray spectroscopy have provided a band-gap value of about 6.2 eV [548, 549]. In 2004, CL experiments on the newly available high purity crystals have confirmed these estimates: a series of peaks between 6.03 and 6.09 eV have been interpreted as phonon-assisted excitonic emissions related

to the 6.25 eV wide indirect band-gap [43]. Synchrotron radiation sources have also been employed to investigate higher-energy spectral regions. From luminescence excitation spectroscopy, a band-gap of about 6.3 eV has been derived [550]. Only nonresonant inelastic x-ray scattering has shown a higher absorption onset, although only non-optical transitions could be accessed and the results have not been discussed extensively.

The experimental investigation of c-BN band-gap can be limited by two main factors: the sample purity degree and the spectral range of the specific technique used. The typical poor quality of c-BN samples has been largely reported, made evident by the yellow-amber coloration usually exhibited by the crystals. The presence of impurities or intrinsic defects would introduce additional electronic levels within the band-gap of the material, misrepresenting the real band-gap width. With respect to this, the mechanism of c-BN formation through transient rhombohedral and wurtzitic phases (summarized in section 5.1) shall also be considered. Moreover, h-BN exhibits strong emissions at almost 6 eV. Concerning the spectroscopic technique, it must be observed that optical excitation or detection above 6 eV is prohibitive. Hence, optical absorption spectroscopy and even CL might not be suitable for this experiment.

**Theoretical simulations**

Several theoretical simulations have been carried out since the 60's to assess the nature and amplitude of c-BN band-gap. It is known that DFT in the local density approximation (LDA) provides underestimated band-gap values for semiconductors and insulators [551]. The introduction of the GW correction for the electron self energy, accounting for electron-electron interaction, expands the calculated band-gap, in better agreement with the experimental results. Finally, excitonic effects can be considered by the solution of the Bethe-Salpeter equation (BSE). This is particularly important for the simulation of optical properties, such as absorption spectra or macroscopic dielectric function and reflectivity. In the specific case of c-BN, DFT-GW simulations have predicted an indirect gap of 6.3 $\pm 0.2$ eV and a direct gap, at the $\Gamma$ point, of 11.4 eV [552]. Later, the BSE has been employed for the simulation of nonresonant x-ray inelastic scattering measurements, resulting in good agreement with the experiments [553], and the macroscopic dielectric function [46]. In this last work, Satta et al. have emphasized some fundamental discrepancies between previous simulations and experimental results, suggesting that c-BN band-gap must be much wider than commonly believed.

They observe that despite the typical DFT-LDA band-gap is underestimated the onset of the calculated imaginary part of the dielectric function ($\epsilon_2$) is blueshifted instead of redshifted with respect to the experiments. Also, previously BSE calculations of non-resonant inelastic x-ray scattering spectra have shown good agreement with the direct experimental results, both with an onset around 10 eV [553]. The macroscopic dielectric function calculated by Satta et al. using the GW-RPA (random phase approximation) and BSE corrections, exhibits an increased optical onset of 11.4, corresponding to a bound exciton in a band-gap of 11.75 eV [46] (Fig. 5.7). The authors finally attribute spectral features below 10 eV to contribution of hexagonal phase domains [46,554].

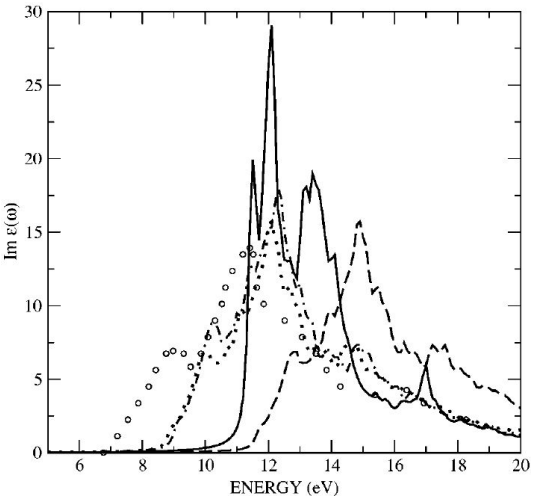


Figure 5.7: *Calculated imaginary part of the dielectric function, from ref. [46]. The solid line represents the BSE calculation, ther other curves are previous, less precise calculations.*

Therefore, several clues suggest that c-BN optical absorption onset should be much wider than measured until today. Indeed, comparison with graphite and diamond, c-BN should have a wider band-gap than h-BN, whose band-gap is about 6 eV. The observation of wurtzitic inclusions in partially converted h-BN precursors shows that c-BN crystals analysed up to now most probably contained extended defects. The optical spectral features attributed to the band-gap are situated in the same spectral range as typical h-BN emissions, and, finally, modern theoretical simulations have predicted an optical onset of 11.4 eV.

## 5.3 Optical band-gap investigation in the STEM microscope

In this thesis we have studied highly pure c-BN crystals in order to identify the true width of c-BN optical gap. We have employed EELS spectroscopy in the low-loss spectral range, in order to have access to high-energy electron transitions above the highest optical limit achieved of 6 eV.

**Sample preparation**

Colourless c-BN crystals have been provided by T. Taniguchi, from the National Institute for Research in Inorganic Materials in Tsukuba. They have been synthesized by spontaneous nucleation at high pressure and high temperatures using the temperature gradient method in $Ba_3B_2N_4$ solvent. As received crystals have been washed in acetone and ethanol to remove sticking gel residues and successively crushed in a mortar. TEM grids have been prepared by drop casting of crystals dispersions in isopropanol.

**EELS**

EELS spectra have been acquired at 100 kV electron acceleration. Hyperspectral images have been collected on the thinner regions of c-BN particles, near the borders. The energy dispersion of the spectra is about 0.1 eV. Spectra with a suitable S/N ratio have been extracted by spatial integration over consecutive hyperspectral pixels. Deconvolution has been performed with Digital Micrograph using a Richardson-Lucy method [555] for deconvolution of the instrument response function and the Fourier-log for the removal of ZLP and plural scattering contributions. Kramers-Kronig analysis have also been performed using Digital Micrograph.

## 5.4 Determination of the optical band-gap

Fig. 5.8 shows a low-loss EELS spectrum acquired from a thin area about 13 nm wide (marked by the red square in the inset image). The main peak, between about 10 eV and 45 eV appears more structured than in previous experimental studies [556, 557] and it is in good agreement with previous theoretical GW simulations [547], which have predicted three intense plasmon peaks at 27.3, 32.5 and 38.5 eV, and less intense peaks at 11.1, 15.0 and 24.4 eV. In EELS spectra, the almost flat spectral region of little intensity, in the range of about 8-10 eV, between the ZLP and the main peak of the spectrum, is indicative of a forbidden energy interval for electronic transitions. Hence, the upper limit of this energy window, above which electron excitation occurs, corresponds to the amplitude of the optical gap. The value is usually roughly identified as the intersection between the extension of the flat background and the slope of the first peak. Fig. 5.9.a shows several low loss spectra of c-BN (the green spectrum is the same of Fig. 5.8), acquired from 5-15 nm wide regions. The thickness t of the the specimen has been calculated from the Poisson statistics as $t/\lambda = \ln(I_t/I_0)$, where $I_t$

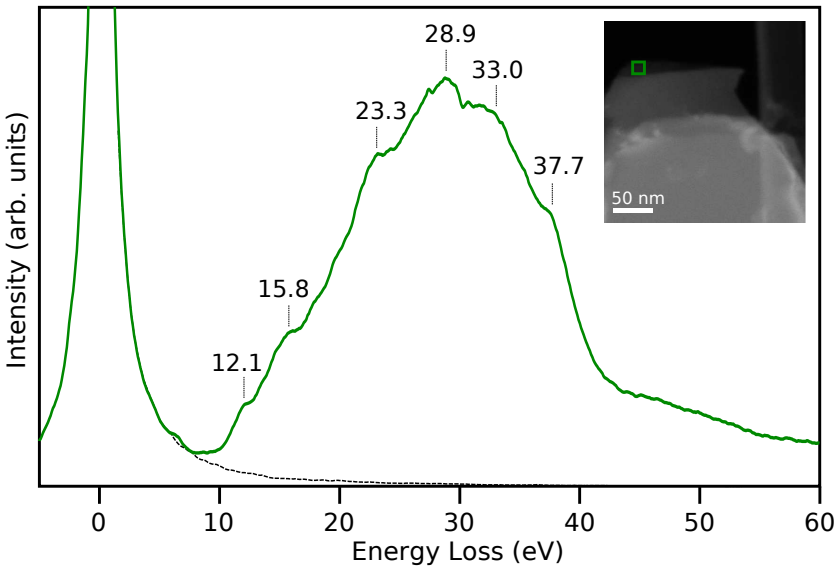


Figure 5.8: *EELS low-loss full spectrum of the thin region (about 11.5 nm thick) indicated by the green square in the inset image, of a c-BN highly pure crystal.*

is the total area of the spectrum, $I_0$ is the area under the ZLP and $\lambda$ is the mean free path for inelastic scattering, estimated from acquisition parameters and the effective atomic number of the specimen [28]. The optical onset has been thus derived for regions of different thicknesses and the obtained average value is $9.97 \pm 0.2$ eV. In Fig. 5.9.b the same low-loss spectra are presented after removal of the ZLP contribution. As shown by the black dotted line in Fig. 5.8, the right-hand tail of the ZLP extends far in the low-loss region, forming a background below the c-BN signature. In each spectrum of Fig. 5.9.b the ZLP has thus been fitted using the experimental ZLP (acquired in a vacuum region of the sample, in a hole of the TEM grid) and subtracted. In the so-obtained loss functions the optical gap corresponds to the first sudden increase in the slope. Differences in the spectra in the low-energy region are due to surface scattering effects. The very shallow peaks that appear at 6-8 eV in several spectra are thought to arise from defect levels within the band-gap, probably related to small inclusions of a crystal phase with hexagonal symmetry. Indeed, the low-loss spectrum of h-BN and h-BN nanotubes is characterized by a doubly structured $\pi$ plasmon between 6 and 10 eV [49, 558, 559] These spectroscopic features will be further characterized in section 5.8.

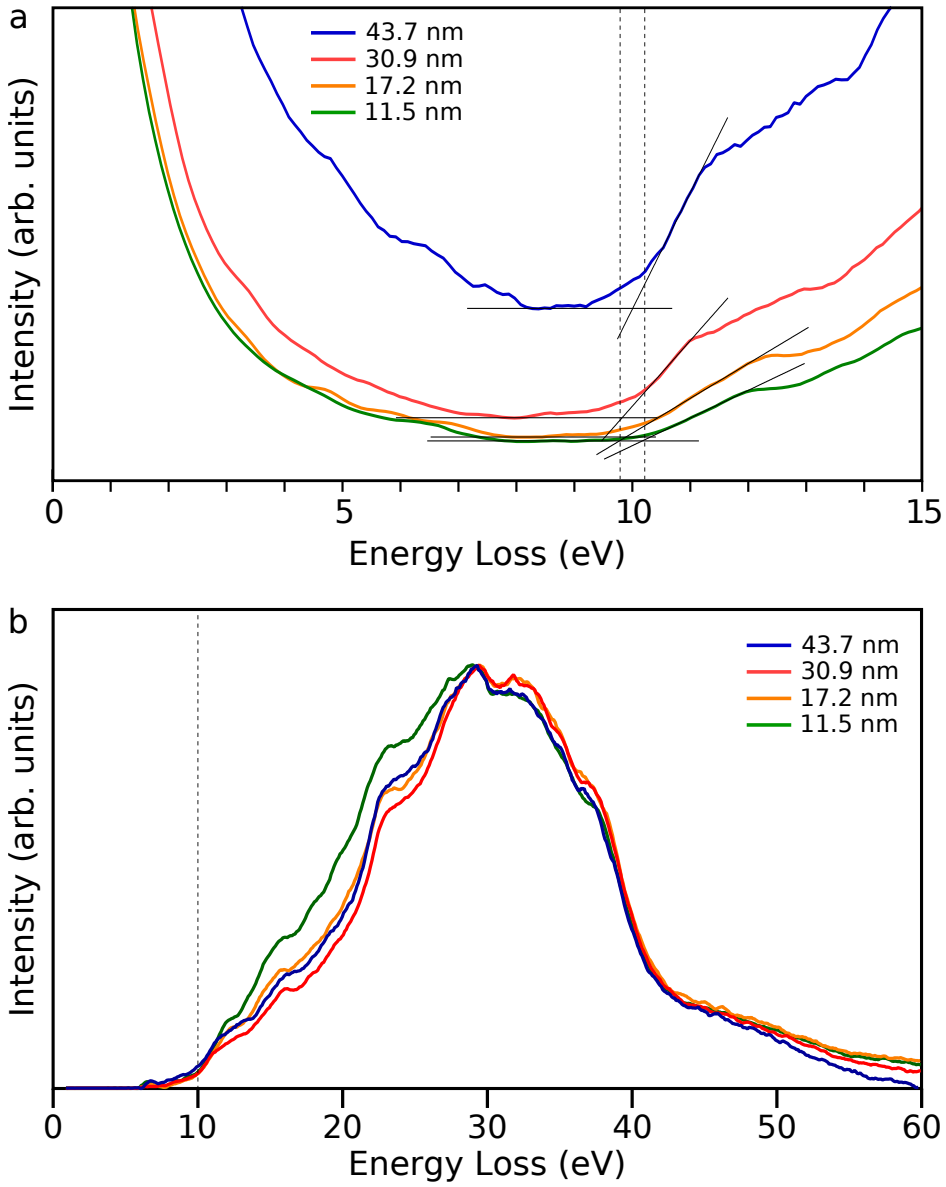


Figure 5.9: *(a) EELS low-loss spectra of different regions of distinct c-BN highly pure crystals. The intersection of the linear fits indicate the value of the optical gap. (b) The same spectra after ZLP subtraction.*

**Kramers Kronig analysis**

The Kramers Kronig analysis allows to derive several optical properties of the specimen starting from its low-loss function, after removal of the ZLP and plural scattering contributions. The analysis has been performed on all the four spectra of Fig. 5.9, but has converged only for the two thicker spectra. Indeed, bulk and surface scattering effects are both contained in the measured loss function and are progressively separated by subsequent iterations of the Kramers Kronig analysis. In very thin specimens, the surface-loss contribution becomes important and the calculation is less accurate [28]. On the other hand, bulk specimens present higher contributions from plural scattering. The Kramers Kronig analysis on the thinner spectra might be attempted again in the near future, with a different code. Fig. 5.10.a,b shows the real and imaginary parts of the dielectric function and the reconstructed loss function derived from the two thicker spectra of Fig. 5.9 (red and blue lines). The maximum of the imaginary part occurs respectively at 10.4 (red line) and 10.3 eV (blue line). These values are about 1 eV lower than the excitonic peak predicted by BSE calculations, which should occur at 11.4 eV (Fig. 5.7). The shallow peak at 6.7 eV (blue line), appearing also in the real part of the dielectric function at about the same energy (6.4 eV), is likely produced by the weak peaks associated with defects, in the experimental loss function (Fig. 5.9). The reconstructed loss functions well reproduce the original loss functions, with only a slight redistribution of the spectral weight due to the removal of surface effects. However, the amount of information that can be extracted from the Kramers Kronig analysis is limited, since its solution is not necessarily univocal and its numerical implementation on experimental spectra can lead to instabilities. The direct comparison of the experimental loss function with state-of-the-art theoretical simulations would be more valuable, but this calculation has not been reported yet. Thanks to a collaboration with the theoretical group at the Laboratoire des Solides Irradiés at École Polytechnique (Palaiseau), already author of the BSE calculation of the imaginary part of the dielectric function referred above [46], new modern calculations are being performed. At present, GW-RPA calculations are already available and its results are reported in Fig. 5.10.c. The agreement with the experimental loss function is not completely satisfactory, but the BSE corrections might be important.

The EELS investigations performed during this thesis have provided evidences for a much higher optical gap for c-BN with respect to the previous experimental studies in the literature. Only the results from nonresonant inelastic x-ray scattering had shown an onset around 10 eV [553],

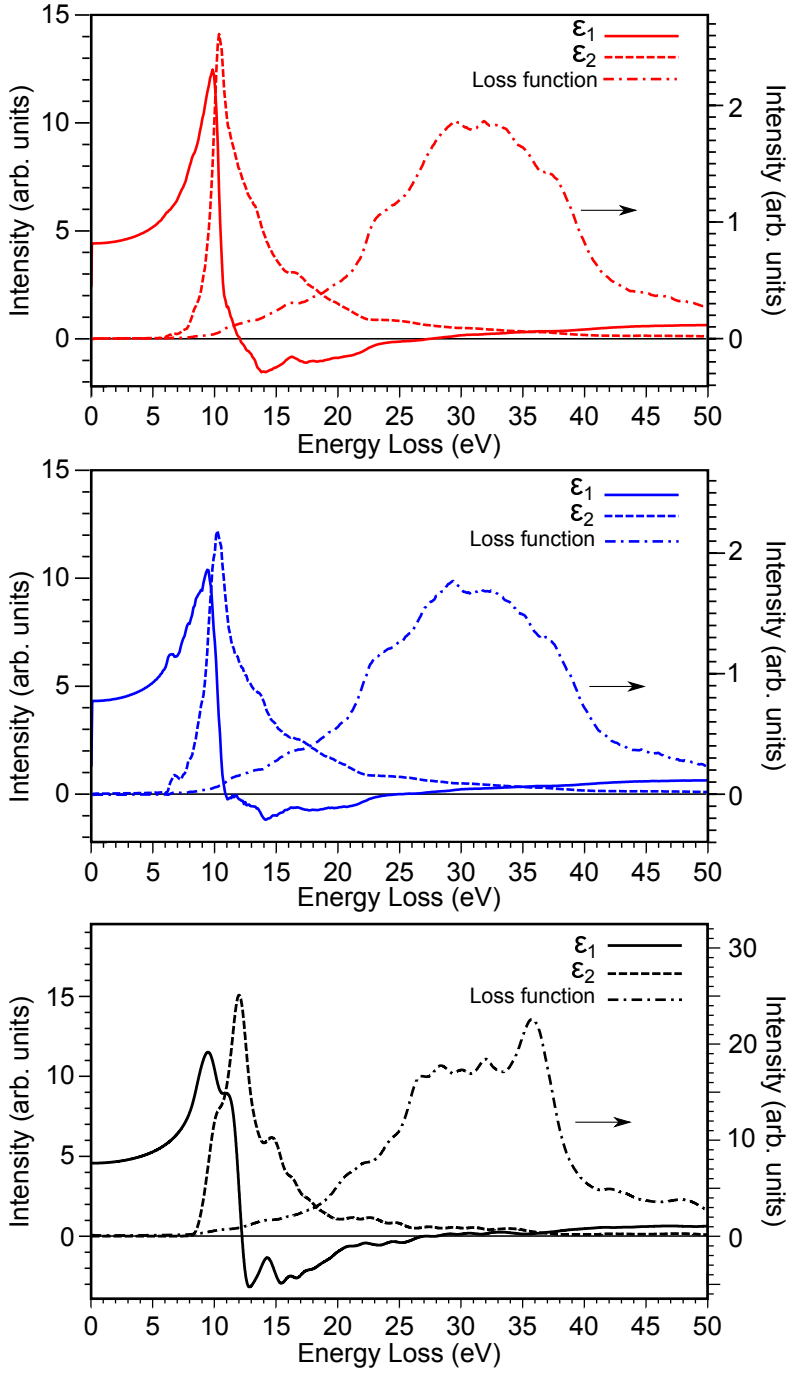


Figure 5.10: *(a,b) Kramers Kronig analysis of two of the spectra in Fig. 5.9 (same colour code). Real (filled line) and imaginary (dashed line) part of the dielectric function, reconstructed loss function (dotted line). (c) GW-RPA recent calculations by the theoretical group of École Polytechnique*

but the precise estimate of the optical gap had not been possible in those experiments due to the lack of optical transitions measurements, at zero momentum transfer (that is vertical electron transitions in the band structure). However, the optical gap value calculated from the low-loss spectra presented here is still lower than predicted by theoretical simulations. The new calculations might provide a better agreement.

## 5.5 Luminescence from defects

Since the 80's, many luminescence features have been observed at energies below the band-gap by PL and CL. Band-like or sharp phonon-assisted emissions have been attributed to electron transitions involving vacancy or impurity levels. Their interpretation has been based on the study of a variety of c-BN samples, including B-rich, N-rich c-BN, annealed, electron-irradiated, ion-bombarded and compressed crystals, and have been compared with numerical simulations. The luminescence features reported in the literature are summarized in the following, and a schematic representation is provided in Fig. 5.11.

- **General cubic series: GC-1, GC-2, GC-3.** The first series of colour centres, known as General Cubic (GC), was reported in 1985 by Tkachev et al. [53]. GC-1, GC-2, GC-3 and GC-4 centres were identified by CL at 1.76 eV, 1.63 eV, 1.55 eV and 1.44 eV, with phonon coupling of 56-64 meV [53,54]. GC-1 and GC-2 have been associated to defect complexes made of an impurity and a vacancy respectively of N and B [53,54].

- **Irradiation-induced defects: RC-1, RC-2, RC-3, RC-4.** CL of electron-bombarded c-BN crystals, electron energy in the order of MeV [55] or in the range 150-300 keV [57], has highlighted a series of emissions named Radiation Cubic (RC): RC-1, RC-2, RC-3 and RC-4, respectively at 2.2 eV, 2.15 eV, 1.99 eV and 1.86 eV, with 64 meV phonon coupling. They have been ascribed to vacancy defects, probably $V_B - O_N$ or $V_N - C_N$ [55,57]. Another electron-irradiation induced emission, named BN-1 centre, was identified at 3.3 eV accompanied by a quite complicated phonon structure. By analogy with a similar centre in diamond and comparison with calculations, BN-1 centre was thought to include an interstitial atom, probably boron [57].

- **Pressure-induced defects: PC-1, PC-2, PC-3.** Emissions observed by CL after high pressure treatment at almost 10 GPa have been classified as Pressure Cubic (PC) and associated to interstitial defects: PC-1, PC-2, PC-3 respectively at 2.84 eV, 2.33 eV and 1.79 eV, interacting with 100 meV local phonons [56].

- **A, B, C bands.** Band-like luminescence have also been reported. Band A and B centred at 2.20 eV and 2.45 eV have been related to multivacancy complexes of $V_N$ and $V_B$ respectively and impurity atoms, while the band C, in the range of 1.55-1.85 eV has appeared enhanced by pressure treatment and has been associated to dislocation density [56].

- **UCL (or US-1), PF-1, PF-2.** The UCL (or also US-1) broad emission has been reported at 3.18 eV, with 130-200 meV phonon coupling [45, 58, 560]. Its origin is unknown. This band is partly superimposed with the PF-1 and PF-2 centres later reported (in the 90's) at 3.57 eV and 3.41 eV respectively, with phonon coupling of 130-136 meV. These features have been interpreted as donor-acceptor recombinations (Frenkel pairs) of $V_N$ and $B_i$, by comparing CL of B-implanted, electron-bombarded and annealed crystals [57, 561]. Manfredotti et al. revised the interpretation of these features identifying a zero-phonon line (ZPL) at 3.57 eV (former PF-1) with several phonon replicas at 141 meV spacing (the first one of them corresponding almost to PF-2). They have assigned this luminescence to a transition from $B_N$ defect level to the valence band [58].

- **GB-1.** A luminescence feature with most intense peak at 3.16 eV (GB-1 centre) and part of a pentet of lines between 3.23 and 3.13 eV and separated by 20-25 meV has been related to the presence of a W impurity [485].

- **4.9 eV ZPL.** Higher energy emissions have been been addressed only recently, using . An emission with ZPL at 4.93 eV and strong phonon coupling, with several lines separated by 152 meV, has been observed by synchrotron luminescence [550]. However no further characterization or investigation about its origin has been performed.

- **h-BN series.** In some (lower purity) c-BN crystals, defect-related emission lines typical of h-BN have been observed (4.09 eV) [485].

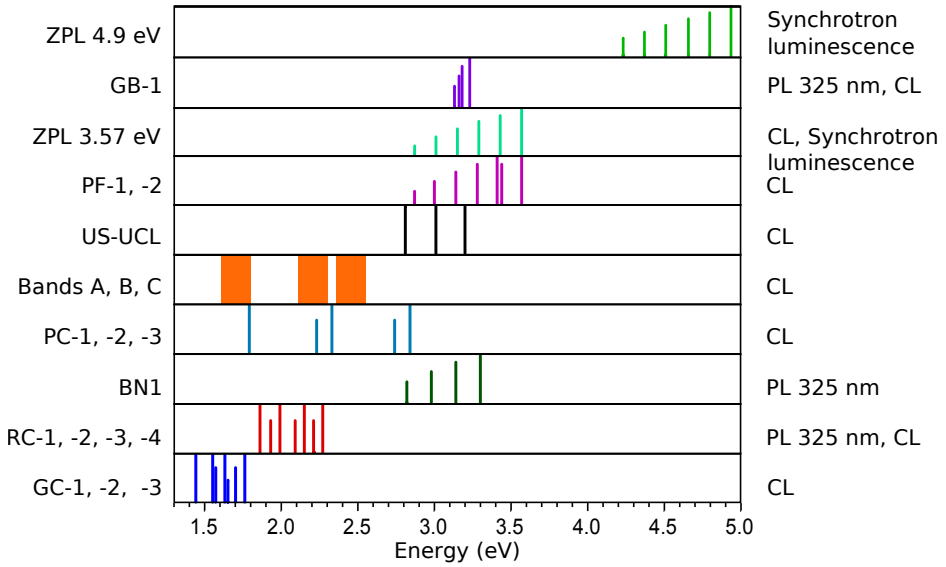


Figure 5.11: *c-BN luminescence features derived from the literature. Full height lines are ZPL, shorter lines are phonon replicas of increasing order.*

Doped c-BN have also been investigated. Two band-like emissions have been reported for Be-doped crystals: one at 3.5 eV, named PCL [45], the other at 4.1 eV and ascribed to a transition from an O donor impurity level to a Be acceptor level [562]. In Si-doped c-BN, band T centred at 4.8 eV has been observed [45].

From the theoretical point of view the stability of intrinsic and extrinsic defects has been studied by *ab initio* calculations. Vacancies have been found to be the most stable defects in c-BN, in particular the $V_N^{3+}$ in N-rich p-type conditions (followed by $N_B^{2+}$), and the $V_B^{3-}$ in B-rich n-type conditions [59]. $V_B$ introduce acceptor levels within the band-gap, while $V_N$ are associated with donor levels [59, 61, 63, 563]. Among impurity atoms, the stability of interstitial and substitutional Li, Be, C and O has been verified [61, 64, 564]. Acceptor levels have been obtained in the case of substitutional Be ($Be_N$), $C_N$ and $O_B$, while $C_B$ and $O_N$ have been demonstrated to be responsible for donor levels [61, 62]. Vacancy-impurity complexes, such as $V_N - C_N$, $V_B - O_N$ and $V_B - C_B$, and vacancy-interstitial complexes have also been considered [62, 63].

This complicated description of c-BN luminescence properties below 6 eV derives from a fragmented investigation, during the last 30 years, focused on different spectral ranges and performed on a great variety of samples, usually of low crystalline quality. Despite the broad nomencla-

ture elaborated up to now, some of the reported emissions are likely to be the same feature: the 3.57 eV emission, the PF, US-UCL and probably also BN-1 emissions overlap fairly well. Moreover, some fundamental experimental characterization is still missing: the spatial distribution of the luminescence features within c-BN crystal, the nature of the emitted radiation (possible single photon emission) and the lifetime of the excited states have not been addressed yet. From another point of view, these studies require isolated defects, so high purity crystals and spatially resolved techniques are needed. The better quality of the samples would also allow to observe more clear phonon sidebands.

## 5.6 Study of CL emissions from defects in the STEM microscope

In this thesis we have investigated the luminescence properties of both highly pure and commercial c-BN crystals, by spatially resolved CL in the STEM microscope. Several phonon-assisted emissions, characterized by a strong coupling with the lattice, have been identified. Some of them have been further characterized by HBT experiments.

**Sample preparation, CL and HBT**

TEM grids of pure and commercial crystals have been prepared as described in section 5.3. Less pure crystals have been obtained from Element Six (De Beers Group Company) [565]. The microscope has been operated at 60 and 100 kV and the experiments have been performed on 150 K cooled samples. For cathodoluminescence diffraction gratings blazed at 2.5 and 4.1 eV have been employed, assuring an energy dispersion of about 0.34 and 0.16 nm respectively. HBT experiments have been performed in the visible-UV region above 2.59 eV, selected by the convergent lens at the entrance of the optical path (no additional filter has been employed). Data analysis of phonon contributions and autocorrelation functions has been implemented with Igor.

## 5.7 Phonon coupling and lifetime of defect-related emissions

Luminescence features in c-BN crystals have been observed in the range of 1.5-5 eV. Two emissions with ZPL at 4.94 eV and 3.57 eV are particu-

larly intense and show a similar pronounced phonon coupling. They have been observed both in commercial and pure crystals, although the 4.94 eV emission appears rarely in pure crystals.

**Emission at 3.57 eV**

The emission with ZPL at 3.57 eV (Fig. 5.12.a) clearly shows six strong phonon replicas. The ZPL is not the most intense peak, and the spectral weight of the whole emission is centred around 3 eV. The emission appears spatially localized, with a variable spot size, which should depend on the number and distribution of the emitting centres. In the case shown in Fig. 5.12.b,c, the emission spot is about 500 nm wide. The intensity map (Fig. 5.12.c) has been obtained by integrating the signal in an energy window about 100 meV wide and centred on the most intense peak (3.00 eV). The phonon structure has been fitted with a multi-Gaussian fit, giving an average line separation of 141 $\pm$ 6 meV. By comparison with the calculated phonon density of state [487, 566–568] (in the inset of Fig. 5.12, from ref. [487]), this spacing is attributed to LO phonons. The Huang-Rhys factor $S$ (section 2.6) represents the average number of phonons involved in the emission. The energy $\hbar\omega_{ZPL} - S\hbar\omega_{phon}$, where $\hbar\omega_{ZPL}$ is the energy of the ZPL (3.57 eV) and $\hbar\omega_{phon}$ is the phonon energy (about 140 meV) should indicate the maximum of intensity of the emission band. By comparing the intensities of the Gaussian fits for the ZPL and the fifth replica, we have obtained a Huang-Rhys factor of 4.07. The maximum of intensity hence is expected $\hbar\omega$ =2.99 eV. A similar characterization of this emission has been performed previously by Manfredotti et al. [58]. They have reported a compatible estimates for the phonon energy (141 $\pm$ 3 meV), but a slightly greater Huang-Rhys factor of 5.26. The mismatch is explained by their considering the area under the peaks of the fit instead of the amplitude (and, but less critical, the use of Lorentzian distributions). However, the maximum of intensity would than be expected at 2.82 eV, which is in less good agreement with the experimental curve.

Thanks to the possibility of connecting the microscope with a unique home-made HBT experiments, we have investigated the quantum nature of this emission. Fig. 5.12.d reports a typical intensity autocorrelation function acquired from this kind of luminescence centres. The function shows an evident zero-delay bunching character and the exponential fit (section ) has provided a lifetime estimate of $1.4 \pm 0.1$ ns. The bunching behaviour describes a photon emission characterized by packets of photons, and could still be an indication of single photon emission. Indeed, although antibunching in the irrefutable evidence of a SPE, in the particu-

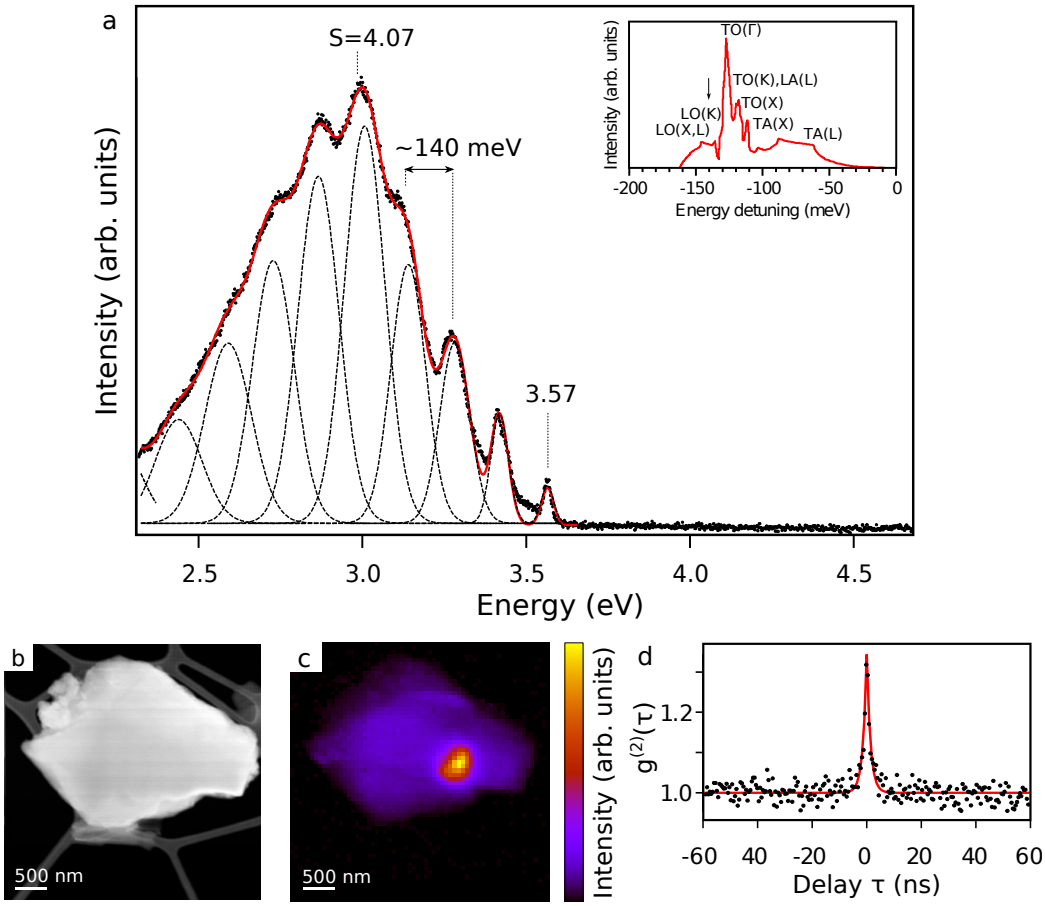


Figure 5.12: *Emission at 3.57 eV, with high phonon coupling (S=4.07), in c-BN commercial crystals. (a) Spectrum with multigaussian fit. In the inset, phonon DOS from ref. [487]. (b) HAADF image and (c) CL intensity map of the emission in (a). (d) Autocorrelation function derived from an HBT experiment.*

lar case of CL bunching can be obtained from a set of SPEs. This behaviour has been recently observed in in diamond and h-BN (the 4.01 eV SPE [10]), and it has been explained as the synchronous photon emission from SPEs: the electron beam excites a plasmon, which decays in several e-h pairs, exciting different luminescence centres at the same time [82]. Hence, the antibunching effect for the 3.57 eV emission in c-BN could possibily be observed in future if an individual centre could be isolated.

**Emission at 4.94 eV**

A similar emission has been identified with ZPL at 4.94 eV (Fig. 5.13.a) and a strong phonon coupling. Given the high energy necessary for its excitation, this emission has previously been reported only once, thanks to

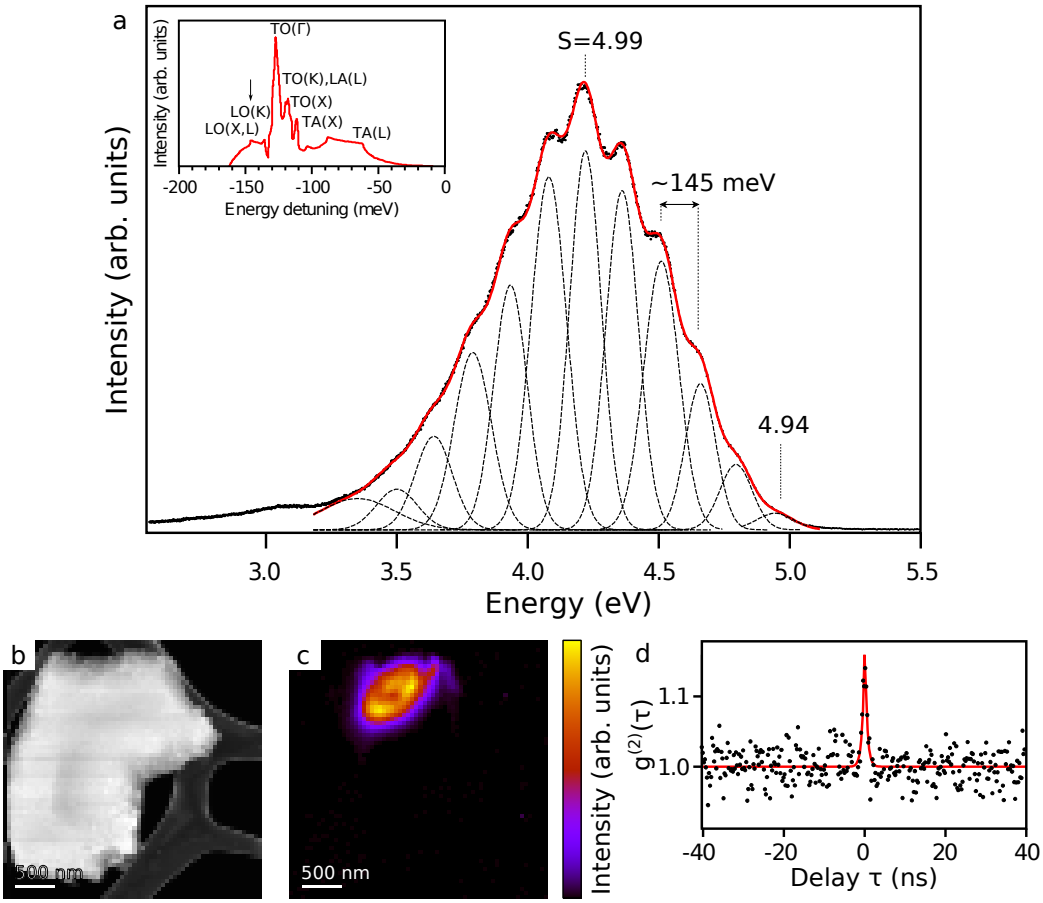


Figure 5.13: *Emission at 4.94 eV, with high phonon coupling (S=4.99), in c-BN commercial crystals. (a) Spectrum with multigaussian fit. In the inset, phonon DOS from ref. [487]. (b) HAADF image and (c) CL intensity map of the emission in (a). (d) Autocorrelation function derived from an HBT experiment.*

the use of a synchrotron light source as the probe. In this thesis, the investigation by STEM-CL has shown spatially localized emission spots. Fig. 5.13.b,c present a microscopy image of a whole c-BN particle and the associated intensity map for the 4.94 eV emission, derived by signal integration in a 100 meV energy window about the most intense peak (4.2 eV). At least three intensity maxima are visible in the map, confirming the dependence of the emission spots size on the spatial distribution of the luminescence centres within c-BN particles. In the spectrum eight phonon replicas are well distinguished. The multi-Gaussian fit of the phonon contributions has provided an average line separation of 145±5 eV, again corresponding to LO phonons (in the inset, the phonon DOS from ref. [487]). The

Huang-Rhys factor calculated from the intensity of the sixth phonon line and ZPL is 4.99. The maximum of intensity of the emission derived from this value is 4.22 eV, in good agreement with the experimental spectrum. HBT experiments have been performed as well, and a typical autocorrelation function is presented in Fig. 5.13.d. From the exponential fit we have obtained an estimated lifetime of $0.55 \pm 0.09$ ns.

**Low-energy emissions**

Fig. 5.14.a provides a summary of all the structured emissions identified during this work. Broad non-structured luminescence bands, probably associated with poorly crystalline regions, have also been observed, but are not discussed here. The emission with ZPL at 3.57 eV has been observed also at a slightly higher energy, 3.62 eV. The phonon energy seems a little higher. This couple of alike emissions probably arise from the same type of defect, and the energy shift is due to a different local environment. Other luminescence peaks have been distinguished below 2.5 eV: two ZPL at 2.31, and 2.17 eV with multiple phonon replicas at about 70 meV, and a ZPL at 1.63 eV (possibly a double peak) with a phonon replica 56 meV apart. All these emissions arise from spatially localized spots, as shown in Fig. 5.14.b-g. The intensity maps have been derived by signal integration within energy windows of about 10 meV and centred at the energy indicated on the map itself. The first two emissions have been observed only in the highly pure c-BN crystals. They might then be more probably related to intrinsic defects. Moreover, they appear in the same energy range as previously reported emissions found in pressure-treated [56] or electron irradiated samples [55, 57]. However, these possible origins shall not be considered for the present case. Even beam-induced damages are little probable (although they cannot be completely excluded), since these experiments have been conducted at only 60 keV, compared to more than 150 keV reported in the literature. The 1.63 eV emission, with its phonon coupling signature, is well compatible with the General Cubic series, attributed to vacancy-impurity complexes [53, 54]. HBT experiments on the luminescence centres reported in this section will be performed in the next future.

The present work provides new insights into the study of c-BN emissions, reporting the first experiments about the spatial distribution and excited state lifetime of the luminescence centres. Although the exact origin of these emissions remains unclear, these results are promising for a better understanding of their nature.

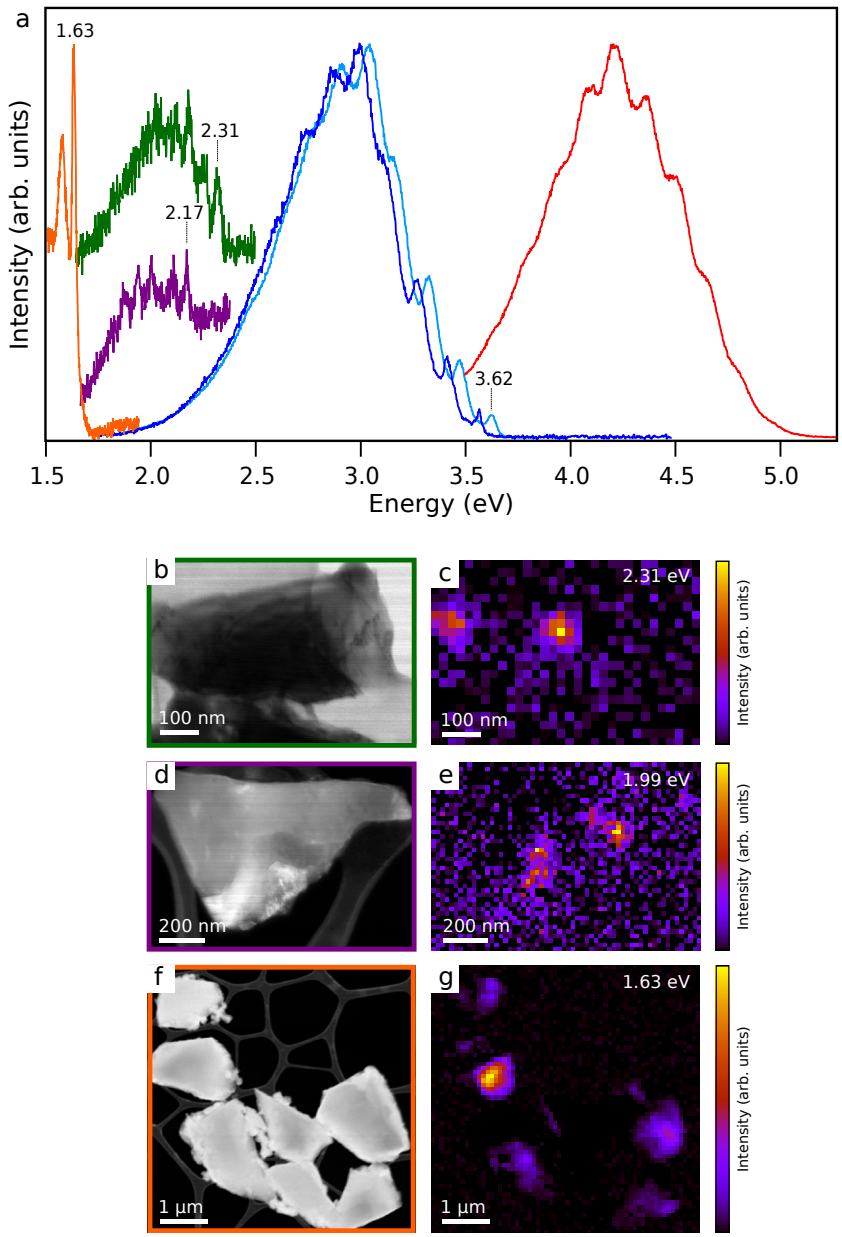


Figure 5.14: *Summary of the c-BN emissions observed during this thesis. The signatures with ZPL at 2.31 eV (green line) and 2.17 eV (violet line) have been observed only in the highly pure crystals.*

## 5.8 Induced phase transition in annealed c-BN crystals

Since the absorption features at 6-8 eV (section 5.4) are probably associated with inclusions of a BN phase of hexagonal symmetry (h-BN, w-BN, r-BN), we have studied thermally treated samples. Indeed, heating at high temperature can be sufficient to overcome the potential barrier for the transition from the metastable c-BN phase to the more stable h-BN phase [569]. c-BN commercial powders have been heated in a oven at 1200 $^{\circ}$C for 36 hours. They have been subsequently crushed in a mortar and dispersed in isopropanol. TEM grids have been prepared as usual by drop casting.

Fig. 5.15 presents some results from an EELS and CL investigation of an annealed c-BN crystal. An EELS hyperspectral image has been acquired in the area marked by the small rectangle in Fig. 5.15.b. Fig. 5.15.c shows typical EELS low-loss spectra: the red spectrum is similar to c-BN spectra acquired on as-synthesized crystals (section 5.4, Fig. 5.8), while the blue spectrum exhibits pronounced features at 6.6 and 8.2 eV. Also the higher energy region appears modified, with a dominant contribution at about 26.0 eV. This signature perfectly corresponds to that of h-BN [558,559]. The map in the inset of the figure represents the intensity of the 8.2 eV peak, obtained by integrated the EELS signal in an energy window about 0.70 eV wide, after ZLP subtraction. The h-BN phase appears localized on the left side of the investigated area. The regions where the two spectra have been extracted are indicated in the map. Fig. 5.15.d-f reports the result from a CL hyperspectral image acquired immediately later, from a wider area of the crystal (Fig. 5.15.b). The typical 3.57 emission is observed, together with new emissions at high energies, between 5.0 and 5.5 eV. These last ones strongly remind h-BN excitonic emissions (section 4.7), although their energies are slightly lower: this could be related to a rhombohedral crystal phase (and indeed h-BN excitonic peaks are affected by stacking order faults [9]) or confinement effects. The intensity maps of the typical c-BN emission and of the additional emission at 5.30 eV (blue spectrum) are shown in Fig. 5.15.e,f. They are both spatially localized, the 5.30 eV emission displaying smaller spots (about 50 nm). More interestingly, the small emission spot in the top left corner, indicated by the arrow, seems correlated with the 8.2 eV intensity map. To safely establish such correlation, EELS and CL hyperspectra should be acquired simultaneously. However, these first results suggest that the EELS and CL additional signatures

arise from the same system. Hence, this constitutes a strong evidence supporting the interpretation of the 6 eV shallow peaks in c-BN low-loss spectrum to h-BN extended defects. The absorption/emission features that in the optical measurements reported in the literature have been attributed to the band-gap edge around 6 eV, are then most probably defect-related signatures, whithin the much wider c-BN band-gap.

## 5.9 Perspectives

In this chapter we have provided an experimental value for the optical band-gap of c-BN of almost 10.0 eV, much higher than the previous experimental investigations and in better agreement with the predicted theoretical value from BSE simulation [46]. Several phonon-assisted emissions have been observed, some of which not yet reported in the literature. Their spatial distribution and excited state lifetime have been studied for the first time.

More insights into the EELS low-loss study of the optical properties of c-BN could be provided by a higher spectral resolution, guaranteed by a monochromatic electron probe. The CHROMATEM microscope, for example, will be able to acquire EELS spectra with $\sim$10 meV resolution, with the additional advantage of lower temperatures (liquid He). CL+EELS experiments could be useful to correlate emission and absorption properties, for example in the case of the hexagonal phase inclusions discussed in this thesis. Moreover, the higher spatial resolution of an aberration corrected microscope could allow a structural study of the luminescence centres, although it may be difficult to obtain thin enough regions at the borders of c-BN particles.

The HBT experiments have provided promising results toward the identification of SPEs in c-BN. Indeed the bunching effect observed is compatible with a set of SPEs. Additional experiments might be successful in isolating a single SPE. Moreover, the other CL emissions at lower energies should be tested as well.

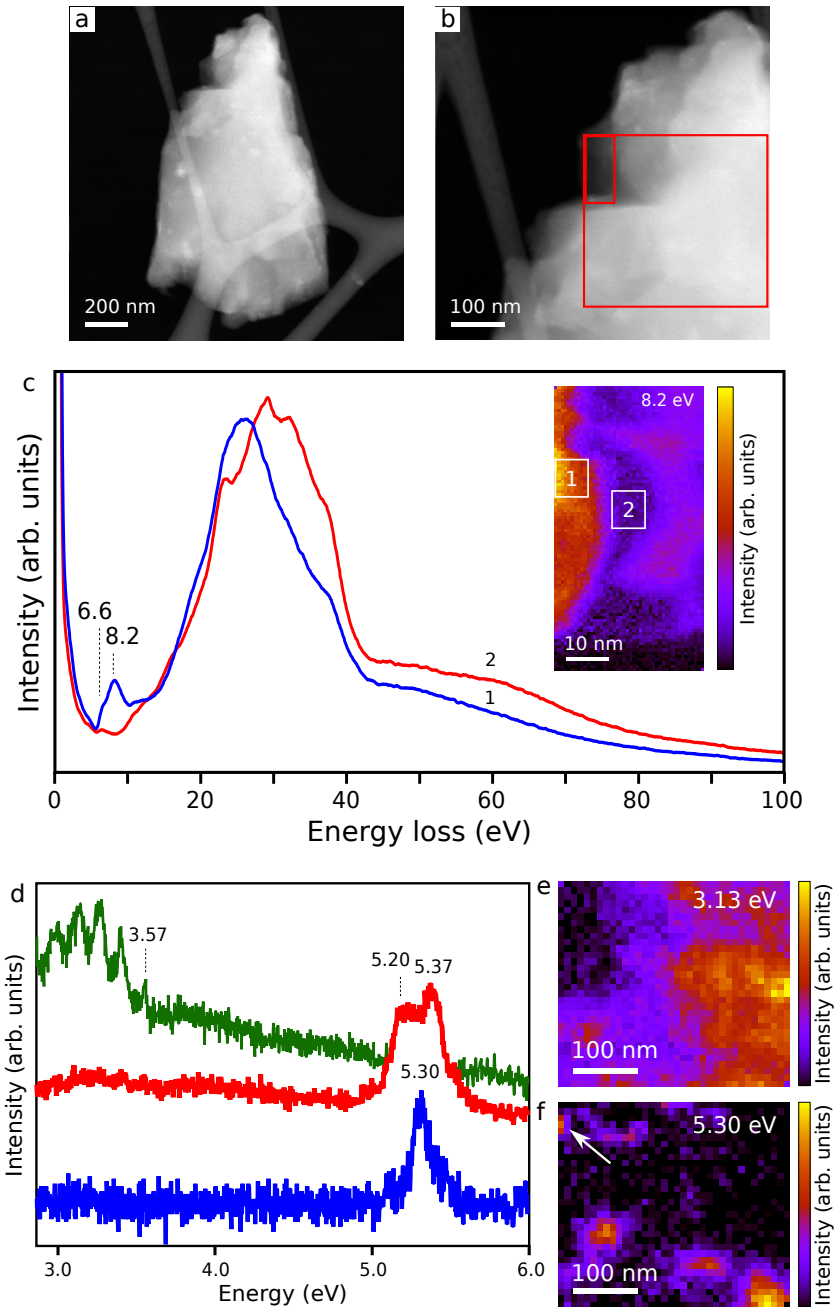


Figure 5.15: *Thermally treated c-BN crystals. (a,b) HAADF images, where the regions investigated by hyperspectral imaging are indicated by the red rectangles. (c) Results from hyperspectral imaging: two spectra extracted from areas indicated by the white square in the intensity map. The map colour scale represents the intensity of the 8.2 eV feature. (d) Few CL spectra and (e-f) associated intensity maps.*

CHAPTER 6

# CONCLUSIONS AND PERSPECTIVES

During this thesis, I have given new insights into the understanding of the properties of fragile materials by means of EELS and CL spectroscopy in the STEM microscope. The development of specific acquisition strategies adapted to the particular archetypical nanosystems studied, has allowed to perform unprecedented experiments. The remarkable results obtained overcome previously reported characterizations, and open new perspectives in the understanding of the investigated materials, the elaboration of technical advances in STEM spectroscopy and the use of STEM spectroscopy in new fields of research.

The spatial resolution of EELS investigation of GO and RGO has been considerably improved by the use of low temperatures and a highly efficient detection system. Temperatures below -100 °C are known to reduce the mass loss damage during EELS: atoms are less mobile and even after chemical bond breakage (radiolysis) diffuse little. This effect is important for core-EELS stoichiometry quantification. The high efficiency of the EELS CCD camera has been fundamental to acquire distinguishable core-loss signals even at the low electron doses imposed by the specimen fragility. The maximal admitted electron dose has been carefully experimentally evaluated on the basis of stoichiometric and structural modifications of the specimen under continuous illumination, through the analysis of the atomic ratio and fine structure peaks. The ultimate spatial resolution of the EELS measurements has been determined by combining the defined electron dose with the requirements on EELS spectra signal intensity, resulting in a lower limit of 3 nm. The noise in quantification maps has been reduced by PCA analysis of the hyperspectral images, while the S/N ratio in fine structure analysis has been improved only by spatial integration.

These experimental conditions have allowed to derive spatially resolved maps of the atomic oxygen content in GO, at the unprecedented resolution of 3 nm (only averaged values have been reported before). The

oxygen content in GO has been observed to vary within the wide range of 10-50 at.%. Moreover, fine structures (ELNES) at the carbon K-edge have been correlated with the amount of oxygen and unreported features have been observed at the highly oxidized regions. These findings have suggested that GO's structure, usually described in terms of a random distribution of epoxide and hydroxyls oxygen groups, should contain regions with a predominance of hydroxyls, up to a limit configuration of full functionalization with hydroxyls, corresponding to 50 oxygen at.%. This model has been supported by DFT-based calculations of the formation energy of hydroxyls and epoxides in oxidative and reducing atmosphere, and the binding energy between two hydroxyls. The interpretation of the fine structure peaks on the basis of this model is compatible with the literature from spectroscopy of molecules. The analysis of RGO has confirmed the reduction of the oxygen content, which is lowered to a few atomic percent. Its ELNES at the carbon K-edge show a good restoration of the graphitic atomic planar symmetry (almost lost in GO) and residual C-O fine structure peaks, which are consistent with those found in GO. These results may be helpful in the understanding of graphene oxide's properties and its interaction with other nanosystems, in sight of functionalization and other applications. The confirmation of the suggested model by means of other experimental techniques based on strongly localized probes is of course desirable. Nano-infrared could represent a suitable technique. From the theoretical point of view, considerable help in the interpretation of the spectroscopic signatures might be provided by core loss spectra simulations taking into account excitonic effects.

The CL investigation of individual molecules has required a different strategy, aimed at avoiding their direct illumination with the electron beam. For this purpose, a suitable substrate was chosen to act as a mediator of the excitation, by absorbing the beam-electrons energy and transferring it to a molecule placed at a certain distance. Exfoliated flakes of h-BN, which is characterized by intense CL emission, chemical stability, wide energy gap, and excitation diffusion, have been used as a substrate for molecule deposition from a solution. In addition, in order to further reduce the illumination effects in the microscope, an innovative random walk scanning routine has been tested, in juxtaposition with the traditional sequential scan. During the random scan acquisition, the distance between two consecutive illumination spots (pixels) is relatively large, and this reduces the accumulation on the specimen of energy deposited by the beam. Its use has eliminated the occurrence of luminescence along a sin-

gle line of the scan, deriving from increasing excitation and dragging of the luminescence source, up to its destruction.

The h-BN-molecules system has revealed a substantial series of localized emissions. They do not correspond to h-BN intrinsic luminescence nor to the emission from molecular crystals, and their intensity is often stronger than h-BN intrinsic luminescence, indicating that the coupling with the substrate and e-h recombination are efficient. The emission spots width of about 100-200 nm demonstrates that molecules excitation does occur at a certain distance from the beam position. The detection of very sharp emission peaks strongly suggests that these emissions are related to molecules. Luminescence from very few molecules down to one individual molecule has most probably been observed. This is a remarkable result, especially considering that this kind of experiments have never been attempted before and were probably not expected to be possible. The interpretation of these CL features is however not straightforward and many questions remain open about the excitation transfer mechanism and the exact molecular electronic levels involved in the radiative emission. Further developments of the experiments presented in this thesis could be achieved by combining CL with high resolution microscopy. This will be possible in the forthcoming CHROMATEM microscope (installation 2017), where also highly resolved EELS (both in space and energy) could be performed after CL investigation, at low electron doses on the 4 K cooled sample.

These experiments open interesting perspectives in single molecules spectroscopy and more in general spectroscopy of fragile materials. Indeed, CL of individual molecules deposited on a surface had not been performed before in a STEM. STEM-CL presents several attractive properties with respect to the techniques normally used in this field of research. The random walk scan, elaborated only a few months ago and tested here for the first time, appears as a powerful tool for the study of sensitive materials.

In the last part of this thesis we have investigated the optical properties of c-BN. The characterization of the most pure crystals now available by EELS spectroscopy in the low-loss region has indicated an optical gap of about 10 eV, which is considerably higher than previous experimental estimates (6.4 eV) and much closer to the theoretical value of 11.4 eV provided by BSE simulations. Such a high experimental value could not be accessed by means of optical absorption or emission, and the often observed features around 6 eV should be attributed to defect levels within the band-

gap, possibly related to h-BN phases. Indeed, a thermal treatment of the highly pure c-BN crystals has revealed additional h-BN-like features in the 6-8 eV range, which are correlated with a CL emission similar to h-BN excitonic peaks at almost 6 eV. The CL investigation of pure and commercial crystals has revealed several emissions associated with defects and impurities, some of them displaying a strong phonon coupling. Few of these emissions had not been reported in literature. The identification of their origin is difficult, but it is probably related to vacancies and carbon and oxygen impurities, as usually ascribed in the literature. No antibunching behaviour has been observed during our HBT experiments on the higher energy emissions. Nevertheless, the two-levels nature of the luminescence source has been demonstrated by the appearance of a bunching effect, from which an estimate of the excited state lifetime has been derived. The antibunching dip has not been detected probably because a single emitter could not be isolated during these experiments.

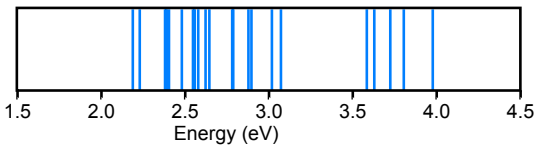


Figure 6.1: *Summary of CL emissions observed in h-BN treated with NaOH.*

In the next future, further developments might be expected from some other studies which have been touched during this thesis. Chemical modification of h-BN has been attempted with concentrated $NaOH$, by dispersing h-BN flakes in a 1 M solution. Although h-BN is chemically inert, remarkable structural changes have been induced: h-BN flakes have revealed unusually round borders and many sharp and intense additional CL emissions (summarized in Fig. 6.1). These ones appear highly spatially localized (about 100 nm) and shall be associated with point structural defects and possibly -OH functionalization. The strong CL of h-BN has driven attention to other layered materials. Transition metal dichalcogenides exhibit an intense PL, especially from monolayers. STEM-CL experiments on $MoS_2$ thin flakes and $WS_2$ nanotubes have been extensively performed during this thesis, and are not presented here. Only very weak emissions have been detected, in contrast with PL investigations. This discrepancy represents a persisted unanswered question. One hypothesis is that the formation of beam-induced defects in these fragile materials quenches the CL emission. STEM-CL measurements with the new random scan acquisition mode might be attempted. The sole intense luminescence has been obtained in $MoS_2$ doped with Nb. In this case, unexpected emission features have been observed: in very thick regions a series of intense and sharp

emissions have been identified in the 1.7-3.2 eV range. Fig. 6.2 shows a CL hyperspectral investigation of a $MoS_2$:Nb flake. The intensity map of these luminescence peaks shows a wave-like pattern, with visible interference effects associated with the lower energy features. This behaviour might be related with a strong modification of the optoelectrical properties of $MoS_2$ by the introduction of Nb impurities, strongly affecting the charge density, and the generation of waveguide plasmon modes.

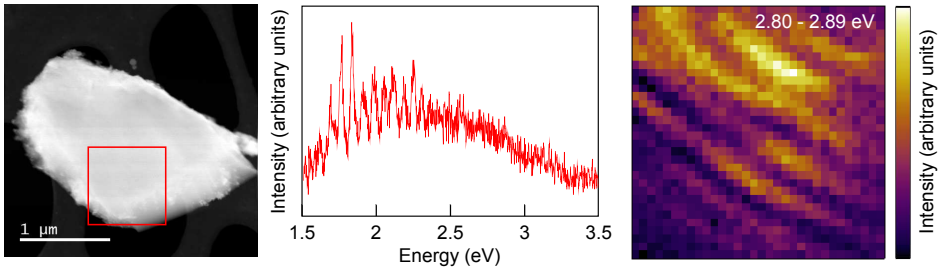


Figure 6.2: *CL investigation of* $MoS_2$*:*Nb*: HAADF image of a particle, typical CL spectrum and CL intensity maps from the region in the red square, calculated in the 2.8-2.89 eV range.*

CHAPTER 7

# EN RÉSUMÉ

La spectroscopie de perte d'énergie des électrons (EELS) et la cathodoluminescence (CL) réalisées dans un microscope électronique en transmission à balayage (STEM) sont des techniques remarquablement puissantes pour l'étude de nanostructures isolées. Cependant, des électrons rapides peuvent endommager fortement des échantillons minces et fragiles, ce qui limite la résolution spatiale et l'intensité des signaux spectroscopiques. Pendant cette thèse, nous avons dépassé cette restriction par le développement de protocoles d'acquisition spécifiques pour l'étude de certains archétypes de nanosystèmes fragiles.

**La caractérisation chimique du GO**

Dans la première partie de cette thèse, j'ai caractérisé des flocons minces de graphène oxydé (GO) et GO réduit (RGO) par spectroscopie EELS dans le STEM. La structure atomique du (R)GO n'est pas encore connue avec certitude et elle se trouve au centre d'un vif débat scientifique. Les obstacles empêchant une étude définitive du GO sont le manque de techniques analytiques adaptées (spectroscopie résolue spatialement à l'échelle atomique) et la sensibilité du matériau à l'illumination par une sonde énergétique et localisée. Dans ce travail de thèse, l'utilisation de basses températures au niveau de l'échantillon et d'une caméra CCD très sensible pour la spectroscopie EELS (toutes les deux spécifiques de notre microscope) ont permis d'obtenir des spectres EELS du GO dans la région des perte profondes d'une qualité inédite. Par l'étude rigoureuse de l'évolution du matériau pendant l'illumination, j'ai défini la dose d'électrons maximale et donc les conditions optimales d'illumination pour l'analyse du GO, avant l'apparition de modifications structurales. Nous avons ainsi obtenu des cartes chimiques du contenu d'oxygène dans le (R)GO à une résolution spatiale de 3 nm, qui n'avait jamais été achevée auparavant dans le cas de ces matériaux. Dans les cartes chimiques nous avons observé un contenu d'oxygène qui varie localement entre environ 10 et 50 % d'oxygène atomique. Il s'agit d'un résultat intéressant car avant seulement une valeur moyennée dans l'espace était connue, comprise en-

tre 20 et 30 % d'oxygène atomique. L'analyse des pics EELS de structure fine au seuil d'absorption du carbone a révélé des signatures spectroscopiques jamais rapportées dans la littérature, qui apparaissent corrélées au taux d'oxygène. Ces importants résultats ouvrent une nouvelle fenêtre sur la complexité de la structure atomique du GO et ils nous ont permis de réviser les modèles atomiques du GO proposés auparavant dans la littérature.

**La luminescence de molécules individuelles**

Je me suis ensuite intéressée à la luminescence de molécules individuelles. Ces nanosystèmes constituent une autre classe de nanomatériaux fortement sensibles à l'irradiation, ainsi que à l'environnement chimique et physique les entourant. La réponse optique des molécules isolées a été étudiée par différentes techniques de spectroscopie de champ proche, alors que l'utilisation de la CL a apparu dès le début extrêmement difficile et impraticable, à cause des dommages d'illumination observés déjà à l'échelle de cristaux moléculaires dans des microscopes électroniques en balayage (SEM). Même si les dommages d'illumination peuvent être encore plus importants dans un microscope STEM, la technique de STEM-CL présente nombreux aspects intéressants : la résolution spatiale est beaucoup plus petite que la longueur d'onde de l'émission CL ; on peut facilement passer d'un fort à un faible agrandissement, donnant accès à un large champ de vision sur l'échantillon ; l'acquisition est rapide, l'excitation du matériaux dispose d'un large intervalle d'énergie et plusieurs signaux peuvent être acquis au même temps (image, signal CL et EELS). Dans ce travail de thèse, les dommages d'illumination ont été limités grâce à un choix avisé du substrat. Le mécanisme de CL se compose de l'excitation d'électrons à travers la bande interdite d'énergie, la thermalisation et diffusion des porteurs de charge et finalement leur recombinaison radiative dans un site favorable tel que un défaut cristallin. La stratégie mise en place dans cette thèse envisage la création de pairs électron-trou dans un substrat et leur recombinaison au site d'une molécules déposée à la surface de celui-ci, à quelques dizaines de nanomètres du site d'illumination. De cette façon, si le transfère de l'excitation est efficace entre substrat et molécule, on peut détecter l'émission par une molécule sans l'illuminer directement avec le faisceau d'électron rapides. Comme substrat nous avons choisi des flocons de nitrure de bore hexagonal (h-BN) pour ses propriétés structurales et électroniques : il est un matériau bidimensionnel et chimiquement inerte, avec une large bande interdite d'énergie. Nos expériences de STEM-CL sur des molécules déposées en régime de forte dilution

sur du h-BN ont révélé de nouveaux pics d'émission, différents des émissions typiques du h-BN et aussi des cristaux moléculaires, spatialement localisées à l'échelle de 100-200 nm. En plus, l'utilisation d'une innovante routine d'acquisition par balayage aléatoire du faisceau électronique nous a permis d'éliminer des effets d'illumination résiduels attribués au traditionnel balayage séquentiel. Même si les expériences de CL ne nous donnent pas directement accès aux mécanismes de transfère de l'excitation du substrat aux molécules et de recombinaison radiative, nous avons proposé quelques hypothèses basées sur la littérature.

**Propriétés optiques du nitrure de bore cubique**

L'efficacité de la technique de STEM-CL pour l'étude des défauts ponctuels luminescents dans le h-BN a inspiré l'étude de la forme allotropique du BN de phase cubique (nitrure de bore cubique, c-BN). Ce matériau a été peu caractérisé auparavant à cause des difficultés rencontrées dans la synthèse des cristaux, qui typiquement contiennent nombreux défauts et impuretés. Les questions ouvertes autour du c-BN concernent la largeur de sa bande interdite d'énergie et l'origine et caractérisation des pics de luminescence. Le premier sujet voit la contradiction entre la valeur d'environ 6 eV dérivée expérimentalement par CL et celle de 11 eV prédite par les calculs théoriques les plus récents. En attribuant ce décalage à la présence de défauts à l'intérieur de la bande interdite et à l'impossibilité de détecter des émissions CL au-delà d'environ 6 eV, nous avons analysé des cristaux de c-BN très purs par EELS, car cette technique donne accès à de plus hautes énergies. J'ai ainsi identifié une largeur de la bande interdite d'énergie plus proche des calculs, correspondante à environ 10 eV. Dans l'étude des émissions CL associées à des défauts, j'ai ensuite analysé pour la première fois la distribution spatiale des pics d'émission. Les cartes d'intensité de STEM-CL montrent des émissions spatialement localisées, de la taille de 100 nm ou plus, selon la concentration des défauts. En plus, grâce à la possibilité de connecter notre microscope STEM avec un interféromètre en intensité de Hanbury-Brown et Twiss (HBT), ce qui constitue à présent un équipement expérimental unique au monde, j'ai réalisé les premières expériences d'optique quantique sur des défaut luminescents dans le c-BN. Les résultats obtenus sont compatibles avec la présence d'émetteurs uniques, même s'ils ne suffisent pas à le démontrer de façon irréfutable, et ils ont permis de calculer le temps de vie de l'état excité associé aux émissions.

Le développement de stratégies d'acquisition adaptées aux particuliers systèmes physiques étudiés et au type d'information recherchée s'est donc avéré très efficace et il a conduit à d'importants avancements dans la connaissance du GO et à un remarquable progrès du point de vue technique dans la détection de la luminescence de molécules individuelles. En particulier, la routine de balayage aléatoire, qui a été testée pour la première fois au cours de cette thèse, fait entrevoir d'intéressantes perspectives dans le cadre plus générale de l'étude de matériaux sensibles à l'illumination par des électrons rapides. Aussi, les résultats obtenus quant à la réponse optique du c-BN, bien qu'en étant encore préliminaires, représentent des caractérisations expérimentales inédites, donnant accès à de nouvelles informations sur la largeur de la bande interdite et la nature des défauts luminescents.

# BIBLIOGRAPHY


[1] C. Jeanguillaume and C. Colliex, *Spectrum-image: The next step in EELS digital acquisition and processing*, Ultramicroscopy **28**, 252 (1989).

[2] C. Colliex, N. Brun, A. Gloter, D. Imhoff, M. Kociak, K. March, C. Mory, O. Stephan, M. Tencé, and M. Walls, *Multi-dimensional and multi-signal approaches in scanning transmission electron microscopes*, Philosophical Transactions of the Royal Society A: Mathematical, Physical and Engineering Sciences **367**, 3845 (2009).

[3] C. Colliex, A. Gloter, K. March, C. Mory, O. Stéphan, K. Suenaga, and M. Tencé, *Capturing the signature of single atoms with the tiny probe of a STEM*, Ultramicroscopy **123**, 80 (2012).

[4] C. Colliex, M. Kociak, and O. Stéphan, *Electron Energy Loss Spectroscopy imaging of surface plasmons at the nanometer scale*, Ultramicroscopy **162**, A1 (2016).

[5] M. Kociak, O. Stéphan, A. Gloter, L. F. Zagonel, L. H. Tizei, M. Tencé, K. March, J. D. Blazit, Z. Mahfoud, A. Losquin, S. Meuret, and C. Colliex, *Seeing and measuring in colours: Electron microscopy and spectroscopies applied to nano-optics*, Comptes Rendus Physique **15**, 158 (2014).

[6] M. M. v. Schooneveld, A. Gloter, O. Stephan, L. F. Zagonel, R. Koole, A. Meijerink, W. J. M. Mulder, and F. M. F. d. Groot, *Imaging and quantifying the morphology of an organic-inorganic nanoparticle at the sub-nanometre level*, Nat. Nanotechnol. **5**, 538 (2010).

[7] L. F. Zagonel, S. Mazzucco, M. Tencé, K. March, R. Bernard, B. Laslier, G. Jacopin, M. Tchernycheva, L. Rigutti, F. H. Julien, R. Songmuang, and M. Kociak, *Nanometer Scale Spectral Imaging of Quantum Emitters in Nanowires and Its Correlation to Their Atomically Resolved Structure*, Nano Letters **11**, 568 (2011).

[8] L. H. G. Tizei and M. Kociak, *Spatially Resolved Quantum Nano-Optics of Single Photons Using an Electron Microscope*, Physical Review Letters **110** (2013).

[9] R. Bourrellier, M. Amato, L. H. Galvão Tizei, C. Giorgetti, A. Gloter, M. I. Heggie, K. March, O. Stéphan, L. Reining, M. Kociak, and A. Zobelli, *Nanometric Resolved Luminescence in h-BN Flakes: Excitons and Stacking Order*, ACS Photonics **1**, 857 (2014).

[10] R. Bourrellier, S. Meuret, A. Tararan, O. Stéphan, M. Kociak, L. H. G. Tizei, and A. Zobelli, *Bright UV Single Photon Emission at Point Defects in h -BN*, Nano Letters **16**, 4317 (2016).

[11] B. C. Brodie, *On the Atomic Weight of Graphite*, Philosophical Transactions of the Royal Society of London **149**, 249 (1859).

[12] L. Staudenmaier, *Verfahren zur Darstellung der Graphitsäure*, Berichte der deutschen chemischen Gesellschaft **31**, 1481 (1898).

[13] W. S. Hummers and R. E. Offeman, *Preparation of Graphitic Oxide*, J. Am. Chem. Soc. **80**, 1339 (1958).

[14] D. R. Dreyer, S. Park, C. W. Bielawski, and R. S. Ruoff, *The chemistry of graphene oxide*, Chem. Soc. Rev. **39**, 228 (2010).

[15] S. Pei and H.-M. Cheng, *The reduction of graphene oxide*, Carbon **50**, 3210 (2012).

[16] G. Eda and M. Chhowalla, *Chemically Derived Graphene Oxide: Towards Large-Area Thin-Film Electronics and Optoelectronics*, Advanced Materials **22**, 2392 (2010).

[17] K. P. Loh, Q. Bao, G. Eda, and M. Chhowalla, *Graphene oxide as a chemically tunable platform for optical applications*, Nat Chem **2**, 1015 (2010).

[18] S. Mao, H. Pu, and J. Chen, *Graphene oxide and its reduction: modeling and experimental progress*, RSC Advances **2**, 2643 (2012).

[19] A. Lerf, H. He, M. Forster, and J. Klinowski, *Structure of Graphite Oxide Revisited*, J. Phys. Chem. B **102**, 4477 (1998).

[20] S. Kim, S. Zhou, Y. Hu, M. Acik, Y. J. Chabal, C. Berger, W. de Heer, A. Bongiorno, and E. Riedo, *Room-temperature metastability of multilayer graphene oxide films*, Nat Mater **11**, 544 (2012).

[21] S. Zhou and A. Bongiorno, *Origin of the Chemical and Kinetic Stability of Graphene Oxide*, Scientific Reports **3** (2013).

[22] S. Eigler, C. Dotzer, A. Hirsch, M. Enzelberger, and P. Müller, *Formation and Decomposition of $CO_2$ Intercalated Graphene Oxide*, Chemistry of Materials **24**, 1276 (2012).

[23] A. M. Dimiev, L. B. Alemany, and J. M. Tour, *Graphene Oxide. Origin of Acidity, Its Instability in Water, and a New Dynamic Structural Model*, ACS Nano **7**, 576 (2013).

[24] N. R. Wilson, P. A. Pandey, R. Beanland, R. J. Young, I. A. Kinloch, L. Gong, Z. Liu, K. Suenaga, J. P. Rourke, S. J. York, and J. Sloan, *Graphene Oxide: Structural Analysis and Application as a Highly Transparent Support for Electron Microscopy*, ACS Nano **3**, 2547 (2009).

[25] K. Erickson, R. Erni, Z. Lee, N. Alem, W. Gannett, and A. Zettl, *Determination of the Local Chemical Structure of Graphene Oxide and Reduced Graphene Oxide*, Advanced Materials **22**, 4467 (2010).

[26] C. Gómez-Navarro, J. C. Meyer, R. S. Sundaram, A. Chuvilin, S. Kurasch, M. Burghard, K. Kern, and U. Kaiser, *Atomic Structure of Reduced Graphene Oxide*, Nano Lett. **10**, 1144 (2010).

[27] D. Pacilé, J. Meyer, A. Fraile Rodríguez, M. Papagno, C. Gómez-Navarro, R. Sundaram, M. Burghard, K. Kern, C. Carbone, and U. Kaiser, *Electronic properties and atomic structure of graphene oxide membranes*, Carbon **49**, 966 (2011).

[28] R. F. Egerton, *Electron energy-loss spectroscopy in the electron microscope*, Springer, New York, third edition edition, 2011.

[29] K. A. Mkhoyan, A. W. Contryman, J. Silcox, D. A. Stewart, G. Eda, C. Mattevi, S. Miller, and M. Chhowalla, *Atomic and Electronic Structure of Graphene-Oxide*, Nano Lett. **9**, 1058 (2009).

[30] D. D'Angelo, C. Bongiorno, M. Amato, I. Deretzis, A. La Magna, G. Compagnini, S. F. Spanò, and S. Scalese, *Electron energy-loss spectra of graphene oxide for the determination of oxygen functionalities*, Carbon **93**, 1034 (2015).

[31] R. Egerton, *Control of radiation damage in the TEM*, Ultramicroscopy **127**, 100 (2013).

[32] K. Watanabe, T. Taniguchi, and H. Kanda, *Direct-bandgap properties and evidence for ultraviolet lasing of hexagonal boron nitride single crystal*, Nature Materials **3**, 404 (2004).

[33] W. E. Moerner and L. Kador, *Optical detection and spectroscopy of single molecules in a solid*, Physical Review Letters **62**, 2535 (1989).

[34] M. Orrit and J. Bernard, *Single pentacene molecules detected by fluorescence excitation in a p-terphenyl crystal*, Physical Review Letters **65**, 2716 (1990).

[35] E. Brooks Shera, N. K. Seitzinger, L. M. Davis, R. A. Keller, and S. A. Soper, *Detection of single fluorescent molecules*, Chemical Physics Letters **174**, 553 (1990).

[36] R. Herbst and D. Hoder, *Cathodoluminescence in biological studies*, Scanning **1**, 35 (1978).

[37] J. Niitsuma, H. Oikawa, E. Kimura, Ushiki, and T. Sekiguchi, *Cathodoluminescence investigation of organic materials*, Journal of Electron Microscopy **54**, 325 (2005).

[38] R. H. J. Wentorf, *Cubic Form of Boron Nitride*, The Journal of Chemical Physics **26**, 956 (1957).

[39] R. H. W. Jr, *Preparation of Semiconducting Cubic Boron Nitride*, The Journal of Chemical Physics **36**, 1990 (1962).

[40] T. Taniguchi, *Comprehensive hard materials*, Elsevier, Amsterdam, 2014.

[41] T. Taniguchi and S. Yamaoka, *Spontaneous nucleation of cubic boron nitride single crystal by temperature gradient method under high pressure*, Journal of Crystal Growth **222**, 549 (2001).

[42] T. Taniguchi and K. Watanabe, *Synthesis of high-purity boron nitride single crystals under high pressure by using Ba–BN solvent*, J. Cryst. Growth **303**, 525 (2007).

[43] K. Watanabe, T. Taniguchi, and H. Kanda, *Ultraviolet luminescence spectra of boron nitride single crystals grown under high pressure and high temperature*, physica status solidi (a) **201**, 2561 (2004).

[44] R. M. Chrenko, *Ultraviolet and infrared spectra of cubic boron nitride*, Solid State Communications **14**, 511 (1974).

[45] O. Mishima and K. Era, *Electric refractory materials*, Marcel Dekker, New York, 2000.

[46] G. Satta, G. Cappellini, V. Olevano, and L. Reining, *Many-body effects in the electronic spectra of cubic boron nitride*, Physical Review B **70** (2004).

[47] A. Zunger, A. Katzir, and A. Halperin, *Optical properties of hexagonal boron nitride*, Physical Review B **13**, 5560 (1976).

[48] C. A. Taylor, S. W. Brown, V. Subramaniam, S. Kidner, S. C. Rand, and R. Clarke, *Observation of near-band-gap luminescence from boron nitride films*, Applied Physics Letters **65**, 1251 (1994).

[49] L. Wirtz, A. Marini, M. Gruning, and A. Rubio, *Excitonic effects in optical absorption and electron-energy loss spectra of hexagonal boron nitride*, arXiv:cond-mat/0508421 (2005).

[50] B. Arnaud, S. Lebègue, P. Rabiller, and M. Alouani, *Huge Excitonic Effects in Layered Hexagonal Boron Nitride*, Physical Review Letters **96** (2006).

[51] K. Watanabe and T. Taniguchi, *Jahn-Teller effect on exciton states in hexagonal boron nitride single crystal*, Phys. Rev. B **79**, 193104 (2009).

[52] G. Cassabois, P. Valvin, and B. Gil, *Hexagonal boron nitride is an indirect bandgap semiconductor*, Nature Photonics **10**, 262 (2016).

[53] V. D. Tkachev, V. B. Shepilo, and A. M. Zaitsev, *Cathodoluminescence of Cubic Boron Nitride - Mössbauer-Type Spectra*, phys. stat. sol. (b) **127**, K65 (1985).

[54] B. V. Shipilo, A. M. Zaitsev, E. M. Shishonok, and A. A. Mel'nikov, *Effect of annealing on cathodoluminescence of cubic boron nitride*, J Appl Spectrosc **45**, 1060 (1986).

[55] A. M. Zaitsev, V. B. Shipilo, E. M. Shishonok, and A. A. Melnikov, *Cathodoluminescence of annealed cubic boron nitride*, phys. stat. sol. (a) **95**, K29 (1986).

[56] V. B. Shipilo, E. M. Shishonok, A. I. Olekhnovich, A. M. Zaitsev, and A. A. Melnikov, *Influence of high pressure on cathodoluminescence of cubic boron nitride*, phys. stat. sol. (a) **108**, 431 (1988).

[57] E. M. Shishonok and J. W. Steeds, *Near-threshold creation of optical centres in electron irradiated cubic boron nitride*, Diamond and Related Materials **11**, 1774 (2002).

[58] C. Manfredotti, R. Cossio, A. L. Giudice, E. Vittone, and F. Fizzotti, *Vibronic spectrum of c -BN measured with cathodoluminescence*, Physical Review B **74** (2006).

[59] W. Orellana and H. Chacham, *Atomic geometry and energetics of vacancies and antisites in cubic boron nitride*, Applied Physics Letters **74**, 2984 (1999).

[60] P. Piquini, R. Mota, T. M. Schmidt, and A. Fazzio, *Theoretical studies of native defects in cubic boron nitride*, Physical Review B **56**, 3556 (1997).

[61] J. L. P. Castineira, J. R. Leite, L. M. R. Scolfaro, R. Enderlein, J. L. A. Alves, and H. W. Leite Alves, *First principles studies of point defects and impurities in cubic boron nitride*, Materials Science and Engineering: B **51**, 53 (1998).

[62] W. Orellana and H. Chacham, *Energetics of carbon and oxygen impurities and their interaction with vacancies in cubic boron nitride*, Phys. Rev. B **62**, 10135 (2000).

[63] W. Orellana and H. Chacham, *Stability of native defects in hexagonal and cubic boron nitride*, Physical Review B **63** (2001).

[64] N. M. C. Pinho, V. J. B. Torres, R. Jones, P. R. Briddon, and S. Öberg, *Mg-H and Be-H complexes in cubic boron nitride*, J. Phys.: Condens. Matter **13**, 8951 (2001).

[65] A. Katzir, J. T. Suss, A. Zunger, and A. Halperin, *Point defects in hexagonal boron nitride. I. EPR, thermoluminescence, and thermally-stimulated-current measurements*, Phys. Rev. B **11**, 2370 (1975).

[66] V. Lopatin and F. Konusov, *Energetic states in the boron nitride band gap*, Journal of Physics and Chemistry of Solids **53**, 847 (1992).

[67] V. Korsaks, B. Berzina, and L. Trinklere, *Influence of Air, Oxygen, Nitrogen and Argon on 400 nm Luminescence in Hexagonal Boron Nitride*, Latvian Journal of Physics and Technical Sciences **49** (2012).

[68] K. Era, F. Minami, and T. Kuzuba, *Fast luminescence from carbon-related defects of hexagonal boron nitride*, Journal of Luminescence **24–25, Part 1**, 71 (1981).

[69] T. T. Tran, C. Zachreson, A. M. Berhane, K. Bray, R. G. Sandstrom, L. H. Li, T. Taniguchi, K. Watanabe, I. Aharonovich, and M. Toth, *Quantum Emission from Defects in Single-Crystalline Hexagonal Boron Nitride*, Physical Review Applied **5** (2016).

[70] T. T. Tran, K. Bray, M. J. Ford, M. Toth, and I. Aharonovich, *Quantum emission from hexagonal boron nitride monolayers*, Nature Nanotechnology **11**, 37 (2015).

[71] T. T. Tran, C. Elbadawi, D. Totonjian, C. J. Lobo, G. Grosso, H. Moon, D. R. Englund, M. J. Ford, I. Aharonovich, and M. Toth, *Robust Multicolor Single Photon Emission from Point Defects in Hexagonal Boron Nitride*, ACS Nano **10**, 7331 (2016).

[72] L. J. Martínez, T. Pelini, V. Waselowski, J. R. Maze, B. Gil, G. Cassabois, and V. Jacques, *Efficient single photon emission from a high-purity hexagonal boron nitride crystal*, Physical Review B **94** (2016).

[73] L. Museur, D. Anglos, J.-P. Petitet, J.-P. Michel, and A. V. Kanaev, *Photoluminescence of hexagonal boron nitride: Effect of surface oxidation under UV-laser irradiation*, Journal of Luminescence **127**, 595 (2007).

[74] L. Museur, E. Feldbach, and A. Kanaev, *Defect-related photoluminescence of hexagonal boron nitride*, Physical Review B **78** (2008).

[75] D. B. Williams and C. B. Carter, *Transmission Electron Microscopy: A Textbook for Materials Science*, Springer, New York, 2nd edition edition, 2009.

[76] E. Ruska, *The development of the electron microscope and of electron microscopy*, Reviews of Modern Physics **59**, 627 (1987).

[77] M. Kociak and O. Stéphan, *Mapping plasmons at the nanometer scale in an electron microscope*, Chemical Society Reviews **43**, 3865 (2014).

[78] F. d. Groot and A. Kotani, *Core level spectroscopy of solids*, Number v. 6 in Advances in condensed matter science, CRC Press, Boca Raton, 2008, OCLC: ocn156785114.

[79] G. Grosso and G. Pastori Parravicini, *Solid state physics*, Academic Press, an imprint of Elsevier, Amsterdam, second edition edition, 2014.

[80] R. Egerton and M. Whelan, *Electron energy loss spectra of diamond, graphite and amorphous carbon*, Journal of Electron Spectroscopy and Related Phenomena **3**, 232 (1974).

[81] Z. Mahfoud, A. T. Dijksman, C. Javaux, P. Bassoul, A.-L. Baudrion, J. Plain, B. Dubertret, and M. Kociak, *Cathodoluminescence in a Scanning Transmission Electron Microscope: A Nanometer-Scale Counterpart of Photoluminescence for the Study of II-VI Quantum Dots*, The Journal of Physical Chemistry Letters **4**, 4090 (2013).

[82] S. Meuret, L. Tizei, T. Cazimajou, R. Bourrellier, H. Chang, F. Treussart, and M. Kociak, *Photon Bunching in Cathodoluminescence*, Physical Review Letters **114** (2015).

[83] B. Sieber, *Cathodoluminescence Principes physiques et systèmes de détection*, Techniques de l'ingénieur. Analyses de surface et de matériaux , 3792 (2016).

[84] M. Fox, *Optical properties of solids*, Number v. 3 in Oxford master series in condensed matter physics, Oxford University Press, Oxford ; New York, 2nd ed edition, 2010.

[85] R. H. Brown and R. Q. Twiss, *Correlation between Photons in two Coherent Beams of Light*, Nature **177**, 27 (1956).

[86] M. Fox, *Quantum optics: an introduction*, Number 15 in Oxford master series in physics, Oxford University Press, Oxford ; New York, 2006.

[87] S. Lukishova, *Efficient single-photon sources with definite polarization*, SPIE Newsroom (2014).

[88] T. Basché, W. E. Moerner, M. Orrit, and H. Talon, *Photon antibunching in the fluorescence of a single dye molecule trapped in a solid*, Physical Review Letters **69**, 1516 (1992).

[89] W. Patrick Ambrose, P. M. Goodwin, J. Enderlein, D. J. Semin, J. C. Martin, and R. A. Keller, *Fluorescence photon antibunching from single molecules on a surface*, Chemical Physics Letters **269**, 365 (1997).

[90] L. Fleury, J.-M. Segura, G. Zumofen, B. Hecht, and U. P. Wild, *Nonclassical Photon Statistics in Single-Molecule Fluorescence at Room Temperature*, Physical Review Letters **84**, 1148 (2000).

[91] B. Lounis and W. E. Moerner, *Single photons on demand from a single molecule at room temperature*, Nature **407**, 491 (2000).

[92] A. Beveratos, S. Kühn, R. Brouri, T. Gacoin, J.-P. Poizat, and P. Grangier, *Room temperature stable single-photon source*, The European Physical Journal D - Atomic, Molecular and Optical Physics **18**, 191 (2002).

[93] S. Meuret, L. H. G. Tizei, T. Auzelle, R. Songmuang, B. Daudin, B. Gayral, and M. Kociak, *Lifetime Measurements Well below the Optical Diffraction Limit*, ACS Photonics **3**, 1157 (2016).

[94] A. Losquin, L. F. Zagonel, V. Myroshnychenko, B. Rodríguez-González, M. Tencé, L. Scarabelli, J. Förstner, L. M. Liz-Marzán, F. J. García de Abajo, O. Stéphan, and M. Kociak, *Unveiling Nanometer Scale Extinction and Scattering Phenomena through Combined Electron Energy Loss Spectroscopy and Cathodoluminescence Measurements*, Nano Letters **15**, 1229 (2015).

[95] R. Egerton, *Mechanisms of radiation damage in beam-sensitive specimens, for TEM accelerating voltages between 10 and 300 kV*, Microscopy Research and Technique **75**, 1550 (2012).

[96] A. Zobelli, *Electron beam generation and structure of defects in carbon and boron nitride nanotubes*, PhD thesis, 2007, Thèse de doctorat dirigée par Colliex, Christian et Seifert, Gotthard Physique Université de Paris-Sud. Faculté des Sciences d'Orsay (Essonne) 2007 Thèse de doctorat Physique Technische Universität Dresden 2007 2007PA112212.

[97] J. C. Meyer, F. Eder, S. Kurasch, V. Skakalova, J. Kotakoski, H. J. Park, S. Roth, A. Chuvilin, S. Eyhusen, G. Benner, A. V. Krasheninnikov, and U. Kaiser, *Accurate Measurement of Electron Beam Induced Displacement Cross Sections for Single-Layer Graphene*, Physical Review Letters **108** (2012).

[98] R. Egerton, P. Crozier, and P. Rice, *Electron energy-loss spectroscopy and chemical change*, Ultramicroscopy **23**, 305 (1987).

[99] R. F. Egerton, *Electron energy-loss spectroscopy in the TEM*, Reports on Progress in Physics **72**, 016502 (2009).

[100] E. G. Rightor, A. P. Hitchcock, H. Ade, R. D. Leapman, S. G. Urquhart, A. P. Smith, G. Mitchell, D. Fischer, H. J. Shin, and T. Warwick, *Spectromicroscopy of Poly(ethylene terephthalate): Comparison of Spectra and Radiation Damage Rates in X-ray Absorption and Electron Energy Loss*, The Journal of Physical Chemistry B **101**, 1950 (1997).

[101] R. Egerton, *Chemical measurements of radiation damage in organic samples at and below room temperature*, Ultramicroscopy **5**, 521 (1980).

[102] K. Pearson, *LIII. On lines and planes of closest fit to systems of points in space*, Philosophical Magazine Series 6 **2**, 559 (1901).

[103] I. T. Jolliffe, *Principal component analysis*, 2002, OCLC: 70737343.

[104] H. P. Boehm, A. Clauss, G. O. Fischer, and U. Hofmann, *Das Adsorptionsverhalten sehr dünner Kohlenstoff-Folien*, Zeitschrift für anorganische und allgemeine Chemie **316**, 119 (1962).

[105] H.-P. Boehm, *Graphene-How a Laboratory Curiosity Suddenly Became Extremely Interesting*, Angewandte Chemie International Edition **49**, 9332 (2010).

[106] K. S. Novoselov, *Electric Field Effect in Atomically Thin Carbon Films*, Science **306**, 666 (2004).

[107] K. S. Novoselov, *Graphene: Materials in the Flatland (Nobel Lecture)*, **50**, 6986 (2011).

[108] R. T. Downs and M. Hall-Wallace, *The American Mineralogist crystal structure database*, American Mineralogist **88**, 247 (2003).

[109] S. Park and R. S. Ruoff, *Chemical methods for the production of graphenes*, Nat Nano **4**, 217 (2009).

[110] C. Hontoria-Lucas, A. López-Peinado, J. D. López-González, M. Rojas-Cervantes, and R. Martín-Aranda, *Study of oxygen-containing groups in a series of graphite oxides: Physical and chemical characterization*, Carbon **33**, 1585 (1995).

[111] H.-K. Jeong, Y. P. Lee, R. J. W. E. Lahaye, M.-H. Park, K. H. An, I. J. Kim, C.-W. Yang, C. Y. Park, R. S. Ruoff, and Y. H. Lee, *Evidence of Graphitic AB Stacking Order of Graphite Oxides*, J. Am. Chem. Soc. **130**, 1362 (2008).

[112] D. Loc Duong, G. Kim, H.-K. Jeong, and Y. Hee Lee, *Breaking AB stacking order in graphite oxide: ab initio approach*, Physical Chemistry Chemical Physics **12**, 1595 (2010).

[113] B. Rezania, N. Severin, A. V. Talyzin, and J. P. Rabe, *Hydration of Bilayered Graphene Oxide*, Nano Letters **14**, 3993 (2014).

[114] S. Eigler and A. Hirsch, *Chemistry with Graphene and Graphene Oxide-Challenges for Synthetic Chemists*, Angewandte Chemie International Edition **53**, 7720 (2014).

[115] C.-Y. Su, Y. Xu, W. Zhang, J. Zhao, X. Tang, C.-H. Tsai, and L.-J. Li, *Electrical and Spectroscopic Characterizations of Ultra-Large Reduced Graphene Oxide Monolayers*, Chem. Mater. **21**, 5674 (2009).

[116] T. Szabó, E. Tombácz, E. Illés, and I. Dékány, *Enhanced acidity and pH-dependent surface charge characterization of successively oxidized graphite oxides*, Carbon **44**, 537 (2006).

[117] D. Li, M. B. Müller, S. Gilje, R. B. Kaner, and G. G. Wallace, *Processable aqueous dispersions of graphene nanosheets*, Nature Nanotechnology **3**, 101 (2008).

[118] S. Stankovich, D. A. Dikin, R. D. Piner, K. A. Kohlhaas, A. Kleinhammes, Y. Jia, Y. Wu, S. T. Nguyen, and R. S. Ruoff, *Synthesis of graphene-based nanosheets via chemical reduction of exfoliated graphite oxide*, Carbon **45**, 1558 (2007).

[119] V. Lee, L. Whittaker, C. Jaye, K. M. Baroudi, D. A. Fischer, and S. Banerjee, *Large-Area Chemically Modified Graphene Films: Electrophoretic Deposition and Characterization by Soft X-ray Absorption Spectroscopy*, Chem. Mater. **21**, 3905 (2009).

[120] H. C. Schniepp, J.-L. Li, M. J. McAllister, H. Sai, M. Herrera-Alonso, D. H. Adamson, R. K. Prud'homme, R. Car, D. A. Saville, and I. A. Aksay, *Functionalized Single Graphene Sheets Derived from Splitting Graphite Oxide*, J. Phys. Chem. B **110**, 8535 (2006).

[121] M. J. McAllister, J.-L. Li, D. H. Adamson, H. C. Schniepp, A. A. Abdala, J. Liu, M. Herrera-Alonso, D. L. Milius, R. Car, R. K. Prud'homme, and I. A. Aksay, *Single Sheet Functionalized Graphene by Oxidation and Thermal Expansion of Graphite*, Chem. Mater. **19**, 4396 (2007).

[122] P. Montes-Navajas, N. G. Asenjo, R. Santamaría, R. Menéndez, A. Corma, and H. García, *Surface Area Measurement of Graphene Oxide in Aqueous Solutions*, Langmuir **29**, 13443 (2013).

[123] J. W. Suk, R. D. Piner, J. An, and R. S. Ruoff, *Mechanical Properties of Monolayer Graphene Oxide*, ACS Nano **4**, 6557 (2010).

[124] D. A. Dikin, S. Stankovich, E. J. Zimney, R. D. Piner, G. H. B. Dommett, G. Evmenenko, S. T. Nguyen, and R. S. Ruoff, *Preparation and characterization of graphene oxide paper*, Nature **448**, 457 (2007).

[125] H. A. Becerril, J. Mao, Z. Liu, R. M. Stoltenberg, Z. Bao, and Y. Chen, *Evaluation of Solution-Processed Reduced Graphene Oxide Films as Transparent Conductors*, ACS Nano **2**, 463 (2008).

[126] S. Park, J. An, R. D. Piner, I. Jung, D. Yang, A. Velamakanni, S. T. Nguyen, and R. S. Ruoff, *Aqueous Suspension and Characterization of Chemically Modified Graphene Sheets*, Chemistry of Materials **20**, 6592 (2008).

[127] W. Gao, L. B. Alemany, L. Ci, and P. M. Ajayan, *New insights into the structure and reduction of graphite oxide*, Nat Chem **1**, 403 (2009).

[128] C. Mattevi, G. Eda, S. Agnoli, S. Miller, K. A. Mkhoyan, O. Celik, D. Mastrogiovanni, G. Granozzi, E. Garfunkel, and M. Chhowalla, *Evolution of Electrical, Chemical, and Structural Properties of Transparent and Conducting Chemically Derived Graphene Thin Films*, Advanced Functional Materials **19**, 2577 (2009).

[129] S. Gilje, S. Han, M. Wang, K. L. Wang, and R. B. Kaner, *A Chemical Route to Graphene for Device Applications*, Nano Letters **7**, 3394 (2007).

[130] G. Eda, G. Fanchini, and M. Chhowalla, *Large-area ultrathin films of reduced graphene oxide as a transparent and flexible electronic material*, Nat Nano **3**, 270 (2008).

[131] P. V. Kumar, N. M. Bardhan, S. Tongay, J. Wu, A. M. Belcher, and J. C. Grossman, *Scalable enhancement of graphene oxide properties by thermally driven phase transformation*, Nature Chemistry **6**, 151 (2013).

[132] Q. Tang, Z. Zhou, and Z. Chen, *Graphene-related nanomaterials: tuning properties by functionalization*, Nanoscale **5**, 4541 (2013).

[133] Z. Luo, P. M. Vora, E. J. Mele, A. T. C. Johnson, and J. M. Kikkawa, *Photoluminescence and band gap modulation in graphene oxide*, Applied Physics Letters **94**, 111909 (2009).

[134] G. Eda, Y.-Y. Lin, C. Mattevi, H. Yamaguchi, H.-A. Chen, I.-S. Chen, C.-W. Chen, and M. Chhowalla, *Blue Photoluminescence from Chemically Derived Graphene Oxide*, Advanced Materials **22**, 505 (2010).

[135] H. K. Jeong, M. H. Jin, K. P. So, S. C. Lim, and Y. H. Lee, *Tailoring the characteristics of graphite oxides by different oxidation times*, J. Phys. D: Appl. Phys. **42**, 065418 (2009).

[136] M. Hirata, T. Gotou, S. Horiuchi, M. Fujiwara, and M. Ohba, *Thin-film particles of graphite oxide 1: High-yield synthesis and flexibility of the particles*, Carbon **42**, 2929 (2004).

[137] T. Szabó, O. Berkesi, P. Forgó, K. Josepovits, Y. Sanakis, D. Petridis, and I. Dékány, *Evolution of Surface Functional Groups in a Series of Progressively Oxidized Graphite Oxides*, Chem. Mater. **18**, 2740 (2006).

[138] D. C. Marcano, D. V. Kosynkin, J. M. Berlin, A. Sinitskii, Z. Sun, A. Slesarev, L. B. Alemany, W. Lu, and J. M. Tour, *Improved Synthesis of Graphene Oxide*, ACS Nano **4**, 4806 (2010).

[139] S. Eigler, M. Enzelberger-Heim, S. Grimm, P. Hofmann, W. Kroener, A. Geworski, C. Dotzer, M. Röckert, J. Xiao, C. Papp, O. Lytken, H.-P. Steinrück, P. Müller, and A. Hirsch, *Wet Chemical Synthesis of Graphene*, Advanced Materials **25**, 3583 (2013).

[140] N. I. Kovtyukhova, P. J. Ollivier, B. R. Martin, T. E. Mallouk, S. A. Chizhik, E. V. Buzaneva, and A. D. Gorchinskiy, *Layer-by-Layer Assembly of Ultrathin Composite Films from Micron-Sized Graphite Oxide Sheets and Polycations*, Chem. Mater. **11**, 771 (1999).

[141] J. Zhao, S. Pei, W. Ren, L. Gao, and H.-M. Cheng, *Efficient Preparation of Large-Area Graphene Oxide Sheets for Transparent Conductive Films*, ACS Nano **4**, 5245 (2010).

[142] H. Wang and Y. H. Hu, *Effect of Oxygen Content on Structures of Graphite Oxides*, Ind. Eng. Chem. Res. **50**, 6132 (2011).

[143] I. Jung, D. Dikin, S. Park, W. Cai, S. L. Mielke, and R. S. Ruoff, *Effect of Water Vapor on Electrical Properties of Individual Reduced Graphene Oxide Sheets*, The Journal of Physical Chemistry C **112**, 20264 (2008).

[144] Y. Yao, X. Chen, H. Guo, and Z. Wu, *Graphene oxide thin film coated quartz crystal microbalance for humidity detection*, Applied Surface Science **257**, 7778 (2011).

[145] H. Bi, K. Yin, X. Xie, J. Ji, S. Wan, L. Sun, M. Terrones, and M. S. Dresselhaus, *Ultrahigh humidity sensitivity of graphene oxide*, Scientific Reports **3** (2013).

[146] S. Borini, R. White, D. Wei, M. Astley, S. Haque, E. Spigone, N. Harris, J. Kivioja, and T. Ryhänen, *Ultrafast Graphene Oxide Humidity Sensors*, ACS Nano **7**, 11166 (2013).

[147] A. Ganguly, S. Sharma, P. Papakonstantinou, and J. Hamilton, *Probing the Thermal Deoxygenation of Graphene Oxide Using High-Resolution In Situ X-ray-Based Spectroscopies*, J. Phys. Chem. C **115**, 17009 (2011).

[148] D. Yang, A. Velamakanni, G. Bozoklu, S. Park, M. Stoller, R. D. Piner, S. Stankovich, I. Jung, D. A. Field, C. A. Ventrice Jr., and R. S. Ruoff, *Chemical analysis of graphene oxide films after heat and chemical treatments by X-ray photoelectron and Micro-Raman spectroscopy*, Carbon **375**, 145 (2009).

[149] G. Williams, B. Seger, and P. V. Kamat, *$TiO_2$-Graphene Nanocomposites. UV-Assisted Photocatalytic Reduction of Graphene Oxide*, ACS Nano **2**, 1487 (2008).

[150] Y. H. Ding, P. Zhang, Q. Zhuo, H. M. Ren, Z. M. Yang, and Y. Jiang, *A green approach to the synthesis of reduced graphene oxide nanosheets under UV irradiation*, Nanotechnology **22**, 215601 (2011).

[151] C. K. Chua and M. Pumera, *Light and Atmosphere Affect the Quasi-equilibrium States of Graphite Oxide and Graphene Oxide Powders*, Small **11**, 1266 (2015).

[152] A. Dimiev, D. V. Kosynkin, L. B. Alemany, P. Chaguine, and J. M. Tour, *Pristine Graphite Oxide*, Journal of the American Chemical Society **134**, 2815 (2012).

[153] S. Stankovich, R. D. Piner, S. T. Nguyen, and R. S. Ruoff, *Synthesis and exfoliation of isocyanate-treated graphene oxide nanoplatelets*, Carbon **44**, 3342 (2006).

[154] J. Shen, Y. Hu, M. Shi, X. Lu, C. Qin, C. Li, and M. Ye, *Fast and Facile Preparation of Graphene Oxide and Reduced Graphene Oxide Nanoplatelets*, Chemistry of Materials **21**, 3514 (2009).

[155] C. Gómez-Navarro, M. Burghard, and K. Kern, *Elastic Properties of Chemically Derived Single Graphene Sheets*, Nano Letters **8**, 2045 (2008).

[156] C. Lee, X. Wei, J. W. Kysar, and J. Hone, *Measurement of the Elastic Properties and Intrinsic Strength of Monolayer Graphene*, Science **321**, 385 (2008).

[157] I. Jung, D. A. Dikin, R. D. Piner, and R. S. Ruoff, *Tunable Electrical Conductivity of Individual Graphene Oxide Sheets Reduced at "Low" Temperatures*, Nano Lett. **8**, 4283 (2008).

[158] G. Eda, C. Mattevi, H. Yamaguchi, H. Kim, and M. Chhowalla, *Insulator to Semimetal Transition in Graphene Oxide*, J. Phys. Chem. C **113**, 15768 (2009).

[159] H. Yamaguchi et al., *Valence-band electronic structure evolution of graphene oxide upon thermal annealing for optoelectronics: Valence-band electronic structure evolution of graphene oxide*, physica status solidi (a) **213**, 2380 (2016).

[160] X. Wang, L. Zhi, and K. Mullen, *Transparent, Conductive Graphene Electrodes for Dye-Sensitized Solar Cells*, Nano Lett. **8**, 323 (2008).

[161] R. R. Nair, H. A. Wu, P. N. Jayaram, I. V. Grigorieva, and A. K. Geim, *Unimpeded Permeation of Water Through Helium-Leak–Tight Graphene-Based Membranes*, Science **335**, 442 (2012).

[162] R. Cruz-Silva, A. Morelos-Gomez, H.-i. Kim, H.-k. Jang, F. Tristan, S. Vega-Diaz, L. P. Rajukumar, A. L. Elías, N. Perea-Lopez, J. Suhr, M. Endo, and M. Terrones, *Super-stretchable Graphene Oxide Macroscopic Fibers with Outstanding Knotability Fabricated by Dry Film Scrolling*, ACS Nano **8**, 5959 (2014).

[163] E. Kymakis, K. Savva, M. M. Stylianakis, C. Fotakis, and E. Stratakis, *Flexible Organic Photovoltaic Cells with In Situ Nonthermal Photoreduction of Spin-Coated Graphene Oxide Electrodes*, Advanced Functional Materials **23**, 2742 (2013).

[164] H. Liang, Y. Bu, J. Zhang, Z. Cao, and A. Liang, *Graphene Oxide Film as Solid Lubricant*, ACS Applied Materials & Interfaces **5**, 6369 (2013).

[165] M. Hu and B. Mi, *Enabling Graphene Oxide Nanosheets as Water Separation Membranes*, Environmental Science & Technology **47**, 3715 (2013).

[166] H. M. Hegab and L. Zou, *Graphene oxide-assisted membranes: Fabrication and potential applications in desalination and water purification*, Journal of Membrane Science **484**, 95 (2015).

[167] I. K. Moon, J. Lee, R. S. Ruoff, and H. Lee, *Reduced graphene oxide by chemical graphitization*, Nature Communications **1**, 1 (2010).

[168] J. E. Kim, T. H. Han, S. H. Lee, J. Y. Kim, C. W. Ahn, J. M. Yun, and S. O. Kim, *Graphene Oxide Liquid Crystals*, Angew. Chem. Int. Ed. **50**, 3043 (2011).

[169] Z. Xu and C. Gao, *Graphene chiral liquid crystals and macroscopic assembled fibres*, Nature Communications **2**, 571 (2011).

[170] Z. Xu, H. Sun, X. Zhao, and C. Gao, *Ultrastrong Fibers Assembled from Giant Graphene Oxide Sheets*, Adv. Mater. **25**, 188 (2013).

[171] X. Wu, M. Sprinkle, X. Li, F. Ming, C. Berger, and W. A. de Heer, *Epitaxial-Graphene/Graphene-Oxide Junction: An Essential Step towards Epitaxial Graphene Electronics*, Phys. Rev. Lett. **101**, 026801 (2008).

[172] C. L. He, F. Zhuge, X. F. Zhou, M. Li, G. C. Zhou, Y. W. Liu, J. Z. Wang, B. Chen, W. J. Su, Z. P. Liu, Y. H. Wu, P. Cui, and R.-W. Li, *Nonvolatile resistive switching in graphene oxide thin films*, Applied Physics Letters **95**, 232101 (2009).

[173] S. Wang, J. Pu, D. S. H. Chan, B. J. Cho, and K. P. Loh, *Wide memory window in graphene oxide charge storage nodes*, Applied Physics Letters **96**, 143109 (2010).

[174] B. Standley, A. Mendez, E. Schmidgall, and M. Bockrath, *Graphene–Graphite Oxide Field-Effect Transistors*, Nano Letters **12**, 1165 (2012).

[175] V. Georgakilas, M. Otyepka, A. B. Bourlinos, V. Chandra, N. Kim, K. C. Kemp, P. Hobza, R. Zboril, and K. S. Kim, *Functionalization of Graphene: Covalent and Non-Covalent Approaches, Derivatives and Applications*, Chem. Rev. **112**, 6156 (2012).

[176] D. R. Dreyer, A. D. Todd, and C. W. Bielawski, *Harnessing the chemistry of graphene oxide*, Chemical Society Reviews **43**, 5288 (2014).

[177] F. Perrozzi, S. Prezioso, and L. Ottaviano, *Graphene oxide: from fundamentals to applications*, Journal of Physics: Condensed Matter **27**, 013002 (2015).

[178] S. Prezioso, F. Perrozzi, L. Giancaterini, C. Cantalini, E. Treossi, V. Palermo, M. Nardone, S. Santucci, and L. Ottaviano, *Graphene Oxide as a Practical Solution to High Sensitivity Gas Sensing*, J. Phys. Chem. C **117**, 10683 (2013).

[179] J. W. Burress, S. Gadipelli, J. Ford, J. M. Simmons, W. Zhou, and T. Yildirim, *Graphene Oxide Framework Materials: Theoretical Predictions and Experimental Results*, Angewandte Chemie International Edition **49**, 8902 (2010).

[180] L. Wang, K. Lee, Y.-Y. Sun, M. Lucking, Z. Chen, J. J. Zhao, and S. B. Zhang, *Graphene Oxide as an Ideal Substrate for Hydrogen Storage*, ACS Nano **3**, 2995 (2009).

[181] L. Wang, F. H. Yang, R. T. Yang, and M. A. Miller, *Effect of Surface Oxygen Groups in Carbons on Hydrogen Storage by Spillover*, Ind. Eng. Chem. Res. **48**, 2920 (2009).

[182] X. Zhang, Y. Huang, Y. Wang, Y. Ma, Z. Liu, and Y. Chen, *Synthesis and characterization of a graphene–C60 hybrid material*, Carbon **47**, 334 (2009).

[183] Y. Xu, Z. Liu, X. Zhang, Y. Wang, J. Tian, Y. Huang, Y. Ma, X. Zhang, and Y. Chen, *A Graphene Hybrid Material Covalently Functionalized with Porphyrin: Synthesis and Optical Limiting Property*, Advanced Materials **21**, 1275 (2009).

[184] J. Liu, M. Durstock, and L. Dai, *Graphene oxide derivatives as hole- and electron-extraction layers for high-performance polymer solar cells*, Energy Environ. Sci. **7**, 1297 (2014).

[185] Z.-B. Liu, Y.-F. Xu, X.-Y. Zhang, X.-L. Zhang, Y.-S. Chen, and J.-G. Tian, *Porphyrin and Fullerene Covalently Functionalized Graphene Hybrid Materials with Large Nonlinear Optical Properties*, The Journal of Physical Chemistry B **113**, 9681 (2009).

[186] F. He, J. Fan, D. Ma, L. Zhang, C. Leung, and H. L. Chan, *The attachment of $Fe_3O_4$ nanoparticles to graphene oxide by covalent bonding*, Carbon **48**, 3139 (2010).

[187] J. Xu, K. Wang, S.-Z. Zu, B.-H. Han, and Z. Wei, *Hierarchical Nanocomposites of Polyaniline Nanowire Arrays on Graphene Oxide Sheets with Synergistic Effect for Energy Storage*, ACS Nano **4**, 5019 (2010).

[188] H. Tateishi, K. Hatakeyama, C. Ogata, K. Gezuhara, J. Kuroda, A. Funatsu, M. Koinuma, T. Taniguchi, S. Hayami, and Y. Matsumoto, *Graphene Oxide Fuel Cell*, Journal of the Electrochemical Society **160**, F1175 (2013).

[189] N. Mohanty and V. Berry, *Graphene-Based Single-Bacterium Resolution Biodevice and DNA Transistor: Interfacing Graphene Derivatives with Nanoscale and Microscale Biocomponents*, Nano Letters **8**, 4469 (2008).

[190] C.-H. Lu, H.-H. Yang, C.-L. Zhu, X. Chen, and G.-N. Chen, *A graphene platform for sensing biomolecules*, Angew. Chem. Int. Ed. Engl. **48**, 4785 (2009).

[191] X. Sun, Z. Liu, K. Welsher, J. T. Robinson, A. Goodwin, S. Zaric, and H. Dai, *Nano-Graphene Oxide for Cellular Imaging and Drug Delivery*, Nano Res **1**, 203 (2008).

[192] Z. Liu, J. T. Robinson, X. Sun, and H. Dai, *PEGylated Nanographene Oxide for Delivery of Water-Insoluble Cancer Drugs*, Journal of the American Chemical Society **130**, 10876 (2008).

[193] J. Liu, L. Cui, and D. Losic, *Graphene and graphene oxide as new nanocarriers for drug delivery applications*, Acta Biomaterialia **9**, 9243 (2013).

[194] K. Yang, S. Zhang, G. Zhang, X. Sun, S.-T. Lee, and Z. Liu, *Graphene in Mice: Ultrahigh In Vivo Tumor Uptake and Efficient Photothermal Therapy*, Nano Letters **10**, 3318 (2010).

[195] S. Liu, T. H. Zeng, M. Hofmann, E. Burcombe, J. Wei, R. Jiang, J. Kong, and Y. Chen, *Antibacterial Activity of Graphite, Graphite Oxide, Graphene Oxide, and Reduced Graphene Oxide: Membrane and Oxidative Stress*, ACS Nano **5**, 6971 (2011).

[196] G.-Y. Chen, D.-P. Pang, S.-M. Hwang, H.-Y. Tuan, and Y.-C. Hu, *A graphene-based platform for induced pluripotent stem cells culture and differentiation*, Biomaterials **33**, 418 (2012).

[197] S. Watcharotone, D. A. Dikin, S. Stankovich, R. Piner, I. Jung, G. H. B. Dommett, G. Evmenenko, S.-E. Wu, S.-F. Chen, C.-P. Liu, S. T. Nguyen, and R. S. Ruoff, *Graphene-Silica Composite Thin Films as Transparent Conductors*, Nano Lett. **7**, 1888 (2007).

[198] S. Stankovich, D. A. Dikin, G. H. B. Dommett, K. M. Kohlhaas, E. J. Zimney, E. A. Stach, R. D. Piner, S. T. Nguyen, and R. S. Ruoff, *Graphene-based composite materials*, Nature **442**, 282 (2006).

[199] Y. I. Avila-Vega, C. C. Leyva-Porras, M. Mireles, M. Quevedo-LÃşpez, J. Macossay, and J. Bonilla-Cruz, *Nitroxide-functionalized graphene oxide from graphite oxide*, Carbon **63**, 376 (2013).

[200] M. Favaro, L. Ferrighi, G. Fazio, L. Colazzo, C. Di Valentin, C. Durante, F. Sedona, A. Gennaro, S. Agnoli, and G. Granozzi, *Single and Multiple Doping in Graphene Quantum Dots: Unraveling the Origin of Selectivity in the Oxygen Reduction Reaction*, ACS Catalysis **5**, 129 (2015).

[201] M. Favaro, F. Carraro, M. Cattelan, L. Colazzo, C. Durante, M. Sambi, A. Gennaro, S. Agnoli, and G. Granozzi, *Multiple doping of graphene oxide foams and quantum dots: new switchable systems for oxygen reduction and water remediation*, J. Mater. Chem. A **3**, 14334 (2015).

[202] T.-F. Yeh, J.-M. Syu, C. Cheng, T.-H. Chang, and H. Teng, *Graphite Oxide as a Photocatalyst for Hydrogen Production from Water*, Advanced Functional Materials **20**, 2255 (2010).

[203] J. Sloan, Z. Liu, K. Suenaga, N. R. Wilson, P. A. Pandey, L. M. Perkins, J. P. Rourke, and I. J. Shannon, *Imaging the Structure, Symmetry, and Surface-Inhibited Rotation of Polyoxometalate Ions on Graphene Oxide*, Nano Letters **10**, 4600 (2010).

[204] C. Bosch-Navarro, L. M. Perkins, R. J. Kashtiban, J. P. Rourke, I. J. Shannon, and J. Sloan, *Selective Imaging of Discrete Polyoxometalate Ions on Graphene Oxide under Variable Voltage Conditions*, ACS Nano **10**, 796 (2016).

[205] R. S. Pantelic, J. C. Meyer, U. Kaiser, W. Baumeister, and J. M. Plitzko, *Graphene oxide: A substrate for optimizing preparations of frozen-hydrated samples*, Journal of Structural Biology **170**, 152 (2010).

[206] G. Eda, J. Ball, C. Mattevi, M. Acik, L. Artiglia, G. Granozzi, Y. Chabal, T. D. Anthopoulos, and M. Chhowalla, *Partially oxidized graphene as a precursor to graphene*, Journal of Materials Chemistry **21**, 11217 (2011).

[207] M. Segal, *Selling graphene by the ton*, Nat Nano **4**, 612 (2009).

[208] K. S. Novoselov, V. I. Fal'ko, L. Colombo, P. R. Gellert, M. G. Schwab, and K. Kim, *A roadmap for graphene*, Nature **490**, 192 (2012).

[209] V. C. Tung, M. J. Allen, Y. Yang, and R. B. Kaner, *High-throughput solution processing of large-scale graphene*, Nat Nanotechnol **4**, 25 (2009).

[210] W. Miao, G. Shim, C. M. Kang, S. Lee, Y. S. Choe, H.-G. Choi, and Y.-K. Oh, *Cholesteryl hyaluronic acid-coated, reduced graphene oxide nanosheets for anti-cancer drug delivery*, Biomaterials **34**, 9638 (2013).

[211] B. A. Aderibigbe, S. J. Owonubi, J. Jayaramudu, E. R. Sadiku, and S. S. Ray, *Targeted drug delivery potential of hydrogel biocomposites containing partially and thermally reduced graphene oxide and natural polymers prepared via green process*, Colloid and Polymer Science **293**, 409 (2015).

[212] O. Akhavan and E. Ghaderi, *Photocatalytic Reduction of Graphene Oxide Nanosheets on $TiO_2$ Thin Film for Photoinactivation of Bacteria in Solar Light Irradiation*, The Journal of Physical Chemistry C **113**, 20214 (2009).

[213] J. T. Robinson, F. K. Perkins, E. S. Snow, Z. Wei, and P. E. Sheehan, *Reduced Graphene Oxide Molecular Sensors*, Nano Letters **8**, 3137 (2008).

[214] V. Dua, S. Surwade, S. Ammu, S. Agnihotra, S. Jain, K. Roberts, S. Park, R. Ruoff, and S. Manohar, *All-Organic Vapor Sensor Using Inkjet-Printed Reduced Graphene Oxide*, Angewandte Chemie International Edition **49**, 2154 (2010).

[215] V. Chandra, J. Park, Y. Chun, J. W. Lee, I.-C. Hwang, and K. S. Kim, *Water-Dispersible Magnetite-Reduced Graphene Oxide Composites for Arsenic Removal*, ACS Nano **4**, 3979 (2010).

[216] T. Ramanathan, A. A. Abdala, S. Stankovich, D. A. Dikin, M. Herrera-Alonso, R. D. Piner, D. H. Adamson, H. C. Schniepp, X. Chen, R. S. Ruoff, S. T. Nguyen, I. A. Aksay, R. K. Prud'Homme, and L. C. Brinson, *Functionalized graphene sheets for polymer nanocomposites*, Nat Nano **3**, 327 (2008).

[217] M. D. Stoller, S. Park, Y. Zhu, J. An, and R. S. Ruoff, *Graphene-Based Ultracapacitors*, Nano Lett. **8**, 3498 (2008).

[218] W. Gao, N. Singh, L. Song, Z. Liu, A. L. M. Reddy, L. Ci, R. Vajtai, Q. Zhang, B. Wei, and P. M. Ajayan, *Direct laser writing of micro-supercapacitors on hydrated graphite oxide films*, Nature Nanotechnology **6**, 496 (2011).

[219] Z.-S. Wu, G. Zhou, L.-C. Yin, W. Ren, F. Li, and H.-M. Cheng, *Graphene/metal oxide composite electrode materials for energy storage*, Nano Energy **1**, 107 (2012).

[220] X. Yang, C. Cheng, Y. Wang, L. Qiu, and D. Li, *Liquid-Mediated Dense Integration of Graphene Materials for Compact Capacitive Energy Storage*, Science **341**, 534 (2013).

[221] R. P. Gandhiraman, D. Nordlund, C. Javier, J. E. Koehne, B. Chen, and M. Meyyappan, *X-ray Absorption Study of Graphene Oxide and Transition Metal Oxide Nanocomposites*, The Journal of Physical Chemistry C **118**, 18706 (2014).

[222] Z. Bo, X. Shuai, S. Mao, H. Yang, J. Qian, J. Chen, J. Yan, and K. Cen, *Green preparation of reduced graphene oxide for sensing and energy storage applications*, Scientific Reports **4** (2014).

[223] S. Pang, H. N. Tsao, X. Feng, and K. Müllen, *Patterned Graphene Electrodes from Solution-Processed Graphite Oxide Films for Organic Field-Effect Transistors*, Advanced Materials **21**, 3488 (2009).

[224] S. Ghosh, B. K. Sarker, A. Chunder, L. Zhai, and S. I. Khondaker, *Position dependent photodetector from large area reduced graphene oxide thin films*, Applied Physics Letters **96**, 163109 (2010).

[225] J. T. Robinson, M. Zalalutdinov, J. W. Baldwin, E. S. Snow, Z. Wei, P. Sheehan, and B. H. Houston, *Wafer-scale Reduced Graphene Oxide Films for Nanomechanical Devices*, Nano Lett. **8**, 3441 (2008).

[226] J. Liang, Y. Chen, Y. Xu, Z. Liu, L. Zhang, X. Zhao, X. Zhang, J. Tian, Y. Huang, Y. Ma, and F. Li, *Toward All-Carbon Electronics: Fabrication of Graphene-Based Flexible Electronic Circuits and Memory Cards Using Maskless Laser Direct Writing*, ACS Applied Materials & Interfaces **2**, 3310 (2010).

[227] Y. Zhang, L. Guo, S. Wei, Y. He, H. Xia, Q. Chen, H.-B. Sun, and F.-S. Xiao, *Direct imprinting of microcircuits on graphene oxides film by femtosecond laser reduction*, Nano Today **5**, 15 (2010).

[228] Z. Wei, D. Wang, S. Kim, S.-Y. Kim, Y. Hu, M. K. Yakes, A. R. Laracuente, Z. Dai, S. R. Marder, C. Berger, W. P. King, W. A. d. Heer, P. E. Sheehan, and E. Riedo, *Nanoscale Tunable Reduction of Graphene Oxide for Graphene Electronics*, Science **328**, 1373 (2010).

[229] Eowyn041084 and A. Mabbett, Portrait of Sir Benjamin Collins Brodie, 2013, Wikipedia, the free encyclopedia.

[230] M. I. López, A. E. Croce, and J. E. Sicre, *Explosive decomposition of gaseous chlorine dioxide*, J. Chem. Soc., Faraday Trans. **90**, 3391 (1994).

[231] A. M. Dimiev and J. M. Tour, *Mechanism of Graphene Oxide Formation*, ACS Nano **8**, 3060 (2014).

[232] T. Nakajima, A. Mabuchi, and R. Hagiwara, *A new structure model of graphite oxide*, Carbon **26**, 357 (1988).

[233] J. H. Kang, T. Kim, J. Choi, J. Park, Y. S. Kim, M. S. Chang, H. Jung, K. T. Park, S. J. Yang, and C. R. Park, *Hidden Second Oxidation Step of Hummers Method*, Chemistry of Materials (2016).

[234] X. Li, H. Wang, J. T. Robinson, H. Sanchez, G. Diankov, and H. Dai, *Simultaneous Nitrogen Doping and Reduction of Graphene Oxide*, J. Am. Chem. Soc. **131**, 15939 (2009).

[235] C. Vallés, J. David Núñez, A. M. Benito, and W. K. Maser, *Flexible conductive graphene paper obtained by direct and gentle annealing of graphene oxide paper*, Carbon **50**, 835 (2012).

[236] X. Chen, D. Meng, B. Wang, B.-W. Li, W. Li, C. W. Bielawski, and R. S. Ruoff, *Rapid thermal decomposition of confined graphene oxide films in air*, Carbon **101**, 71 (2016).

[237] S. Kim, D. D. Kulkarni, M. Henry, P. Zackowski, S. S. Jang, V. V. Tsukruk, and A. G. Fedorov, *Localized conductive patterning via focused electron beam reduction of graphene oxide*, Applied Physics Letters **106**, 133109 (2015).

[238] C. Botas, P. Álvarez, P. Blanco, M. Granda, C. Blanco, R. Santamaría, L. J. Romasanta, R. Verdejo, M. A. López-Manchado, and R. Menéndez, *Graphene materials with different structures prepared from the same graphite by the Hummers and Brodie methods*, Carbon **65**, 156 (2013).

[239] I. Jung, D. A. Field, N. J. Clark, Y. Zhu, D. Yang, R. D. Piner, S. Stankovich, D. A. Dikin, H. Geisler, C. A. Ventrice, and R. S. Ruoff, *Reduction Kinetics of Graphene Oxide Determined by Electrical Transport Measurements and Temperature Programmed Desorption*, The Journal of Physical Chemistry C **113**, 18480 (2009).

[240] C. Botas, P. Álvarez, C. Blanco, R. Santamaría, M. Granda, M. D. Gutiérrez, F. Rodríguez-Reinoso, and R. Menéndez, *Critical temperatures in the synthesis of graphene-like materials by thermal exfoliation–reduction of graphite oxide*, Carbon **52**, 476 (2013).

[241] N. A. Kotov, I. Dékány, and J. H. Fendler, *Ultrathin graphite oxide-polyelectrolyte composites prepared by self-assembly: Transition between conductive and non-conductive states*, Advanced Materials **8**, 637 (1996).

[242] S. Stankovich, R. D. Piner, X. Chen, N. Wu, S. T. Nguyen, and R. S. Ruoff, *Stable aqueous dispersions of graphitic nanoplatelets via the reduction of exfoliated graphite oxide in the presence of poly(sodium 4-styrenesulfonate)*, J. Mater. Chem. **16**, 155 (2006).

[243] D. Prat, O. Pardigon, H.-W. Flemming, S. Letestu, V. Ducandas, P. Isnard, E. Guntrum, T. Senac, S. Ruisseau, P. Cruciani, and P. Hosek, *Sanofi's Solvent Selection Guide: A Step Toward More Sustainable Processes*, Organic Process Research & Development **17**, 1517 (2013).

[244] R. A. Sheldon, I. W. C. E. Arends, and U. Hanefeld, *Green Chemistry and Catalysis*, Wiley-VCH Verlag GmbH & Co. KGaA, Weinheim, Germany, 2007.

[245] C. Zhu, S. Guo, Y. Fang, and S. Dong, *Reducing Sugar: New Functional Molecules for the Green Synthesis of Graphene Nanosheets*, ACS Nano **4**, 2429 (2010).

[246] M. Favaro, S. Agnoli, C. Di Valentin, C. Mattevi, M. Cattelan, L. Artiglia, E. Magnano, F. Bondino, S. Nappini, and G. Granozzi, *$TiO_2$/graphene nanocomposites from the direct reduction of graphene oxide by metal evaporation*, Carbon **68**, 319 (2014).

[247] S. W. Lee, C. Mattevi, M. Chhowalla, and R. M. Sankaran, *Plasma-Assisted Reduction of Graphene Oxide at Low Temperature and Atmospheric Pressure for Flexible Conductor Applications*, The Journal of Physical Chemistry Letters **3**, 772 (2012).

[248] A. Esfandiar, O. Akhavan, and A. Irajizad, *Melatonin as a powerful bio-antioxidant for reduction of graphene oxide*, Journal of Materials Chemistry **21**, 10907 (2011).

[249] Y. Wang, Z. Shi, and J. Yin, *Facile Synthesis of Soluble Graphene via a Green Reduction of Graphene Oxide in Tea Solution and Its Biocomposites*, ACS Applied Materials & Interfaces **3**, 1127 (2011).

[250] K.-H. Liao, A. Mittal, S. Bose, C. Leighton, K. A. Mkhoyan, and C. W. Macosko, *Aqueous Only Route toward Graphene from Graphite Oxide*, ACS Nano **5**, 1253 (2011).

[251] M. C. Kim, G. S. Hwang, and R. S. Ruoff, *Epoxide reduction with hydrazine on graphene: A first principles study*, The Journal of Chemical Physics **131**, 064704 (2009).

[252] H.-J. Shin, K. K. Kim, A. Benayad, S.-M. Yoon, H. K. Park, I.-S. Jung, M. H. Jin, H.-K. Jeong, J. M. Kim, J.-Y. Choi, and Y. H. Lee, *Efficient Reduction of Graphite Oxide by Sodium Borohydride and Its Effect on Electrical Conductance*, Advanced Functional Materials **19**, 1987 (2009).

[253] C. Gómez-Navarro, R. T. Weitz, A. M. Bittner, M. Scolari, A. Mews, M. Burghard, and K. Kern, *Electronic Transport Properties of Individual Chemically Reduced Graphene Oxide Sheets*, Nano Lett. **7**, 3499 (2007).

[254] J. T. Paci, T. Belytschko, and G. C. Schatz, *Computational Studies of the Structure, Behavior upon Heating, and Mechanical Properties of Graphite Oxide*, J. Phys. Chem. C **111**, 18099 (2007).

[255] X. Gao, J. Jang, and S. Nagase, *Hydrazine and Thermal Reduction of Graphene Oxide: Reaction Mechanisms, Product Structures, and Reaction Design*, J. Phys. Chem. C **114**, 832 (2010).

[256] D. W. Boukhvalov and M. I. Katsnelson, *Modeling of Graphite Oxide*, J. Am. Chem. Soc. **130**, 10697 (2008).

[257] M. Acik, G. Lee, C. Mattevi, A. Pirkle, R. M. Wallace, M. Chhowalla, K. Cho, and Y. Chabal, *The Role of Oxygen during Thermal Reduction of Graphene Oxide Studied by Infrared Absorption Spectroscopy*, The Journal of Physical Chemistry C **115**, 19761 (2011).

[258] V. Lee, R. V. Dennis, B. J. Schultz, C. Jaye, D. A. Fischer, and S. Banerjee, *Soft X-ray Absorption Spectroscopy Studies of the Electronic Structure Recovery of Graphene Oxide upon Chemical Defunctionalization*, J. Phys. Chem. C **116**, 20591 (2012).

[259] C.-H. Chuang, Y.-F. Wang, Y.-C. Shao, Y.-C. Yeh, D.-Y. Wang, C.-W. Chen, J. W. Chiou, S. C. Ray, W. F. Pong, L. Zhang, J. F. Zhu, and J. H. Guo, *The Effect of Thermal Reduction on the Photoluminescence and Electronic Structures of Graphene Oxides*, Scientific Reports **4** (2014).

[260] U. Hofmann and R. Holst, *Über die Säurenatur und die Methylierung von Graphitoxyd*, Berichte der deutschen chemischen Gesellschaft (A and B Series) **72**, 754 (1939).

[261] G. Ruess, *Über das Graphitoxyhydroxyd (Graphitoxyd)*, Monatshefte für Chemie **76**, 381 (1947).

[262] A. Clauss, R. Plass, H.-P. Boehm, and U. Hofmann, *Untersuchungen zur Struktur des Graphitoxyds*, Zeitschrift für anorganische und allgemeine Chemie **291**, 205 (1957).

[263] W. Scholz and H. P. Boehm, *Untersuchungen am Graphitoxid. VI. Betrachtungen zur Struktur des Graphitoxids*, Z Anorg Allg Chem **369**, 327 (1969).

[264] M. Mermoux, Y. Chabre, and A. Rousseau, *FTIR and 13C NMR study of graphite oxide*, Carbon **29**, 469 (1991).

[265] W. Cai, R. D. Piner, F. J. Stadermann, S. Park, M. A. Shaibat, Y. Ishii, D. Yang, A. Velamakanni, S. J. An, M. Stoller, J. An, D. Chen, and R. S. Ruoff, *Synthesis and Solid-State NMR Structural Characterization of 13C-Labeled Graphite Oxide*, Science **321**, 1815 (2008).

[266] L. B. Casabianca, M. A. Shaibat, W. W. Cai, S. Park, R. Piner, R. S. Ruoff, and Y. Ishii, *NMR-Based Structural Modeling of Graphite Oxide Using Multidimensional 13C Solid-State NMR and ab Initio Chemical Shift Calculations*, J. Am. Chem. Soc. **132**, 5672 (2010).

[267] H.-K. Jeong, L. Colakerol, M. H. Jin, P.-A. Glans, K. E. Smith, and Y. H. Lee, *Unoccupied electronic states in graphite oxides*, Chemical Physics Letters **460**, 499 (2008).

[268] O. Akhavan, *The effect of heat treatment on formation of graphene thin films from graphene oxide nanosheets*, Carbon **48**, 509 (2010).

[269] B. J. Schultz, R. V. Dennis, J. P. Aldinger, C. Jaye, X. Wang, D. A. Fischer, A. N. Cartwright, and S. Banerjee, *X-ray absorption spectroscopy studies of electronic structure recovery and nitrogen local structure upon thermal reduction of graphene oxide in an ammonia environment*, RSC Adv. **4**, 634 (2014).

[270] H.-K. Jeong, H.-J. Noh, J.-Y. Kim, M. H. Jin, C. Y. Park, and Y. H. Lee, *X-ray absorption spectroscopy of graphite oxide*, EPL **82**, 67004 (2008).

[271] X. Fan, W. Peng, Y. Li, X. Li, S. Wang, G. Zhang, and F. Zhang, *Deoxygenation of Exfoliated Graphite Oxide under Alkaline Conditions: A Green Route to Graphene Preparation*, Advanced Materials **20**, 4490 (2008).

[272] D. Zhan, Z. Ni, W. Chen, L. Sun, Z. Luo, L. Lai, T. Yu, A. T. S. Wee, and Z. Shen, *Electronic structure of graphite oxide and thermally reduced graphite oxide*, Carbon **49**, 1362 (2011).

[273] J. G. Zhou, J. Wang, C. L. Sun, J. M. Maley, R. Sammynaiken, T. K. Sham, and W. F. Pong, *Nano-scale chemical imaging of a single sheet of reduced graphene oxide*, Journal of Materials Chemistry **21**, 14622 (2011).

[274] D. Lee, J. Seo, X. Zhu, J. Lee, H.-J. Shin, J. M. Cole, T. Shin, J. Lee, H. Lee, and H. Su, *Quantum confinement-induced tunable exciton states in graphene oxide*, Scientific Reports **3** (2013).

[275] Y. Ma, P. Skytt, N. Wassdahl, P. Glans, J. Guo, and J. Nordgren, *Core excitons and vibronic coupling in diamond and graphite*, Physical Review Letters **71**, 3725 (1993).

[276] P. A. Brühwiler, A. J. Maxwell, C. Puglia, A. Nilsson, S. Andersson, and N. Mårtensson, *$\pi^*$ and $\sigma^*$ Excitons in C $1s$ Absorption of Graphite*, Phys. Rev. Lett. **74**, 614 (1995).

[277] A. A. El-Barbary, S. Trasobares, C. P. Ewels, O. Stephan, A. V. Okotrub, L. G. Bulusheva, C. J. Fall, and M. I. Heggie, *Electron spectroscopy of carbon materials: experiment and theory*, J. Phys. Conf. Ser. **26**, 149 (2006).

[278] R. A. Rosenberg, P. J. Love, and V. Rehn, *Polarization-dependent C(K) near-edge x-ray-absorption fine structure of graphite*, Physical Review B **33**, 4034 (1986).

[279] J. A. Brandes, G. D. Cody, D. Rumble, P. Haberstroh, S. Wirick, and Y. Gelinas, *Carbon K-edge XANES spectromicroscopy of natural graphite*, Carbon **46**, 1424 (2008).

[280] J. T. Francis and A. P. Hitchcock, *Inner-shell spectroscopy of p-benzoquinone, hydroquinone, and phenol: distinguishing quinoid and benzenoid structures*, J. Phys. Chem. **96**, 6598 (1992).

[281] I. Christl and R. Kretzschmar, *C-1s NEXAFS spectroscopy reveals chemical fractionation of humic acid by cation-induced coagulation*, Environ. Sci. Technol. **41**, 1915 (2007).

[282] M. Acik, C. Mattevi, C. Gong, G. Lee, K. Cho, M. Chhowalla, and Y. J. Chabal, *The Role of Intercalated Water in Multilayered Graphene Oxide*, ACS Nano **4**, 5861 (2010).

[283] A. Hunt, E. Z. Kurmaev, and A. Moewes, *A Re-evaluation of How Functional Groups Modify the Electronic Structure of Graphene Oxide*, Adv. Mater. **26**, 4870 (2014).

[284] D. Pandey, R. Reifenberger, and R. Piner, *Scanning probe microscopy study of exfoliated oxidized graphene sheets*, Surface Science **602**, 1607 (2008).

[285] A. Zobelli, A. Gloter, C. P. Ewels, G. Seifert, and C. Colliex, *Electron knock-on cross section of carbon and boron nitride nanotubes*, Phys. Rev. B **75**, 245402 (2007).

[286] R. J. W. E. Lahaye, H. K. Jeong, C. Y. Park, and Y. H. Lee, *Density functional theory study of graphite oxide for different oxidation levels*, Phys. Rev. B **79**, 125435 (2009).

[287] J.-A. Yan, L. Xian, and M. Y. Chou, *Structural and Electronic Properties of Oxidized Graphene*, Phys. Rev. Lett. **103**, 086802 (2009).

[288] A. Bagri, C. Mattevi, M. Acik, Y. J. Chabal, M. Chhowalla, and V. B. Shenoy, *Structural evolution during the reduction of chemically derived graphene oxide*, Nat Chem **2**, 581 (2010).

[289] J.-A. Yan and M. Y. Chou, *Oxidation functional groups on graphene: Structural and electronic properties*, Physical Review B **82** (2010).

[290] N. Ghaderi and M. Peressi, *First-Principle Study of Hydroxyl Functional Groups on Pristine, Defected Graphene, and Graphene Epoxide*, J. Phys. Chem. C **114**, 21625 (2010).

[291] J.-L. Li, K. N. Kudin, M. J. McAllister, R. K. Prud'homme, I. A. Aksay, and R. Car, *Oxygen-Driven Unzipping of Graphitic Materials*, Phys. Rev. Lett. **96**, 176101 (2006).

[292] P. Johari and V. B. Shenoy, *Modulating Optical Properties of Graphene Oxide: Role of Prominent Functional Groups*, ACS Nano **5**, 7640 (2011).

[293] L. Wang, Y. Y. Sun, K. Lee, D. West, Z. F. Chen, J. J. Zhao, and S. B. Zhang, *Stability of graphene oxide phases from first-principles calculations*, Physical Review B **82** (2010).

[294] R. Larciprete, S. Fabris, T. Sun, P. Lacovig, A. Baraldi, and S. Lizzit, *Dual Path Mechanism in the Thermal Reduction of Graphene Oxide*, J. Am. Chem. Soc. **133**, 17315 (2011).

[295] T. Sun, S. Fabris, and S. Baroni, *Surface Precursors and Reaction Mechanisms for the Thermal Reduction of Graphene Basal Surfaces Oxidized by Atomic Oxygen*, The Journal of Physical Chemistry C **115**, 4730 (2011).

[296] J. P. Rourke, P. A. Pandey, J. J. Moore, M. Bates, I. A. Kinloch, R. J. Young, and N. R. Wilson, *The Real Graphene Oxide Revealed: Stripping the Oxidative Debris from the Graphene-like Sheets*, Angewandte Chemie International Edition **50**, 3173 (2011).

[297] H. R. Thomas, S. P. Day, W. E. Woodruff, C. Vallés, R. J. Young, I. A. Kinloch, G. W. Morley, J. V. Hanna, N. R. Wilson, and J. P. Rourke, *Deoxygenation of Graphene Oxide: Reduction or Cleaning?*, Chemistry of Materials **25**, 3580 (2013).

[298] H. R. Thomas, C. Vallés, R. J. Young, I. A. Kinloch, N. R. Wilson, and J. P. Rourke, *Identifying the fluorescence of graphene oxide*, Journal of Materials Chemistry C **1**, 338 (2013).

[299] T. Wang, H. Ade, X. Wang, L. Qiao, S. Wang, X. Wang, W. Zheng, and Y. Liu, *Electrical conductivity of alkaline-reduced graphene oxide*, Chem. Res. Chin. Univ. **27**, 857 (2011).

[300] A. M. Dimiev and T. A. Polson, *Contesting the two-component structural model of graphene oxide and reexamining the chemistry of graphene oxide in basic media*, Carbon **93**, 544 (2015).

[301] A. Naumov, F. Grote, M. Overgaard, A. Roth, C. E. Halbig, K. Nørgaard, D. M. Guldi, and S. Eigler, *Graphene Oxide: A One- versus Two-Component Material*, Journal of the American Chemical Society (2016).

[302] G. Bertoni and J. Verbeeck, *Accuracy and precision in model based EELS quantification*, Ultramicroscopy **108**, 782 (2008).

[303] F. de la Peña, M.-H. Berger, J.-F. Hochepied, F. Dynys, O. Stephan, and M. Walls, *Mapping titanium and tin oxide phases using EELS: An application of independent component analysis*, Ultramicroscopy **111**, 169 (2011).

[304] F. de la Peña, P. Burdet, M. Sarahan, M. Nord, T. Ostasevicius, J. Taillon, A. Eljarrat, S. Mazzucco, V. T. F. G. Donval, L. F. Zagonel, I. Iyengar, and M. Walls, Hyperspy 0.8, 2015.

[305] X. Liang, Y. Wang, H. Zheng, and Z. Wu, *X-ray absorption spectroscopy study on the thermal and hydrazine reduction of graphene oxide*, Journal of Electron Spectroscopy and Related Phenomena **196**, 89 (2014).

[306] N. Lu, D. Yin, Z. Li, and J. Yang, *Structure of Graphene Oxide: Thermodynamics versus Kinetics*, J. Phys. Chem. C **115**, 11991 (2011).

[307] D. C. Elias, R. R. Nair, T. M. G. Mohiuddin, S. V. Morozov, P. Blake, M. P. Halsall, A. C. Ferrari, D. W. Boukhvalov, M. I. Katsnelson, A. K. Geim, and K. S. Novoselov, *Control of Graphene's Properties by Reversible Hydrogenation: Evidence for Graphane*, Science **323**, 610 (2009).

[308] R. Jones and P. R. Briddon, *The Ab Initio Cluster Method and the Dynamics of Defects in Semiconductors*, Semiconduct. Semimet. **51**, 287 (1998).

[309] M. Rayson and P. Briddon, *Rapid iterative method for electronic-structure eigenproblems using localised basis functions*, Comput. Phys. Commun. **178**, 128 (2008).

[310] C. Hartwigsen, S. Goedecker, and J. Hutter, *Relativistic separable dual-space Gaussian pseudopotentials from H to Rn*, Phys. Rev. B **58**, 3641 (1998).

[311] P. Wagner, C. P. Ewels, V. V. Ivanovskaya, P. R. Briddon, A. Pateau, and B. Humbert, *Ripple edge engineering of graphene nanoribbons*, Phys. Rev. B **84**, 134110 (2011).

[312] Q. Zhu, Y. Lu, and J. Jiang, *Stability and Properties of Two-Dimensional Graphene Hydroxide*, J. Phys. Chem. Lett. **2**, 1310 (2011).

[313] J. D. Núñez, A. M. Benito, R. González, J. Aragón, R. Arenal, and W. K. Maser, *Integration and bioactivity of hydroxyapatite grown on carbon nanotubes and graphene oxide*, Carbon **79**, 590 (2014).

[314] A. Dazzi, R. Prazeres, F. Glotin, and J. M. Ortega, *Local infrared microspectroscopy with subwavelength spatial resolution with an atomic force microscope tip used as a photothermal sensor*, Optics Letters **30**, 2388 (2005).

[315] J. C. Meyer, A. K. Geim, M. I. Katsnelson, K. S. Novoselov, T. J. Booth, and S. Roth, *The structure of suspended graphene sheets*, Nature **446**, 60 (2007).

[316] N. R. Wilson, P. A. Pandey, R. Beanland, J. P. Rourke, U. Lupo, G. Rowlands, and R. A. Römer, *On the structure and topography of free-standing chemically modified graphene*, New Journal of Physics **12**, 125010 (2010).

[317] J. J. Macklin, J. K. Trautman, T. D. Harris, and L. E. Brus, *Imaging and Time-Resolved Spectroscopy of Single Molecules at an Interface*, Science **272**, 255 (1996).

[318] J. K. Trautman, J. J. Macklin, L. E. Brus, and E. Betzig, *Near-field spectroscopy of single molecules at room temperature*, Nature **369**, 40 (1994).

[319] W. P. Ambrose, P. M. Goodwin, J. C. Martin, and R. A. Keller, *Single molecule detection and photochemistry on a surface using near-field optical excitation*, Physical Review Letters **72**, 160 (1994).

[320] X. S. Xie and R. C. Dunn, *Probing Single Molecule Dynamics*, Science **265**, 361 (1994).

[321] W. W. E. Moerner, *Nobel Lecture: Single-molecule spectroscopy, imaging, and photocontrol: Foundations for super-resolution microscopy*, Reviews of Modern Physics **87**, 1183 (2015).

[322] S. Kummer, F. Kulzer, R. Kettner, T. BaschÃľ, C. Tietz, C. Glowatz, and C. Kryschi, *Absorption, excitation, and emission spectroscopy of terrylene in p-terphenyl: Bulk measurements and single molecule studies*, The Journal of Chemical Physics **107**, 7673 (1997).

[323] A. M. Stoneham, *Shapes of Inhomogeneously Broadened Resonance Lines in Solids*, Reviews of Modern Physics **41**, 82 (1969).

[324] P. Tamarat, A. Maali, B. Lounis, and M. Orrit, *Ten Years of Single-Molecule Spectroscopy*, The Journal of Physical Chemistry A **104**, 1 (2000).

[325] W. E. Moerner, *Illuminating Single Molecules in Condensed Matter*, Science **283**, 1670 (1999).

[326] W. P. Ambrose and W. E. Moerner, *Fluorescence spectroscopy and spectral diffusion of single impurity molecules in a crystal*, Nature **349**, 225 (1991).

[327] H. P. Lu and X. S. Xie, *Single-molecule spectral fluctuations at room temperature*, Nature **385**, 143 (1997).

[328] S. Weiss, *Fluorescence Spectroscopy of Single Biomolecules*, Science **283**, 1676 (1999).

[329] T. Cordes and S. A. Blum, *Opportunities and challenges in single-molecule and single-particle fluorescence microscopy for mechanistic studies of chemical reactions*, Nature Chemistry **5**, 993 (2013).

[330] J. Park, A. N. Pasupathy, J. I. Goldsmith, C. Chang, Y. Yaish, J. R. Petta, M. Rinkoski, J. P. Sethna, H. D. Abruña, P. L. McEuen, and D. C. Ralph, *Coulomb blockade and the Kondo effect in single-atom transistors*, Nature **417**, 722 (2002).

[331] G. Reecht, F. Scheurer, V. Speisser, Y. J. Dappe, F. Mathevet, and G. Schull, *Electroluminescence of a Polythiophene Molecular Wire Suspended between a Metallic Surface and the Tip of a Scanning Tunneling Microscope*, Physical Review Letters **112** (2014).

[332] L. Bogani and W. Wernsdorfer, *Molecular spintronics using single-molecule magnets*, Nature Materials **7**, 179 (2008).

[333] R. M. Dickson, A. B. Cubitt, R. Y. Tsien, and W. E. Moerner, *On/off blinking and switching behaviour of single molecules of green fluorescent protein*, Nature **388**, 355 (1997).

[334] T. Basché and W. E. Moerner, *Optical modification of a single impurity molecule in a solid*, Nature **355**, 335 (1992).

[335] W. E. Moerner, T. Plakhotnik, T. Irngartinger, M. Croci, V. Palm, and U. P. Wild, *Optical Probing of Single Molecules of Terrylene in a Shpol'kii Matrix: A Two-State Single-Molecule Switch*, The Journal of Physical Chemistry **98**, 7382 (1994).

[336] F. Kulzer, S. Kummer, R. Matzke, C. Brauchle, and T. Basché, *Single-molecule optical switching of terrylene in p-terphenyl*, Nature **387**, 688 (1997).

[337] X. H. Qiu, G. V. Nazin, and W. Ho, *Mechanisms of Reversible Conformational Transitions in a Single Molecule*, Physical Review Letters **93** (2004).

[338] M. Lastapis, *Picometer-Scale Electronic Control of Molecular Dynamics Inside a Single Molecule*, Science **308**, 1000 (2005).

[339] S. W. Wu, N. Ogawa, G. V. Nazin, and W. Ho, *Conductance Hysteresis and Switching in a Single-Molecule Junction*, The Journal of Physical Chemistry C **112**, 5241 (2008).

[340] T. Ha, T. Enderle, D. F. Ogletree, D. S. Chemla, P. R. Selvin, and S. Weiss, *Probing the interaction between two single molecules: fluorescence resonance energy transfer between a single donor and a single acceptor.*, Proceedings of the National Academy of Sciences **93**, 6264 (1996).

[341] K. P. F. Janssen, G. De Cremer, R. K. Neely, A. V. Kubarev, J. Van Loon, J. A. Martens, D. E. De Vos, M. B. J. Roeffaers, and J. Hofkens, *Single molecule methods for the study of catalysis: from enzymes to heterogeneous catalysts*, Chem. Soc. Rev. **43**, 990 (2014).

[342] E. Betzig, *Proposed method for molecular optical imaging*, Optics Letters **20**, 237 (1995).

[343] E. Betzig, G. H. Patterson, R. Sougrat, O. W. Lindwasser, S. Olenych, J. S. Bonifacino, M. W. Davidson, J. Lippincott-Schwartz, and H. F. Hess, *Imaging Intracellular Fluorescent Proteins at Nanometer Resolution*, Science **313**, 1642 (2006).

[344] E. Betzig, *Single Molecules, Cells, and Super-Resolution Optics (Nobel Lecture)*, Angewandte Chemie International Edition **54**, 8034 (2015).

[345] S. W. Hell, *Nanoscopy with Focused Light (Nobel Lecture)*, Angewandte Chemie International Edition **54**, 8054 (2015).

[346] M. J. Rust, M. Bates, and X. Zhuang, *Sub-diffraction-limit imaging by stochastic optical reconstruction microscopy (STORM)*, Nature Methods **3**, 793 (2006).

[347] S. T. Hess, T. P. Girirajan, and M. D. Mason, *Ultra-High Resolution Imaging by Fluorescence Photoactivation Localization Microscopy*, Biophysical Journal **91**, 4258 (2006).

[348] C. Brunel, B. Lounis, P. Tamarat, and M. Orrit, *Triggered Source of Single Photons based on Controlled Single Molecule Fluorescence*, Physical Review Letters **83**, 2722 (1999).

[349] K. G. Lee, X. W. Chen, H. Eghlidi, P. Kukura, R. Lettow, A. Renn, V. Sandoghdar, and S. Götzinger, *A planar dielectric antenna for directional single-photon emission and near-unity collection efficiency*, Nature Photonics **5**, 166 (2011).

[350] J.-B. Trebbia, P. Tamarat, and B. Lounis, *Indistinguishable near-infrared single photons from an individual organic molecule*, Physical Review A **82** (2010).

[351] P. Siyushev, G. Stein, J. Wrachtrup, and I. Gerhardt, *Molecular photons interfaced with alkali atoms*, Nature **509**, 66 (2014).

[352] B. Lounis and M. Orrit, *Single-photon sources*, Reports on Progress in Physics **68**, 1129 (2005).

[353] A. Kiraz, M. Ehrl, T. Hellerer, o. E. MüstecaplÄśoğlu, C. Bräuchle, and A. Zumbusch, *Indistinguishable Photons from a Single Molecule*, Physical Review Letters **94** (2005).

[354] J. L. O'Brien, A. Furusawa, and J. Vuć, *Photonic quantum technologies*, Nature Photonics **3**, 687 (2009).

[355] P. J. Bustard, R. Lausten, D. G. England, and B. J. Sussman, *Toward Quantum Processing in Molecules: A THz-Bandwidth Coherent Memory for Light*, Physical Review Letters **111** (2013).

[356] Y. L. A. Rezus, S. G. Walt, R. Lettow, A. Renn, G. Zumofen, S. Götzinger, and V. Sandoghdar, *Single-Photon Spectroscopy of a Single Molecule*, Physical Review Letters **108** (2012).

[357] J. M. Tour, M. Kozaki, and J. M. Seminario, *Molecular Scale Electronics: A Synthetic/Computational Approach to Digital Computing*, Journal of the American Chemical Society **120**, 8486 (1998).

[358] A. Troisi and M. Ratner, *Molecular Signatures in the Transport Properties of Molecular Wire Junctions: What Makes a Junction "Molecular"?*, Small **2**, 172 (2006).

[359] S. V. Aradhya and L. Venkataraman, *Single-molecule junctions beyond electronic transport*, Nature Nanotechnology **8**, 399 (2013).

[360] A. Nitzan, *Electron Transport in Molecular Wire Junctions*, Science **300**, 1384 (2003).

[361] M. A. Reed, *Conductance of a Molecular Junction*, Science **278**, 252 (1997).

[362] X. D. Cui, *Reproducible Measurement of Single-Molecule Conductivity*, Science **294**, 571 (2001).

[363] S. W. Wu, G. V. Nazin, X. Chen, X. H. Qiu, and W. Ho, *Control of Relative Tunneling Rates in Single Molecule Bipolar Electron Transport*, Physical Review Letters **93** (2004).

[364] H. Park, J. Park, A. K. L. Lim, E. H. Anderson, A. P. Alivisatos, and P. L. McEuen, *Nanomechanical oscillations in a single-C60 transistor*, Nature **407**, 57 (2000).

[365] W. Liang, M. P. Shores, M. Bockrath, J. R. Long, and H. Park, *Kondo resonance in a single-molecule transistor*, Nature **417**, 725 (2002).

[366] W.-Y. Lo, W. Bi, L. Li, I. H. Jung, and L. Yu, *Edge-on Gating Effect in Molecular Wires*, Nano Letters **15**, 958 (2015).

[367] J. Hwang, M. Pototschnig, R. Lettow, G. Zumofen, A. Renn, S. Götzinger, and V. Sandoghdar, *A single-molecule optical transistor*, Nature **460**, 76 (2009).

[368] A. Aviram and M. A. Ratner, *Molecular rectifiers*, Chemical Physics Letters **29**, 277 (1974).

[369] P. Kornilovitch, A. Bratkovsky, and R. Stanley Williams, *Current rectification by molecules with asymmetric tunneling barriers*, Physical Review B **66** (2002).

[370] C. P. Collier, *Electronically Configurable Molecular-Based Logic Gates*, Science **285**, 391 (1999).

[371] Z. J. Donhauser, *Conductance Switching in Single Molecules Through Conformational Changes*, Science **292**, 2303 (2001).

[372] A. S. Blum, J. G. Kushmerick, D. P. Long, C. H. Patterson, J. C. Yang, J. C. Henderson, Y. Yao, J. M. Tour, R. Shashidhar, and B. R. Ratna, *Molecularly inherent voltage-controlled conductance switching*, Nature Materials **4**, 167 (2005).

[373] S. Sanvito, *Molecular spintronics*, Chemical Society Reviews **40**, 3336 (2011).

[374] M. Galbiati, S. Tatay, C. Barraud, A. V. Dediu, F. Petroff, R. Mattana, and P. Seneor, *Spinterface: Crafting spintronics at the molecular scale*, MRS Bulletin **39**, 602 (2014).

[375] E. A. Osorio, K. Moth-Poulsen, H. S. J. van der Zant, J. Paaske, P. Hedegård, K. Flensberg, J. Bendix, and T. Bj, *Electrical Manipulation of Spin States in a Single Electrostatically Gated Transition-Metal Complex*, Nano Letters **10**, 105 (2010).

[376] F. Pointillart, J. Jung, R. Berraud-Pache, B. Le Guennic, V. Dorcet, S. Golhen, O. Cador, O. Maury, Y. Guyot, S. Decurtins, S.-X. Liu, and L. Ouahab, *Luminescence and Single-Molecule Magnet Behavior in Lanthanide Complexes Involving a Tetrathiafulvalene-Fused Dipyridophenazine Ligand*, Inorganic Chemistry **54**, 5384 (2015).

[377] S. Fahrendorf, N. Atodiresei, C. Besson, V. Caciuc, F. Matthes, S. Blügel, P. Kögerler, D. E. Bürgler, and C. M. Schneider, *Accessing 4f-states in single-molecule spintronics*, Nature Communications **4** (2013).

[378] Perrin, *Fluorescence*, Annales de Physique **9**, 133 (1918).

[379] E. Betzig and R. J. Chichester, *Single Molecules Observed by Near-Field Scanning Optical Microscopy*, Science **262**, 1422 (1993).

[380] R. Kasper, B. Harke, C. Forthmann, P. Tinnefeld, S. W. Hell, and M. Sauer, *Single-Molecule STED Microscopy with Photostable Organic Fluorophores*, Small **6**, 1379 (2010).

[381] D. W. Pohl, W. Denk, and M. Lanz, *Optical stethoscopy: Image recording with resolution λ/20*, Applied Physics Letters **44**, 651 (1984).

[382] A. Lewis, M. Isaacson, A. Harootunian, and A. Muray, *Development of a 500 Å spatial resolution light microscope*, Ultramicroscopy **13**, 227 (1984).

[383] E. Betzig, A. Lewis, A. Harootunian, M. Isaacson, and E. Kratschmer, *Near Field Scanning Optical Microscopy (NSOM)*, Biophysical Journal **49**, 269 (1986).

[384] E. Betzig and J. K. Trautman, *Near-Field Optics: Microscopy, Spectroscopy, and Surface Modification Beyond the Diffraction Limit*, Science **257**, 189 (1992).

[385] W. P. Ambrose, P. M. Goodwin, R. A. Keller, and J. C. Martin, *Alterations of Single Molecule Fluorescence Lifetimes in Near-Field Optical Microscopy*, Science **265**, 364 (1994).

[386] J. Wrachtrup, C. von Borczyskowski, J. Bernard, M. Orritt, and R. Brown, *Optical detection of magnetic resonance in a single molecule*, Nature **363**, 244 (1993).

[387] M. Eigen and R. Rigler, *Sorting single molecules: application to diagnostics and evolutionary biotechnology*, Proc. Natl. Acad. Sci. U.S.A. **91**, 5740 (1994).

[388] R. Rigler, *Fluorescence correlations, single molecule detection and large number screening Applications in biotechnology*, Journal of Biotechnology **41**, 177 (1995).

[389] S. Nie, *Probing Single Molecules and Single Nanoparticles by Surface-Enhanced Raman Scattering*, Science **275**, 1102 (1997).

[390] K. Kneipp, Y. Wang, H. Kneipp, L. T. Perelman, I. Itzkan, R. R. Dasari, and M. S. Feld, *Single Molecule Detection Using Surface-Enhanced Raman Scattering (SERS)*, Physical Review Letters **78**, 1667 (1997).

[391] l. Mets and R. Rigler, *Submillisecond detection of single rhodamine molecules in water*, Journal of Fluorescence **4**, 259 (1994).

[392] S. Nie, D. T. Chiu, and R. N. Zare, *Probing individual molecules with confocal fluorescence microscopy*, Science **266**, 1018 (1994).

[393] T. Funatsu, Y. Harada, M. Tokunaga, K. Saito, and T. Yanagida, *Imaging of single fluorescent molecules and individual ATP turnovers by single myosin molecules in aqueous solution*, Nature **374**, 555 (1995).

[394] S. Nie and R. N. Zare, *OPTICAL DETECTION OF SINGLE MOLECULES*, Annual Review of Biophysics and Biomolecular Structure **26**, 567 (1997).

[395] S. W. Hell and J. Wichmann, *Breaking the diffraction resolution limit by stimulated emission: stimulated-emission-depletion fluorescence microscopy*, Optics Letters **19**, 780 (1994).

[396] S. W. Hell, *Far-Field Optical Nanoscopy*, Science **316**, 1153 (2007).

[397] V. Westphal and S. W. Hell, *Nanoscale Resolution in the Focal Plane of an Optical Microscope*, Physical Review Letters **94** (2005).

[398] S.-E. Zhu et al., *Self-Decoupled Porphyrin with a Tripodal Anchor for Molecular-Scale Electroluminescence*, Journal of the American Chemical Society **135**, 15794 (2013).

[399] C. Chen, P. Chu, C. A. Bobisch, D. L. Mills, and W. Ho, *Viewing the Interior of a Single Molecule: Vibronically Resolved Photon Imaging at Submolecular Resolution*, Physical Review Letters **105** (2010).

[400] J. S. Foster, J. E. Frommer, and P. C. Arnett, *Molecular manipulation using a tunnelling microscope*, Nature **331**, 324 (1988).

[401] J. A. Stroscio and D. M. Eigler, *Atomic and Molecular Manipulation with the Scanning Tunneling Microscope*, Science **254**, 1319 (1991).

[402] G. Dujardin, R. E. Walkup, and P. Avouris, *Dissociation of Individual Molecules with Electrons from the Tip of a Scanning Tunneling Microscope*, Science **255**, 1232 (1992).

[403] D. P. E. Smith, M. D. Kirk, and C. F. Quate, *Molecular images and vibrational spectroscopy of sorbic acid with the scanning tunneling microscope*, The Journal of Chemical Physics **86**, 6034 (1987).

[404] R. Berndt, R. Gaisch, J. K. Gimzewski, B. Reihl, R. R. Schlittler, W. D. Schneider, and M. Tschudy, *Photon Emission at Molecular Resolution Induced by a Scanning Tunneling Microscope*, Science **262**, 1425 (1993).

[405] E. Flaxer, O. Sneh, and O. Cheshnovsky, *Molecular Light Emission Induced by Inelastic Electron Tunneling*, Science **262**, 2012 (1993).

[406] B. C. Stipe, *Single-Molecule Vibrational Spectroscopy and Microscopy*, Science **280**, 1732 (1998).

[407] B. C. Stipe, M. A. Rezaei, and W. Ho, *Coupling of Vibrational Excitation to the Rotational Motion of a Single Adsorbed Molecule*, Physical Review Letters **81**, 1263 (1998).

[408] S.-W. Hla, L. Bartels, G. Meyer, and K.-H. Rieder, *Inducing All Steps of a Chemical Reaction with the Scanning Tunneling Microscope Tip: Towards Single Molecule Engineering*, Physical Review Letters **85**, 2777 (2000).

[409] A. J. Mayne, G. Dujardin, G. Comtet, and D. Riedel, *Electronic Control of Single-Molecule Dynamics*, Chemical Reviews **106**, 4355 (2006).

[410] L. Soukiassian, A. J. Mayne, G. Comtet, L. Hellner, G. Dujardin, and A. Gourdon, *Selective internal manipulation of a single molecule by scanning tunneling microscopy*, The Journal of Chemical Physics **122**, 134704 (2005).

[411] M. Cranney, A. Mayne, A. Laikhtman, G. Comtet, and G. Dujardin, *STM excitation of individual biphenyl molecules on Si(100) surface: DIET or DIEF?*, Surface Science **593**, 139 (2005).

[412] G. Dujardin, E. Boer-Duchemin, E. Le Moal, A. Mayne, and D. Riedel, *DIET at the nanoscale*, Surface Science **643**, 13 (2016).

[413] S. W. Wu, G. V. Nazin, and W. Ho, *Intramolecular photon emission from a single molecule in a scanning tunneling microscope*, Physical Review B **77** (2008).

[414] H. Yang, A. J. Mayne, G. Comtet, G. Dujardin, Y. Kuk, S. Nagarajan, and A. Gourdon, *Single-molecule light emission at room temperature on a wide-band-gap semiconductor*, Physical Review B **90** (2014).

[415] X. H. Qiu, *Vibrationally Resolved Fluorescence Excited with Submolecular Precision*, Science **299**, 542 (2003).

[416] J. Lee, S. M. Perdue, A. Rodriguez Perez, and V. A. Apkarian, *Vibronic Motion with Joint Angstrom–Femtosecond Resolution Observed through Fano Progressions Recorded within One Molecule*, ACS Nano **8**, 54 (2014).

[417] E. Ćavar, M.-C. Blüm, M. Pivetta, F. Patthey, M. Chergui, and W.-D. Schneider, *Fluorescence and Phosphorescence from Individual $C_{60}$ Molecules Excited by Local Electron Tunneling*, Physical Review Letters **95** (2005).

[418] Z.-C. Dong, X.-L. Guo, A. S. Trifonov, P. S. Dorozhkin, K. Miki, K. Kimura, S. Yokoyama, and S. Mashiko, *Vibrationally Resolved Fluorescence from Organic Molecules near Metal Surfaces in a Scanning Tunneling Microscope*, Physical Review Letters **92** (2004).

[419] G. Tian and Y. Luo, *Fluorescence and Phosphorescence of Single $C_{60}$ Molecules as Stimulated by a Scanning Tunneling Microscope*, Angewandte Chemie International Edition **52**, 4814 (2013).

[420] Z. C. Dong, X. L. Zhang, H. Y. Gao, Y. Luo, C. Zhang, L. G. Chen, R. Zhang, X. Tao, Y. Zhang, J. L. Yang, and J. G. Hou, *Generation of molecular hot electroluminescence by resonant nanocavity plasmons*, Nature Photonics **4**, 50 (2010).

[421] N. L. Schneider and R. Berndt, *Plasmonic excitation of light emission and absorption by porphyrine molecules in a scanning tunneling microscope*, Physical Review B **86** (2012).

[422] L. Gross, F. Mohn, N. Moll, P. Liljeroth, and G. Meyer, *The Chemical Structure of a Molecule Resolved by Atomic Force Microscopy*, Science **325**, 1110 (2009).

[423] F. Mohn, L. Gross, N. Moll, and G. Meyer, *Imaging the charge distribution within a single molecule*, Nature Nanotechnology **7**, 227 (2012).

[424] K. Iwata, S. Yamazaki, P. Mutombo, P. Hapala, M. Ondráček, P. Jelínek, and Y. Sugimoto, *Chemical structure imaging of a single molecule by atomic force microscopy at room temperature*, Nature Communications **6**, 7766 (2015).

[425] P. Hapala, M. Švec, O. Stetsovych, N. J. van der Heijden, M. Ondráček, J. van der Lit, P. Mutombo, I. Swart, and P. Jelínek, *Mapping the electrostatic force field of single molecules from high-resolution scanning probe images*, Nature Communications **7**, 11560 (2016).

[426] C. Weiss, C. Wagner, C. Kleimann, M. Rohlfing, F. S. Tautz, and R. Temirov, *Imaging Pauli Repulsion in Scanning Tunneling Microscopy*, Physical Review Letters **105** (2010).

[427] L. Novotny and S. J. Stranick, *NEAR-FIELD OPTICAL MICROSCOPY AND SPECTROSCOPY WITH POINTED PROBES**, Annual Review of Physical Chemistry **57**, 303 (2006).

[428] A. Hartschuh, *Tip-enhanced optical spectroscopy*, Philosophical Transactions of the Royal Society A: Mathematical, Physical and Engineering Sciences **362**, 807 (2004).

[429] T. Kalkbrenner, M. Ramstein, J. Mlynek, and V. Sandoghdar, *A single gold particle as a probe for apertureless scanning near-field optical microscopy*, Journal of Microscopy **202**, 72 (2001).

[430] H. G. Frey, S. Witt, K. Felderer, and R. Guckenberger, *High-Resolution Imaging of Single Fluorescent Molecules with the Optical Near-Field of a Metal Tip*, Physical Review Letters **93** (2004).

[431] S. Kühn, U. H, L. Rogobete, and V. Sandoghdar, *Enhancement of Single-Molecule Fluorescence Using a Gold Nanoparticle as an Optical Nanoantenna*, Physical Review Letters **97** (2006).

[432] P. Anger, P. Bharadwaj, and L. Novotny, *Enhancement and Quenching of Single-Molecule Fluorescence*, Physical Review Letters **96** (2006).

[433] P. Bharadwaj and L. Novotny, *Spectral dependence of single molecule fluorescence enhancement*, Optics Express **15**, 14266 (2007).

[434] A. Kinkhabwala, Z. Yu, S. Fan, Y. Avlasevich, K. Müllen, and W. E. Moerner, *Large single-molecule fluorescence enhancements produced by a bowtie nanoantenna*, Nature Photonics **3**, 654 (2009).

[435] J. Steidtner and B. Pettinger, *Tip-Enhanced Raman Spectroscopy and Microscopy on Single Dye Molecules with 15 nm Resolution*, Physical Review Letters **100** (2008).

[436] M. D. Sonntag, J. M. Klingsporn, L. K. Garibay, J. M. Roberts, J. A. Dieringer, T. Seideman, K. A. Scheidt, L. Jensen, G. C. Schatz, and R. P. Van Duyne, *Single-Molecule Tip-Enhanced Raman Spectroscopy*, The Journal of Physical Chemistry C **116**, 478 (2012).

[437] C. C. Neacsu, J. Dreyer, N. Behr, and M. B. Raschke, *Scanning-probe Raman spectroscopy with single-molecule sensitivity*, Physical Review B **73** (2006).

[438] R. Zhang, Y. Zhang, Z. C. Dong, S. Jiang, C. Zhang, L. G. Chen, L. Zhang, Y. Liao, J. Aizpurua, Y. Luo, J. L. Yang, and J. G. Hou, *Chemical mapping of a single molecule by plasmon-enhanced Raman scattering*, Nature **498**, 82 (2013).

[439] B. W. Smith, M. Monthioux, and D. E. Luzzi, *Encapsulated $C_{60}$ in carbon nanotubes*, Nature **396**, 323 (1998).

[440] K. Hirahara, K. Suenaga, S. Bandow, H. Kato, T. Okazaki, H. Shinohara, and S. Iijima, *One-Dimensional Metallofullerene Crystal Generated Inside Single-Walled Carbon Nanotubes*, Physical Review Letters **85**, 5384 (2000).

[441] J. Sloan, R. E. Dunin-Borkowski, J. L. Hutchison, K. S. Coleman, V. Clifford Williams, J. B. Claridge, A. P. York, C. Xu, S. R. Bailey, G. Brown, S. Friedrichs, and M. L. Green, *The size distribution, imaging and obstructing properties of $C_{60}$ and higher fullerenes formed within arc-grown single walled carbon nanotubes*, Chemical Physics Letters **316**, 191 (2000).

[442] K. Suenaga, *Element-Selective Single Atom Imaging*, Science **290**, 2280 (2000).

[443] J. H. Warner, Y. Ito, M. Zaka, L. Ge, T. Akachi, H. Okimoto, K. Porfyrakis, A. A. R. Watt, H. Shinohara, and G. A. D. Briggs, *Rotating Fullerene Chains in Carbon Nanopeapods*, Nano Letters **8**, 2328 (2008).

[444] E. Nakamura, *Movies of Molecular Motions and Reactions: The Single-Molecule, Real-Time Transmission Electron Microscope Imaging Technique*, Angewandte Chemie International Edition **52**, 236 (2013).

[445] K. Harano, S. Takenaga, S. Okada, Y. Niimi, N. Yoshikai, H. Isobe, K. Suenaga, H. Kataura, M. Koshino, and E. Nakamura, *Conformational Analysis of Single Perfluoroalkyl Chains by Single-Molecule Real-Time Transmission Electron Microscopic Imaging*, Journal of the American Chemical Society **136**, 466 (2014).

[446] L. H. Tizei, Z. Liu, M. Koshino, Y. Iizumi, T. Okazaki, and K. Suenaga, *Single Molecular Spectroscopy: Identification of Individual Fullerene Molecules*, Physical Review Letters **113** (2014).

[447] Z. Liu, K. Suenaga, and S. Iijima, *Imaging the Structure of an Individual $C_{60}$ Fullerene Molecule and its Deformation Process Using HRTEM with*

*Atomic Sensitivity*, Journal of the American Chemical Society **129**, 6666 (2007).

[448] M. Koshino, Y. Niimi, E. Nakamura, H. Kataura, T. Okazaki, K. Suenaga, and S. Iijima, *Analysis of the reactivity and selectivity of fullerene dimerization reactions at the atomic level*, Nature Chemistry **2**, 117 (2010).

[449] D. A. Morgan, J. Sloan, and M. L. H. Green, *Direct imaging of o-carborane molecules within single walled carbon nanotubes*, Chemical Communications , 2442 (2002).

[450] M. Koshino, T. Tanaka, N. Solin, K. Suenaga, H. Isobe, and E. Nakamura, *Imaging of Single Organic Molecules in Motion*, Science **316**, 853 (2007).

[451] T. Okazaki, Y. Iizumi, S. Okubo, H. Kataura, Z. Liu, K. Suenaga, Y. Tahara, M. Yudasaka, S. Okada, and S. Iijima, *Coaxially Stacked Coronene Columns inside Single-Walled Carbon Nanotubes*, Angewandte Chemie **123**, 4955 (2011).

[452] I. V. Anoshkin, A. V. Talyzin, A. G. Nasibulin, A. V. Krasheninnikov, H. Jiang, R. M. Nieminen, and E. I. Kauppinen, *Coronene Encapsulation in Single-Walled Carbon Nanotubes: Stacked Columns, Peapods, and Nanoribbons*, ChemPhysChem **15**, 1660 (2014).

[453] T. W. Chamberlain, J. Biskupek, S. T. Skowron, P. A. Bayliss, E. Bichoutskaia, U. Kaiser, and A. N. Khlobystov, *Isotope Substitution Extends the Lifetime of Organic Molecules in Transmission Electron Microscopy*, Small **11**, 622 (2015).

[454] J. C. Meyer, C. O. Girit, M. F. Crommie, and A. Zettl, *Imaging and dynamics of light atoms and molecules on graphene*, Nature **454**, 319 (2008).

[455] R. R. Nair, P. Blake, J. R. Blake, R. Zan, S. Anissimova, U. Bangert, A. P. Golovanov, S. V. Morozov, A. K. Geim, K. S. Novoselov, and T. Latychevskaia, *Graphene as a transparent conductive support for studying biological molecules by transmission electron microscopy*, Applied Physics Letters **97**, 153102 (2010).

[456] F. Schäffel, M. Wilson, and J. H. Warner, *Motion of Light Adatoms and Molecules on the Surface of Few-Layer Graphene*, ACS Nano **5**, 9428 (2011).

[457] J. Choe, Y. Lee, L. Fang, G.-D. Lee, Z. Bao, and K. Kim, *Direct imaging of rotating molecules anchored on graphene*, Nanoscale **8**, 13174 (2016).

[458] Z. Liu, L. Lavis, and E. Betzig, *Imaging Live-Cell Dynamics and Structure at the Single-Molecule Level*, Molecular Cell **58**, 644 (2015).

[459] D. Smith, R. Polk, and T. Miller, *Measurement of the response of several organic scintillators to electrons, protons and deuterons*, Nuclear Instruments and Methods **64**, 157 (1968).

[460] D. L. Horrocks, Some Recent Developments in Organic Scintillators, in *Developments in Applied Spectroscopy: Selected papers from the Eighteenth Annual Mid-America Spectroscopy Symposium Held in Chicago, Illinois May 15–18, 1967*, edited by W. K. Baer, A. J. Perkins, and E. L. Grove, pages 145–160, Springer US, Boston, MA, 1968.

[461] J. B. Birks, *Scintillations from Organic Crystals: Specific Fluorescence and Relative Response to Different Radiations*, Proceedings of the Physical Society. Section A **64**, 874 (1951).

[462] P. J. Fisher, W. S. Wessels, A. B. Dietz, and F. G. Prendergast, *Enhanced biological cathodoluminescence*, Optics Communications **281**, 1901 (2008).

[463] N. de Jonge and F. M. Ross, *Electron microscopy of specimens in liquid*, Nature Nanotechnology **6**, 695 (2011).

[464] M. Mets and A. Lagasse, *An investigation of some organic chemicals as cathodoluminescent dyes using the scanning electron microscope*, Journal of Microscopy **94**, 151 (1971).

[465] M. Mets, K. J. Howlett, and A. D. Yoffe, *Cathodoluminescence spectra of organic compounds*, Journal of Microscopy **102**, 125 (1974).

[466] J. Trautman and J. Macklin, *Time-resolved spectroscopy of single molecules using near-field and far-field optics*, Chemical Physics **205**, 221 (1996).

[467] J. Repp, G. Meyer, S. M. Stojković, A. Gourdon, and C. Joachim, *Molecules on Insulating Films: Scanning-Tunneling Microscopy Imaging of Individual Molecular Orbitals*, Physical Review Letters **94** (2005).

[468] F. Geng, Y. Kuang, Y. Yu, Y. Liao, Y. Zhang, Y. Zhang, and Z. Dong, *Tunneling electron induced luminescence from porphyrin molecules on monolayer graphene*, Journal of Luminescence **157**, 39 (2015).

[469] A. Bellec, F. Ample, D. Riedel, G. Dujardin, and C. Joachim, *Imaging Molecular Orbitals by Scanning Tunneling Microscopy on a Passivated Semiconductor*, Nano Letters **9**, 144 (2009).

[470] L. H. G. Tizei and M. Kociak, *Spectrally and spatially resolved cathodoluminescence of nanodiamonds: local variations of the $NV^0$ emission properties*, Nanotechnology **23**, 175702 (2012).

[471] A. Catellani, M. Posternak, A. Baldereschi, and A. J. Freeman, *Bulk and surface electronic structure of hexagonal boron nitride*, Physical Review B **36**, 6105 (1987).

[472] S. Joshi, F. Bischoff, R. Koitz, D. Ecija, K. Seufert, A. P. Seitsonen, J. Hutter, K. Diller, J. I. Urgel, H. Sachdev, J. V. Barth, and W. Auwärter, *Control of Molecular Organization and Energy Level Alignment by an Electronically Nanopatterned Boron Nitride Template*, ACS Nano **8**, 430 (2014).

[473] V. V. Korolkov, S. A. Svatek, A. Summerfield, J. Kerfoot, L. Yang, T. Taniguchi, K. Watanabe, N. R. Champness, N. A. Besley, and P. H. Beton, *van der Waals-Induced Chromatic Shifts in Hydrogen-Bonded Two-Dimensional Porphyrin Arrays on Boron Nitride*, ACS Nano , 150914094420003 (2015).

[474] J. N. Coleman et al., *Two-Dimensional Nanosheets Produced by Liquid Exfoliation of Layered Materials*, Science **331**, 568 (2011).

[475] R. Bourrellier, *Luminescence at Defects in h-BN : Excitons at Stacking Faults and Single Photon Emitters*, PhD thesis, 2014, Thèse de doctorat dirigée par Stephan, Odile Physique Paris 11 2014 2014PA112285.

[476] J. Kotakoski, C. H. Jin, O. Lehtinen, K. Suenaga, and A. V. Krasheninnikov, *Electron knock-on damage in hexagonal boron nitride monolayers*, Physical Review B **82** (2010).

[477] P. Jaffrennou, J. Barjon, J.-S. Lauret, B. Attal-Trétout, F. Ducastelle, and A. Loiseau, *Origin of the excitonic recombinations in hexagonal boron nitride by spatially resolved cathodoluminescence spectroscopy*, Journal of Applied Physics **102**, 116102 (2007).

[478] L. Museur and A. Kanaev, *Near band-gap photoluminescence properties of hexagonal boron nitride*, Journal of Applied Physics **103**, 103520 (2008).

[479] E. Tiede and H. Tomaschek, *Über das aktivierende Element im leuchtenden Borstickstoff*, Zeitschrift für anorganische und allgemeine Chemie **147**, 111 (1925).

[480] M. G. Silly, P. Jaffrennou, J. Barjon, J.-S. Lauret, F. Ducastelle, A. Loiseau, E. Obraztsova, B. Attal-Tretout, and E. Rosencher, *Luminescence properties of hexagonal boron nitride: Cathodoluminescence and photoluminescence spectroscopy measurements*, Physical Review B **75** (2007).

[481] K. Hara, X. Liu, M. Yamauchi, Y. Kawanishi, H. Kominami, and Y. Nakanishi, *Effects of annealing on 320 nm cathodoluminescence from hexagonal boron nitride powders*, Phys. Status Solidi C **8**, 2509 (2011).

[482] X. Z. Du, J. Li, J. Y. Lin, and H. X. Jiang, *The origin of deep-level impurity transitions in hexagonal boron nitride*, Applied Physics Letters **106**, 021110 (2015).

[483] T. Vuong, G. Cassabois, P. Valvin, A. Ouerghi, Y. Chassagneux, C. Voisin, and B. Gil, *Phonon-Photon Mapping in a Color Center in Hexagonal Boron Nitride*, Physical Review Letters **117** (2016).

[484] A. Zunger and A. Katzir, *Point defects in hexagonal boron nitride. II. Theoretical studies*, Phys. Rev. B **11**, 2378 (1975).

[485] E. M. Shishonok, *Luminescence centers in cubic boron nitride*, J Appl Spectrosc **74**, 272 (2007).

[486] C. Attaccalite, M. Bockstedte, A. Marini, A. Rubio, and L. Wirtz, *Coupling of excitons and defect states in boron-nitride nanostructures*, Physical Review B **83** (2011).

[487] G. Kern, G. Kresse, and J. Hafner, *Ab initio calculation of the lattice dynamics and phase diagram of boron nitride*, Phys. Rev. B **59**, 8551 (1999).

[488] S. Reich, A. C. Ferrari, R. Arenal, A. Loiseau, I. Bello, and J. Robertson, *Resonant Raman scattering in cubic and hexagonal boron nitride*, Physical Review B **71** (2005).

[489] J. Serrano, A. Bosak, R. Arenal, M. Krisch, K. Watanabe, T. Taniguchi, H. Kanda, A. Rubio, and L. Wirtz, *Vibrational Properties of Hexagonal Boron Nitride: Inelastic X-Ray Scattering and \textit{Ab Initio} Calculations*, Phys. Rev. Lett. **98**, 095503 (2007).

[490] F. e Silva, J. Menezes, G. Rocha, S. Alves, H. Brito, R. Longo, and O. Malta, *Emission quantum yield of europium (III) mixed complexes with thenoyltrifluoroacetonate and some aromatic ligands*, Journal of Alloys and Compounds **303-304**, 364 (2000).

[491] N. B. D. Lima, S. M. C. Gon, S. A. Júnior, and A. M. Simas, *A Comprehensive Strategy to Boost the Quantum Yield of Luminescence of Europium Complexes*, Scientific Reports **3** (2013).

[492] G. Muller, *Luminescent chiral lanthanide(iii) complexes as potential molecular probes*, Dalton Transactions , 9692 (2009).

[493] K. Binnemans, *Interpretation of europium(III) spectra*, Coordination Chemistry Reviews **295**, 1 (2015).

[494] U. Vetter, H. Hofsäss, and T. Taniguchi, *Visible cathodoluminescence from Eu-implanted single- and polycrystal c-BN annealed under high-temperature, high-pressure conditions*, Applied Physics Letters **84**, 4286 (2004).

[495] C. Adachi, M. A. Baldo, and S. R. Forrest, *Electroluminescence mechanisms in organic light emitting devices employing a europium chelate doped in a wide energy gap bipolar conducting host*, Journal of Applied Physics **87**, 8049 (2000).

[496] S. Pandya, J. Yu, and D. Parker, *Engineering emissive europium and terbium complexes for molecular imaging and sensing*, Dalton Transactions , 2757 (2006).

[497] C. R. Ronda, T. Jüstel, and H. Nikol, *Rare earth phosphors: fundamentals and applications*, Journal of Alloys and Compounds **275–277**, 669 (1998).

[498] T. Baby and V. Nampoori, *Flourescence emission of SrS: $Eu^{2+}$ phosphor-energy level splitting of $Eu^{2+}$*, Solid State Communications **81**, 367 (1992).

[499] G. Inan Akmehmet, S. Šturm, L. Bocher, M. Kociak, B. Ambrožič, and C. W. Ow-Yang, *Structure and Luminescence in Long Persistence Eu, Dy, and B Codoped Strontium Aluminate Phosphors: The Boron Effect*, Journal of the American Ceramic Society **99**, 2175 (2016).

[500] Z. Wang, I.-H. Chu, F. Zhou, and S. P. Ong, *Electronic Structure Descriptor for the Discovery of Narrow-Band Red-Emitting Phosphors*, Chemistry of Materials **28**, 4024 (2016).

[501] N. Kunkel, A. Meijerink, and H. Kohlmann, *Bright yellow and green Eu(ii) luminescence and vibronic fine structures in $LiSrH_3$, $LiBaH_3$ and their corresponding deuterides*, Physical Chemistry Chemical Physics **16**, 4807 (2014).

[502] J. M. Rey, J. R. G. Thorne, R. G. Denning, and H. Bill, *Inter- and intra-configurational transitions of europium (II) in $Ba_2Mg_3F_{10}$*, Journal of Physics: Condensed Matter **17**, 1861 (2005).

[503] J. Garcia and M. J. Allen, *Developments in the Coordination Chemistry of Europium(II): Developments in the Coordination Chemistry of Europium(II)*, European Journal of Inorganic Chemistry **2012**, 4550 (2012).

[504] S. H. M. Poort, W. P. Blokpoel, and G. Blasse, *Luminescence of $Eu^{2+}$ in barium and strontium aluminate and gallate*, Chemistry of Materials **7**, 1547 (1995).

[505] N. Sabbatini, M. Ciano, S. Dellonte, A. Bonazzi, and V. Balzani, *Absorption and emission properties of a europium(II) cryptate in aqueous solution*, Chemical Physics Letters **90**, 265 (1982).

[506] P. Gawryszewska, L. Jerzykiewicz, M. Pietraszkiewicz, J. Legendziewicz, and J. P. Riehl, *Photophysics and Crystal Structure of a Europium(III) Cryptate Incorporating 3,3'-Biisoquinoline-2,2'-dioxide*, Inorganic Chemistry **39**, 5365 (2000).

[507] O. M. Tedmann, S. K. Madan, P. Y. Zavalij, and S. R. Oliver, *Crystal structure and fluorescence of a europium (III) complex: EuCl3(2,2'-bipyridine N,N dioxide) $2CH_3OH$*, Inorganica Chimica Acta **360**, 3408 (2007).

[508] N. Nijegorodov, R. Mabbs, and W. Downey, *Evolution of absorption, fluorescence, laser and chemical properties in the series of compounds perylene, benzo(ghi)perylene and coronene*, Spectrochimica Acta Part A: Molecular and Biomolecular Spectroscopy **57**, 2673 (2001).

[509] J. M. Robertson and J. G. White, *Crystal Structure of Coronene*, Nature **154**, 605 (1944).

[510] K. Takazawa, J.-i. Inoue, and K. Mitsuishi, *Self-assembled coronene nanofibers: optical waveguide effect and magnetic alignment*, Nanoscale **6**, 4174 (2014).

[511] A. T. R. Williams, S. A. Winfield, and J. N. Miller, *Relative fluorescence quantum yields using a computer-controlled luminescence spectrometer*, The Analyst **108**, 1067 (1983).

[512] S. Hirayama, H. Sakai, Y. Araki, M. Tanaka, M. Imakawa, T. Wada, T. Takenobu, and T. Hasobe, *Systematic Control of the Excited-State Dynamics and Carrier-Transport Properties of Functionalized Benzo[ ghi ]perylene and Coronene Derivatives*, Chemistry - A European Journal , n/a (2014).

[513] T. Itoh, *Multiple fluorescence and the electronic relaxation processes of coronene vapor: The fluorescence from the $S_1$, $S_2$, and $S_3$ states*, Journal of Molecular Spectroscopy **252**, 115 (2008).

[514] R. Zhang, H. Zheng, and J. Shen, *Blue light-emitting diodes based on coronene-doped polymers*, Synthetic Metals **105**, 49 (1999).

[515] A. V. Talyzin, I. V. Anoshkin, A. V. Krasheninnikov, R. M. Nieminen, A. G. Nasibulin, H. Jiang, and E. I. Kauppinen, *Synthesis of Graphene Nanoribbons Encapsulated in Single-Walled Carbon Nanotubes*, Nano Letters **11**, 4352 (2011).

[516] X. Wan, K. Chen, J. Du, D. Liu, J. Chen, X. Lai, W. Xie, and J. Xu, *Enhanced Performance and Fermi-Level Estimation of Coronene-Derived Graphene Transistors on Self-Assembled Monolayer Modified Substrates in Large Areas*, The Journal of Physical Chemistry C **117**, 4800 (2013).

[517] M. Sakurai, M. Furukawa, K.-i. Mizuno, and A. Matsui, *Free-Exciton Luminescence and Weak-Exciton Scattering in Coronene Crystals*, Journal of the Physical Society of Japan **61**, 445 (1992).

[518] F. A. Rabuffetti, S. P. Culver, J. S. Lee, and R. L. Brutchey, *Local structural investigation of $Eu^{3+}$-doped $BaTiO_3$ nanocrystals*, Nanoscale **6**, 2909 (2014).

[519] F. J. d. Sousa, G. P. A. d. Lima, L. R. Ávila, K. J. Ciuffi, P. S. Calefi, and E. J. Nassar, *Incorporation of europium III complex into nanoparticles and films obtained by the Sol-Gel methodology*, Materials Research **13**, 71 (2010).

[520] T. Basché, S. Kummer, and C. Bräuchle, *Direct spectroscopic observation of quantum jumps of a single molecule*, Nature **373**, 132 (1995).

[521] W. E. Moerner and W. P. Ambrose, *Comment on "Single pentacene molecules detected by fluorescence excitation in a p-terphenyl crystal"*, Physical Review Letters **66**, 1376 (1991).

[522] L. Novotny and B. Hecht, *Principles of nano-optics*, Cambridge University Press, Cambridge, 2nd ed edition, 2012.

[523] C. Zhang, Y. S. Zhao, and J. Yao, *Organic composite nanomaterials: energy transfers and tunable luminescent behaviors*, New Journal of Chemistry **35**, 973 (2011).

[524] D. Kozawa, A. Carvalho, I. Verzhbitskiy, F. Giustiniano, Y. Miyauchi, S. Mouri, A. H. Castro Neto, K. Matsuda, and G. Eda, *Evidence for Fast Interlayer Energy Transfer in $MoSe_2$ /$WS_2$ Heterostructures*, Nano Letters **16**, 4087 (2016).

[525] D. L. Dexter, *A Theory of Sensitized Luminescence in Solids*, The Journal of Chemical Physics **21**, 836 (1953).

[526] M. Hallermann, S. Haneder, and E. Da Como, *Charge-transfer states in conjugated polymer/fullerene blends: Below-gap weakly bound excitons for polymer photovoltaics*, Applied Physics Letters **93**, 053307 (2008).

[527] P. Cudazzo, M. Gatti, A. Rubio, and F. Sottile, *Frenkel versus charge-transfer exciton dispersion in molecular crystals*, Physical Review B **88** (2013).

[528] F. Roth, P. Cudazzo, B. Mahns, M. Gatti, J. Bauer, S. Hampel, M. Nohr, H. Berger, M. Knupfer, and A. Rubio, *Loss spectroscopy of molecular solids: combining experiment and theory*, New Journal of Physics **15**, 125024 (2013).

[529] X. Blase and C. Attaccalite, *Charge-transfer excitations in molecular donor-acceptor complexes within the many-body Bethe-Salpeter approach*, Applied Physics Letters **99**, 171909 (2011).

[530] C. Faber, I. Duchemin, T. Deutsch, C. Attaccalite, V. Olevano, and X. Blase, *Electron-phonon coupling and charge-transfer excitations in organic systems from many-body perturbation theory: The Fiesta code, an efficient Gaussian-basis implementation of the GW and Bethe-Salpeter formalisms*, Journal of Materials Science **47**, 7472 (2012).

[531] N. S. Sariciftci, L. Smilowitz, A. J. Heeger, and F. Wudl, *Photoinduced Electron Transfer from a Conducting Polymer to Buckminsterfullerene*, Science **258**, 1474 (1992).

[532] I.-W. Hwang, D. Moses, and A. J. Heeger, *Photoinduced Carrier Generation in P3HT/PCBM Bulk Heterojunction Materials*, The Journal of Physical Chemistry C **112**, 4350 (2008).

[533] S. M. Falke, C. A. Rozzi, D. Brida, M. Maiuri, M. Amato, E. Sommer, A. De Sio, A. Rubio, G. Cerullo, E. Molinari, and C. Lienau, *Coherent ultrafast charge transfer in an organic photovoltaic blend*, Science **344**, 1001 (2014).

[534] K. Osada, M. Tanaka, S. Ohno, and T. Suzuki, *Photoinduced charge transfer from vacuum-deposited molecules to single-layer transition metal dichalcogenides*, Japanese Journal of Applied Physics **55**, 065201 (2016).

[535] M. Kasha, *Characterization of electronic transitions in complex molecules*, Discussions of the Faraday Society **9**, 14 (1950).

[536] M. D. Galanin and Z. A. Chizhikova, *Applications of fluorescence from the second excited electronic level of rhodamine 6G*, Journal of Applied Spectroscopy **37**, 1440 (1982).

[537] A. Nakayama, T. Taniguchi, Y. Kubota, K. Watanabe, S. Hishita, and H. Kanda, *Characterization of luminous-cubic boron-nitride single-crystals doped with $Eu^{3+}$ and $Tb^{3+}$ ions*, Applied Physics Letters **87**, 211913 (2005).

[538] F. P. Bundy, H. T. Hall, H. M. Strong, and R. H. Wentorf, *Man-Made Diamonds*, Nature **176**, 51 (1955).

[539] H. T. Hall, *The synthesis of diamond*, J. Chem. Educ. **38**, 484 (1961).

[540] P. B. Mirkarimi, K. F. McCarty, and D. L. Medlin, *Review of advances in cubic boron nitride film synthesis*, Materials Science and Engineering: R: Reports **21**, 47 (1997).

[541] L. C. Nistor, G. Van Tendeloo, and G. Dinca, *Crystallographic aspects related to the high pressure–high temperature phase transformation of boron nitride*, Philosophical Magazine **85**, 1145 (2005).

[542] S. Horiuchi, L.-L. He, M. Onoda, and M. Akaishi, *Monoclinic phase of boron nitride appearing during the hexagonal cubic phase transition at high pressure and high temperature*, Applied Physics Letters **68**, 182 (1996).

[543] D. McKenzie, W. McFall, W. Sainty, C. Davis, and R. Collins, *Compressive stress induced formation of cubic boron nitride*, Diamond and Related Materials **2**, 970 (1993).

[544] X. W. Zhang, H.-G. Boyen, N. Deyneka, P. Ziemann, F. Banhart, and M. Schreck, *Epitaxy of cubic boron nitride on (001)-oriented diamond*, Nature Materials **2**, 312 (2003).

[545] W. J. Zhang, X. Jiang, and S. Matsumoto, *High-quality, faceted cubic boron nitride films grown by chemical vapor deposition*, Applied Physics Letters **79**, 4530 (2001).

[546] J. Narayan and A. Bhaumik, *Research Update: Direct conversion of h-BN into pure c-BN at ambient temperatures and pressures in air*, APL Materials **4**, 020701 (2016).

[547] Y.-N. Xu and W. Y. Ching, *Calculation of ground-state and optical properties of boron nitrides in the hexagonal, cubic, and wurtzite structures*, Physical Review B **44**, 7787 (1991).

[548] N. Miyata, K. Moriki, O. Mishima, M. Fujisawa, and T. Hattori, *Optical constants of cubic boron nitride*, Physical Review B **40**, 12028 (1989).

[549] A. Agui, S. Shin, M. Fujisawa, Y. Tezuka, T. Ishii, Y. Muramatsu, O. Mishima, and K. Era, *Resonant soft-x-ray emission study in relation to the band structure of cBN*, Physical Review B **55**, 2073 (1997).

[550] D. A. Evans, A. G. McGlynn, B. M. Towlson, M. Gunn, D. Jones, T. E. Jenkins, R. Winter, and N. R. J. Poolton, *Determination of the optical band-gap energy of cubic and hexagonal boron nitride using luminescence excitation spectroscopy*, Journal of Physics: Condensed Matter **20**, 075233 (2008).

[551] G. Onida, L. Reining, and A. Rubio, *Electronic excitations: density-functional versus many-body Green's-function approaches*, Reviews of Modern Physics **74**, 601 (2002).

[552] M. P. Surh, S. G. Louie, and M. L. Cohen, *Quasiparticle energies for cubic BN, BP, and BAs*, Phys. Rev. B **43**, 9126 (1991).

[553] S. Galambosi, J. A. Soininen, K. Hämäläinen, E. L. Shirley, and C.-C. Kao, *Nonresonant inelastic x-ray scattering study of cubic boron nitride*, Physical Review B **64** (2001).

[554] G. Cappellini, G. Satta, M. Palummo, and G. Onida, *Optical properties of BN in cubic and layered hexagonal phases*, Physical Review B **64** (2001).

[555] A. Gloter, A. Douiri, M. Tencé, and C. Colliex, *Improving energy resolution of EELS spectra: an alternative to the monochromator solution*, Ultramicroscopy **96**, 385 (2003).

[556] Y. Osaka, A. Chayahara, H. Yokoyama, M. Okamoto, T. Hamada, T. Imura, and M. Fujisawa, *Characterization of BN Thin Films Deposited by Plasma CVD*, Materials Science Forum **54-55**, 277 (1990).

[557] H. K. Schmid, *Phase Identification in Carbon and BN Systems by EELS*, Microscopy Microanalysis Microstructures **6**, 99 (1995).

[558] R. Arenal, O. Stéphan, M. Kociak, D. Taverna, A. Loiseau, and C. Colliex, *Electron Energy Loss Spectroscopy Measurement of the Optical Gaps on Individual Boron Nitride Single-Walled and Multiwalled Nanotubes*, Physical Review Letters **95**, 127601 (2005).

[559] C. Tarrio and S. E. Schnatterly, *Interband transitions, plasmons, and dispersion in hexagonal boron nitride*, Physical Review B **40**, 7852 (1989).

[560] W. J. Zhang, H. Kanda, and S. Matsumoto, *Cathodoluminescence of cubic boron nitride films deposited by chemical vapor deposition*, Applied Physics Letters **81**, 3356 (2002).

[561] V. B. Shipilo, E. M. Shishonok, and A. I. Lukomskii, *Electron-vibrational structure in the 2.8–3.6 eV range of the cathodoluminescence spectra of sphaleritic boron nitride*, J Appl Spectrosc **53**, 1017 (1990).

[562] T. Taniguchi, K. Watanabe, S. Koizumi, I. Sakaguchi, T. Sekiguchi, and S. Yamaoka, *Ultraviolet light emission from self-organized p–n domains in cubic boron nitride bulk single crystals grown under high pressure*, Applied Physics Letters **81**, 4145 (2002).

[563] V. A. Gubanov, Z. W. Lu, B. M. Klein, and C. Y. Fong, *Electronic structure of defects and impurities in III-V nitrides: Vacancies in cubic boron nitride*, Phys. Rev. B **53**, 4377 (1996).

[564] I. A. Howard, *Stability of interstitials in cubic boron nitride*, Solid State Communications **99**, 697 (1996).

[565] Element Six, De Beers Group Company, http://www.e6.com/wps/wcm/connect/E6ContentEN/Home.

[566] K. Karch and F. Bechstedt, *Ab initio lattice dynamics of BN and AlN: Covalent versus ionic forces*, Phys. Rev. B **56**, 7404 (1997).

[567] F. Bechstedt, U. Grossner, and J. Furthmüller, *Dynamics and polarization of group-III nitride lattices: A first-principles study*, Physical Review B **62**, 8003 (2000).

[568] S. Bağcı, S. Duman, H. Tütüncü, G. Srivastava, and G. Uğur, *Ab initio calculation of the structural and dynamical properties of the zinc-blende BN and its (110) surface*, Diamond and Related Materials **15**, 1161 (2006).

[569] M. I. Eremets, K. Takemura, H. Yusa, D. Golberg, Y. Bando, V. D. Blank, Y. Sato, and K. Watanabe, *Disordered state in first-order phase transitions: Hexagonal-to-cubic and cubic-to-hexagonal transitions in boron nitride*, Physical Review B **57**, 5655 (1998).

université PARIS-SACLAY
ÉCOLE DOCTORALE
Ondes et Matière (EDOM)

**Titre :** Spectroscopie de matériaux 2D fragiles: du Graphène Oxydé aux molécules isolées sur du Nitrure de Bore hexagonal

**Mots clefs :** EELS, cathodoluminescence, défauts cristallins, nitrure de bore, graphène oxydé, molécules isolées

**Résumé :** La spectroscopie de perte d'énergie des électrons (EELS) et la cathodoluminescence (CL) dans un microscope électronique en transmission à balayage (STEM) sont des techniques puissantes pour l'étude des nanostructures isolées. Cependant, des électrons rapides peuvent endommager fortement des échantillons minces et fragiles, ce qui limite la résolution spatiale et l'intensité des signaux spectroscopiques. Pendant cette thèse, nous avons dépassé cette restriction par le développement de protocoles d'acquisition spécifiques pour l'étude de certains archétypes de nanosystèmes fragiles. Dans la première partie de cette thèse, j'ai analysée la chimie du graphène oxydé (GO) et GO réduit (RGO) par spectroscopie EELS. Grâce aux spécificités techniques de notre microscope et à la définition des conditions d'illumination optimales, j'ai obtenu des spectres du (R)GO d'une qualité inédite, à une résolution spatiale jamais achevée auparavant. Ensuite, j'ai réalisé les premières expériences de STEM-CL sur des molécules individuelles déposées sur du nitrure de bore hexagonal (h-BN). Les effets d'illumination ont été réduits en utilisant un mécanisme d'excitation indirect et une routine innovante d'acquisition par balayage aléatoire. L'intérêt porté aux propriétés optiques du h-BN a inspiré l'étude du BN cubique (c-BN). Dans des cristaux très purs, j'ai identifié par EELS une bande interdite d'énergie plus grande que précédemment rapportée et plus proche des calculs. Dans des cristaux moins purs, j'ai caractérisé plusieurs émissions associées à des défauts en utilisant les techniques de CL et interférométrie en intensité de Hanbury-Brown et Twiss dans le STEM.

**Title :** Spectroscopy in Fragile 2D Materials: from Graphene Oxide to Single Molecules at Hexagonal Boron Nitride

**Keywords :** EELS, cathodoluminescence, crystal defects, boron nitride, graphene oxide, isolated molecules

**Abstract :** Electron energy loss spectroscopy (EELS) and cathodoluminescence (CL) in a scanning transmission electron microscope (STEM) are extremely powerful techniques for the study of individual nanostructures. Nevertheless, fast electrons damage extremely sensitive thin specimens, imposing strong limitations on the spatial resolution and the intensity of spectroscopic signals. During this thesis we have overcome this restriction by developing material-specific acquisition protocols for the study of some archetypical fragile nanosystems. In the first part of this thesis I have analysed the chemistry of graphene oxide (GO) and reduced GO (RGO) by EELS spectroscopy. Thanks to the particular set-up of our microscope and by experimentally defining the optimal illumination conditions, I have obtained EELS spectra of (R)GO of an unprecedented quality, at a spatial resolution never achieved before. Afterwards, I have performed the first STEM-CL investigation of isolated molecules deposited on hexagonal boron nitride (h-BN). We have lowered the illumination effects by using an indirect excitation mechanism and an innovative random scan acquisition routine. Finally, the attractive optical properties of h-BN have led to the study of cubic BN (c-BN). In highly pure crystals, I have identified by EELS a wider optical band-gap with respect to previous experimental studies and in better agreement with recent calculations. In commercial crystals, I have characterized several defect-related emissions using CL and Hanbury-Brown and Twiss intensity interferometry in the STEM.

**Université Paris-Saclay**
Espace Technologique / Immeuble Discovery
Route de l'Orme aux Merisiers RD 128 / 91190 Saint-Aubin, France